

A Numerical Study on the Structural Implications of Utilising Bio-Based Materials in Wind Turbine Blades

Kimberly M.M. van den Bogaard

Master of Science Thesis

A Numerical Study on the Structural Implications of Utilising Bio-Based Materials in Wind Turbine Blades

MASTER OF SCIENCE THESIS

For the degree of Master of Science in European Wind Energy Master -
Rotor Design - Structures & Composites at Delft University of
Technology and Technical University of Denmark

Kimberly M.M. van den Bogaard

Supervisors:

Lars Pilgaard Mikkelsen

Philipp U. Haselbach

Jenni Rinker

Julie Teuwen

January 31, 2025

Faculty of Aerospace Engineering · Delft University of Technology
Department of Wind and Energy Systems · Technical University of Denmark



Copyright © Department of Wind and Energy Systems
All rights reserved.



Copyright © Wind Energy Group
All rights reserved.

A numerical study on the structural implications of utilising bio-based materials in wind turbine blades



Kimberly Margaretha Maria van den Bogaard

DTU Wind Energy-M-0517

January 2025

Author: Kimberly Margaretha Maria van den Bogaard

DTU Wind Energy-M-0517
January 2025

Title:

A numerical study on the structural implications of utilising bio-based materials in wind turbine blades

ECTS: 45

Education: Master of Science

Supervisors:

Lars Pilgaard Mikkelsen
Philipp U. Haselbach
Jenni Rinker

DTU Wind Energy

Julie Teuwen
TU Delft

Remarks:

This report is submitted as partial fulfillment of the requirements for graduation in the above education at the Technical University of Denmark.

DTU Wind Energy is a department of the Technical University of Denmark with a unique integration of research, education, innovation and public/private sector consulting in the field of wind energy. Our activities develop new opportunities and technology for the global and Danish exploitation of wind energy. Research focuses on key technical-scientific fields, which are central for the development, innovation and use of wind energy and provides the basis for advanced education at the education.

Technical University of Denmark
Depart. of Wind and Energy Systems
Frederiksborgvej 399
4000 Roskilde
Denmark
www.vindenergi.dtu.dk

Abstract

The growing wind energy industry is crucial in addressing climate change, but the environmental sustainability of wind turbine components, particularly blades, remains a pressing concern. This study explores the potential of natural fibre-reinforced polymer composites (NFRCs) as a sustainable alternative for wind turbine blade design, thereby addressing both sourcing and manufacturing stages as well as the end-of-life stage of blades. This thesis specifically explores the structural implications of integrating bio-based materials in wind turbine blades. The research focuses on redesigning the DTU 12.6 m research blade's structural design to enhance environmental sustainability while maintaining structural integrity.

The findings from the literature study reveal that while NFRCs have the potential to reduce the environmental footprint of wind turbine blades, their lower mechanical properties, including stiffness, strength, and torsional rigidity, pose challenges to their direct replacement of traditional glass fibre composites. A sensitivity study on the implications of the different material engineering constants identified the critical design parameters when switching to NFRCs. The UD longitudinal stiffness, in the direction of the blade length, drives the deflections which in turn effect the failure limits defined by the Tsai-Wu criterion. This emphasized the importance of the strength values of the materials. The shear stiffness of the BIAx material is critical for the torsional rigidity of the blade for which the thickness of the core material needs to be considered as well. Based on the results of the sensitivity study, the materials for the redesign of the DTU 12.6 m blade were selected as UD Flax/PLA and BIAx Ramie/PLA.

The structural redesign process showed that the torsional rigidity and material strengths are the primary drivers for the bio-based blade design. This differs from the conventional blade design where the tip deflection and therefore specific stiffnesses are the main drivers. Furthermore, adjustments to the shear web core thickness proved ineffective in improving torsional rigidity within the 2D shell element modelling framework, pointing to the necessity of advanced 3D modelling for accurate analysis. Using the 2D shell model, the hybridization of NFRCs emerged as a potential solution to enhance performance. However, achieving structural requirements required increased material usage, resulting in a blade mass over 15% higher than the original design. Further structural innovations, such as incorporating stiffen-

ers and ribs, are proposed to address these challenges. Additionally, the redesigned blade's estimated structural Campbell diagram indicates potential resonance issues, necessitating comprehensive aeroelastic analyses to confirm operational stability.

The study highlights the need for further refinement of NFRC material properties, advancing modelling techniques, and exploring alternative design approaches to fully realize the potential of bio-based materials in wind turbine applications. Key recommendations include experimental validation of NFRC properties, micro-mechanical model refinement, enhancement of mechanical performance of NFRCs, exploration of alternative NFRC materials like bamboo strips, and further structural and aeroelastic studies. The research concludes with a call for life cycle assessments to evaluate the environmental impacts comprehensively, thereby supporting the development of sustainable and structurally viable bio-based wind turbine blades.

Table of Contents

Acknowledgements	xix
1 Introduction	1
2 State of the Art Wind Turbine Blade Design and Materials	5
2-1 Wind Turbine Blade Design Methodology	5
2-2 Wind Turbine Blade Materials	8
2-2-1 Conventional Composite Materials	8
2-2-2 Bio-based alternatives	11
2-2-3 Existing examples on bio-based blades	16
2-3 Research Questions	17
3 DTU 12.6 m Wind Turbine Blade Models	19
3-1 HAWC2 model	19
3-2 Abaqus Models	24
3-2-1 Continuum shell element model	25
3-2-2 Conventional shell element model	26
3-3 Blade Modelling Tool and Baseline Lay-up Design	27
4 Methodology - Sensitivity Study	31
4-1 Sensitivity Study on the Relation between Material Engineering Constants and Blade Behaviour	31
4-1-1 Loadcase Selection	32
4-1-2 Method to establish the composite material properties for the selected NFRCs to inform the Sensitivity Study	36
4-1-3 Dry fibre and matrix properties	37
4-1-4 Calculated composite material properties for the selected NFRCs	39
4-1-5 Input parameters	44
4-1-6 Output Parameters	48

4-2	Verification of geometric linearity assumption	49
5	Results & Discussion: Sensitivity Analysis	51
5-1	Core material test results	51
5-2	Torque loadcase results	52
5-3	Pressure-to-Suction loadcase results	53
5-4	Trailing-to-Leading edge loadcase results	56
5-5	Results of verification of geometric linearity	60
5-6	Material selection based on results sensitivity study	63
6	Methodology - Structural Redesign of DTU 12.6 m Blade with NFRCs	65
6-1	Model parameters	65
6-2	Redesign evaluation methodology	68
7	Results & Discussion: Structural Redesign DTU 12.6 m Blade with NFRCs	71
7-1	Design Iteration 1 - 1 on 1 material replacement	71
7-2	Design Iteration 2 - match tip deflection curve of PTS loadcase	72
7-3	Design Iteration 3 - match tip deflection curve of TTL loadcase	74
7-4	Design Iteration 4 - match RM3 of Torque loadcase	77
7-5	Final redesign evaluation	82
7-5-1	Estimated Structural Campbell Diagram and Aeroelasticity Predictions	86
8	Conclusions	89
8-1	Conclusions	89
8-2	Recommendations	90
A	HAWC2 controller re-tuning process	93
A-1	Final HAWC2 model results - DLC1.1 statistical data	110
A-1-1	AEP comparison	118
B	Micro-Mechanical Model for Fibre Reinforced Composite Lamina	119
C	Classical Laminate Theory	125
D	Natural Fibre Material Properties from Literature	129
E	Sensitivity Study Details	133
E-1	Calculation volume percentage UD/BIAX material	133
E-2	Torque full results	134
E-3	PTS full results	135
E-4	STP full results	139
E-5	TTL full results	147
	Bibliography	155

Glossary

163

List of Figures

1-1	Waste treatment hierarchy [8].	2
2-1	Typical process for the design and analytical evaluation of wind turbine blades [22].	6
2-2	Application of limit states design approach for structural blade design verification as prescribed by the international standards IEC 61400-5 [22].	7
2-3	General workflow for the structural design of a wind turbine blade.	7
2-4	Schematic representation of the hierarchical structure of flax; from plant to cellulose [41].	13
2-5	Influence of the microfibril angle (MFA) on the mechanical properties of plant fibres [41]. (A) Fibre like Hemp. (B) Fibre like Cotton.	14
2-6	Schematic illustration of the four different porosity sub-components that have been identified from composite cross-sections [43].	14
3-1	HAWC2 model depiction.	21
3-2	Stepwind results of the HAWC2 model of the DTU 12.6 m blade. Top left is the input windspeed, the other plots are the operational output channels.	22
3-3	Blade bending moment load envelops of design loadcases DLC 1.1 and DLC 1.3, calculated with the HAWC2 model with the DTU 12.6 m blade. Flapwise load direction is denoted by M_x , edgewise load direction is denoted by M_y	23
3-4	Schematic representation of the wind turbine in the HAWC2 model with the DTU 12.6 m blade.	24
3-5	Geometry of the DTU 12.6 m blade [21] as defined in the Abaqus models.	25
3-6	Cross-section with section definitions in the Abaqus continuum shell element (SC8R) model of the DTU 12.6 m blade [21] at a radial position of 5.23 m.	26
3-7	Ply stack plot of trailing edge panel at a radial position of 5.23 m of the DTU 12.6 m blade model [21] with 8-noded reduced integration continuum shell elements (SC8R) in Abaqus.	26
3-8	Ply stack plot of upper sparcap at a radial position of 4.74 m of the DTU 12.6 m blade model [21] with 8-noded reduced integration conventional shell elements (S8R) in Abaqus.	27

3-9	Section distribution per cross-section of the DTU 12.6 m blade from the Blade Modelling Tool.	28
3-10	Print screen of the "LayupID" sheet of the Blade Modelling Tool of the Technical University of Denmark [58] based in Excel.	29
3-11	Blade structural design of the DTU 12.6 m blade from the Blade Modelling Tool [58]. Total material thickness distribution visualised composed of all materials present.	30
4-1	Flow diagram on the general methodology for the sensitivity study on material properties and blade behaviour for the DTU 12.6 m blade.	32
4-2	The Abaqus blade model of the DTU 12.6 m blade with the applied loads defined.	33
4-3	The Abaqus visualisation of the results of the DTU 12.6 m baseline blade model under the PTS loadcase. The deformed blade is visualised on top of the undeformed blade to visualise the change under loading. Subfigure (a) displays the stress distribution σ_{11} using the material coordinate system where the 1 direction is in the direction of the blade length. Subfigure (b) displays the deflection U1 where the 1 direction aligns with the global coordinate system in the direction of the blade chord.	35
4-4	Flow diagram on the methodology to obtain the composite material properties for UD and BIAx lamina of several NFRCs.	37
4-5	Comparison between absolute stiffness E_1 and specific stiffness E_1/ρ for the UD and BIAx composites in MPa, comparing GFRC with several NFRCs.	42
4-6	Comparison between absolute shear stiffness G_{12} and specific shear stiffness G_{12}/ρ for the UD and BIAx composites in MPa, comparing GFRC with several NFRCs.	42
4-7	Flow diagram on the methodology to obtain the input parameters for the sensitivity analysis on the DTU 12.6 m blade.	44
5-1	Significant results of sensitivity study on torque loadcase of the DTU 12.6 m blade: percentage difference in RM3.	52
5-2	Percentage difference in RM3 vs percentage change in G_{12} input for the torque loadcase in the sensitivity study on the DTU 12.6 m blade.	53
5-3	Significant results of sensitivity study on PTS loadcase of the DTU 12.6 m blade: percentage difference in tip deflection magnitude.	54
5-4	Percentage difference in tip deflection magnitude vs percentage change in E_1 input for the PTS loadcase in the sensitivity study on the DTU 12.6 m blade.	55
5-5	Percentage difference in max. Tsai-Wu value vs percentage change in ν_{12} input for the PTS loadcase of the sensitivity study on the DTU 12.6 m blade.	56
5-6	Significant results of the sensitivity study on the TTL loadcase for the DTU 12.6 m blade: percentage difference in maximum Tsai-Wu value.	57
5-7	Percentage difference in max. Tsai-Wu value vs percentage change in E_1 input for the TTL loadcase of the sensitivity study on the DTU 12.6 m blade.	59
5-8	Percentage difference in tip deflection magnitude vs percentage change in E_1 input for the TTL loadcase of the sensitivity study on the DTU 12.6 m blade. Note: $E_1 = E_2$ for the BIAx material.	59
5-9	Percentage difference in max. Tsai-Wu value vs percentage change in ν_{12} input for the TTL loadcase of the sensitivity study on the DTU 12.6 m blade.	60
6-1	Clamped surface of the DTU 12.6 m blade at $r = 10.8$ m for load application.	66
6-2	Workflow to generate Abaqus conventional shell element model of the DTU 12.6 m blade from the BMT where the lay-up design is specified.	68

6-3	Methodology of the redesign process where NFRCs will replace the GFRCs in the DTU 12.6 m research wind turbine blade. The workflow in the dotted lines, using NFRCs, is the scientific contribution of this thesis.	69
7-1	DTU 12.6 m blade flapwise deflection under PTS loading for different designs with NFRCs (left) compared to the baseline design with GFRC, with a zoom-in on the blade tip deflection (right).	73
7-2	Comparison of layup design of the sparcaps (indicated by "flanges" in the BMT) for the DTU 12.6 m blade baseline layup of design iteration 1 and the PTS redesign iteration layup with NFRCs.	74
7-3	DTU 12.6 m blade deflection under TTL loading for different design iterations with NFRCs compared to that of the baseline design with GFRC.	75
7-4	Layup design for all sections of the DTU 12.6 m blade in the TTL redesign iteration with NFRCs.	76
7-5	Evolution of the required torque RM3 (a) and total blade mass (b) through the different redesign iterations of the DTU 12.6 m blade with NFRCs.	78
7-6	Cross-section at $r = 2.6$ m of DTU 12.6 m redesign iteration 3 and a test design for the Torque redesign iteration where the core thickness of the shearwebs have been increased significantly.	78
7-7	Rotational displacement along the DTU 12.6 m blade (left) leading to the applied twist of 10° at $r = 10.8$ m, with a zoom-in on the twist at $r = 7.9$ m (right).	79
7-8	Layup design for all sections of the DTU 12.6 m blade in the final (Torque) redesign iteration with NFRCs.	81
7-9	Maximum Tsai-Wu value distribution of DTU 12.6 m blade baseline design under PTS loading.	82
7-10	Maximum Tsai-Wu value distribution of DTU 12.6 m blade design iteration 4, redesign for Torque with NFRCs, under PTS loading.	83
7-11	Maximum Tsai-Wu value distribution of DTU 12.6 m blade design iteration 4, redesign for Torque with NFRCs, under PTS loading. Zoom-in on location with overall highest Tsai-Wu value at $r = 3.72$ m.	83
7-12	Maximum Tsai-Wu value distribution of DTU 12.6 m baseline design under TTL loading.	84
7-13	Maximum Tsai-Wu value distribution of DTU 12.6 m blade design iteration 4, redesign for Torque with NFRCs, under TTL loading.	84
7-14	Maximum Tsai-Wu value distribution of DTU 12.6 m design iteration 4, redesign for Torque, under TTL loading. Zoom-in on location with overall highest Tsai-Wu value: TE at the root at $r = 1$ m.	85
7-15	Maximum Tsai-Wu value distribution DTU 12.6 m blade design iteration 4, redesign for Torque with NFRCs, under Torsion load. Zoom-in on blade tip at with load introduction at $r = 10.8$ m.	85
7-16	Maximum Tsai-Wu value distribution of the DTU 12.6 m baseline design under Torsion load. Zoom-in on blade tip at with load introduction at $r = 10.8$ m.	86
7-17	The estimated structural Campbell diagram for the first order blade modes of the DTU 12.6 m redesigned blade with NFRCs.	87
A-1	Extreme design loads from DLC1.3 calculated from received HAWC2 model and provided to the Abaqus model of the DTU 12.6 m blade. Upper left subplot: flapwise bending moment towards tower, upper right subplot: flapwise bending moment away from tower, lower left subplot: edgewise bending moment towards trailing edge, lower right subplot: edgewise bending moment towards leading edge.	93

A-2	Stepwind results of original HAWC2 model of the DTU 12.6 m blade as received.	94
A-3	Stepwind results of new HAWC2 model of the DTU 12.6 m blade with the controller tuning parameters from attempt 5 and attempt 6.	98
A-4	Zoom in on stepwind pitch and electrical power results of new HAWC2 model of the DTU 12.6 m blade with the controller tuning parameters from attempt 5 and attempt 6.	99
A-5	Aeroelastic campbell diagram of new stable HAWC2 model of the DTU 12.6 m blade.	100
A-6	Aeroelastic damping diagram of new stable HAWC2 model of the DTU 12.6 m blade.	101
A-7	Minimum tower clearance comparison between new and original HAWC2 model for the DTU 12.6 m blade in DLC1.1.	102
A-8	Aerodynamic thrust maxima, minima and mean comparison between new and original HAWC2 model for the DTU 12.6 m blade in DLC 1.1	102
A-9	Out of plane blade root moment maxima, minima and mean comparison between new and original HAWC2 model for the DTU 12.6 m blade in DLC 1.1	102
A-10	Time series outputs for original simulation dlc12_wsp16_wdir010_s16005.htc for the DTU 12.6 m blade. Showing from top to bottom the wind speed, pitch angle, rotor speed, electrical power and generator torque.	103
A-11	Close-up of time series outputs for original simulation dlc12_wsp16_wdir010_s16005.htc for the DTU 12.6 m blade. Showing from top to bottom the wind speed, pitch angle, rotor speed, electrical power and generator torque.	104
A-12	Close-up of time series outputs for dlc12_wsp16_wdir010_s16005.htc for the DTU 12.6m blade with variations in controller parameters 33 and 34. Showing from top to bottom the wind speed, pitch angle, rotor speed, electrical power and generator torque.	105
A-13	Close-up of time series outputs for dlc12_wsp16_wdir010_s16005.htc for the DTU 12.6 m blade with variations in controller parameters 19 and 20. Showing from top to bottom the wind speed, pitch angle, rotor speed, electrical power and generator torque.	106
A-14	Close-up of time series outputs for dlc12_wsp16_wdir010_s16005.htc for the DTU 12.6 m blade with variations in controller parameter 19. Showing from top to bottom the wind speed, pitch angle, rotor speed, electrical power and generator torque.	107
A-15	Close-up of time series outputs for dlc12_wsp16_wdir010_s16005.htc for the DTU 12.6 m blade with variations in controller parameter 20. Showing from top to bottom the wind speed, pitch angle, rotor speed, electrical power and generator torque.	108
A-16	Close-up of time series outputs for dlc12_wsp16_wdir010_s16005.htc for the DTU 12.6 m blade with variations in controller parameters 19, 20, 33 and 34. Showing from top to bottom the wind speed, pitch angle, rotor speed, electrical power and generator torque.	109
A-17	Pitch angle maxima, minima and mean comparison between final and original HAWC2 model of the DTU 12.6 m blade in DLC1.1.	111
A-18	Rotor speed maxima, minima and mean comparison between final and original HAWC2 model of the DTU 12.6 m blade in DLC1.1.	111
A-19	Electrical power maxima, minima and mean comparison between final and original HAWC2 model of the DTU 12.6 m blade in DLC1.1.	112
A-20	Generator torque maxima, minima and mean comparison between final and original HAWC2 model of the DTU 12.6 m blade in DLC1.1.	112
A-21	Aerodynamic thrust maxima, minima and mean comparison between final and original HAWC2 model of the DTU 12.6 m blade in DLC1.1.	113

A-22	Tower base Fore-Aft moment maxima, minima and mean comparison between final and original HAWC2 model of the DTU 12.6 m blade in DLC1.1.	114
A-23	Tower base Side-Side moment maxima, minima and mean comparison between final and original HAWC2 model of the DTU 12.6 m blade in DLC1.1.	114
A-24	Yaw bearing pitch moment maxima, minima and mean comparison between final and original HAWC2 model of the DTU 12.6 m blade in DLC1.1.	115
A-25	Yaw bearing roll moment maxima, minima and mean comparison between final and original HAWC2 model of the DTU 12.6 m blade in DLC1.1.	115
A-26	Shaft torsion moment maxima, minima and mean comparison between final and original HAWC2 model of the DTU 12.6 m blade in DLC1.1.	116
A-27	Flapwise blade root moment maxima, minima and mean comparison between final and original HAWC2 model of the DTU 12.6 m blade in DLC1.1.	117
A-28	Edgewise blade root moment maxima, minima and mean comparison between final and original HAWC2 model of the DTU 12.6 m blade in DLC1.1.	117
A-29	Minimum tower clearance comparison between final and original HAWC2 model of the DTU 12.6 m blade in DLC1.1.	118
B-1	Schematic illustration of the four different porosity sub-components that have been identified from composite cross-sections [43].	119
E-1	Percentage difference in RM3 as a result of a 10° twist at $r = 10.8$ m of the DTU 12.6 m blade: UD sensitivity results.	134
E-2	Percentage difference in RM3 as a result of a 10° twist at $r = 10.8$ m of the DTU 12.6 m blade: BIAx sensitivity results.	135
E-3	Percentage difference in tip deflection magnitude of the DTU 12.6 m blade: UD sensitivity results in PTS loading	136
E-4	Percentage difference in tip deflection magnitude of the DTU 12.6 m blade: BIAx sensitivity results in PTS loading	137
E-5	Percentage difference in maximum Tsai-Wu value of the DTU 12.6 m blade: UD sensitivity results under PTS loading.	138
E-6	Percentage difference in maximum Tsai-Wu value of the DTU 12.6 m blade: BIAx sensitivity results under PTS loading.	139
E-7	Percentage difference in tip deflection magnitude of the DTU 12.6 m blade: UD sensitivity results under STP loading.	140
E-8	Percentage difference in tip deflection magnitude of the DTU 12.6 m blade: BIAx sensitivity results under STP loading.	141
E-9	Percentage difference in tip deflection magnitude of the DTU 12.6 m blade under STP loading: significant parameters from sensitivity study.	142
E-10	Percentage difference in tip deflection magnitude vs percentage change in E_1 input for the DTU 12.6 m blade under STP loading.	143
E-11	Percentage difference in maximum Tsai-Wu value of the DTU 12.6 m blade: UD sensitivity results under STP loading.	144
E-12	Percentage difference in maximum Tsai-Wu value of the DTU 12.6 m blade: BIAx sensitivity results under STP loading.	145
E-13	Percentage difference in maximum Tsai-Wu value for the DTU 12.6 m blade under STP loading: significant parameters from sensitivity study.	146
E-14	Percentage difference in max. Tsai-Wu value vs percentage change in E_1 input for the DTU 12.6 m blade under STP loading.	146

E-15 Percentage difference in max. Tsai-Wu value vs percentage change in ν_{12} input for the DTU 12.6 m blade under STP loading.	147
E-16 Percentage difference in tip deflection magnitude of the DTU 12.6 m blade: UD sensitivity results under TTL loading.	148
E-17 Percentage difference in tip deflection magnitude of the DTU 12.6 m blade: BIAX sensitivity results under TTL loading.	149
E-18 Percentage difference in maximum Tsai-Wu value for the DTU 12.6 m blade: UD sensitivity results under TTL loading.	150
E-19 Percentage difference in maximum Tsai-Wu value for the DTU 12.6 m blade: BIAX sensitivity results under TTL loading.	151
E-20 Significant results of sensitivity study on TTL loadcase for the DTU 12.6 m blade: percentage difference in tip deflection magnitude.	152
E-21 Percentage difference in tip deflection magnitude vs percentage change in E_1 input for the TTL loadcase of the sensitivity study on the DTU 12.6 m blade.	153

List of Tables

2-1	Material properties of the materials used in the DTU 12.6 m blade model [21]. Fibre volume fractions for the unidirectional (UD) and bi-axial (BIAX) glass epoxy composites are $V_f = 0.53$	10
2-2	Material properties of the glass fibres and the epoxy resin used by DTU.	11
3-1	Wind turbine dimensions of the HAWC2 model with the DTU 12.6 m blade [21].	20
4-1	The applied loads used in the sensitivity study on the DTU 12.6 m blade, which are the applied loads in the received 3D continuum shell element Abaqus model of the DTU 12.6 m blade.	33
4-2	Comparison of the absolute deflection and stress levels between two flapwise loads for the DTU 12.6 m baseline blade using the 3D continuum shell element Abaqus model. Difference is given by $\frac{STP-PTS}{PTS} \cdot 100\%$	34
4-3	Comparison of deflection and stress levels between two edgewise loads for the DTU 12.6 m baseline blade using the 3D continuum shell element Abaqus model. Difference is given by $\frac{TTL-LTT}{LTT} \cdot 100\%$	34
4-4	Dry fibre properties of several natural fibres, alongside the glass fibre properties used by DTU.	38
4-5	Material properties of bio-based resins PLA and PLLA, along with the epoxy resin used by DTU. The asterix (*) indicates that the value is assumed equal to the epoxy resin due to the lack of available information.	39
4-6	UD composite properties of GFRC used by DTU with provided and calculated values, as well as the calculated UD composite properties of several NFRCs. Green cells indicate the maximum value among the NFRCs, while red cells indicates the minimum values among the NFRCs.	40
4-7	Flax/Epoxy composite properties from test data from literature [64] as well as calculated values using the micro-mechanical model. The calculation uses the material properties of the flax fibres and epoxy as specified in Section 4-1-3.	40
4-8	UD strength correction factors for the micro-mechanical model calculated from the difference between the calculated values and test values of the GFRC used by DTU, see Table 4-6.	41

4-9	BIAX strength correction factors for the micro-mechanical model calculated from the difference between the calculated values and test values of the GFRC used by DTU.	43
4-10	BIAX composite properties of GFRC used by DTU with provided and calculated values, as well as the calculated BIAX composite properties of several NFRCs. Green cells indicate the maximum value among the NFRCs, while red cells indicates the minimum values among the NFRCs.	43
4-11	Test cases for the sensitivity study on the UD material properties for the DTU 12.6 m blade. The terms "min" and "max" indicate whether the extreme test value is a minimum or maxima compared to the baseline values. The term "mid" refers to the test value at the midpoint of the baseline and extreme test value. The term "quarter" refers to the test value at one quarter from the baseline to the extreme test value. Red indicates the values changed compared to the baseline model. . .	46
4-12	Test cases for the sensitivity study on the BIAX material properties for the DTU 12.6 m blade. The terms "min" and "max" indicate whether the extreme test value is a minimum or maxima compared to the baseline values. The term "mid" refers to the test value at the midpoint of the baseline and extreme test value. The term "quarter" refers to the test value at one quarter from the baseline to the extreme test value. Red indicates the values changed compared to the baseline model. . .	47
5-1	DTU 12.6 m baseline blade model outputs that will be used in the analyses of the sensitivity study on the impact of individual material properties on the blade's behaviour.	51
5-2	Results of the sensitivity study on the Young's modulus of the core material of the DTU 12.6 m blade.	52
5-3	Outputs of the linear analysis of the selected Torque loadcases on the DTU 12.6 m blade, to verify with the guidelines for the incorporation of geometric non-linearity. . .	61
5-4	Outputs of the linear analysis of the selected PTS loadcases on the DTU 12.6 m blade, to verify with the guidelines for the incorporation of geometric non-linearity. . .	61
5-5	Percentage difference in sensitivity study output between the linear model and non-linear model of the DTU 12.6 m blade for the selected Torque and PTS loadcases.	62
5-6	Summary of the minima and maxima values for the design driving engineering constants within the set of NFRCs and their corresponding NFRC, along with values of the selected NFRCs for the redesign in Chapter 6 and Chapter 7.	63
6-1	Point forces to represent the DLC1.3 loadcase in the Abaqus DTU 12.6 m blade model.	66
6-2	Material properties of the NFRCs that will be used during the DTU 12.6 m blade redesign process along side the material properties of the conventional GFRCs [21] used in the baseline design.	67
7-1	Natural frequencies as calculated by Abaqus for the conventional shell element model of the DTU 12.6 m baseline (GFRC) and redesigned (NFRCs) blade.	87
A-1	Poles for the controller re-tuning of the DTU 12.6 m HAWC2 model.	96
A-2	Controller tuning parameters for the DTU 12.6 m blade for the various controller poles in Table A-1, alongside those of the model in the reference article by Gözcü et al. [76].	97
A-3	Content "wpdata.100" file specifying the minimum pitch angle for HAWC2.	99
D-1	Bamboo dry fibre properties obtained from literature.	129

D-2	Hemp dry fibre properties obtained from literature.	129
D-3	Flax dry fibre properties obtained from literature.	130
D-4	Sisal dry fibre properties obtained from literature.	130
D-5	Ramie dry fibre properties obtained from literature.	130
D-6	Jute dry fibre properties obtained from literature.	131
E-1	Volume percentage UD and BIAx material for different blade components of the DTU 12.6 m blade.	134

Acknowledgements

I would like to express my gratitude to my supervisors, Lars Mikkelsen, Julie Teuwen, Philipp Haselbach, and Jenni Rinker, for their continuous support, guidance, and valuable insights throughout this project. Your feedback and expertise were vital to the development of this research.

My appreciation also goes to David Robert Verelst, Ozan Gozcu, and Alan Wai Hou Lio for their assistance with HAWC2. Your expertise greatly enhanced the computational aspects of this work. Special thanks to Peter Berring for his help with BMT and Abaqus, which were essential for the structural analysis.

To my family, I am eternally grateful for your unwavering encouragement and love, which have been a constant source of strength throughout this journey. I also wish to thank my friends and roommates for their companionship and understanding during the most challenging times. A special mention goes to my yoga instructor, whose classes provided much-needed balance and calmness throughout the thesis process.

I would also like to extend my heartfelt thanks to Marie Gamborg Laursen, the DTU psychologist, and to the rehabilitation team at the Center for Rehabilitering og Forebyggelse in Hellerup, including Christina, Thomas, Anne Madde, and others. Your support was crucial to my recovery from post-concussion syndrome. Irene Verdouw, my occupational therapist in the Netherlands, has also been an indispensable part of my recovery journey, and I am deeply grateful for her help. Finally, I would like to express my gratitude to all the other healthcare professionals and providers who have aided in my recovery.

To everyone who played a role in this journey, thank you for your encouragement and care.

Sassenheim, the Netherlands
January 31, 2025

Kimberly M.M. van den Bogaard

“The greatest threat to our planet is the belief that someone else will save it.”

— *Robert Swan*

“What goes up must come down.”

— *Isaac Newton*

Chapter 1

Introduction

Human activities have unequivocally led to a significant increase in greenhouse gas concentrations since 1750 [1], with CO₂ emissions being the dominant contributor [2]. Addressing the climate crisis requires rapid and sustained emission reductions. "Accelerating the decarbonisation of the electricity mix is the single most important lever available to policy makers: it closes more than one-third of the emissions gap between the Announced Pledges Scenario (APS) and the Net Zero Emissions (NZE)", according to the World Energy Outlook of 2021 [3].

The wind energy industry, now cost-competitive [4], plays a critical role. However, wind companies must ensure that their growth does not come at unchecked cost [5]. The wind industry itself needs to keep developing to optimise the technology while minimising waste and decarbonising the supply chain.

Generally, the manufacturing and installation stages account for 90% and 70% of the total carbon emissions for onshore and offshore wind farms respectively [5]. Furthermore, over 80% of a wind turbine mass is made of materials that can be recycled at End of Life (EoL), like steel and copper. However, the sourcing of these materials are CO₂ and energy intensive [6]. The other 20% mainly consist of fibre reinforced composite materials, which are difficult to recycle on a commercial scale with the currently available technologies [5]. The wind turbine blades are made of these fibre reinforced composite materials and face many challenge in terms of sustainability. The presented research will focus on the challenges associated with the wind turbine blades.

The concept of the circular economy provides a guideline for improving the sustainability of wind turbine blades. The aim is to maintain the highest product value for as long as possible. The waste treatment hierarchy follows this principle and is outlined in Figure 1-1. But there is more to the circular economy than the cascading product/material use. The circular economy also promotes the efficient use of resources, both recycled and virgin resources. The idea is to lose nothing and feed everything in a new cycle. The circular economy can be further enhanced when combined with the bio-economy to close biomass loops [7]. The implementation of the Circular Bio-Economy can contribute to limiting environmental impact and GHG emissions

by reducing required energy and resources through the closed loops. To succeed in establishing a circular bio-economy, it is important that all processes along the cascading product use are fully developed, energy efficient, cost effective and have low carbon intensity.

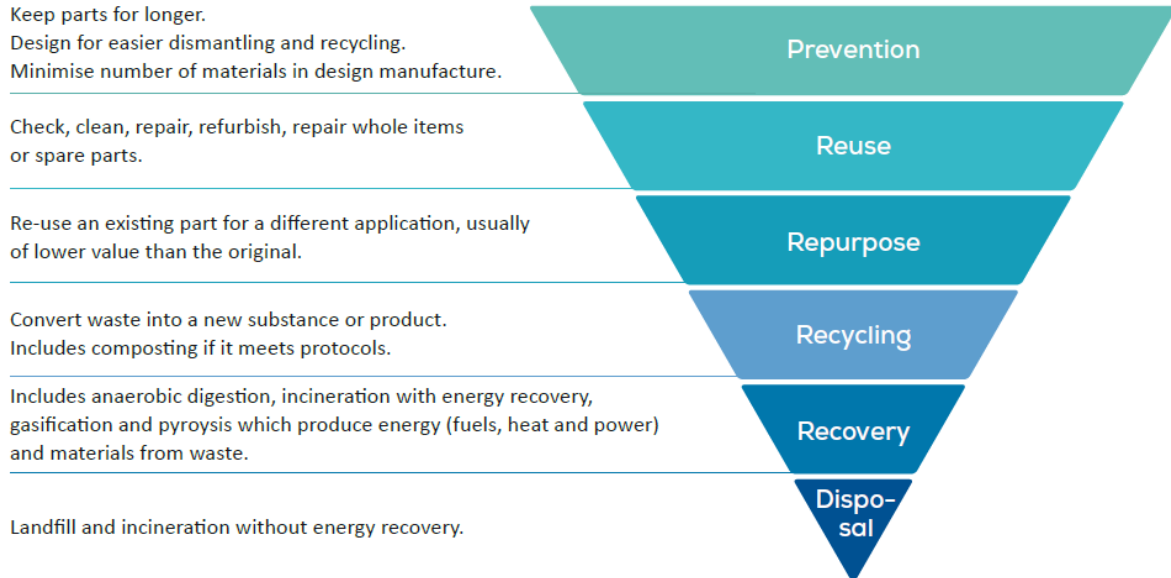


Figure 1-1: Waste treatment hierarchy [8].

Applying this framework to the wind turbine blade industry requires the establishment of refurbishing, repurposing and recycling technologies for the currently installed wind turbine blades. Moreover, the new wind turbine blades shall be designed to minimise waste streams, enable high level waste treatment and close biomass loops. The former includes waste stream reduction through life time extension as well as easing of the refurbishing, repurposing and recycling of the blades. Furthermore, closing biomass loops also requires the analysis of the material sourcing and manufacturing processes.

Maintenance and repair combined with health monitoring of wind turbine blades can facilitate life time extensions. The ReliaBlade project [9], a Danish-German joint research, investigates techniques to establish a unique Digital Twin for individual wind turbine blades. The twin includes all defects and imperfections of the manufactured blade. This allows for the tracking and prediction of the blade's current and future state in order to schedule maintenance and repair efficiently.

When refurbished blades come to their End of Life and can no longer be refurbished, the next best step is to repurpose them for alternative uses. Examples are the use of wind turbine blades as a playground for kids or for city benches [10]. However, finding suitable applications is challenging due to the varying blade sizes in the waste stream.

Once the repurposed products also reach their End of Life and further repurposing is not possible, the materials will need to enter the recycling stage. There are different recycling technologies that are currently being developed of which many are still at a low to medium Technology Readiness Level (TRL) [11][10]. The most mature technology is mechanical recycling, which involves the shredding or grinding of the blades to different particle sizes which can be used as fibrous reinforcement or powdered fillers. This method is relatively simple at

low cost and has reached industrial scale, however, the recycled materials are of significantly lower value compared to the original material [11].

The DecomBlades project [12] explores industrializing mechanical recycling and pyrolysis (thermal recycling) combined with cement co-processing to recycle composite blades. Siemens Gamesa has also developed recyclable blades utilising a resin that dissolves through solvolysis, a chemical recycling technique. Their first recyclable blades were installed in 2022 [13][14].

If recycling is not an option, energy recovery through incineration is the next step, followed by disposal in landfills as a last resort. Landfill is the most cheap and easy option but has large impacts on the environment on top of which value is lost. Recognising these drawbacks, the European industry organisation for wind energy, has called for a Europe-wide landfill ban on decommissioned wind turbine blades by 2025 [15], while other countries like "Germany, Austria, the Netherlands and Finland have already banned landfilling of turbine blades" [16] (and restricted landfilling in general [17][18]).

The above outlined strategies to improve the sustainability of wind turbine blades mainly focus on the end of life stages. However, in the circular bio-economy the goal is to minimise the environmental footprint throughout a products life while simultaneously closing biomass loops. This means that the material sourcing and manufacturing also need to be considered. The conventional wind turbine blades are made with glass and/or carbon fibres embedded in a plastic matrix material. The sourcing and manufacturing of these materials rely heavily on fossil fuels and consequently have a significant environmental impact [19]. The alternative use of bio-based materials provides a possible solution to reduce the environmental footprint of wind turbine blades throughout their lifetime while closing biomass loops. In the case of wind turbine blades this would mean the utilisation of natural fibre reinforced composites with a bio-based matrix material, as well as bio-based core materials (like the currently used balsa wood) and bio-based adhesives.

While bio-based materials provide a sustainable alternative, they still need to fulfil the structural requirements set by the design standards for wind turbine blades [20]. The current work will explore the structural implications of utilising bio-based materials in wind turbine blades through a numerical investigation. To perform the research, the DTU 12.6 m research wind turbine blade is taken as case study [21]. A sensitivity study will be performed, investigating the impact of different material engineering constants on the blade's performance. This will help identify which bio-based materials can potentially be applied in wind turbine blades. A structural redesign of the DTU 12.6 m blade with bio-based materials will follow to further investigate the implications of the use of bio-based alternatives.

Chapter 2 outlines the state of the art in wind turbine blade design, focussing on the structural design. After discussing the wind turbine blade materials and their bio-based alternatives, the research questions will be introduced. In Chapter 3 the different models of the DTU 12.6 m blade will be presented which form the baseline models for the rest of the work. Chapter 4 and Chapter 6 outline the applied methodologies to answer the research questions. Chapter 5 and Chapter 7 provide the results. Finally, Chapter 8 summarises the conclusions and provides recommendations for future research.

State of the Art Wind Turbine Blade Design and Materials

In this chapter the state of the art design practices for wind turbine blades are elaborated upon. The focus is placed on the structural design of the blades. The materials used are a critical component of the structural design. Therefore, the conventional materials used are elaborated upon and connected to the state of the art research on bio-based alternatives. The chapter concludes by presenting the research questions that will be addressed in the remainder of the work.

2-1 Wind Turbine Blade Design Methodology

The design of wind turbine blades is two-fold and consists of the aerodynamic design and the structural design. The aerodynamic forces, generated by the flow of wind over the blades, interacts with the blade structure. Consequential changes in the blade shape due to deformation of the structure will in turn affect the aerodynamic forces. This interaction between the aerodynamics and structure is defined as aeroelasticity. This interaction makes the design of a wind turbine blade complex, requiring an iterative process. A schematic overview of a typical design process for wind turbine blades is specified by the international standard IEC 61400-5 [22] and presented in Figure 2-1. The process consists of analytical and numerical calculations that are combined with validated material data and full scale blade testing. Details on the full scale blade testing are provided in IEC 61400-23 [23].

The essential design specification or requirements that the blade design needs to fulfil are outlined in the international standard IEC 61400-1 [20] and IEC 61400-5 [22]. The standard outlines a range of design loadcases for which the structure needs to be verified. These account for all relevant combinations of external conditions and design situations that a wind turbine may experience throughout its lifetime. The minimum required lifetime of a wind turbine is 20 years [20].

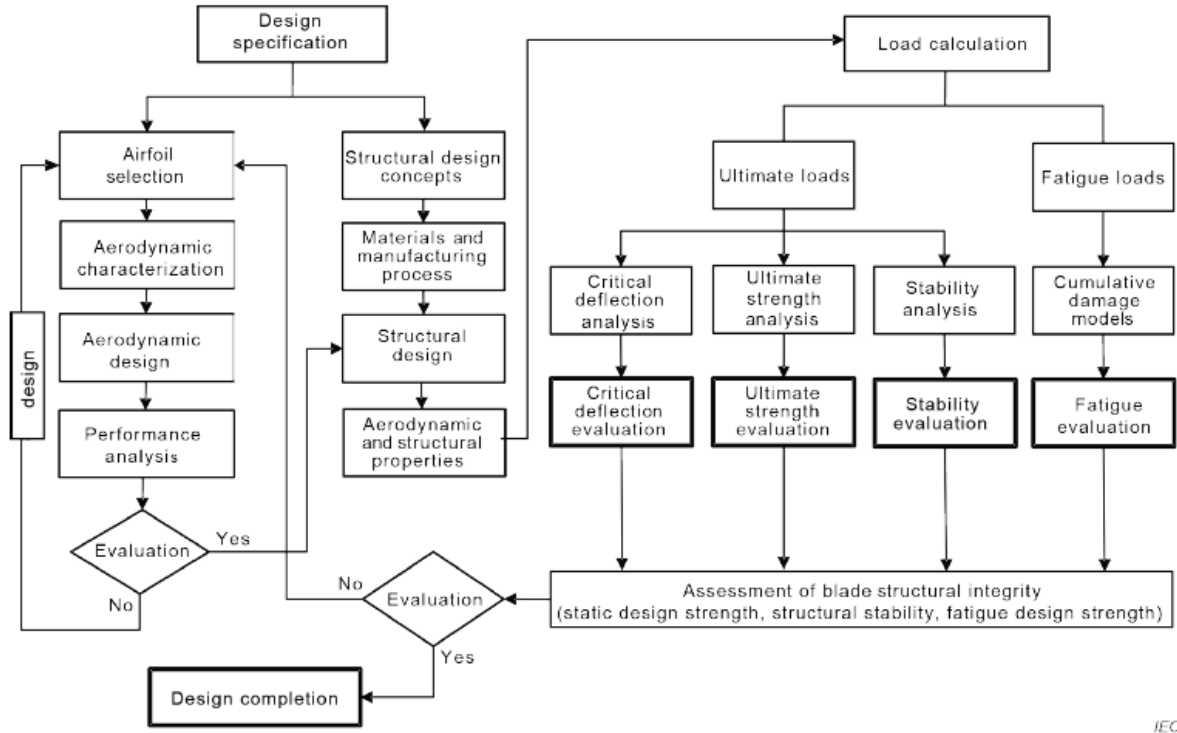


Figure 2-1: Typical process for the design and analytical evaluation of wind turbine blades [22].

A wind turbine's design is characterised by the wind conditions of the intended site. For this purpose several wind classes are defined in order to represent most applications. The wind turbine classes are specified through wind speed and turbulence parameters [20]. The specified wind conditions will be used to calculate the design loads from the different design loadcases as defined by IEC 61400-1 [20]. The calculation of the design loads requires the use of aeroservoelastic simulations that account for the fluid-structure interaction as well as the influence of the turbine control system. An example of such software is the Horizontal Axis Wind turbine simulation Code 2nd generation (HAWC2) developed by the Technical University of Denmark [24]. This simulation software calculates the wind turbine's response in the time domain from which the blade loads can be derived.

The limit states design approach [22] is required by the standards to ensure sufficient protection against damage throughout a turbine's lifetime. This approach applies a partial safety factor to both the calculated characteristic loads and the resistance to these loads. The partial safety factors account for uncertainties in the calculated response. The resistance can be expressed by stresses or strains. The limit state approach is schematically presented in Figure 2-2 and its general formulation is expressed by Equation 2-1:

$$S(\gamma_f F_k) \leq \frac{R_k}{\gamma_m \gamma_n} \quad (2-1)$$

Where S is a function of the structural response, F_k is the characteristic load, R_k is the characteristic material resistance and the γ 's the partial safety factors. The requirement is that the response of the design does not exceed the design resistance.

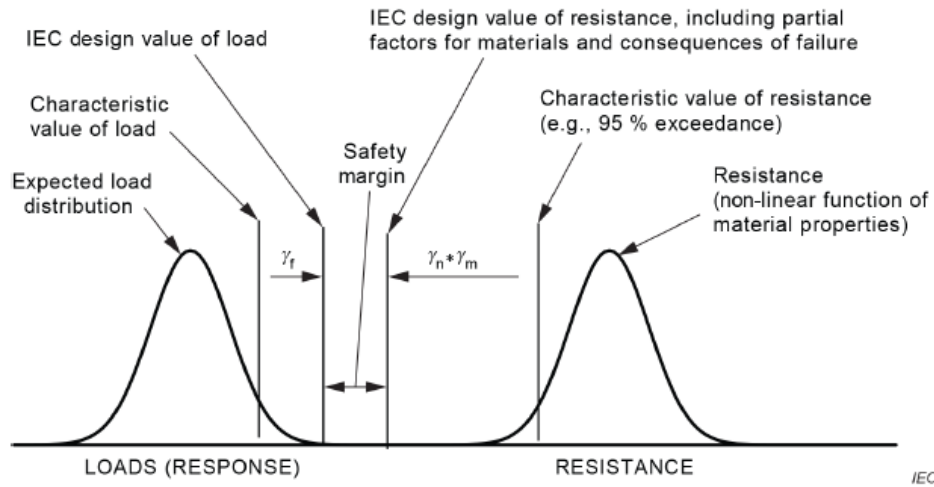


Figure 2-2: Application of limit states design approach for structural blade design verification as prescribed by the international standards IEC 61400-5 [22].

The structural design and verification of a wind turbine blade shall ensure the blade withstands both ultimate loads and fatigue loads [22]. Moreover, the analysis of critical deflection levels and stability issues are required [22]. Resonance issues as a result of aeroservoelastic interactions need to be addressed as well [22]. A general work flow for the structural design is presented in Figure 2-3. All possible failure modes need to be considered. Generally the resulting bending moments cover a wide range of failure modes [22]. However, combined loading may lead to different critical load directions other than flapwise/edgewise that need to be considered as well. Moreover, torsion loads need to be considered as well to account for bond strength failure for example [22].

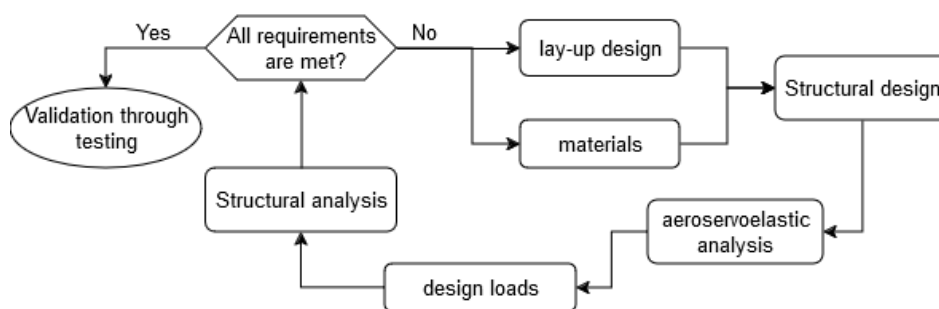


Figure 2-3: General workflow for the structural design of a wind turbine blade.

With the established design methodology for the structural design of a wind turbine blade, the next step is to look at the material selection. The material selection will determine the design resistance against which the response of the design needs to be compared for each design loadcase.

2-2 Wind Turbine Blade Materials

As visualised in Figure 2-3, the materials form an integral part of the structural design process of wind turbine blades. Therefore, the conventional composite materials used in the design will be introduced along with its environmental challenges. Since the research of this work utilises the DTU 12.6 m research wind turbine blade, its materials and their properties will be presented as well. The alternative bio-based materials with their advantages and challenges will be discussed afterwards. This section is concluded with examples from literature on the use of bio-based materials in wind turbine blades.

2-2-1 Conventional Composite Materials

The conventional wind turbine blades are made of composite materials which consists of strong and stiff fibres immersed in relatively soft matrix. The use of material in fibre form provides a much stronger and often stiffer material than when used in monolithic form. This is due to the fact that fibres contain fewer and smaller defects than the monolithic material [25]. Therefore, a collection of fibres of a given volume will be much stronger than the same volume of the monolithic material. Moreover, the increased number of interfaces make the material more damage tolerant. The increased strength holds for the direction parallel to fibres but not for loads perpendicular to the fibres, meaning that the material is highly anisotropic in contrast to the isotropic nature of the monolithic homogeneous materials with equal properties in all directions. This provides opportunities to tailor a material to its specific application by placing layers of fibres in specific directions. The fibres can also be woven into a fabric which can be draped to make complex structures.

The most commonly used fibre materials in wind turbine blades are glass and carbon fibres. Glass fibres are silica based and their Si and O atoms form a lattice without crystallographic order, leading to an amorphous structure with isotropic properties [26]. Glass fibres can be produced for specific purposes by adjusting their chemical composition. The most widely used form is E-glass which have superior mechanical properties. The fibres are treated with a surface coating to protect the fibres and improve the interface bonding between the fibres and the polymer matrix to improve composite properties [26][25]. In general, glass fibres have moderate stiffness, high strength and moderate density [26].

Carbon fibres have a high carbon content which form a highly aligned micro-structure leading to a high degree of anisotropy [26][25]. Their crystallographic lattice has a hexagonal shape called graphite. The graphite hexagon planes are aligned with the fibre direction, leading to few available pendant atomic bonds on the surface with which the matrix can bond. Surface treatments oxidise the fibre surfaces to increase the interface bonding [25]. In general, carbon fibres exhibit very high stiffness, high strength and low density [26].

The hybridisation of glass and carbon fibres is used for very long wind turbine blades. This approach takes advantage of the high stiffness and low density of carbon fibres as well as the low cost and ease of manufacturing of glass fibres [25][26].

To form a composite the fibres are combined with a matrix material. The matrix material is typically either a thermoset or a thermoplastic resin. Both matrix options are soft and flexible and their purpose is to bind the fibres together to form a functional composite material. Their moderate to high toughness and failure strain also induce toughness in the composite by means

of energy absorbing mechanisms in the interfaces [26].

Thermoset resins go through an irreversible curing reaction, cross-linking, upon manufacturing requiring low processing temperatures and resulting in a high temperature stability of the final product. Thermoplastics, on the other hand, go through a melting and consolidation process which is potentially fast and provides opportunities for recycling at end of life [26]. However, the downside is the high process temperature, requiring high temperature resistant tooling [26]. Additionally, the thermal stability of the final product depends on the melting temperature of the thermoplastic with respect to the expected operational temperatures.

Different ongoing projects investigate the use of thermoplastics for the production of wind turbine blades [27]. For example, the "Thermo-Blade-Spine" project [28] develops automated manufacturing processes for the production of thermoplastic composites. Furthermore, the ZEBRA (Zero waste Blade ReseArch) project [29] has developed a process for the recycling of thermoplastic blades to form a closed loop.

When the fibres and matrix are combined to form a composite, the matrix functions to transfer the applied loads to the high performance fibres through the fibre-matrix interface. This makes that the properties of the final composite material are dependent on both the fibre and matrix properties as well as the strength of the interface. The most important parameters for the composite properties are the relative amounts of the individual components as well as the spatial orientation of the fibres. It is the fibres in the composites that are normally the dominant contributor to the composite mechanical properties [26].

With the established background on conventional composite materials, its associated challenges with respect to the sustainability of these wind turbine blades can be discussed.

2-2-1-1 Challenges for improving the sustainability of wind turbine blades

Most wind turbine blades are made of thermoset composites. These are difficult to recycle, among others due to the cross-linked polymers in the matrix, which cannot be re-melted or remoulded to re-manufacture or recycle the composite at End of Life [11]. The heterogeneous nature of composite material further complicates these processes. Furthermore, the flow of decommissioned blades will consist of blades of different designs, materials and lengths. This all combined creates a huge challenge for recycling wind turbine blades upon their decommissioning [11][30][10]. "Ideally, a recycling solution would involve little reprocessing to produce a cheap valuable material, which can be used in many applications" [10].

It is important to invest in sustainable solutions as the onshore market in Europe alone encompasses almost 12,000 wind turbines that are expected to be decommissioned by 2024 [5]. Every year there will be a stream of blade waste material and every newly build turbine will be decommissioned in 20-25 years and need to be dealt with as well. The resulting waste stream is likely to increase with the expected and required growth of the wind industry to meet the 2050 goals of the Paris Agreement [31].

This means that there are two pathways that need to be considered in improving the sustainability of wind turbine blades. One must invest in technologies to recycle the current blade waste stream in a more sustainable manner. Simultaneously, new technologies need to be explored to improve the sustainability of the future wind turbine blades by considering their entire life cycle in the design, including End of Life options.

The use of bio-based materials will be presented as a possible solution for the sustainability of future wind turbine blades. Before diving into the world of bio-based composites, the details of the conventional materials as used in the DTU 12.6 m research blade will be presented in the next sub-section.

2-2-1-2 Mechanical properties of the materials in the DTU 12.6 m blade

The DTU 12.6 m research wind turbine blade [21] is made of glass fibre reinforced composites (GFRC). The matrix material used is a thermoset epoxy resin. Furthermore the shearwebs, trailing edge and leading edge panels contain foam core material to create a sandwich structure. Adhesive is used to assemble the blade. The material properties of the DTU 12.6 m blade are presented in Table 2-1.

Table 2-1: Material properties of the materials used in the DTU 12.6 m blade model [21]. Fibre volume fractions for the unidirectional (UD) and bi-axial (BIAX) glass epoxy composites are $V_f = 0.53$.

Property	UD GFRC	BIAX GFRC	Core	Adhesive
E_1 [MPa]	42706	14300	550	3420
E_2 [MPa]	12585	14300	550	3420
E_3 [MPa]	12585	13400	550	3420
G_{12} [MPa]	4613	12500	200	1300
G_{13} [MPa]	4613	4610	200	1300
G_{23} [MPa]	4613	4610	200	1300
ν_{12} [-]	0.258	0.55	0.4	0.3
ν_{13} [-]	0.258	0.17	0.4	0.3
ν_{23} [-]	0.364	0.17	0.4	0.3
ρ [g/cm ³]	1.95	1.94	0.24	3.75
σ_1^t [MPa]	1000	223	-	-
σ_2^t [MPa]	47	223	-	-
σ_1^c [MPa]	813	209	-	-
σ_2^c [MPa]	146.5	209	-	-
τ_{12} [MPa]	48	155	-	-
V_f [-]	0.534	0.53	-	-

The properties of the epoxy resin and glass fibres used by DTU are presented in Table 2-2. It must be noted that the glass fibre strength value is the average of the range provided by the technical data sheet of the fibreglass company [32]. The other glass fibre properties were provided in the in-house Blade Modelling Tool from DTU used to generate the current blade design, see Section 3-3. Furthermore, the epoxy resin strength values were provided through an e-mail exchange with Hexion. The other epoxy properties were provided in the Blade Modelling Tool as well.

Table 2-2: Material properties of the glass fibres and the epoxy resin used by DTU.

	ρ g/cm ³	E MPa	G MPa	ν_{12} -	σ^t MPa	σ^c MPa	τ MPa
Epoxy resin	1.2	3850	1392	0.35	67	93	45
Glass fibres	2.6	76600	31250	0.2	2350 [32]	-	-

2-2-2 Bio-based alternatives

Strategies to improve the sustainability of wind turbine blades that are being explored often focus mainly on the end of life stages. For example by focussing on lifetime extensions or recycling technologies for the conventional composite blades [9][10][12]–[14]. However, in the circular bio-economy the goal is to minimise the environmental footprint throughout a products life while simultaneously closing biomass loops. This means that the material sourcing and manufacturing also need to be considered. It has been established that the conventional wind turbine blades are made with glass and/or carbon fibres embedded in a plastic matrix material. The sourcing and manufacturing of these materials rely heavily on fossil fuels and consequently have a significant environmental impact [19]. The alternative use of bio-based materials provides a possible solution to reduce the environmental footprint of wind turbine blades throughout their lifetime, by reducing the embodied energy of the materials and closing a biomass loop. In the case of wind turbine blades this would mean the use of natural fibre reinforced composites with a bio-based matrix material.

Moreover, a sustainable bio-based product can be defined as being "derived from renewable resources having recycling capability and triggered biodegradability (i.e. stable in their intended lifetime but would biodegrade after disposal in composting conditions) with commercial viability and environmental acceptability" [33]. The definition of environmental acceptability is however poor which can be demonstrated through the definition of *green composites*.

Green composites are defined as composites consisting of bio-fibre and bio-based matrix from renewable resources. Mohanty et al. [33] argue that by this definition, it can be expected that a green composite is biodegradable. This will however largely depend on the type of bio-based matrix being used. La Rosa et al. [34] states that depending on their chemical structure, bio-resins can be biodegradable or not. The bio-based matrix in a green composite can be a bio-derived non-biodegradable thermoset with 20-50% bio-content, a non-biodegradable thermoplastic, a biodegradable resin or even a petroleum-based resin from recycled thermoplastics. So even if only a small percentage of the matrix comes from a biological source and is not biodegradable it can be called a green composites. However, one can argue that a non-biodegradable composite which is only partly bio-sourced is not environmentally acceptable as it still results in waste that can threaten the ecosystem. The added benefit of fully biodegradable composites is a reduction in plastic waste and in the cost of waste management [35]. Nonetheless, replacing only part of the matrix by bio-based content can already have a positive effect on the environmental impact of a composite as is shown through a Life Cycle Assessment (LCA) by La Rosa et al., 2014 [36].

2-2-2-1 Bio-based matrix materials

Reducing the environmental impact of the matrix material becomes increasingly important when considering natural fibre reinforced composites as their matrix content is generally higher compared to the traditional GFRCs [37]. The literature has been consulted to identify the bio-based matrix materials that are currently available. The focus was placed on materials with a Young's modulus above 3000 MPa to stay within range of the currently used epoxy by DTU (Table 2-2). The companies Sicomin and Entropy Resin both sell bio-based epoxy resins with a Young's modulus of roughly 3200 MPa, a density of about 1.1 g/cm³ and strength values comparable to the DTU epoxy resin. However, their bio-based content is on average only 30%. Moreover, no information is available on whether these epoxies are biodegradable. Most likely they are not given that 70% of the materials content is not bio-based.

Other bio-based plastics are the biopolymers PLA, PLLA, PHB and PGA. The latter has a significantly higher Young's modulus of about 6500 MPa, but the density is also significantly higher at 1.6 g/cm³ [38]. The other biopolymers show an average Young's modulus of about 3500 MPa with a density of roughly 1.2-1.3 g/cm³. PLA is a well known 100% biosourced polymer, which has been extensively researched and utilised. However, not all PLA materials are also biodegradable depending on their chemical composition. The material property database MatWeb [39] also contains biodegradable PLA materials. Biodegradable PLA from the company FKUR show an average Young's modulus of 2600 MPa, which is lower than our desired minimum of 3000 MPa. However, depending on the blend, a Young's modulus of 3000 MPa can also be reached. Other biodegradable PLA materials in the MatWeb database show a wide range of Young's moduli of which some even exceed the Young's modulus of the DTU epoxy. It will therefore be assumed that biodegradable PLA can obtain the same general characteristics as commercial PLA.

Considering the different bio-based options for the matrix materials it is decided that the bio-epoxies are not environmentally friendly enough due to their low bio-based content. Comparing the biopolymers PLA and PHB, the main difference lies in the tensile strength which is higher for the PLA materials. Therefore, it is decided to use biodegradable PLA as the matrix material for the NFRCs explored in the current work.

2-2-2-2 Natural fibres

Natural fibres, can be seen as green materials that "can be produced starting from renewable materials and production techniques that consume lower energy relative to synthetic fibre production techniques" [36]. Natural fibres are also claimed to "offer environmental advantages such as reduced dependence on non-renewable energy/material sources, lower pollutant emissions, lower greenhouse gas emissions, and end of life biodegradability" [40]. The reduced dependence on non-renewable energy and material sources is important as the supply of petroleum is uncertain [33] and the sources threaten to run out.

The natural fibres can also be considered carbon neutral in that perspective as the carbon emissions upon burning equal the carbon captured by the fibre during its growth process. This carbon neutrality relates purely to the material and does not take into account the emissions during the sourcing, production, transport, etc. of the fibre product. Moreover, landfill might be preferred if the composite is fully biodegradable to avoid the health hazards

related to incineration [36].

There exist an enormous variety of plant fibres with different characteristics and mechanical properties. Of special interest to composite applications are the so-called bast fibres which originate from the bark of dicotyledonous plants [41]. The bast fibres extracted from plants are referred to as 'fibre bundles' which consist of smaller fibres adhered to each other. These smaller fibres, referred to as 'single fibres', can be approximated as hollow tubes with a cell wall enclosing a void called the lumen. The cell wall structure consists of microfibrils, which are highly ordered cellulose molecules bonded by a matrix of hemi-cellulose and lignin [41]. Cellulose is a long chain molecule with reported axial stiffness of up to 135 GPa [41], and is the reinforcement component in plant fibres. Figure 2-4 presents a schematic representation of the flax plant, and breaking it down to its fibres and cellulose.

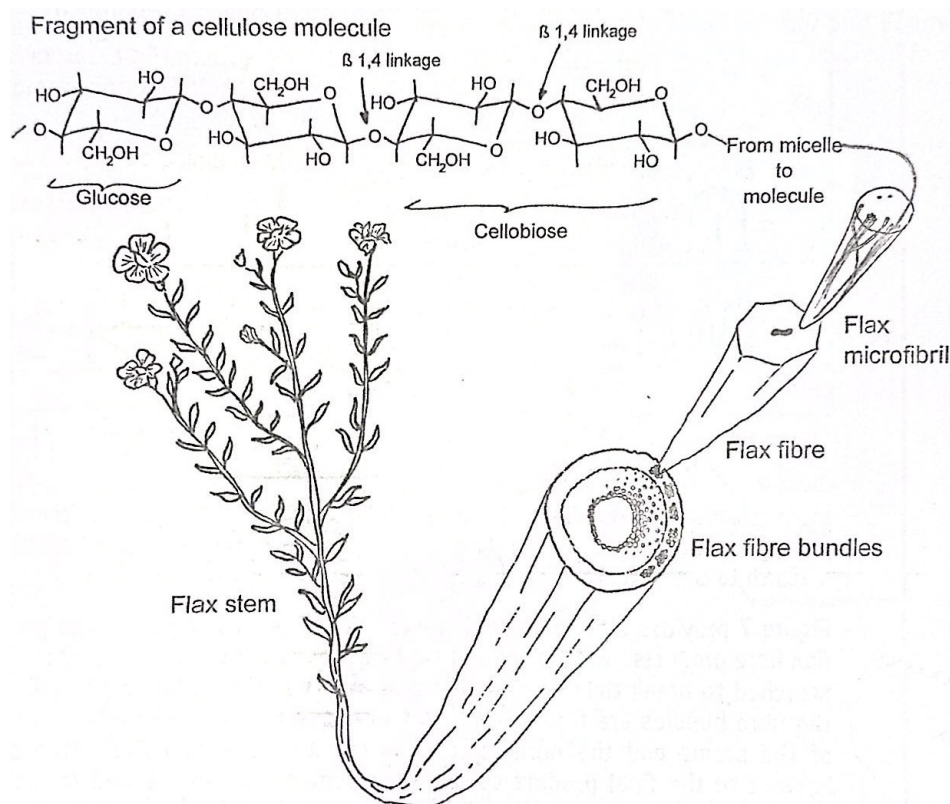


Figure 2-4: Schematic representation of the hierarchical structure of flax; from plant to cellulose [41].

The outer layer of natural fibre cell walls, the primary wall, consists of randomly oriented microfibrils. The inner layers of the cell wall, the secondary wall, consists of microfibrils that are aligned in parallel to each other at an inclination angle relative to the fibre axis, the microfibril angle (MFA). This MFA strongly affects the tensile properties of the plant fibres, see Figure 2-5. The microfibril angle of bast fibres is generally low, below 10 degree [41], and as such the stiffness of the cellulose molecule largely translates to the fibre stiffness. Therefore, bast fibres with a high cellulose content become the most interesting reinforcement for composites. Examples of such fibres are flax, hemp, ramie and jute [41].

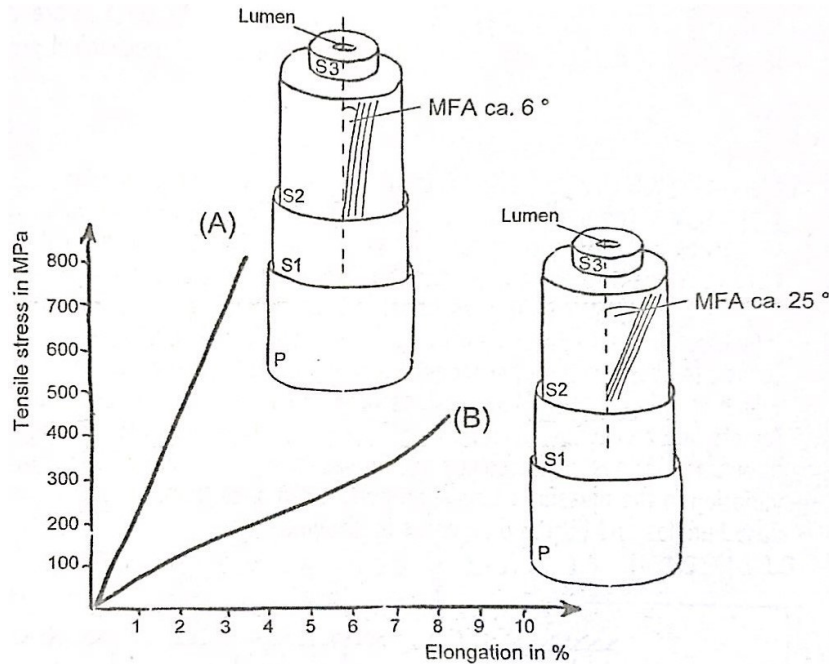


Figure 2-5: Influence of the microfibril angle (MFA) on the mechanical properties of plant fibres [41]. (A) Fibre like Hemp. (B) Fibre like Cotton.

The process of extracting and processing the fibres can cause damages in the form of dislocations which reduce their mechanical properties [42]. Therefore, plant fibres can in practice not realise their full potential. Compared to glass fibres, the stiffness of plant fibres is lower which affects the achievable stiffness of the composite. What makes plant fibres a viable option for structural applications is the relatively low density of around 1.5 g/cm^3 , compared to the average density of glass fibres of 2.6 g/cm^3 [42]. As a result, the stiffness per unit weight (specific stiffness) becomes comparable for some natural fibres.

The lower density of plant fibres is in part due to the presence of porosity, particularly the lumen inside the fibre. However, their composites can contain an even higher porosity content. The heterogenous form and dimensions of the plant fibres reduce the packing ability of the fibre assemblies and complicate the matrix impregnation [43]. The fibre volume of the composite is limited by the packing ability of the fibres and directly influence the composite performance. Furthermore, the hydrophilic nature of the fibres complicates the adhesion to the generally hydrophobic matrix which impacts the interface properties. Surface treatments exist to improve the interface adhesion but require chemicals which can again have a negative

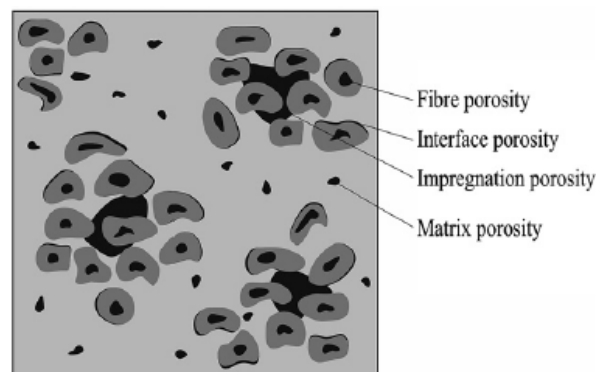


Figure 2-6: Schematic illustration of the four different porosity sub-components that have been identified from composite cross-sections [43].

impact on the environment depending on the specific chemicals used.

As the porosity content becomes significant for natural fibre composites, the micro-mechanical model to predict the composite mechanical properties from its constituents needs to account for this. Research has been done to expand the traditional model to account for the porosity in natural fibres. This expanded model and its equations is outlined in Appendix B. Figure 2-6 identifies the different types of porosity that are present in natural fibre composites.

Another consequence of the hydrophilic nature of the fibres is their ability to absorb moisture. Changes in moisture content lead to swelling and shrinking of the fibres which can induce tensile stresses normal to the interface leading to de-bonding. Moreover, a higher moisture content can reduce the mechanical properties of the fibres themselves. Chemical and/or physical treatments of the fibres can improve dimensional stability making them better suited for application in composites [41]. The level of moisture resistance is of importance for the durability of the composites. In terms of environmental impact the advantage of natural fibre composites in wind turbine blades depends on whether their lifetime is comparable to the traditional synthetic blades, a shorter life time reduces the advantage [40]. However, this could be counteracted if the bio-based blades can be reused, repurposed and recycled for other applications before the material needs to be disposed.

Another factor to consider is the reduced thermal resistance of natural fibres compared to glass and carbon fibres [34][37]. The thermal resistance is important to consider when selecting the resin and production method for the composite, as one does not want to degrade the natural fibre upon production of the composite.

Generally, the raw material cost of natural fibres are lower than that of glass and carbon fibres [33], as they are derived from low-cost biomass resources [42]. However, the required manufacturing steps to obtain the fibres and process them into suitable preforms for composites will add to the costs of using natural fibres [42][44]. Therefore, the cost of natural fibre fabrics can exceed those of the traditional glass and carbon fabrics [45][44]. A growth in the market of natural fibres could reduce their cost as the current limited market plays a significant role in their higher price point [45]. Another aspect that leads to higher prices for the natural fibre composites is the increase in matrix content as well as the generally increased cost of using bio-based resin in composites [33].

Other considerations are the larger land occupation [36] and use of pesticides and fertilizer [40] during the growth of the fibres. The use of organic fibres could resolve the latter issue [36]. The consideration of land use and water requirements for the growth of the fibre is important as it should not compete with food and feed stocks.

Furthermore, different natural fibres can exhibit different properties and hybridization of a composite through the use of multiple different natural fibres could lead to improved mechanical performance for its application [33].

In conclusion, the use of green composites has its advantages and disadvantages. These should all be considered upon the design of such a composite. However, Life cycle assessment studies show that the combined effect of the pros and cons of green composites still result in an environmental advantage with respect to the currently used glass and carbon fibre composites [34][46]–[48].

2-2-3 Existing examples on bio-based blades

To be able to make the switch to the use of green composites in wind turbine blades it is important to also compare the mechanical properties of green composites with synthetic composites. Several researchers have investigated the use of different natural fibres for wind turbine blade applications, mainly for small wind turbines. A wind turbine blade with a radius of 5 m was analysed by comparing 11 different natural fibres with E-glass composite, all with the same matrix. The composite properties were derived with a micro-mechanical model with the modified Halpin-Tsai method. The study found that almost all natural fibres fit the strength requirement. However, for wind turbine blades the stiffness is driving. The study showed that some natural fibres compared in stiffness to the E-glass blade. However, the stiffness was only evaluated by comparing the deflection of the 5 m blade. The stiffness might be insufficient for larger blades. The natural fibre blades also showed a reduction in weight which allows the turbine to rotate at lower wind speeds which increases its performance. A modal analysis was performed as well showing similar behaviour for the the natural and E-glass fibre composites [49]. It must be noted that the used material properties for all fibres are the highest values found in literature by the researchers which shows a non-conservative approach.

Another study performed single point static flap-wise bending tests on a 3.5 m wind turbine blade comparing the use of E-glass with the use of flax fibres [44]. It was concluded that flax can replace E-glass in terms of normal and worst case loading of the specific test blade. However, the important flexural stiffness for the flax blade was halved with respect to the E-glass blade, which can become an issue for the tower clearance. The load-displacement curve for E-glass composite was linear while that of the flax composite was quadratic [44]. Furthermore, the E-glass and flax blades exhibited distinct failure mechanisms [44]. The E-glass blade experienced cracking at the root-hub interface, which propagated further, leading to significant delamination and ultimately causing the trailing edge along the maximum chord length to split open. In contrast, the flax blade began to buckle and delaminate approximately 1 meter from the root, a location corresponding to a step-change in the laminate's stacking sequence. Upon further loading the blade eventually collapsed. The failure mechanisms in a full scale natural fibre blade are still poorly understood and need further research. The work [44] also mentions that many processing steps can be involved in the production of aligned flax fibre fabrics for the use in composites resulting in high cost, contrary to claims of other literature.

Another research evaluated specimens of pure glass fibre composites, pure hemp fibre composites and two hybrid composites of glass and hemp fibre. The tensile test results show a strong reduction in strength and stiffness for the hemp composites compared to glass. The hybrid composites showed value in between. The bending test results also show a reduction in strength and stiffness for the hemp composite while the hybrid composites show equal behaviour to the glass composite [50]. It must be noted that these conclusions were made from the absolute strength and stiffness values measured using the same number of plies. The difference in density and therefore specific strength and stiffness were not considered and cannot be derived from the article. It is the specific properties that are of interest for wind turbine blades and the reason that natural fibres are considered. The hemp composite might turn up to be more comparable to the glass composite in terms of specific properties.

The hybridization with two natural fibres and no glass fibres was investigated in another

research [51]. The hybridization of bamboo and jute fibres had a positive effect on the tensile strength. The flexural strength was however highest for the pure bamboo fibre composite. The results are said to be promising for the application in small wind turbine blades but were not evaluated in the mentioned research. Moreover, the research only investigated the strength properties of the composites while the stiffness properties are the main interest for wind turbine blades.

The study of a 4.4 m wind turbine blade made of palm fibre composite [52] showed to withstand climatic severe conditions without any damage over a test period of one month in April of 2020. The power generation had also increased as a result of the reduced weight of the palm fibre composite compared to the traditional synthetic fibre composite blades [52]. The reduction in weight resulted in higher rotational speeds at lower wind speeds.

Contrary to the mainly positive outcomes of the above researches, another research concludes that it is not possible to use natural fibres alone for high strength applications [53]. They conclude this by comparing the properties of a flax/sisal composite and a flax/sisal/E-glass composite where the addition of glass fibres significantly increased the mechanical performance [53].

From the available literature on test specimens and small wind turbine blades it can be concluded that the use of natural fibres results in a weight reduction, which improves the wind turbine performance. Furthermore, the hybridization of the composite is seen as an opportunity to overcome the reduced mechanical properties seen in single natural fibre composites. There is however no agreement whether natural fibres can replace glass fibres in wind turbine blades. The potential is mentioned but challenges remain with respect to the mechanical performance and consequently up-scaling to larger blades.

2-3 Research Questions

The comparisons made in literature between glass and natural fibres involve blades with the same structural design for both fibre types. There is little research done in designing a wind turbine blade specifically for the use of bio-composites. Moreover, available research on bio-composites in wind energy only involve very small blades.

Therefore, the current work will address the following research question:

- What are the structural implications of utilising bio-based materials in wind turbine blades?

The first step to answer this question is to establish which bio-based composite systems can potentially be utilised in wind turbine blades. Moreover, the influence of the switch in materials on the structural performance of the blade need to be understood. Additionally, knowing what changes to the blade design are required to meet design standards using the bio-based composites will provide additional insights. In summary, the sub-questions are the following:

1. Which bio-based composite systems are suitable for application in wind turbine blades?
2. How does the use of bio-based materials influence blade performance?
3. What changes in the blade design are required for the bio-based blade to meet the design requirements?

A case study on the DTU 12.6 m research wind turbine blade [21] will aid in answering the different research questions. The larger blade length compared to other studies will lead to a more realistic impression of the implications of bio-based composites.

A sensitivity analysis will be performed to investigate the relation between the composite material engineering constants and the blade behaviour. This will contribute to the selection of potential bio-based composites for the application in wind turbine blades. Thereby informing the answers to research sub-questions 1 and 2.

Using the answer to sub-question 1, a bio-based composite material will be selected with which a structural redesign of the DTU 12.6 m blade will be performed. As the research focusses on the structural implications, the aerodynamic shape of the DTU 12.6 m blade will be unchanged. The redesign will be informed by the knowledge obtained from the sensitivity analysis. The structural redesign will contribute to the answer of sub-question 2 and provide an answer to sub-question 3. The structural design will be addressed with the Finite Element Method for which the Abaqus software is used.

Combining the results of both the sensitivity study and structural redesign will result in an answer for the main research question.

The next chapter describes the different models used in this research. The chapters thereafter will discuss the method and results of the sensitivity analysis followed by the method and results for the structural redesign of the DTU 12.6 m blade with bio-based composites. The report is wrapped up with a conclusion and recommendations for future research.

DTU 12.6 m Wind Turbine Blade Models

In order to answer the research questions a sensitivity study as well as a structural redesign will be performed for the DTU 12.6 m research wind turbine blade. For this purpose it is important to establish the different models of this blade that will be used. The aeroelastic model of the DTU 12.6 m blade is used to calculate the design loads that will be applied in the current work. Furthermore, the Finite Element models of the blade defined in the software Abaqus are presented. Finally, the to be used in-house Blade Modelling Tool from the Technical University of Denmark is outlined.

3-1 HAWC2 model

To analyse how a wind turbine with the DTU 12.6 m research wind turbine blade performs, the HAWC2 code can be used [24]. This analysis is required to certify a wind turbine and will provide the design loads for the different turbine parts. With the HAWC2 model the redesigned blade can also be tested on the same wind turbine platform to compare the aeroelastic behaviour of a turbine with each blade version.

HAWC2 is an aeroelastic simulation tool developed primarily between 2003 and 2006 as part of the aeroelastic design research program at Risoe National Laboratory in Denmark. However, it has undergone continuous updates and refinements since then. The version used in this study is version 12.9, released in October 2021 [24]. This software is designed to simulate the dynamic response of wind turbines in the time domain. The structural framework of HAWC2 employs a multi-body system approach, with each component modelled as a collection of Timoshenko beam elements [24]. On the aerodynamic side, the software builds upon the blade element momentum theory but enhances it to account for phenomena such as dynamic inflow, dynamic stall, skewed inflow, wind shear effects on induction, and the impact of significant structural deformations [24]. Extensive validation of the code has been conducted at Risoe, comparing its results against the older HAWC software, the Ellipsys computational

fluid dynamics (CFD) tool, and various experimental measurements [24].

The controller used in the model of the DTU 12.6 m blade is the DTU Wind Energy controller, as described in [54], which is designed for pitch-regulated, variable-speed wind turbines. This controller can operate in both partial-load and full-load conditions, utilising the classical proportional-integral (PI) control principles [54]. The generator speed serves as the main feedback signal for the controller. Additionally, the reference generator power is incorporated as a feedback element to ensure a seamless transition between partial-load and full-load operations [54]. To regulate the turbine, the controller adjusts both the collective blade pitch angle and the electromagnetic generator torque, as detailed in [54].

The DTU 12.6 m research wind turbine blade is modelled in HAWC2 as a 3-bladed pitch regulated wind turbine mounted on a 24 m tubular steel tower, as described in [21]. The generator used is a 150 kW generator with a synchronous speed of 1500 rpm and a nominal slip of 0.02. The used turbine platform and controller in the HAWC2 model are academic but representative [21]. The blade is designed for wind class IA from IEC 61400-1 [20] meaning that the HAWC2 simulations use an average wind speed of 10 m/s, a reference wind speed of 50 m/s and a reference wind turbulence intensity of 0.16 [20]. For each blade, the main body is split up into 19 body segments to allow the modelling of geometric non-linear behaviour of the blade. The model uses the small deformation assumption within each sub-body, whereas large deflections are possible between sub-bodies. A schematic representation of the HAWC2 model is presented in Figure 3-1a, and the orientations of the various body-coordinates are presented in Figure 3-1b. Each main body coordinate system is defined relative to the previous body via Euler angle rotations, starting from the tower with respect to the global coordinate system, to the tower top, shaft, hubs and blades. The dimensions of the wind turbine model are summarised in Table 3-1.

Table 3-1: Wind turbine dimensions of the HAWC2 model with the DTU 12.6 m blade [21].

Parameter	Value	Parameter	Value
Blade length	12.6 m	Tower length	24 m
Hub length	0.4 m	Tower top length	1.13 m
Rotor diameter	26 m	Tower base diameter	2.15 m
Shaft length	1.67 m	Tower upper diameter	0.82 m
Shaft tilt	4 °	Tower material thickness	12 mm

The optimal tip speed ratio is set to 9.77, while, the rated rotor speed is based on the maximum allowable tip speed of 95 m/s, which lead to a rated rotor speed of 68 rpm. Together with the rotor radius of 13 m this results in a rated wind speed of 9.475 m/s. The minimum rotor speed is set equal to 20 rpm. The aerodynamic rated power is assumed equal to the electrical rated power divided by the generator efficiency: $\frac{150}{0.98} = 153.06$ kW. The minimum pitch is set to -1.1 degrees. The frequency and damping ratio for the partial load region are 0.1 Hz and 70% respectively, and 0.2 Hz and 70% respectively for the full load region.

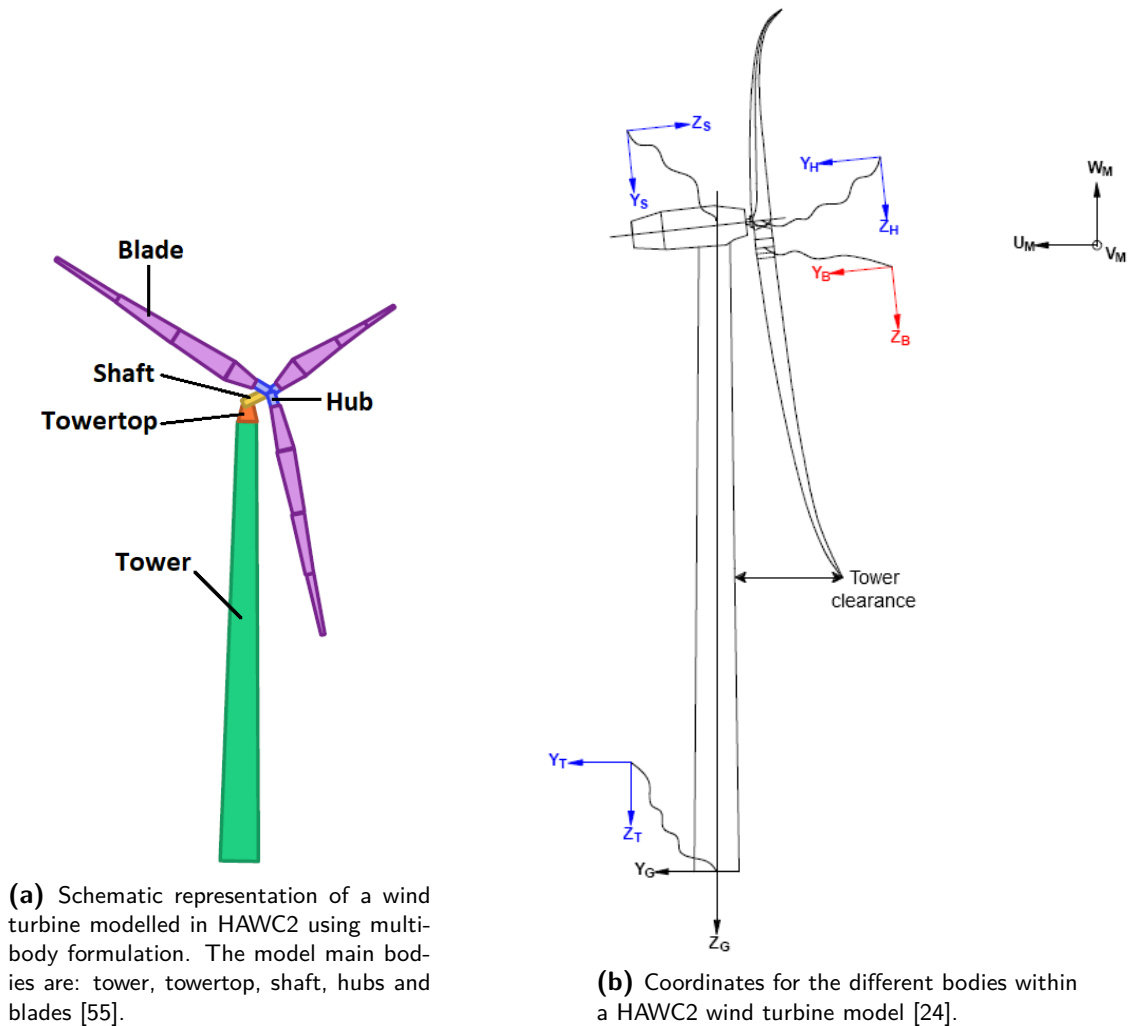


Figure 3-1: HAWC2 model depiction.

Finally, it must be noted that the tower was modelled as a stiff tower by increasing the stiffness properties significantly. This was done as there was no information available on the origin of the tower parameters adding uncertainty to the model. Moreover, the aim of the present study is to investigate the wind turbine's blade design. By using a stiff tower its influence on the blade's behaviour is eliminated.

A stepwind simulation with the HAWC2 model provides the turbine's behaviour at different steady windspeeds. Furthermore, it shows how quickly the turbine responds to a change in windspeed by finding its new equilibrium state. The latter information can give an indication of how well the controller works. The stepwind results for the HAWC2 model are presented in Figure 3-2. The simulation starts at the cut-in wind speed of 4 m/s and ends at the cut-out wind speed of 25 m/s where each step has a duration of 40 seconds. The first 100 seconds are disregarded to eliminate transient influences from starting up the simulation. The high frequency oscillations in the thrust curve are due to wind shear being included in the simulation.

It must be noted that the stepwind simulation of the HAWC2 model as originally received

lead to the conclusion that the model was unstable. The model was stabilised by retuning the controller. The details of this process can be found in Appendix A. Only the results of the stable model will be presented in the main body of the work.

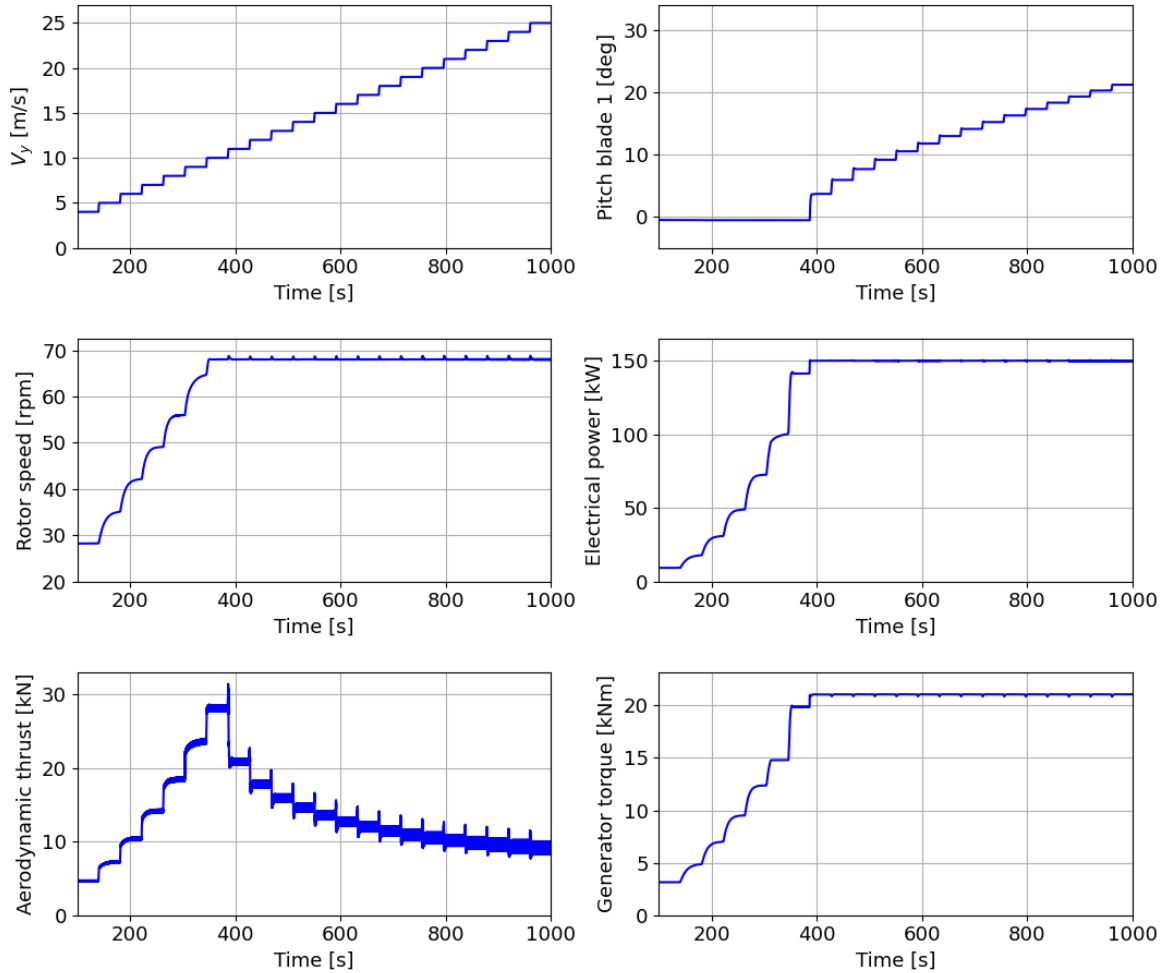


Figure 3-2: Stepwind results of the HAWC2 model of the DTU 12.6 m blade. Top left is the input windspeed, the other plots are the operational output channels.

Furthermore, the design loadcases that have been evaluated for the current blade design are DLC1.2 and DLC1.3 from the IEC 61400-1 standard [20]. DLC1.2 provides the fatigue loads under normal operation using a normal turbulence model. These are derived from DL1.1 which provide the extreme loads under normal operation. DLC1.3 provides the ultimate loads under normal operation with an extreme turbulence model. The obtained extreme loads have been used to optimise the structural design of the DTU 12.6 m blade.

To determine the extreme load envelope, multiple time-domain simulations are conducted using a turbulent wind model. At each wind speed, simulations are run for six different turbulence seeds, providing a total effective duration of 600 seconds after excluding the initial 100 seconds to eliminate the influence of transient effects. Additionally, three different yaw

alignment scenarios are analysed for each wind speed, with angles of 0, +10, and -10 degrees [21]. The extreme loads are derived from the HAWC2 simulation by taking the maxima from all simulations at each radial position of the blade. The resulting load envelop is thus a combination of different loadcases.

The extreme loads for the DTU 12.6 m wind turbine blade calculated by the HAWC2 model are presented in Figure 3-3, showing the bending moment distributions. The load envelop for the flapwise loadcases is denoted by M_x , where PTS defines the Pressure To Suction side direction and STP defines the Suction To Pressure side direction. The load envelop for the edgewise loadcases is denoted by M_y , where LTT defines the Leading edge To Trailing edge direction and TTL defines the Trailing edge To Leading edge direction. The irregularity in the edgewise bending distribution are caused by the nature of the extreme load envelop consisting of a combination of different loadcases.

The DLC1.3 loads in Figure 3-3 will be used as design loads for the redesign process with bio-based materials.

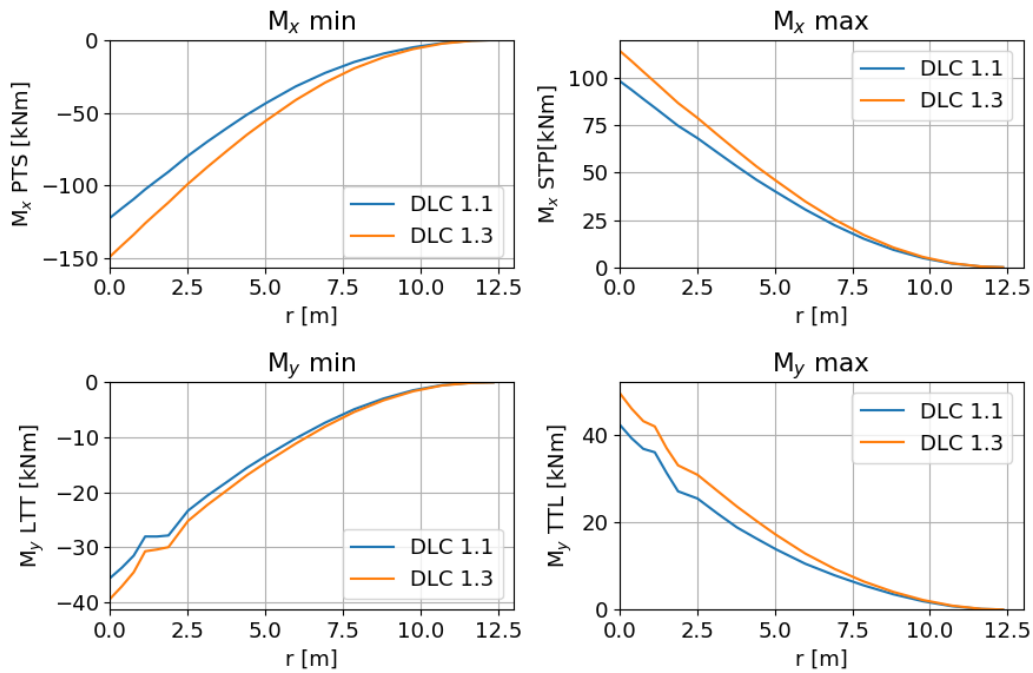


Figure 3-3: Blade bending moment load envelops of design loadcases DLC 1.1 and DLC 1.3, calculated with the HAWC2 model with the DTU 12.6 m blade. Flapwise load direction is denoted by M_x , edgewise load direction is denoted by M_y .

Lastly, another critical parameter for the design is the tower clearance. The tower clearance resulting from DLC1.3 is 0.82 m which needs to be compared with the minimum tower clearance specified by the design standards. The minimum tower clearance is specified by DNV GL as 30% of the unloaded tower clearance [56]. The tower clearance was calculated using the basic geometry as outlined in Figure 3-4 and the assumption of no pre-bend. The numbers ① to ⑤ in Figure 3-4 indicate the order in which the different distances are calculated to find the tower clearance. The calculations of each distance are presented below:

- ① = rotor centre = $25.13 + 1.67 \cdot \sin(4^\circ) = 25.25$ m
 ② = blade tip vertical position = $① - 13 \cdot \cos(4^\circ) = 12.28$ m
 ③ = blade tip horizontal position = $13 \cdot \sin(4^\circ) + 1.67 \cdot \cos(4^\circ) = 2.573$ m
 ④ = tower radius at position blade tip (linear interpolation) = $② \cdot \tan(\frac{1.06-0.45}{24}) = 0.31$ m
 ⑤ = tower clearance = $③ - ④ = 2.26$ m

The calculated tower clearance is 2.26 m from which the minimum tower clearance is calculated to be 0.68 m. The tower clearance of 0.82 m as calculated from DLC1.3 is above the minimum tower clearance, thus fulfilling the requirement.

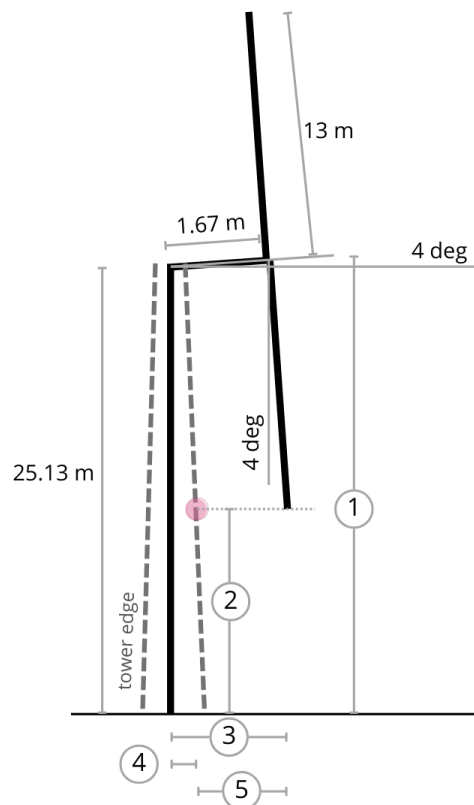


Figure 3-4: Schematic representation of the wind turbine in the HAWC2 model with the DTU 12.6 m blade.

3-2 Abaqus Models

There are two Abaqus models of the DTU 12.6 m wind turbine blade. One model is a continuum shell element model which is used during the sensitivity study described in Chapter 4. The other model is a conventional shell element model which is used during the redesign process as described in Chapter 6.

The main difference between the two models is the manner in which the thickness of the shell structure is defined [57]. The continuum shell element model defines the thickness in the geometry of the blade. Both the inner and outer surface of the blade are defined. Subsequently,

the composite lay-up definition is defined in the section assignment. The thickness of each lamina layer is normalised with respect to the geometric thickness, thus the sum of the thickness in the section assignment equals one. The geometry in the conventional shell element model only defines one surface, typically the outer (aerodynamic) surface of the blade. The thickness of the shell is defined in the section assignment where the absolute thickness of each layer of the composites are defined, its summation being equal to the shell thickness.

Compared with the continuum shell element model, the conventional shell element model is computationally more efficient. This makes the model suitable for large-scale models and/or parametric studies. However, due to the indirect thickness definition, the model might be unable to fully capture the torsional stiffness of the structure. The continuum shell element model generally predicts the torsional stiffness more accurately. Therefore, a detailed analysis and design of the blade structure is preferably done with the continuum shell element model.

3-2-1 Continuum shell element model

The continuum shell element model of the wind turbine blade was obtained from Philipp Haselbach [58] and is constructed similar to the model in [59]. The volumetric representation of the blade geometry was generated using the Blade Modelling Tool (BMT) developed at the Technical University of Denmark, see Section 3-3, and implemented in the commercial finite element software Abaqus. A visualization of the blade geometry is provided in Figure 3-5. The model was discretized using 208,744 8-node continuum shell elements with reduced integration (Abaqus element type SC8R), resulting in a mesh containing 405,648 nodes.

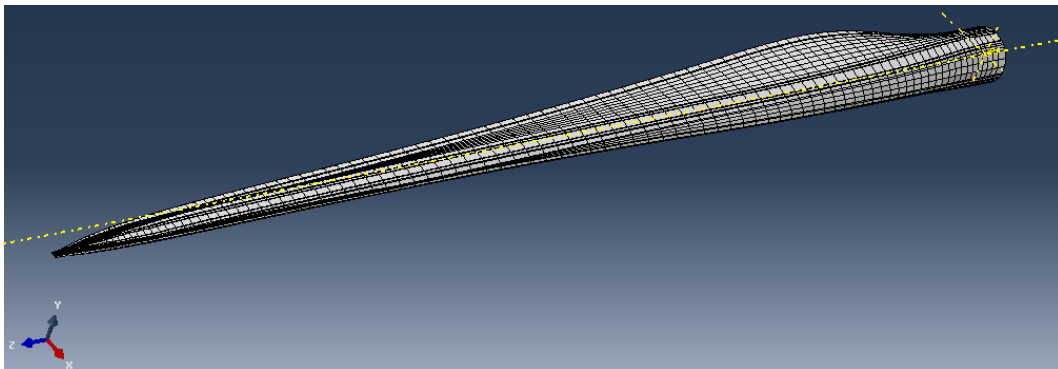


Figure 3-5: Geometry of the DTU 12.6 m blade [21] as defined in the Abaqus models.

The blade geometry and composite layup are modelled using layered elements, with a single element spanning the entire thickness. The element thickness corresponds to the volumetric height in the 3-direction (perpendicular to the blade's surface), and the thickness of individual plies is defined relative to the total stack height. The characteristic length of the elements ranges between 0.01 m and 0.015 m. To accommodate variations in the composite layup, each cross-section is divided into 59 distinct regions, as illustrated in Figure 3-6.

Numerical integration is employed in Abaqus to compute stresses and strains at section integration points through the shell thickness, allowing for non-linear material behaviour. For the layered shell elements, three integration points per layer through the thickness are used,

which is the default configuration [60]. As depicted in Figure 3-7, each SC8R element has, depending on the number of layers, n number of layer \times 3 section integration points \times 4 in-plane integration points. The total number of Degrees of Freedom (DOF) amounts to 1,218,672 for the DTU 12.6 m blade baseline design.

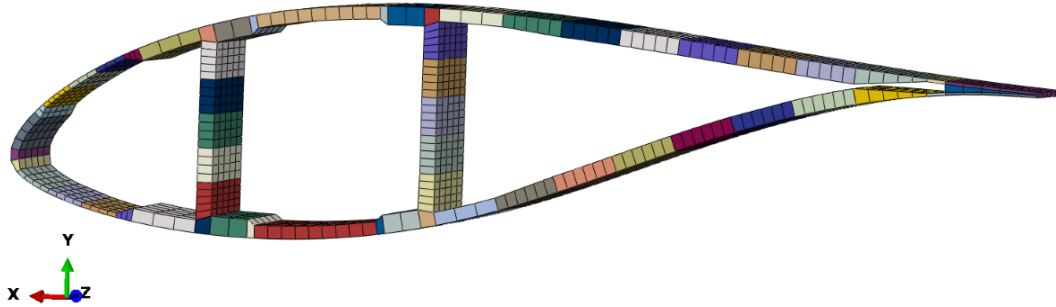


Figure 3-6: Cross-section with section definitions in the Abaqus continuum shell element (SC8R) model of the DTU 12.6 m blade [21] at a radial position of 5.23 m.

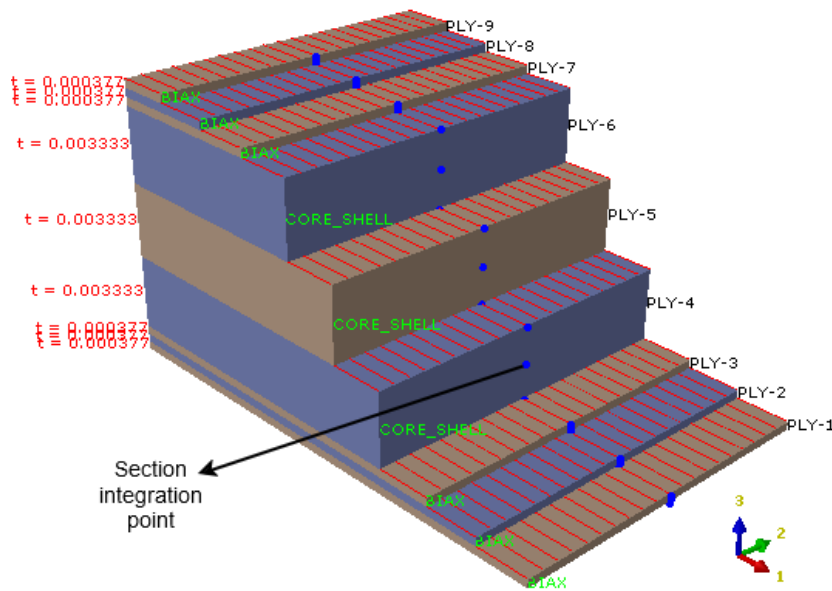


Figure 3-7: Ply stack plot of trailing edge panel at a radial position of 5.23 m of the DTU 12.6 m blade model [21] with 8-noded reduced integration continuum shell elements (SC8R) in Abaqus.

3-2-2 Conventional shell element model

The conventional shell element model of the wind turbine blade was developed by Philipp Haselbach [58], similar to his model in [61]. A geometric model of the blade was constructed using the commercial finite element analysis software Abaqus. Python scripts were employed to generate 98 cross-sectional profiles that represent the airfoil data. A 3D lofting function connects these 2D cross sections, including the airfoil shape and shear web geometry, to complete the three-dimensional shell geometry. The model was discretized with the conventional 8-node doubly curved thick shell elements (Abaqus element type: S8R) that feature reduced

integration. An approximate characteristic element length of 0.05 m was employed, resulting in a mesh with 23,999 elements and 71,123 nodes.

The composite material layup defines the thickness of the layered-shell elements. The plies are ordered in the direction of the positive shell normal, which is oriented inward toward the blade's interior. The reference surface from which the shell normal is defined is the aerodynamic blade profile. To preserve the aerodynamic profile's accuracy, an offset from the shell's mid-surface was applied, ensuring the reference surface corresponds to the blade's external shape. This method ensures that the varying thickness of the material layup design does not effect the aerodynamic shape. For the shear webs, no offset was applied; the geometric mid-plane of the webs was used as the reference surface [62][63].

For the stress and strain computations through the shell thickness, the default configuration of three integration points per layer through the thickness was adopted for the layered shell elements [60]. As illustrated in Figure 3-8 each S8R element has n number of layers \times 3 section integration points \times 4 in-plane integration points. The resulting total number of degrees of freedom amounts to 426,738 for the DTU 12.6 m blade baseline design.

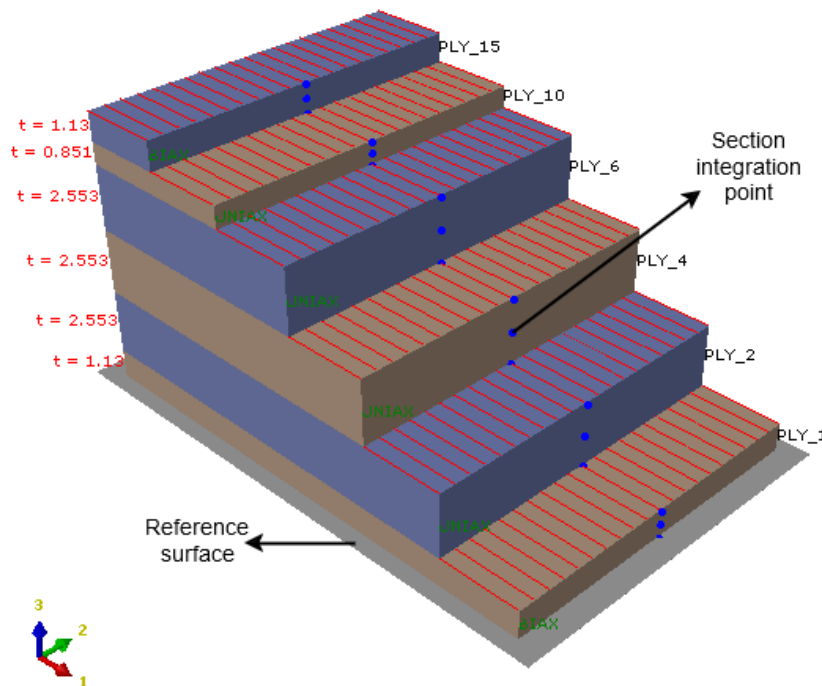


Figure 3-8: Ply stack plot of upper sparcap at a radial position of 4.74 m of the DTU 12.6 m blade model [21] with 8-noded reduced integration conventional shell elements (S8R) in Abaqus.

3-3 Blade Modelling Tool and Baseline Lay-up Design

The in-house Blade Modelling Tool from the Technical University of Denmark is based in Microsoft Excel, and was provided by Philipp U. Haselbach. This Excel consists of a number of sheets specifying different parts of the blade design. These sheets also include macros that generate scripts from the specified data to be able to create the continuum shell finite

element model described in Section 3-2-1. The Excel sheet that is used in the current work, as described in Section 3-2-2, is the "LayupID" sheet as depicted in Figure 3-10. This sheet specifies the lay-up per cross-sectional sub-element along the full blade length.

Each cross-section is divided into 59 elements or "Solids". The distribution is shown in Figure 3-9. These elements can be grouped in a total of 10 sections, as defined in Figure 3-9, each section having their own layup design. There are four sections specifying the tail design. The lay-up of elements 1 and 49 contain the layer of glue that bonds the pressure-side and suction-side panels of the blade. The same holds for the "nose" section. The other sections of the Tail specify the transition in lay-up from Tail to the Trailing Edge (TE) panel, the latter lay-up is a sandwich structure with a core material in the middle just like the Shearwebs. The TE panel transitions into the Flanges (no core) which is another term for the sparcaps. The Flange design is split up into two sections as one part also contains the connection with the Shearwebs. The Flanges transition into the Leading Edge (LE) panels and finally the Nose where the two blade panels connect again.

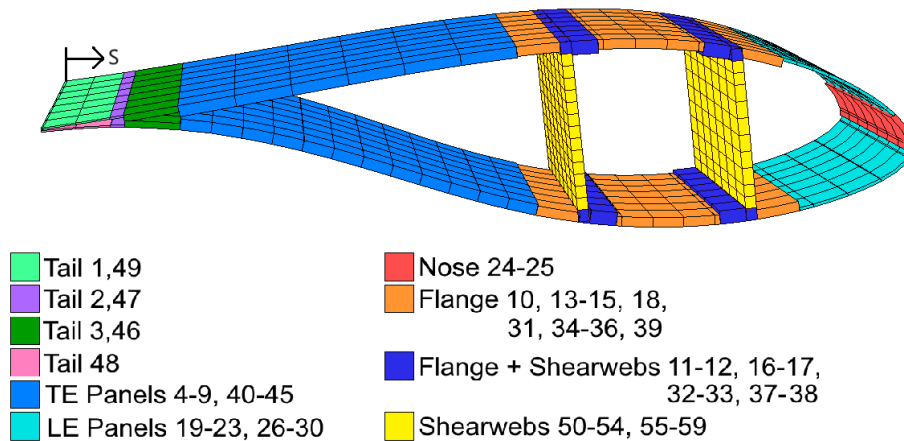


Figure 3-9: Section distribution per cross-section of the DTU 12.6 m blade from the Blade Modelling Tool.

With 10 sections per cross-section and a total of 98 radial positions, the design is extensive. To be able to showcase the lay-up design of the entire blade, the thickness distribution along the blade per section per material is visualised, see Figure 3-11. The thickness of each individual material is staggered so that the total thickness of the layup per section along the blade is also visualised.

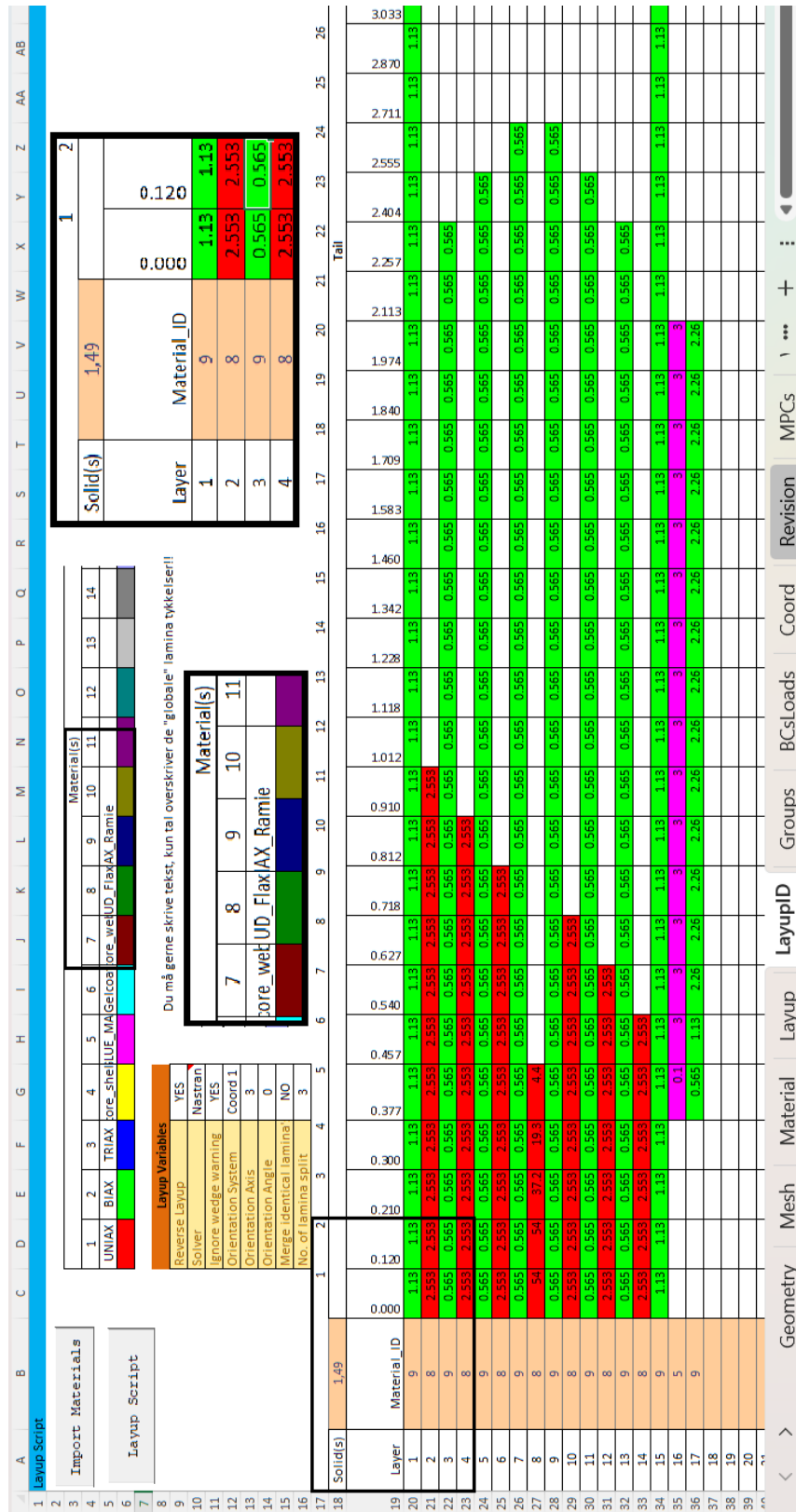


Figure 3-10: Print screen of the "LayupID" sheet of the Blade Modelling Tool of the Technical University of Denmark [58] based in Excel.

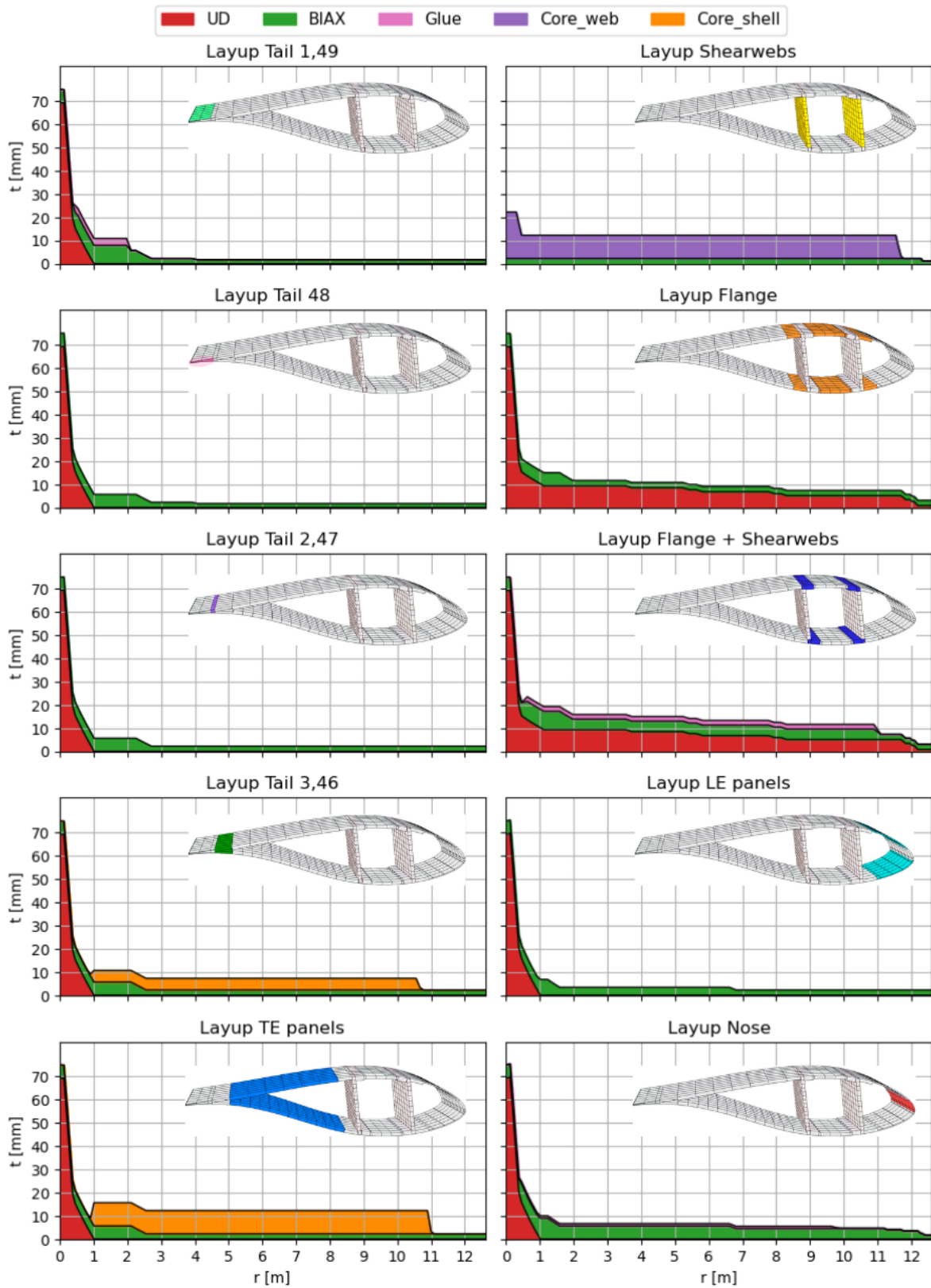


Figure 3-11: Blade structural design of the DTU 12.6 m blade from the Blade Modelling Tool [58]. Total material thickness distribution visualised composed of all materials present.

Methodology - Sensitivity Study

This chapter will focus on the methodology to perform the sensitivity study on the relation between material engineering constants and blade behaviour. This will include the process of obtaining the material engineering constants of several natural fibre reinforced composite systems. There will be an additional sensitivity study to investigate the validity of the geometric linearity assumption. The description of its methodology will conclude this chapter.

4-1 Sensitivity Study on the Relation between Material Engineering Constants and Blade Behaviour

In order to provide an answer to research questions 1 and 2, a sensitivity study will be performed. This study will investigate which material engineering constants have a significant influence on the blade behaviour. Moreover, the relation between the material input and blade behaviour will be established for the significant parameters. This sensitivity study will provide the necessary information to be able to select which NFRC systems are suitable for application in wind turbine blades. Moreover, it allows for the prediction of the impact of the use of NFRCs in wind turbine blades.

Figure 4-1 outlines the methodology that will be applied for the sensitivity study. The next sections of this chapter will outline the details of each of the steps of the method.

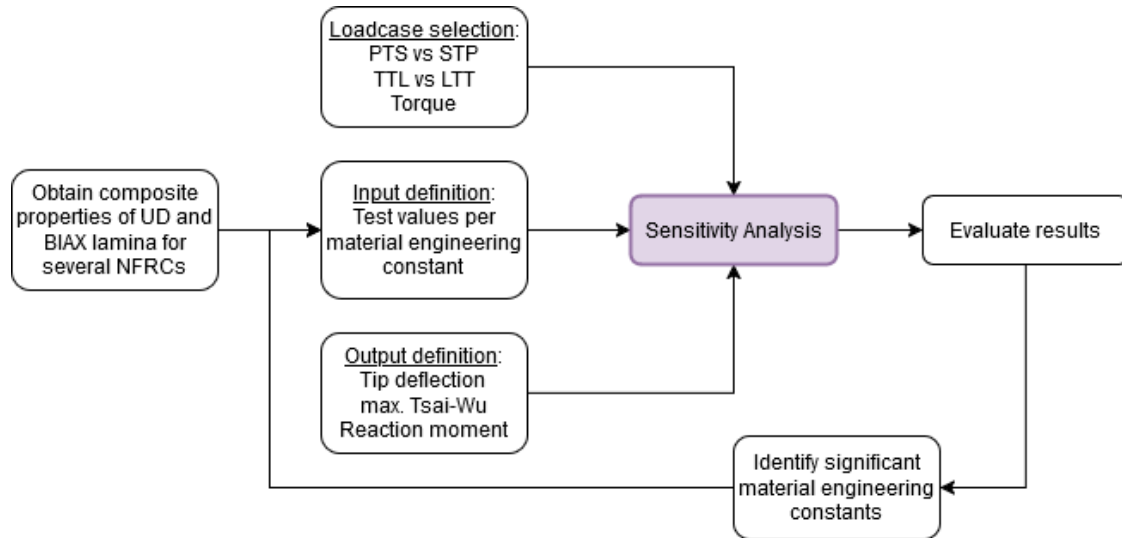


Figure 4-1: Flow diagram on the general methodology for the sensitivity study on material properties and blade behaviour for the DTU 12.6 m blade.

4-1-1 Loadcase Selection

The first step for setting up the sensitivity study is to identify the load-cases for which the material sensitivity will be investigated. The four load-cases for which the current design has been analysed are flapwise up/down and edgewise forwards/backwards. These four load-cases are identified by their directionality through the following abbreviations:

- PTS: from Pressure side Towards Suction side, or flapwise towards the tower.
- STP: from Suction side Towards Pressure side, or flapwise away from the tower.
- LTT: from the Leading edge Towards the Trailing edge, or edgewise backwards.
- TTL: from the Trailing edge Towards the Leading edge, or edgewise forwards.

A visualisation of the applied loads are presented in Figure 4-2a and Figure 4-2b. Only the TTL and PTS loads are presented as the LTT and STP are applied in the same manner but of opposite sign.

Since the sensitivity study was performed early on in the project, it must be noted that the 3D continuum shell element Abaqus model was used as described in Section 3-2-1. Moreover, the applied loads in the loadcases for the sensitivity study are those that were present in the received 3D continuum shell element model. These loads are presented in Table 4-1 and differ from the loads obtained from the stable HAWC2 model described in Section 3-1. Furthermore, the layup design of the blade used in the sensitivity study is that of the baseline model as defined in Figure 3-11.

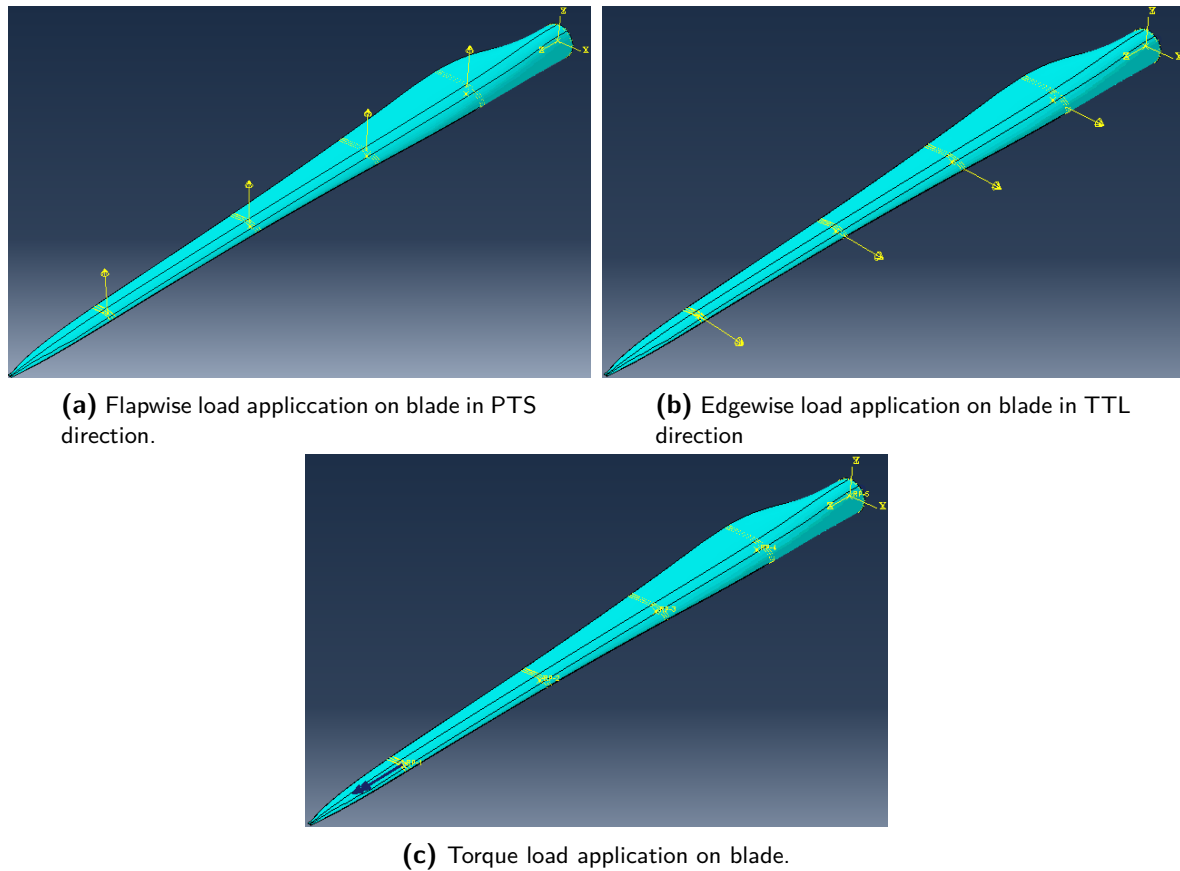


Figure 4-2: The Abaqus blade model of the DTU 12.6 m blade with the applied loads defined.

Table 4-1: The applied loads used in the sensitivity study on the DTU 12.6 m blade, which are the applied loads in the received 3D continuum shell element Abaqus model of the DTU 12.6 m blade.

R [m]	PTS [N]	STP [N]	TTL [N]	LTT [N]
2.6	8020	-2820	2270	-1050
5.2	7550	-6910	2310	-1940
7.9	6590	-4880	2580	-2160
10.8	7970	-8790	4390	-3950

The literature studied in Chapter 2 established that the stiffness and strength values of NFRCs are lower than the GFRC. Hence, it is expected to see larger deflections as well as higher stress levels when replacing the materials. It is therefore important to select the load-cases with the largest deflections and stress/strain levels so that the extremes can be identified. At minimum one flapwise and one edgewise load will need to be analysed. To determine which loadcase in each direction needs to be analysed, the absolute maximum deflections, stresses and strains will be compared in Table 4-2 and Table 4-3. The absolute maximum deflections in all three directions are denoted by U1, U2 and U3. The coordinates 1, 2, 3 correspond with the global axes directions of x, y, z respectively as defined in Figure 4-2. The stresses and strains are denoted by σ_{11} , σ_{22} , σ_{12} and ϵ_{11} , ϵ_{22} , ϵ_{12} , respectively. The directions of the stress and strains

components correspond to the material coordinate system where the 1 direction is in the blade length direction and the 2 direction is in the blade chord direction. The percentage difference between the two flapwise loadcases is given by comparing the STP results with the PTS results, and thus equals $\frac{STP-PTS}{PTS} \cdot 100\%$. The percentage difference between the two edgewise loadcases is given by comparing the TTL results with the LTT results, and thus equals $\frac{TTL-LTT}{LTT} \cdot 100\%$.

Table 4-2: Comparison of the absolute deflection and stress levels between two flapwise loads for the DTU 12.6 m baseline blade using the 3D continuum shell element Abaqus model. Difference is given by $\frac{STP-PTS}{PTS} \cdot 100\%$.

	Unit	PTS	STP	% Diff.
max abs. U1	m	0.23	0.23	0
max abs. U2	m	2.17	2.22	2.3
max abs. U3	m	0.085	0.088	3.3
max abs. σ_{11}	MPa	165	167	1.2
max abs. σ_{22}	MPa	37	41	10.3
max abs. σ_{12}	MPa	23	26	10.4
max abs. ϵ_{11}	-	0.00398	0.00402	1.2
max abs. ϵ_{22}	-	0.0022	0.0020	-8.0
max abs. ϵ_{12}	-	0.0019	0.0021	10.3

Legend
± 5%
± 5-10%
>± 10%

Table 4-3: Comparison of deflection and stress levels between two edgewise loads for the DTU 12.6 m baseline blade using the 3D continuum shell element Abaqus model. Difference is given by $\frac{TTL-LTT}{LTT} \cdot 100\%$.

	Unit	LTT	TTL	% Diff.
max abs. U1	m	0.25	0.29	13.7
max abs. U2	m	0.1	0.113	13.3
max abs. U3	m	0.013	0.014	13.2
max abs. σ_{11}	MPa	50	59	16.8
max abs. σ_{22}	MPa	15	18	17.3
max abs. σ_{12}	MPa	7.7	9.0	15.7
max abs. ϵ_{11}	-	0.0024	0.0028	13.5
max abs. ϵ_{22}	-	0.0014	0.0017	17.7
max abs. ϵ_{12}	-	0.00062	0.00072	15.7

Legend
5%
5-10%
>10%

An example will be given to show the methodology used to obtain the values in Table 4-2 and Table 4-3. For this purpose the results of the PTS loadcase on the baseline blade model will be partly presented. The absolute maximum stress levels are obtained by analysing the stress levels throughout the blade as well as through all material layers. This is done by using the "Envelop" function in Abaqus where the maximum absolute value throughout the thickness is selected for each location on the blade. The resulting colour map is used to identify the maximum across the entire blade. Figure 4-3a presents the results of the σ_{11} stress component (in direction of blade length). Its maximum occurs on top of the upper spar cap in the mid section of the blade and its value is reported in Table 4-2. The result is as expected for this loadcase. Figure 4-3b presents the results of the U1 deflection component in the direction

of the blade chord with its maximum at the blade tip as expected. The same method is repeated for the other deflection and stress/strain components. This same method will be used to obtain the results of the different test cases of the sensitivity study which will be selected in Section 4-1-5.

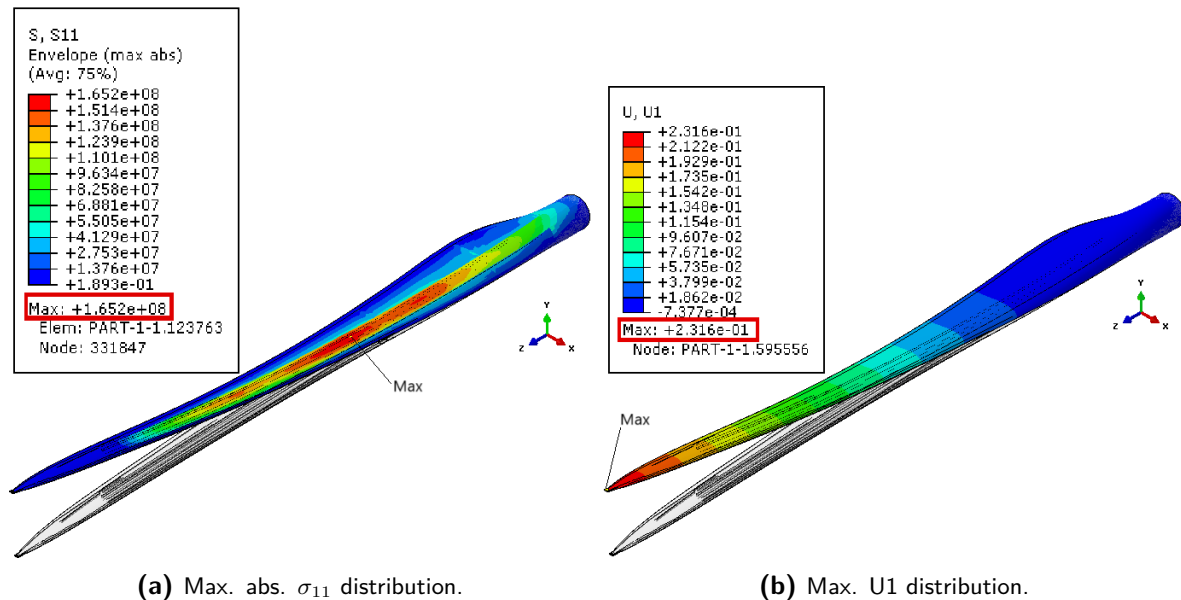


Figure 4-3: The Abaqus visualisation of the results of the DTU 12.6 m baseline blade model under the PTS loadcase. The deformed blade is visualised on top of the undeformed blade to visualise the change under loading. Subfigure (a) displays the stress distribution σ_{11} using the material coordinate system where the 1 direction is in the direction of the blade length. Subfigure (b) displays the deflection U1 where the 1 direction aligns with the global coordinate system in the direction of the blade chord.

The PTS loadcase is selected for the flapwise loadcase as this load direction is critical for the tower clearance to prevent collision with the tower. When comparing the deflections of the PTS and STP loadcases the STP shows higher deflection levels, however, the absolute differences are rather small. The largest differences between the two loadcases is observed in the stress levels. However, blade designs are typically driven by stiffness rather than strength. Hence, it is decided to focus on the PTS loadcase only.

The TTL loadcase is selected for the edgewise loadcase since the stress levels are the highest compared to the LTT loadcase. Since the edgewise deflection is less critical due to the absence of a tower clearance, the stress levels are the most interesting output to analyse. In this case the TTL loadcase did not only show the highest stress levels but also the largest deflections.

In addition to the PTS and TTL loadcases, a Torque loadcase will also be analysed. The reason is the fact that the torsional stiffness of the blade affects the aeroelastic behaviour of the blade and thus the turbine's performance. As the material properties of the NFRCS are so different from the GFRC it is important to investigate the effect on the torsional stiffness of the blade. A significant change in torsional stiffness can introduce new challenges for the controller design for example.

The Torque loadcase is generated by applying a prescribed rotation to the outer most reference

point at $r = 10.8$ m. This rotation will be 10 degrees which converts to 0.175 radians. The application of the torque load is visualised in Figure 4-2c.

In conclusion, the selected loadcases that will be analysed in the sensitivity study are: PTS, TTL and Torque.

4-1-2 Method to establish the composite material properties for the selected NFRCs to inform the Sensitivity Study

In order to provide an answer to research questions 1 and 2, it is important to select input values for the material engineering constants that are in the range of what can be expected when switching to NFRCs. For that purpose the first step is to establish the engineering constants for several NFRCs with potential for application in wind turbine blades. The engineering constants consist of the Young's moduli E_i , the shear moduli G_{ij} and Poisson's ratios ν_{ij} in all three directions, as well as the tensile and compression strength properties in both the longitudinal and transverse direction of the material together with the shear strength.

Normally, the material properties would be obtained by testing the materials. Unfortunately, this method was not available for this project. Therefore, the intention became to take the material properties from the literature on NFRCs. Unfortunately, literature on the material properties of NFRCs was very limited for both UD and BIAx composites. Often only the tensile stiffness and strength was given without any information on the fibre volume fraction of the tested composite. Only one unidirectional Flax fibre reinforced epoxy composite provided sufficient information.

To be able to establish the material properties of UD composites of different natural fibres, the micro-mechanical model for fibre reinforced composites had to be used as described in Appendix B. The Classical Laminate Theory (CLT) could then be used to obtain the BIAx composite properties, and is outlined in Appendix C. The BIAx strength values are derived from the UD material using the transformation matrix, see Equation 4-1, where $c = \cos(\theta)$ and $s = \sin(\theta)$ with θ the orientation of the fibres in the in BIAx ply. The same transformation will be used for both the compression and tensile strengths. The laminate layup that will represent the BIAx lamina is [+45,-45,-45,+45] with a ply thickness of 0.14 mm so that the total thickness equals the lamina thickness of 0.565 mm of the actual BIAx ply in the blade design.

$$\begin{Bmatrix} \sigma_1 \\ \sigma_2 \\ \tau_{12} \end{Bmatrix} = \begin{bmatrix} c^2 & s^2 & cs \\ s^2 & c^2 & -cs \\ -2cs & 2cs & c^2 - s^2 \end{bmatrix} \begin{Bmatrix} \sigma_x \\ \sigma_y \\ \tau_{xy} \end{Bmatrix} \quad (4-1)$$

The full methodology to obtain the material properties for the UD and BIAx natural fibre reinforced composites is outlined in Figure 4-4. The details of the workflow to obtain the material properties of the dry fibres and matrix materials (the white blocks) will be elaborated upon in the next section.

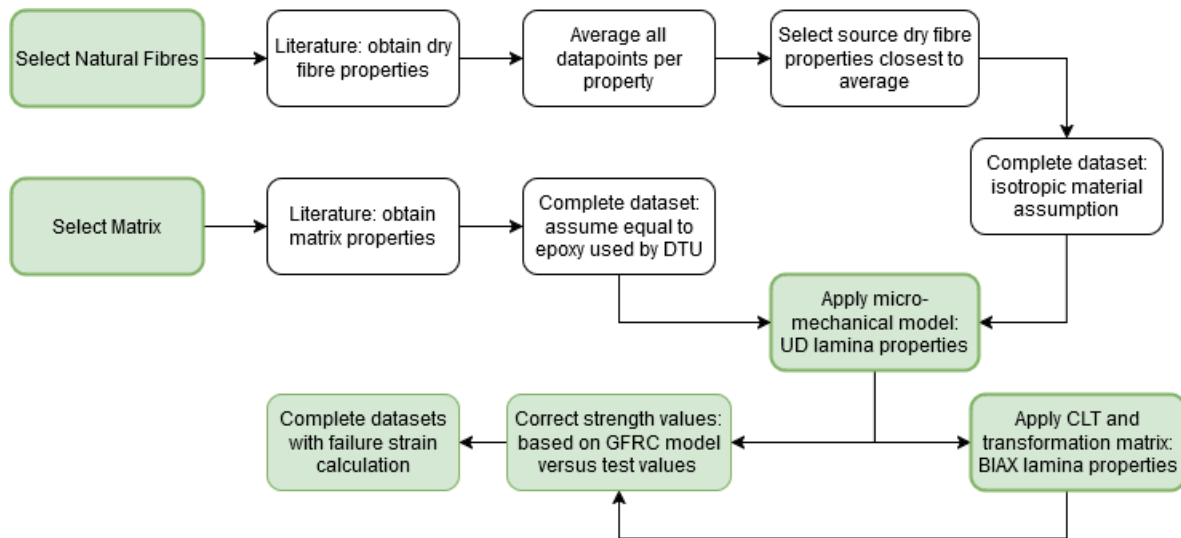


Figure 4-4: Flow diagram on the methodology to obtain the composite material properties for UD and BIAx lamina of several NFRCs.

4-1-3 Dry fibre and matrix properties

To obtain the material properties of a composite with the micro-mechanical model, the material properties of the individual components are needed as input. Specifically the longitudinal and transverse stiffness, the shear stiffness, the Poisson's ratio, the density and the longitudinal tensile strength. For the matrix the longitudinal compression strength and shear strength are also required. Furthermore, the relative amount of fibres and matrix needs to be specified, either through the fibre volume fraction or the fibre weight fraction. Finally, the fibre and matrix porosity constants α_i will need to be provided to adequately model the NFRCs.

Literature was consulted to find the required inputs for the micro-mechanical model for various natural fibres. However, the literature did not provide sufficient information on the material properties of wide range of natural fibres. The selection of natural fibres for which sufficient information was found includes Flax, Bamboo, Hemp, Sisal, Ramie and Jute. All data collected from literature on these six natural fibres can be found in Appendix D.

The average of all data for each fibre type was calculated as a first step. Then the data of one source was selected which lied closest to the established average. This data then becomes the selected input for the micro-mechanical model. This decision was made to ensure that the values are still based on a real material and not just on assumptions.

For the flax fibre properties an alternative approach was used. Instead of selecting one data source from the calculated average, the calculated average itself is the selected input for the micro-mechanical model. This decision was made as no data source provided all the desired material properties, only by combining all data into an average a full material properties input could be established.

Finally, for all natural fibres except the flax fibres, the transverse stiffness, shear stiffness and Poisson's ratio were not provided in the literature. Therefore assumption had to be made to complete the material properties input for the micro-mechanical model. For the transverse

stiffness and shear stiffness, the assumption of an isotropic material was made. While natural fibres are known to be anisotropic, this inaccuracy will need to be accepted given the lack of information available in the current body of literature. This means the transverse stiffness will be assumed equal to the longitudinal stiffness and the shear stiffness is calculated with the following equation:

$$G = \frac{E}{2(1 + \nu)} \quad (4-2)$$

For the Poisson's ratio the value is assumed to be equal to 0.3. Whenever one of these assumptions had to be made, the value is presented accompanied by an asterisk (*).

Finally, the fibre volume fraction need to be established for each NFRCs to be able to calculate the composite properties with the micro-mechanical model. The fibre volume fraction for the flax composite will be set to 41%, equal to the value used in the article by Saadati et. al., 2020 [64] that provides a full material dataset for a flax/epoxy composite. This same article is used to verify the micro-mechanical model. For the Hemp and Sisal NFRCs, instead of using the fibre volume fraction the fibre weight fraction is set to 34%, which is the value used in the selected source [34]. For the other fibres, the fibre volume fraction is set to 45% which is a typical value for NFRCs [65][37].

The final material properties of the selection of natural fibres is presented in Table 4-4.

Table 4-4: Dry fibre properties of several natural fibres, alongside the glass fibre properties used by DTU.

	V_f -	ρ g/cm ³	E_1 MPa	E_2 MPa	G_{12} MPa	ν_{12} -	σ_1^t MPa
Flax	0.41	1.45	66600	8000	2410	0.498	960
Bamboo [66]	0.45	0.86	28590	28590*	10996*	0.3*	470.87
Hemp [34]	$W_f = 0.34$	1.45	56750	56750*	21827*	0.3*	585
Sisal [34]	$W_f = 0.34$	1.42	23500	23500*	9038*	0.3*	531.5
Ramie [67]	0.4	1.5	44000	44000*	16923*	0.3*	685
Jute [49]	0.3	1.46	30000	30000*	11538*	0.3*	800
Glass	0.53	2.6	76600	76600	31250	0.2	2350

*Based on isotropic assumption

The literature has also been consulted to identify the bio-based matrix materials that are currently available. The focus was placed on materials with a Young's modulus above 3000 MPa to stay within range of the currently used epoxy (Table 2-2). From the range of bio-based plastic options identified in Chapter 2, the biopolymer PLA was selected as matrix material for the NFRCs. This decision was based on the biodegradable nature of the material, along with acceptable material properties when compared to the epoxy used by DTU.

The to be used material properties are presented in Table 4-5 and are the general characteristics of commercial PLA as specified in [38]. It must be noted that the compression and shear strength values had to be assumed, denoted by the asterisk (*), as no values were specified in the material source. As the material properties are of the same order of magnitude as the epoxy used by DTU, the compression and shear strength are assumed to be equal to the epoxy values specified in Table 2-2.

Finally, the PLA material used for the hemp and sisal NFRCs is the PLLA (polymerisation of L-lactide) material used in the selected source for these fibres [34]. The source also provides the resulting composite properties which can then be used to compare with the results from the micro-mechanical model. The source provides the density, Young's modulus and tensile strength, the other missing properties are assumed equal to the epoxy used by DTU. The final dataset for the PLLA material is presented in Table 4-5 along with the PLA material.

Table 4-5: Material properties of bio-based resins PLA and PLLA, along with the epoxy resin used by DTU. The asterisk (*) indicates that the value is assumed equal to the epoxy resin due to the lack of available information.

	ρ g/cm ³	E MPa	ν_{12} -	σ^t MPa	σ^c MPa	τ MPa
PLA [38]	1.27	3500	0.36	73	93*	45*
PLLA [39]	1.25	3600	0.36	70	93*	45*
Epoxy	1.2	3850	0.35	67	93	45

Typically, the porosity constants α for the micro-mechanical model are obtained by analysing a cross-section (perpendicular to the fibres) of a piece of manufactured composite. As this is not possible in the scope of this project the literature was consulted to obtain reasonable values. Research by Madsen et. al., 2007 [43] provides the porosity constants for four different natural fibre reinforced composites. As the micro-mechanical model is verified with the flax fibre composite, the "flax/PP I" composite porosity constants are chosen for use in the current work. This composite also has a similar fibre volume fraction to the value used in the current work. It amounts to the assumption of no matrix porosity, a fibre porosity constant of 0.026, an interface porosity constant of 0.013 and an impregnation porosity factor of 0.185. Summed together the fibre porosity constant equals 0.224. These porosity constants will be used for all natural fibre reinforced composites under consideration as no other information is currently available.

Finally, the empirical correction factor k for the longitudinal compression strength of the composite was obtained by fitting the Flax/Epoxy data from [64], it was found that $k = 0.066$. As no other information is currently available for the other natural fibres, it is assumed that $k = 0.066$ for all NFRCs considered in the current work. Through fitting the DTU GFRC data it was found that $k = 0.175$ for the GFRC model.

4-1-4 Calculated composite material properties for the selected NFRCs

Table 4-6 presents the calculated UD material properties for the selected NFRCs alongside those of the GFRC used by DTU. The maxima and minima among the NFRCs for each property are highlighted by green and red respectively. Comparing the calculated properties of the GFRC with the properties as used by DTU show that the stiffnesses and poisson ratio's originate from the calculations. This data can thus not be used to validate the model. The strength values differ more and it will be assumed that the values used by DTU originate from experiment. To verify the model, the Flax/Epoxy system will be used since a full dataset is available from the experiments performed by Saadati et. al. [64]. The research by Saadati et. al. exposed the non-linear behaviour of the tensile Young's modulus of a Flax/Epoxy

unidirectional composite. The very first part of the stress-strain curve indicates a modulus of 30.04 GPa. Under the loading the fibres straighten and the microfibrils in the flax fibres reorient, resulting in a decreased modulus down to 21.26 GPa. This knee point occurs at 0.1% strain with the failure strain being 1.35%. Since the majority of the stress-strain curve belongs to the modulus of 21.26 GPa, it is this value that will be used to verify the micro-mechanical model. The dry fibre properties and epoxy properties were not provided in the article, hence, the values as defined in Section 4-1-3 will be used as input.

Table 4-6: UD composite properties of GFRC used by DTU with provided and calculated values, as well as the calculated UD composite properties of several NFRCs. Green cells indicate the maximum value among the NFRCs, while red cells indicates the minimum values among the NFRCs.

Property	GFRC used by DTU	GFRC micro-mechanics	Flax/ PLA	Bamboo/ PLA	Hemp/ PLLA	Sisal/ PLLA	Ramie/ PLA	Jute/ PLA
E_1 [MPa]	42706	42700	24000	11700	16000	8150	16100	9760
E_2 [MPa]	12585	12600	5500	8500	7100	6700	8400	6800
E_3 [MPa]	12585	12600	5500	8500	7100	6700	8400	6800
G_{12} [MPa]	4613	4610	1830	3160	2560	2440	3100	2500
G_{13} [MPa]	4613	4610	1830	3160	2560	2440	3100	2500
G_{23} [MPa]	4613	4610	1830	3160	2560	2440	3100	2500
ν_{12} [-]	0.258	0.27	0.38	0.3	0.32	0.32	0.3	0.32
ν_{13} [-]	0.258	0.27	0.38	0.3	0.32	0.32	0.3	0.32
ν_{23} [-]	0.364	0.36	0.49	0.35	0.39	0.38	0.35	0.35
ρ [g/cm ³]	1.95	1.95	1.23	0.96	1.25	1.19	1.25	1.24
σ_1^t [MPa]	1000	1250	340	194	151	149	244	191
σ_2^t [MPa]	47	41	19	24	36	32	30	35
σ_1^c [MPa]	813	807	120	210	170	162	206	167
σ_2^c [MPa]	146.5	57	53	70	110	95	84	99
τ_{12} [MPa]	48	37	29	25	30	30	26	30
V_f [-]	0.53	0.53	0.41	0.45	0.28	0.3	0.4	0.3
W_f [-]	0.71	0.71	0.48	0.4	0.34	0.34	0.48	0.35
ϵ_f [-]	0.023	0.029	0.014	0.017	0.01	0.018	0.015	0.02

Table 4-7: Flax/Epoxy composite properties from test data from literature [64] as well as calculated values using the micro-mechanical model. The calculation uses the material properties of the flax fibres and epoxy as specified in Section 4-1-3.

	V_f -	E_1 MPa	E_2 MPa	G_{12} MPa	ν_{12} -	ρ g/cm ³	σ_1^t MPa	σ_2^t MPa	σ_1^c MPa	σ_2^c MPa	τ_{12} MPa
Saadati[64]	0.41	21260	4240	1920	0.373	1.28	300	15	126	72	45
Computed	0.41	23830	5480	1910	0.38	1.19	406	14	126	19	23

Table 4-7 compares the material properties from literature with the computed values. Overall the stiffness properties are relatively similar. The differences that are visible can be due to

differences in the properties of the materials used by the article and the computation. An important difference that is unknown is the porosity volume in the composite manufactured for the article. Moreover, transverse stiffness calculation in the model does not include porosity. This might cause the overestimation of this property. The same analysis can be applied to the comparison of the longitudinal tension strength. Contrary, the transverse compression strength and shear strength are highly underestimated.

The difficulty of predicting the lamina strength values from its constituents is under-scribed by other studies who investigate the accuracy of different strength models [68][69]. These studies compare the predicted values from different models with experimental results. A study by Huang et. al. [69] concluded that the inclusion of the stress concentration factor (SCF) on the strength values of the matrix improve the accuracy of the models in terms of their strength predictions: "A matrix plate with a hole generates a stress concentration in its neighborhood if the plate is subjected to an external load. Similarly, when the hole is filled with a fiber of different properties the matrix sustains a stress concentration as well"[69]. However, even with the SCFs included the models have a strength prediction with an error margin of 20-30%.

The measured strength values of the GFRC used by DTU are available and the micro-mechanical model results use the same dry fibre and matrix properties as input. Therefore the difference with the micro-mechanical model is quantified through the calculation of their fraction: $\frac{\text{measured}}{\text{models}}$. Multiplying the results of the micro-mechanical model with these fractions results in the given measured strength values. Hence, these fractions can be used as a correction on the micro-mechanical model. As test data is not available for the strength values of the NFRCs, the correction factors of the GFRCs will be used to correct the strength values that come out of the micro-mechanical model. The used correction factors for the strengths of the UD composites is presented in Table 4-8. The presented strength values of the NFRCs in Table 4-6 have already been corrected.

Table 4-8: UD strength correction factors for the micro-mechanical model calculated from the difference between the calculated values and test values of the GFRC used by DTU, see Table 4-6.

σ_1^t	σ_1^c	σ_2^t	σ_2^c	τ
0.80	1.01	1.14	2.55	1.31

From the comparison between the GFRC and the NFRCs, a few observations can be made. Firstly, the stiffness of the NFRCs is significantly lower due to the reduced properties of the natural fibres compared to glass fibres. This is also partly due to the lower fibre content in the NFRCs as well as the inclusion of porosity. On the other hand, the density of the NFRCs is also significantly reduced which is beneficial for the blade design. Hence, in terms of specific stiffness (E/ρ) the NFRC's stiffnesses come closer to that of the GFRCs than the absolute stiffness. The comparison between the absolute and specific longitudinal stiffness for the composites are presented in Figure 4-5. For the BIAx composite the Bamboo even succeeds the specific stiffness property of the GFRC. The same comparison for the shear stiffness is made in Figure 4-6 where the specific shear stiffness of the UD Bamboo and Ramie succeed that of the GFRC. Furthermore, the strengths of the NFRCs are also lower due to the lower fibre strengths. The significant strength reduction also results in smaller failure strains which can become a challenge for a NFRC wind turbine blade design.

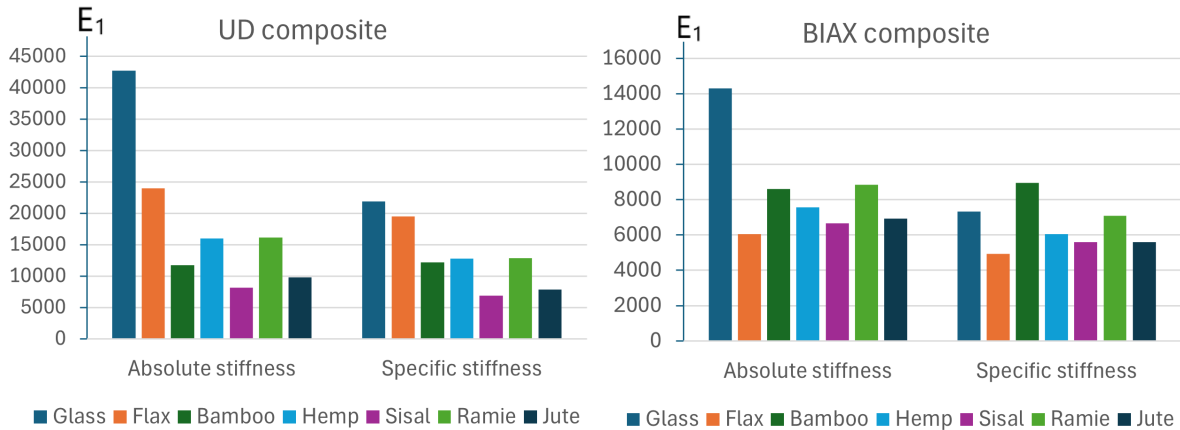


Figure 4-5: Comparison between absolute stiffness E_1 and specific stiffness E_1/ρ for the UD and BIAx composites in MPa, comparing GFRC with several NFRCs.

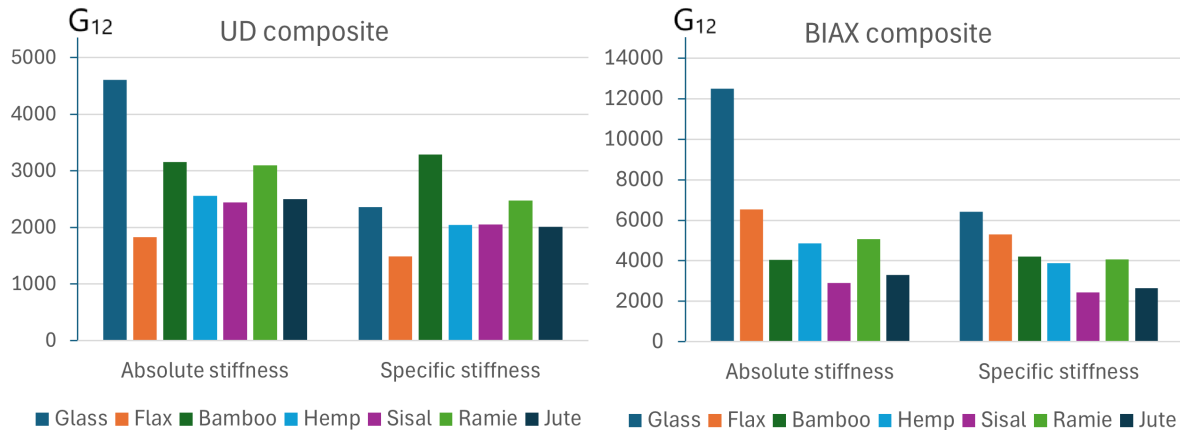


Figure 4-6: Comparison between absolute shear stiffness G_{12} and specific shear stiffness G_{12}/ρ for the UD and BIAx composites in MPa, comparing GFRC with several NFRCs.

The final resulting datasets for the BIAx composites are presented in Table 4-10. The BIAx material properties are derived from the presented UD composite properties using the classical laminate theory and the transformation matrix. Again the strength values from the micro-mechanical model for the NFRCs are corrected with the fraction quantifying the difference between the measured values and the micro-mechanical model results for the DTU GFRC, see Table 4-9. It must be noted that the strength values are highly overestimated with the model, rather than underestimated as for the UD composite values. This could be because the strength values are calculated from the UD values using the transformation matrix. This method does not grasp the characteristics of the BIAx material as in a non-crimp biaxial fabric, like the fibre-matrix interaction. Since no other method is available to this project the corrected strength values based on the GFRCs is the best estimate available.

Table 4-9: BIAx strength correction factors for the micro-mechanical model calculated from the difference between the calculated values and test values of the GFRC used by DTU.

σ_1^t	σ_1^c	σ_2^t	σ_2^c	τ
0.36	0.53	0.33	0.45	0.41

Table 4-10: BIAx composite properties of GFRC used by DTU with provided and calculated values, as well as the calculated BIAx composite properties of several NFRCs. Green cells indicate the maximum value among the NFRCs, while red cells indicates the minimum values among the NFRCs.

Property	GFRC characteristic	GFRC micro-mechanics	Flax/PLA	Bamboo/PLA	Hemp/PLLA	Sisal/PLLA	Ramie/PLA	Jute/PLA
E_1 [MPa]	13920	14300	6060	8600	7570	6650	8850	6930
E_2 [MPa]	13920	14300	6060	8600	7570	6650	8850	6930
E_3 [MPa]	13920	13400	6190	8580	7390	6780	8550	6840
G_{12} [MPa]	11500	12500	6530	4040	4860	2900	5080	3290
G_{13} [MPa]	5536	4610	1830	3160	2560	2440	3100	2500
G_{23} [MPa]	5536	4610	1830	3160	2560	2440	3100	2500
ν_{12} [-]	0.533	0.55	0.65	0.36	0.48	0.36	0.43	0.38
ν_{13} [-]	0.533	0.17	0.2	0.28	0.24	0.31	0.24	0.28
ν_{23} [-]	0.257	0.17	0.2	0.28	0.24	0.31	0.24	0.28
ρ [g/cm ³]	1.94	1.94	1.23	0.96	1.25	1.19	1.25	1.24
σ_1^t [MPa]	223	612	72	41	32	31	53	41
σ_2^t [MPa]	223	685	79	49	44	42	61	51
σ_1^c [MPa]	209	396	26	52	44	40	52	42
σ_2^c [MPa]	209	469	42	61	57	54	62	56
τ_{12} [MPa]	155	375	21	38	26	26	36	26
V_f [-]	0.53	0.53	0.41	0.45	0.28	0.3	0.4	0.3
W_f [-]	0.71	0.71	0.48	0.4	0.34	0.34	0.48	0.35
ϵ_f [-]	0.16	0.016	0.012	0.0048	0.0042	0.0046	0.0060	0.0059

Comparing the data of the NFRCs with that of the GFRC, it can again be stated that the stiffness, strengths, density and failure strains of the NFRCs is significantly lower. This result is expected as the BIAx properties are derived from the UD material properties where the same trends were observed.

What stands out for the BIAx material used by DTU is that the Poisson ratio ν_{13} is equal to ν_{12} instead of the other out of plane Poisson ratio ν_{23} . As the properties in the 1 and 2 direction are equal it is expected that both out of plane properties in the 13 and 23 direction are also equal. Furthermore, the out of plane tensile stiffness is typically slightly lower than the in plane stiffness of a BIAx material as the fibres run in the perpendicular plane.

The data from the GFRCs as calculated with the micro-mechanical model is used as the baseline for the sensitivity study. This will provide a fair comparison between the GFRC and NFRCs, making the results also valuable for a redesign of the blade with NFRCs.

4-1-5 Input parameters

Now that the value range for each material engineering constant for NFRCs is established, the input for the sensitivity study can be defined. The methodology to obtain the final inputs for the sensitivity study is outlined in Figure 4-7.

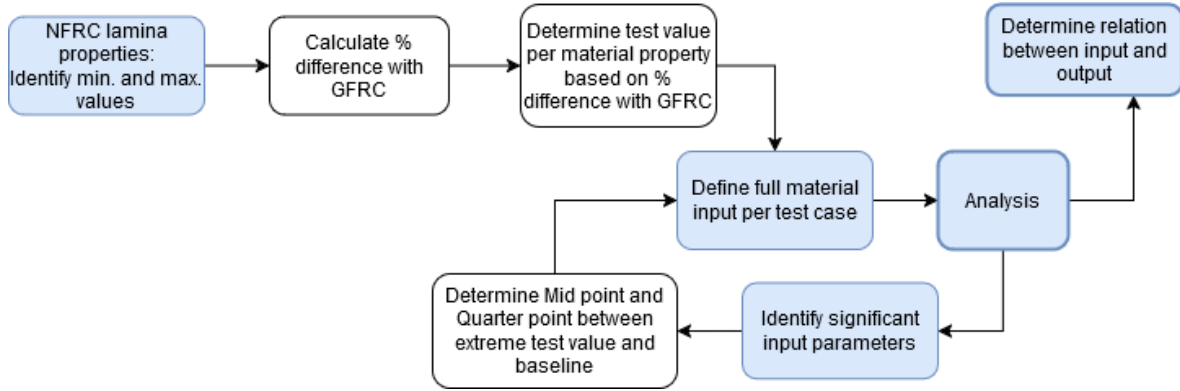


Figure 4-7: Flow diagram on the methodology to obtain the input parameters for the sensitivity analysis on the DTU 12.6 m blade.

The extrema within the NFRCs for each engineering constant are specified in Table 4-6 and Table 4-10 for the UD and BIAX materials respectively. For each identified extreme value of the material engineering constants, the percentage difference with respect to the DTU GFRCs is calculated. This calculated percentage is then rounded up to find the final percentage difference between the baseline and the extreme test value for the sensitivity study. It is chosen to round off the values to an integer value that is a multiple of 5 to ease post-processing of the results. The percentages are rounded up as this creates extreme input values slightly more extreme than what is found in the NFRCs. This way the full range of what can be expected when switching to NFRCs can be analysed, especially given the fact that the used material properties are estimates. If the minimum in the NFRCs range is higher than the value of the GFRC and vice versa, no test case will be created for that material property in that direction. In those cases the material property of NFRCs will not reach those levels, making that range of values not of interest.

For each test case in the sensitivity study, one engineering constant will be changed while keeping the other engineering constants equal to the baseline values. However, a few engineering constants are equal and shall be changed simultaneously. For a UD composite the properties in the two transverse directions are approximately the same meaning the following engineering constants are set equal: the Young's moduli E_2 and E_3 , the Poisson's ratio ν_{12} and ν_{13} , and the shear moduli G_{12} and G_{13} . Moreover, to keep the tests as realistic as possible it is important to adjust the Poisson's ratios accordingly when changing the Young's moduli of the material. To relate the Poisson's ratios with the Young's moduli the following equations will be used:

$$\nu_{12} = \frac{\nu_{21} \cdot E_1}{E_2} \quad (4-3) \quad \nu_{13} = \frac{\nu_{31} \cdot E_1}{E_3} \quad (4-4) \quad \nu_{23} = \frac{\nu_{32} \cdot E_2}{E_3} \quad (4-5)$$

It must be noted that for UD material $\nu_{12} = \nu_{13}$ and $\nu_{23} = \nu_{32}$ as $E_2 = E_3$. To calculate the desired Poisson's ratios an estimate for the value ν_{21} is required. For this purpose the ν_{21}

will be calculated using Equation 4-3 and Table 4-6 for the relevant NFRCs. The extreme minimum test value for E_1 originates from the Sisal-PLLA material and thus the ν_{21} value from Sisal-PLLA will be used to calculate ν_{12} for this test case. Similarly the ν_{21} from Flax-PLA will be used when E_2 and E_3 are changed. Additionally, when changing E_2 and E_3 the engineering constant ν_{23} will also be changed to the value of Flax-PLA as this Poisson's ratio relates to E_2 and E_3 .

Similarly, for a $\pm 45^\circ$ BIAX material the engineering constants in the two in-plane direction are equal. Hence, the following engineering constants will be changed in pairs: the Young's moduli E_1 and E_2 , the Poisson's ratio ν_{13} and ν_{23} , and the shear moduli G_{13} and G_{23} . Equation 4-3, Equation 4-4 and Equation 4-5 are again used to calculate somewhat realistic Poisson's ratios when changing the Young's moduli. As $\nu_{13} = \nu_{23}$ only the Poisson's ratios ν_{21} and ν_{32} are needed in the calculation. The extreme minimum test values for E_1 , E_2 and E_3 originate from Flax-PLA and this material's Poisson's ratios ν_{21} and ν_{32} will thus be used to calculate the required Poisson's ratios for the different tests.

Furthermore, changing from one material to another will in most cases result in multiple engineering constants changing. Therefore, an extreme case will also be tested where all the UD engineering constants are set equal to the extreme minimum test values. For this test case the $\nu_{12} = \nu_{13}$ value is calculated using ν_{21} from Sisal-PLLA as the combination of E_1 and E_2 is most similar to this material. The value ν_{23} is set equal to the Flax-PLA material as E_2 and E_3 originate from this material. Similarly, there will be an extreme test case with all the BIAX engineering constants set to the extreme minimum test values.

It must be noted that for both the UD and BIAX material, only an extreme case is tested where all the material engineering constants are set to the extreme minimum test values. This is due to the fact that the stiffnesses of the NFRCs do not reach higher than that of the GFRCs. Only the Poisson's ratios show values higher than GFRCs. The sensitivity of the Poisson's ratios, although analysed separately, will already be tested in the test cases for the Poisson's ratios making the extreme maximum test case redundant.

A final case will be analysed where both the UD and BIAX engineering constants will be set equal to the "extreme min" case. This test is useful as both the UD and BIAX material will be replaced in a redesign. Thus, this case will provide information on what extreme can be expected when changing both materials simultaneously.

All the inputs per test case for the UD and BIAX material are combined in Table 4-11 and Table 4-12 respectively, where the changed parameters are indicated in red. Each test case is given the name of the format "[material]_[input]_[min/max]".

Table 4-11: Test cases for the sensitivity study on the UD material properties for the DTU 12.6 m blade. The terms "min" and "max" indicate whether the extreme test value is a minimum or maxima compared to the baseline values. The term "mid" refers to the test value at the midpoint of the baseline and extreme test value. The term "quarter" refers to the test value at one quarter from the baseline to the extreme test value. Red indicates the values changed compared to the baseline model.

Test case	E_1 MPa	E_2 MPa	E_3 MPa	ν_{12} -	ν_{13} -	ν_{23} -	G_{12} MPa	G_{13} MPa	G_{23} MPa
Baseline	42705.8	12585.4	12585.4	0.2577	0.2577	0.3640	4613.36	4613.36	4613.36
E_1 min	6405.87	12585.4	12585.4	0.1336	0.1336	0.3640	4613.36	4613.36	4613.36
E_1 mid min	24555.8	12585.4	12585.4	0.1699	0.1699	0.3640	4613.36	4613.36	4613.36
E_1 quarter min	33630.8	12585.4	12585.4	0.2029	0.2029	0.3640	4613.36	4613.36	4613.36
E_2+E_3 min	42705.8	5034.16	5034.16	0.7165	0.7165	0.4219	4613.36	4613.36	4613.36
$G_{12}+G_{13}$ min	42705.8	12585.4	12585.4	0.2577	0.2577	0.3640	1614.68	1614.68	4613.36
$G_{12}+G_{13}$ mid min	42705.8	12585.4	12585.4	0.2577	0.2577	0.3640	3114.02	3114.02	4613.36
$G_{12}+G_{13}$ quarter min	42705.8	12585.4	12585.4	0.2577	0.2577	0.3640	3863.69	3863.67	4613.36
G_{23} min	42705.8	12585.4	12585.4	0.2577	0.2577	0.3640	4613.36	4613.36	1614.68
$\nu_{12}+\nu_{13}$ max	42705.8	12585.4	12585.4	0.3866	0.3866	0.3640	4613.36	4613.36	4613.36
ν_{23} max	42705.8	12585.4	12585.4	0.2577	0.2577	0.4550	4613.36	4613.36	4613.36
ν_{23} min	42705.8	12585.4	12585.4	0.2577	0.2577	0.3458	4613.36	4613.36	4613.36
Extreme min	6405.87	5034.16	5034.16	0.3340	0.3340	0.5369	1614.68	1614.68	1614.68

Table 4-12: Test cases for the sensitivity study on the BIAx material properties for the DTU 12.6 m blade. The terms "min" and "max" indicate whether the extreme test value is a minimum or maxima compared to the baseline values. The term "mid" refers to the test value at the midpoint of the baseline and extreme test value. The term "quarter" refers to the test value at one quarter from the baseline to the extreme test value. Red indicates the values changed compared to the baseline model.

Test case	E_1 Mpa	E_2 Mpa	E_3 Mpa	ν_{12} -	ν_{13} -	ν_{23} -	G_{12} Mpa	G_{13} Mpa	G_{23} Mpa
Baseline	14273.3	14273.3	13351.3	0.5470	0.1698	0.1698	12448.8	4613.36	4613.36
E_1+E_2 min	5709.34	5709.34	13351.3	0.6451	0.0738	0.0738	12448.8	4613.36	4613.36
E_1+E_2 mid min	9991.34	9991.34	13351.3	0.3545	0.2183	0.2183	12448.8	4613.36	4613.36
E_1+E_2 quarter min	12132.3	12132.3	13351.3	0.5467	0.1444	0.1444	12448.8	4613.36	4613.36
E_3 min	14273.3	14273.3	5340.5	0.5470	0.4614	0.4614	12448.8	4613.36	4613.36
G_{12} min	14273.3	14273.3	13351.3	0.5470	0.1698	0.1698	2489.76	4613.36	4613.36
G_{12} mid min	14273.3	14273.3	13351.3	0.5470	0.1698	0.1698	7469.27	4613.36	4613.36
G_{12} quarter min	14273.3	14273.3	13351.3	0.5467	0.1698	0.1698	9959.02	4613.36	4613.36
$G_{13}+G_{23}$ min	14273.3	14273.3	13351.3	0.5470	0.1698	0.1698	12448.8	1614.68	1614.68
ν_{12} max	14273.3	14273.3	13351.3	0.6561	0.1698	0.1698	12448.8	4613.36	4613.36
ν_{12} mid max	14273.3	14273.3	13351.3	0.6017	0.1698	0.1698	12448.8	4613.36	4613.36
ν_{12} quarter max	14273.3	14273.3	13351.3	0.5743	0.1698	0.1698	12448.8	4613.36	4613.36
ν_{12} min	14273.3	14273.3	13351.3	0.3555	0.1698	0.1698	12448.8	4613.36	4613.36
ν_{12} mid min	14273.3	14273.3	13351.3	0.4512	0.1698	0.1698	12448.8	4613.36	4613.36
ν_{12} quarter min	14273.3	14273.3	13351.3	0.4991	0.1698	0.1698	12448.8	4613.36	4613.36
$\nu_{13}+\nu_{23}$ max	14273.3	14273.3	13351.3	0.5470	0.3142	0.3142	12448.8	4613.36	4613.36
Extreme min	5709.34	5709.34	5340.52	0.6451	0.1845	0.1845	2489.76	1614.68	1614.68

It is not only of interest to identify the engineering constants that drive the blade behaviour, but also to know the relation between the input and output parameters. Moreover, the percentage change in inputs for the UD and BIAx materials differ, thus their results cannot be directly compared. Establishing the relation between input and output for each material allows for the assessment of their relative impacts on the blade behaviour. This will be a valuable input for redesign of the blade with NFRCs. The methodology to obtain these results is presented in the lower part of Figure 4-7.

To evaluate the relation between the input and output, additional data points need to be evaluated. This will only be done for the input parameters that were found to bring about significant changes in the outputs analysed. The additional data points that will be evaluated are the mid point and quarter point between the baseline and extreme test case. So for example, the change in shear stiffness of the BIAx material for the extreme test case was 80%, thus the mid point will now yield a change of 40% and the quarter point a change of 20%. These additional test cases have also been added to Table 4-11 and Table 4-12. The names of these test cases are of the format "[material]_[input]_[mid/quarter]_[min/max]". The additional test cases related to the UD material are for E1 and G12=G13. The additional test cases related to the BIAx material are for E1=E2, G12 and ν_{12} .

Finally, the sensitivity of the blade to the core material stiffness will also be evaluated. For the bending stiffness the thickness of the core material is generally more important than the stiffness of the core itself. For example, increasing the core thickness of a sandwich plate will increase the distance of the stiff composite plates to the neutral axis, thereby increasing the moment of inertia which in turn increases the bending stiffness of the plate. To verify this prediction, each loadcase will be analysed with the core's Young's modulus reduced by 50% while keeping all other values equal to the baseline. This means the Young's modulus is reduced to 275 MPa. As the core material is isotropic, the change in Young's modulus will impact both the bending stiffness and torsional stiffness.

4-1-6 Output Parameters

The output parameters that will be analysed are the following:

- **Tip deflection U:** Due to the blade-tower interface, the maximum tip deflection is of special interest for the PTS loadcase.
- **Reaction moment RM3:** For the Torque loadcase the torsional rigidity " $G \cdot J$ " of the blade is of interest. Due to the complexity of determining the torsional rigidity of the full blade, an alternative approach is used for the sensitivity analysis. The torsional rigidity $G \cdot J$ expressed by the general torsion equation [70] is:

$$G \cdot J = \frac{T \cdot L}{\theta} \quad (4-6)$$

Where G is the torsional stiffness, J is the polar moment of inertia, T is the applied torque, L is the length over which the torque is applied, and θ is the angle of twist. By applying a prescribed rotation $\theta = 10^\circ$ to the blade of 12.6 m at the location $L = 10.8$ m, the required torque to reach this rotation becomes an indication of the level of torsional rigidity. The larger the required torque, the larger the torsional rigidity. Therefore, the reaction moment at the blade root around the blade z-axis, $RM3$, becomes the to be analysed output. The reaction moment at the root thus equals the required torque: $T = RM3$.

- **Maximum Tsai-Wu value:** The level of change in stress levels and possible resulting material failure is important to analyse given the reduced strength values of NFRcs. The Tsai-Wu failure criterion is selected for this purpose. This failure criteria considers

the absolute stresses as well as the interaction between stresses. Moreover, the different strengths in tension and compression for composite materials are taken into account. The general formulation is given in Equation 4-7 [71].

$$\frac{\sigma_x^2}{X^t X^c} + \frac{\sigma_y^2}{Y^t Y^c} - \sqrt{\frac{1}{X^t X^c} \frac{1}{Y^t Y^c}} \sigma_x \sigma_y + \left(\frac{1}{X^t} - \frac{1}{X^c} \right) \sigma_x + \left(\frac{1}{Y^t} - \frac{1}{Y^c} \right) \sigma_y + \frac{\tau_{xy}^2}{S^2} = 1 \quad (4-7)$$

If the Tsai-Wu failure criteria is above 1 it means that material failure has occurred in one or more plies. The maximum envelop Tsai-Wu value will be used as output in the sensitivity study.

Before the maximum Tsai-Wu outputs are interpreted, it is important to check the validity of the results. Numerical failure, due to for example bad meshing, can lead to artificial failure results. The results are considered real if the maximum Tsai-Wu value originates from a large region with high maximum Tsai-Wu values. The value is artificial if the region is highly localized and the maximum Tsai-Wu value location is next to a drop from a high to a low value. The maximum Tsai-Wu value is then likely caused by issues with the mesh in the FE model and thus called artificial. Through Hooke's law it is likely to see the maximum Tsai-Wu location coincide with the maximum strain location. This becomes an additional check for the validity of the results. Furthermore, it will be checked whether the max Tsai-Wu failure occurs in a UD or BIAx ply as their failure differ in criticality.

For all loadcases, the results will be presented by the absolute percentage difference with respect to the baseline results.

4-2 Verification of geometric linearity assumption

All the FEM simulations of the sensitivity study have been performed using a linear static analysis. The linear static analysis has the advantage that the behaviour scales with the applied loading as the stiffness is constant with changing shape [57]. However, geometric linearity can only be applied under the small strain assumption. Geometric non-linearity considers the effect of the change in shape on the stiffness. Only if the change in shape is small the effect can be neglected and the results from both analysis types will be similar. For the geometric non-linear analysis the stiffness will thus need to be re-computed at each increment making this analysis much more computationally expensive. There are three guidelines that generally indicate that geometric non-linearity should be used for a cantilever beam [72][73]:

- Guideline 1: Beam's deflection is more than half the beam's thickness. This yields deflections larger than 0.34 m for the DTU 12.6 m blade.
- Guideline 2: The deformation anywhere in the beam is larger than $\frac{1}{20}$ th of the largest dimension [74]. This yields deformations larger than 0.63 m for the DTU 12.6 m blade.
- Guideline 3: The strains in the beam exceed 5% and/or the angles of rotation in the beam exceed 5 to 10 degrees.

It is important to check if the difference between the linear and non-linear analysis is significant. If the difference is significant this can affect the type of analysis that is chosen to perform the redesign of the blade.

To test the effect of incorporating geometric non-linearity a few test cases will be analysed. The most critical loadcase in terms of deflection is the PTS loadcase where the longitudinal stiffness of both materials have the largest impact on the blade's deflection and stress levels. Therefore, the "PTS Baseline", PTS "UD_E1_min" and PTS "BIAX_E1_E2_min" test cases will be analysed. Furthermore, it is also important to analyse the effect of geometric non-linearity on the torsional stiffness of the blade as that affects the aeroelastic behaviour of the blade. The material's shear stiffness has the largest impact on the torsional stiffness, hence, the test cases "Torque Baseline", Torque "UD_G12_G13_min" and Torque "BIAX_G12_min" will be analysed.

The required output to compare with guidelines 1 and 2 is the magnitude of the tip deflection "Tip U mag" and/or the maximum deflection anywhere in the blade "Max (U mag)". For guideline 3 the maximum magnitude of angle of rotation "Max(UR mag.)", and the percentages strains " ϵ_{11} , ϵ_{22} , ϵ_{12} " are the required outputs.

It must be noted that the maximum angle of rotation for the Torque loadcases equal the threshold of 10 degrees as the load is applied through the prescribed rotation of 10 degrees. The results will establish whether the threshold of guideline 3 for this specific blade is higher or lower than 10 degrees.

The conclusions from the application of the guidelines will be verified by running the non-linear analysis for the selected test cases. The results are presented as the percentage difference of the outputs of the non-linear analysis with respect to the linear analysis, so $\frac{nonlinear-linear}{linear} \times 100\%$.

Results & Discussion: Sensitivity Analysis

The outputs of all the different test cases will need to be compared to the baseline model outputs to be able to draw conclusions on the sensitivity of the various outputs to each input parameter. The to be analysed outputs for the baseline model are summarised in Table 5-1. All the results of the sensitivity study will be presented as the percentage difference with respect to these baseline model results.

Table 5-1: DTU 12.6 m baseline blade model outputs that will be used in the analyses of the sensitivity study on the impact of individual material properties on the blade's behaviour.

	Unit	PTS	TTL	Torque
RM3 due to 10° twist at $r = 10.8$ m	Nm	-	-	-4050
Max tip deflection in load direction	m	2.18	0.31	-
Max. Tsai-Wu	-	0.71	0.41	-
Location of: max. Tsai-Wu	-	Upper spar-cap $r \approx 6$ m	Trailing edge $r \approx 4$ m	-

5-1 Core material test results

The results of the sensitivity study where the Young's modulus of the core material is halved are presented in Table 5-2. From the results it can be concluded that the stiffness of the core material does not play a significant role in the blade performance. However, the thickness of the core material will play a significant role as it influences the moment of inertia. This will be of special interest when designing for the torsion during the redesign process.

Table 5-2: Results of the sensitivity study on the Young's modulus of the core material of the DTU 12.6 m blade.

	Baseline	Core_E_min	Difference
PTS max U2 tip deflection [m]	2.18	2.17	-0.5%
TTL max U1 tip deflection [m]	0.31	0.30	-3%
Torque RM3 root [Nm]	4050	4020	-0.7%

5-2 Torque loadcase results

The results of the sensitivity study of the torsional stiffness of the blade showed that only a few material engineering constants have a significant impact. The results of the other material engineering constants only had a very small impact, of which most less than 1% change. The results of all material engineering constants can be found in Appendix E. The significant results of the sensitivity study on torsional stiffness are presented in Figure 5-1, where the blue corresponds to the UD material test cases, the orange corresponds to the BIAx material test cases and the red corresponds to the "extreme_min" test case where all properties for both the UD and BIAx material are set to the minima of the test ranges.

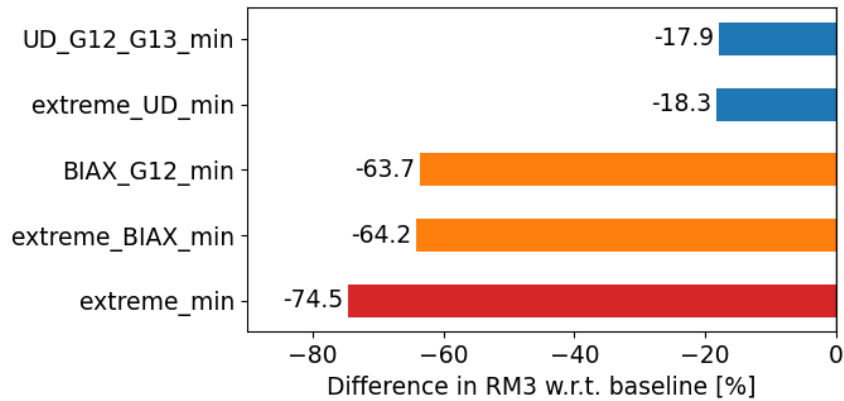


Figure 5-1: Significant results of sensitivity study on torque loadcase of the DTU 12.6 m blade: percentage difference in RM3.

Analysing the results it can be stated that the torsional stiffness of the blade is only significantly impacted by the shear moduli $G_{12}=G_{13}$ for the UD material and the shear modulus G_{12} for the BIAx material. The comparison of the "extreme_UD_min" result with the "UD_G12_G13_min" result confirms this as they are almost equal meaning that the $G_{12}=G_{13}$ property has the largest contribution, the same holds for the BIAx material. These results are expected as the torsional stiffness mainly depends on the shear stiffness of the materials.

Comparing the "extreme_min" results with the results of "extreme_UD_min" and "extreme_BIAx_min" show that the impact is more or less the summation of the two individual material's results. This is expected as now both materials have a lower shear stiffness and one material now cannot counteract the reduced performance of the other material anymore.

The relation between the shear stiffness' and the required torque are established in Figure 5-2. The percentage difference in input and output with respect to the baseline model is plotted for both materials. The results show that the relation is linear for both materials. Moreover, the slope of the linear relation is significantly larger for the BIAx material compared to the UD material confirming that the shear stiffness of the BIAx material has a significantly larger impact on the torsional stiffness of the blade. This result is expected as the BIAx material has a higher shear stiffness with its fibres aligned with the load direction resulting from applying shear loading.

Furthermore, the thickness of the shearwebs is another significant design parameter for the torsional rigidity as it influences the polar moment of inertia.

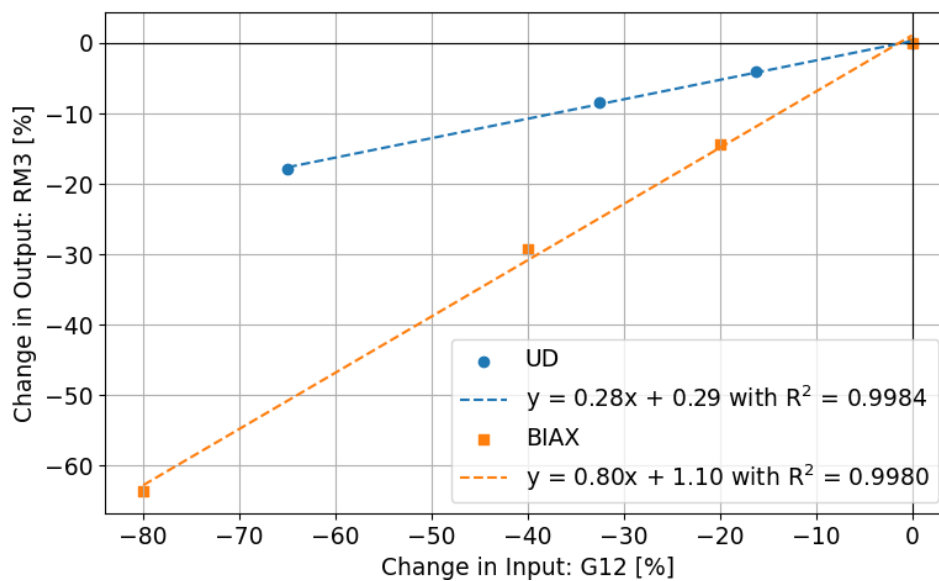


Figure 5-2: Percentage difference in RM3 vs percentage change in G_{12} input for the torque loadcase in the sensitivity study on the DTU 12.6 m blade.

In conclusion, the most critical material design parameter for the torsional stiffness is the shear stiffness of the BIAx material. Additionally, the thickness of the shearwebs influence the polar moment of inertia which directly relates to the torsional rigidity of the blade as well.

5-3 Pressure-to-Suction loadcase results

The full results of the sensitivity study of the tip deflection for the PTS loadcase are presented in Appendix E. The significant results are presented in Figure 5-3. The results of the other material engineering constants only had a very small impact of less than 1% change. Analysing the results it can be stated that the flapwise tip deflection of the blade is only significantly impacted by the longitudinal bending stiffness E_1 of the UD material and the bending stiffness $E_1=E_2$ of the BIAx material. These results are as expected as the flapwise tip deflection mainly depends on the longitudinal bending stiffness of the blade which is provided by the longitudinal bending stiffness of the used materials. Moreover, the impact

of the the longitudinal stiffness of the UD material is highly significant with a tripling of the tip deflection for a significant reduction of that property. This is expected as the flapwise deflection of the blade mainly depends on the longitudinal stiffness provided by the spar-caps which are made up of mostly the UD material. This also explains why the impact of the BIAx longitudinal stiffness is less significant, on top of the fact that the stiffness of the UD materials is higher than that of the BIAx material.

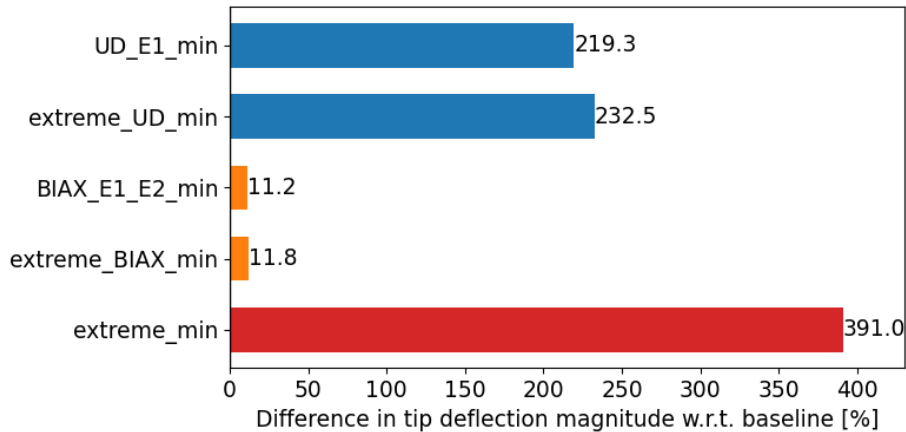


Figure 5-3: Significant results of sensitivity study on PTS loadcase of the DTU 12.6 m blade: percentage difference in tip deflection magnitude.

Finally, the "extreme_min" result is compared to the "extreme_UD_min" and "extreme_BIAx_min" results. It can be seen that the tip deflection when changing both materials to their minimum is much larger than either of the tip deflections of changing only one of the materials and their summation. The UD stiffness does have the most significant impact as its individual results is more than half of the combined result. While the individual BIAx result is only 12% which is significantly smaller than the increase of 158% from only changing the UD material to also changing the BIAx material. This result can be explained by comparing the E1 values for all three test cases. When changing only the UD material, the stiffness of the BIAx material is higher than that of the UD material and will contribute most to the total blade stiffness. The BIAx stiffness is significantly lower than the original UD stiffness, hence the tripling of the tip deflection. Changing only the BIAx material has less impact on the tip deflection as the UD stiffness is already much higher than the original BIAx stiffness and thus provides most of the total blade stiffness. However, when on top of changing the UD material the BIAx material is also changed, the BIAx stiffness drops again below the already low UD stiffness. The BIAx material can no longer compensate for the low UD stiffness causing a significant additional increase in tip deflection.

The relation between the longitudinal stiffness' and the tip deflection magnitude are established in Figure 5-4. The percentage difference in input and output with respect to the baseline model is plotted for both materials. Both a linear and quadratic curve-fitting is presented to evaluate which type of relation better fits the data. For the BIAx material the linear and quadratic curve are almost equal and it can be said that the relation is practically linear. For the UD material the quadratic curve fits the data better. This is an important observation as it makes the selection of a UD material with a high longitudinal stiffness even

more significant for the redesign in order to limit the blade deflections.

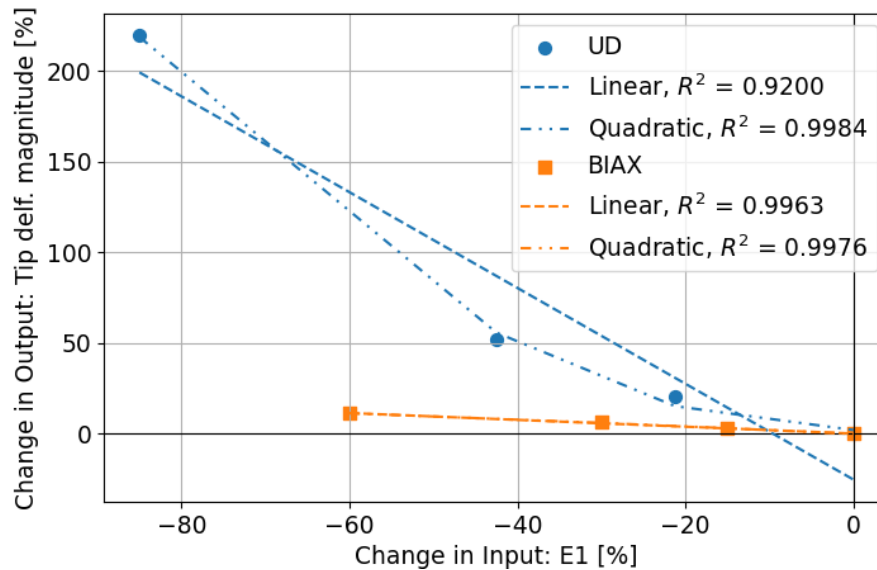


Figure 5-4: Percentage difference in tip deflection magnitude vs percentage change in E_1 input for the PTS loadcase in the sensitivity study on the DTU 12.6 m blade.

The full results of the sensitivity study of the maximum Tsai-Wu value for the PTS loadcase are presented in Appendix E. The results are similar to the presented results of the deflection. Higher deflections will lead to larger strains which induces larger stresses which in turn will increase the value of the Tsai-Wu criteria through its definition in Equation 4-7. However, in terms of the BIAx material not only the longitudinal bending stiffness has a relatively significant impact on the maximum Tsai-Wu value, but also the in-plane Poisson's ratio. The percentages of the Poisson's ratio test cases can be trusted as the maximum Tsai-Wu values all originate from the same location as the baseline results. The relation between the BIAx in-plane Poisson's ratio ν_{12} and the maximum Tsai-Wu value is exponential, see Figure 5-5. Although the impact is relatively small, a lower value is preferred to limit the stresses.

The Poisson ratios of the NFRCs are highly estimated. When analysing the Tsai-Wu values during the redesign process this has to be considered. Given the variability of the Tsai-Wu value with the Poisson ratio the Tsai-Wu value can only give an estimate. Combining the Tsai-Wu criterion with the maximum stress criterion will increase confidence in the redesign.

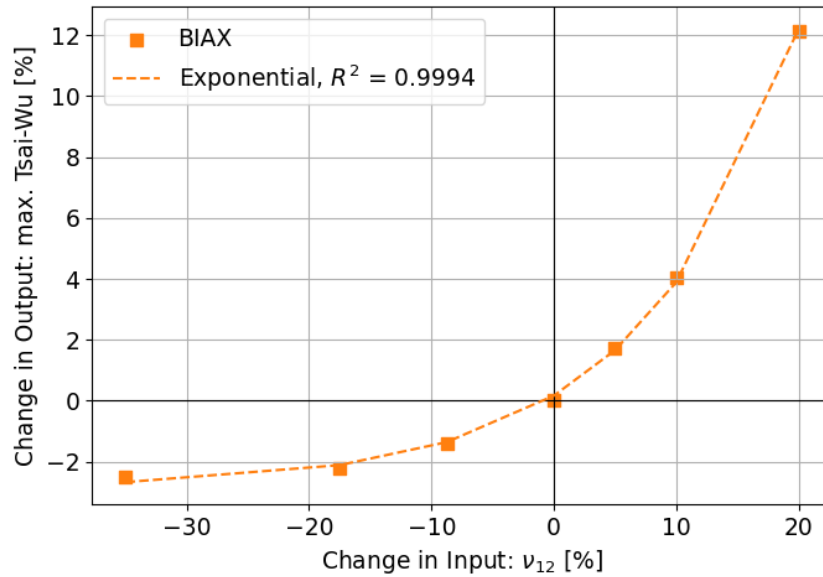


Figure 5-5: Percentage difference in max. Tsai-Wu value vs percentage change in ν_{12} input for the PTS loadcase of the sensitivity study on the DTU 12.6 m blade.

For the PTS loadcase it can be concluded that changes in the BIAX material properties does not result in the blade failing. However, the blade can fail dramatically if the longitudinal stiffness of the UD material is reduced significantly. Similarly to the tip deflection the relation between the UD longitudinal bending stiffness and the maximum Tsai-Wu value is quadratic. With the curve-fitting it can be established that a reduction of more than 30% in UD longitudinal bending stiffness results in material failure if the BIAX materials is kept equal to the baseline.

5-4 Trailing-to-Leading edge loadcase results

The full results of the sensitivity study of the tip deflection for the TTL loadcase are presented in Appendix E. These results may be of interest for a further study into the aeroelastic behaviour of the blade once a redesign is established. For now the focus is on the structural performance of the blade for which the tip deflection in the TTL is not as interesting due to the absence of a tower interface. The most interesting parameter in the TTL loadcase is the stress levels in relation to material performance. Hence, the results for the maximum Tsai-Wu value are of interest to see if the blade starts failing for certain material property combinations. The full sensitivity study results can be found in Appendix E while the significant results are presented in Figure 5-6.

The TTL loadcase can be interpreted as a bending beam problem. Therefore, the stiffness in the direction of the length of the beam will have the largest impact on the deflection of the beam. Larger deflections lead to larger strain levels which increase the stress levels and in turn increases the value of the maximum Tsai-Wu criterion. Therefore, the changes in longitudinal stiffness of the UD and BIAX material are expected to impact the maximum Tsai-Wu value. The results confirm the impact of the longitudinal stiffness of the UD material. However, the results of the longitudinal stiffness of the BIAX material produced an artificial Tsai-Wu value

making the result invalid for this analysis. Therefore, only the longitudinal stiffness of the UD material is present in Figure 5-6. That said, the analysis of the tip deflection of the blade did confirm the significant impact of the longitudinal stiffness of the BIAx material on the edgewise blade's deflection.

The TTL loadcase will also lead to tension/compression in the direction of the transverse stiffness E_2 of the materials. Changes in this material property might also lead to changes in the maximum Tsai-Wu value. However, the longitudinal stiffness E_1 of the UD material is significantly larger than that of the transverse stiffness of both materials and might dominate the results. The latter is indeed the case for the transverse stiffness of the UD material. The transverse stiffness of BIAx material equals that of its longitudinal stiffness due to the fibre alignment. Therefore, the individual influence of the transverse stiffness cannot be established and becomes irrelevant. Nonetheless, it is already established that the in-plane stiffness of the BIAx material does have a significant influence on the edgewise blade behaviour. The result of the BIAx in-plane stiffness in relation to the maximum Tsai-Wu value produced artificial results. However, the midpoint test case did produce a valid result. A reduction in BIAx stiffness of 30% did not lead to a significant change in the maximum Tsai-Wu value. Hence, the longitudinal stiffness of the UD material dominates the blade's performance in the edgewise bending loadcase in terms of material stress levels.

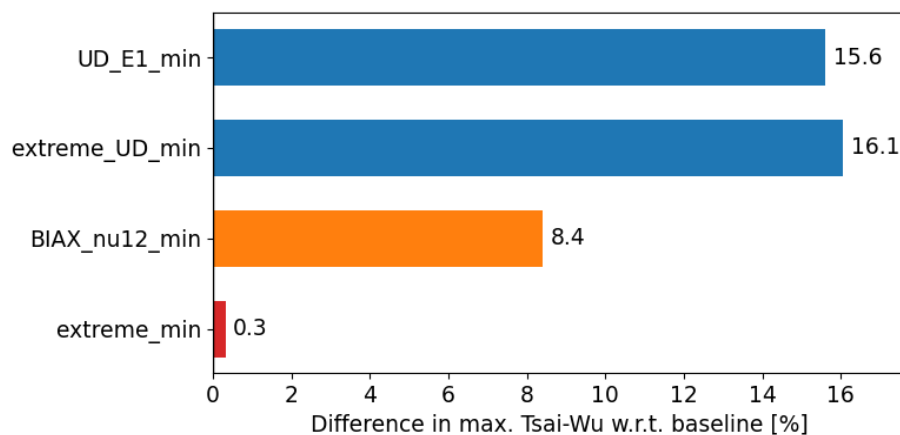


Figure 5-6: Significant results of the sensitivity study on the TTL loadcase for the DTU 12.6 m blade: percentage difference in maximum Tsai-Wu value.

Furthermore, it can be observed that the maximum Tsai-Wu value did not reach critical levels for all the test cases. The baseline maximum Tsai-Wu value was already relatively low at 0.41 and is located in the outer BIAx ply at a third of the blade span on the trailing edge. The maximum Tsai-Wu value of the "UD_E1_min" and "UD_extreme_min" test cases occur at roughly the same location so that the calculated percentage difference originates from a fair comparison. With only a difference of 16% it can be concluded that the UD longitudinal stiffness is much less critical for the TTL loadcase compared to the flapwise loadcases. So it is likely that if the UD stiffness is sufficient for the flapwise loads that the blade will also withstand the edgewise loads.

Similarly to the flapwise loadcases the Poisson's ratio of the BIAx material plays an additional

significant role in terms of the maximum Tsai-Wu value. The value originates from the same location as the baseline so the percentage difference result can be trusted. The impact is significant compared to the other material properties, but critical levels are not reached.

Finally, it must be noted that the impact of "extreme_min" loadcase is significantly lower than that of the other significant loadcases. It seems that the reduction in BIAX properties on top of the reduction in UD properties counteracts the increase in maximum Tsai-Wu value that is observed when only reducing the UD material properties, which was unexpected. A possible explanation could be obtained from the Hooke's law: $\sigma = \epsilon \cdot E$. Reducing the stiffness will lead to larger deflections and thus larger strain levels which would increase the stress levels. However, the stress level also depend on the stiffness and is therefore determined by the combination of the increase in strain and decrease in stiffness. The strong reduction in stiffness could explain the lower maximum Tsai-Wu value for the "extreme_min" test case compared to the "extreme_UD_min" test case. However, a detailed investigation into these results is outside the scope of the current work. However, the verification of this theory is complicated by the fact that not all test cases produced valid and consistent results and that the location of the maximum Tsai-Wu value of the "extreme_min" test case differs from the baseline result. Further investigations into these results is outside the scope of the current work.

The results that are valid show that the TTL loadcase is less critical compared to the other loadcases, it is therefore decided to accept that not all results can be used in the sensitivity study of the maximum Tsai-Wu value for the TTL loadcase. It will be assumed that if the blade design can meet the requirements for the flapwise loads, that it will also sustain the edgewise loads safely. The structural redesign process that will follow in Chapter 7 will provide information on the validity of this assumption.

Where possible it is still of interest to investigate the relation between the significant changes in input versus output to inform the material selection and redesign process.

The results for the longitudinal stiffness are presented in Figure 5-7. For the UD material all three results were real and from the same location and ply, so that all results could be used to find the relation type. Similarly to the tip deflection the relation between the UD longitudinal bending stiffness and the maximum Tsai-Wu value is quadratic. For the BIAX results only the mid point results were not artificial and originates from the same location as the baseline. This leaves too little data-points to be able to draw conclusions on the relation between that input and the maximum Tsai-Wu value output. What can be identified is the relation between the BIAX longitudinal stiffness and the tip deflection which can also be compared with that of the UD longitudinal stiffness. These results are presented in Figure 5-8, showing similar relations compared to the PTS loadcase; quadratic for the UD material and linear for the BIAX material. What differs is the relative impact of the two materials. For the edgewise deflection the impact of the longitudinal stiffness of the two materials is similar, and even slightly larger for the BIAX material. This can be explained by the fact that the material furthest away from the neutral axis, which influences the moment of inertia, consists of BIAX material. Furthermore, comparing Figure 5-7 and Figure 5-8 it can be seen that the impact of the longitudinal stiffness on the tip deflection is significantly larger than on the maximum Tsai-Wu value. The increase in tip deflection could be seen as a summation of the increase in local strains. The local strains thus change less compared to the global tip deflection which explains the difference between the result of Figure 5-7 and Figure 5-8.

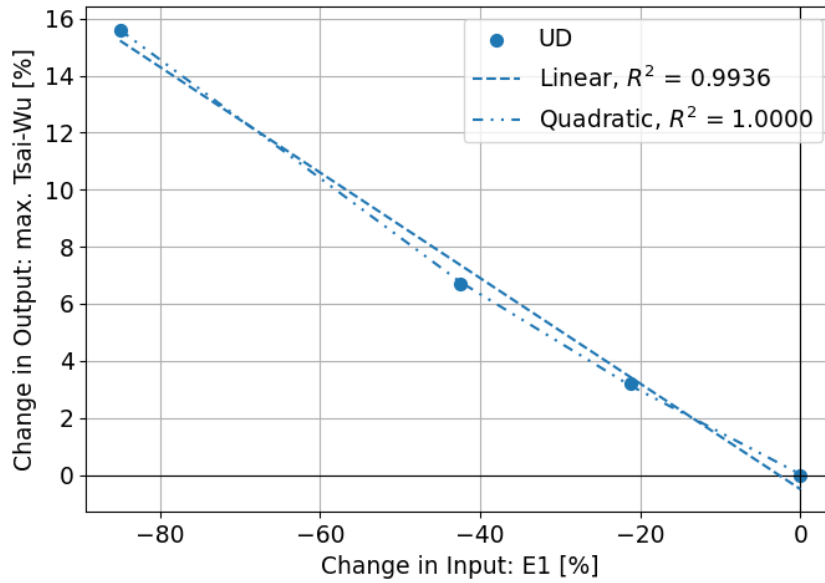


Figure 5-7: Percentage difference in max. Tsai-Wu value vs percentage change in E_1 input for the TTL loadcase of the sensitivity study on the DTU 12.6 m blade.

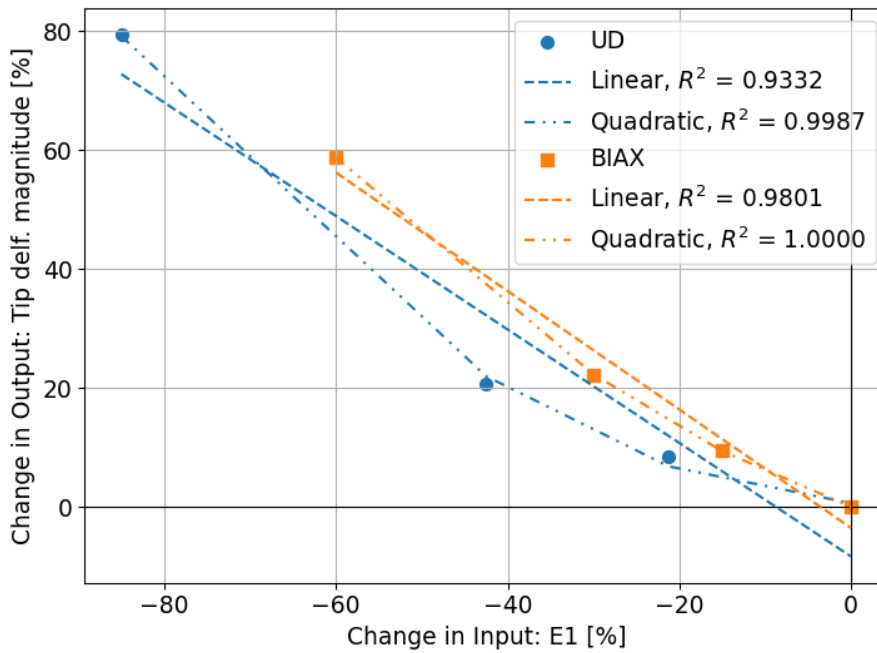


Figure 5-8: Percentage difference in tip deflection magnitude vs percentage change in E_1 input for the TTL loadcase of the sensitivity study on the DTU 12.6 m blade. Note: $E_1 = E_2$ for the BIAX material.

The percentage input change in BIAX in-plane Poisson’s ratio versus the maximum Tsai-Wu output is presented in Figure 5-9. All results are not artificial and originate from the same location and ply as the baseline result, except for the "BIAX_nu12_max" test case which is excluded from the graph. This leaves enough data points to identify the relation type.

The relation between the BIAx in-plane poisson's ratio and the maximum Tsai-Wu value is quadratic. This means that for the BIAx material selection a value close to the baseline is desired for the in-plane Poisson's ratio to minimize the stress levels in the blade.

The same remark can be made here as for the PTS loadcase. The Poisson ratios of the NFRCs are highly estimated which must be considered during the redesign when analysing the Tsai-Wu values. Given the variability of the Tsai-Wu value with the Poisson ratio the Tsai-Wu value can only give an estimate. Combining the Tsai-Wu criterion with the maximum stress criterion will increase confidence in the redesign.

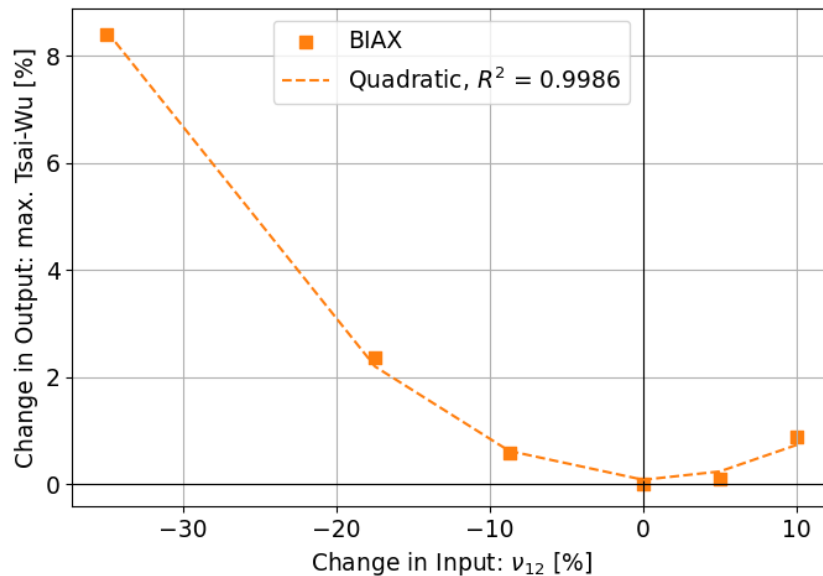


Figure 5-9: Percentage difference in max. Tsai-Wu value vs percentage change in ν_{12} input for the TTL loadcase of the sensitivity study on the DTU 12.6 m blade.

5-5 Results of verification of geometric linearity

The outputs for the selected Torque loadcases to verify the linear assumption of the analysis are presented in Table 5-3. The last column indicates the thresholds for the blade provided by the three guidelines outlines in the methodology. The maximum deflection and strains in the blade for all three cases are well below the thresholds set by the guidelines [72][73][74]. This suggest that the deformations are relatively small and that the linear assumption is still valid for a rotation angle of 10 degrees.

Table 5-3: Outputs of the linear analysis of the selected Torque loadcases on the DTU 12.6 m blade, to verify with the guidelines for the incorporation of geometric non-linearity.

		Torque Baseline	Torque UD $G_{12}+G_{13}$ min	Torque BIAx G_{12} min	Upper threshold from guidelines
Max(U mag.)	[m]	0.0467 ✓	0.04674 ✓	0.04645 ✓	0.34 or 0.63
Max(UR mag.)	[deg]	10.0	10.0	10.0	5 to 10
ϵ_{11}	[%]	0.346 ✓	0.309 ✓	0.316 ✓	5
ϵ_{22}	[%]	0.419 ✓	0.344 ✓	0.19 ✓	5
ϵ_{12}	[%]	1.12 ✓	0.946 ✓	1.18 ✓	5

The outputs for the selected PTS loadcases to verify the linear assumption of the analysis are presented in Table 5-4. The last column indicates the thresholds for the blade provided by the three guidelines outlines in the methodology.

The tip deflection for all three PTS cases analysed is larger than the threshold for both guidelines 1 and 2, and thus suggest a need for including geometric non-linearity. However, the maximum strains are well below the threshold of 5% of guideline 3. On the other hand, the maximum angle of rotation is well above the threshold of 10 degrees. This result emphasises the importance of analysing both the strains and the maximum angle of rotation to be able to draw conclusions about geometric non-linearity. Geometric non-linearity is either driven by strain or by the angle of rotation. For the current blade model it is clear that the angles of rotation drive the geometric non-linearity. As both the tip deflection and angles of rotation suggest large deformations the linear assumption is likely not valid for the PTS loadcase.

Table 5-4: Outputs of the linear analysis of the selected PTS loadcases on the DTU 12.6 m blade, to verify with the guidelines for the incorporation of geometric non-linearity.

		PTS Baseline	PTS UD E_1 min	PTS BIAx E_1+E_2 min	Upper threshold from guidelines
Tip U mag.	[m]	2.18 ✗	6.96 ✗	2.42 ✗	0.34 or 0.63
Max(UR mag.)	[deg]	21.3 ✗	68.3 ✗	23.6 ✗	5 to 10
ϵ_{11}	[%]	0.398 ✓	1.29 ✓	0.447 ✓	5
ϵ_{22}	[%]	0.22 ✓	0.58 ✓	0.28 ✓	5
ϵ_{12}	[%]	0.187 ✓	0.228 ✓	0.202 ✓	5

The conclusion from the PTS loadcase analysis raises questions about the validity of the sensitivity study results described previously. Before answering this question the impact of the inclusion of the geometric non-linearity will be evaluated first. This will verify the conclusions from the applications of the guidelines.

The results are presented in Table 5-5 as the percentage difference of the outputs of the non-linear analysis with respect to the linear analysis.

The torque loadcases all show a difference of less than 1% in the results between the linear and non-linear analysis. This confirms that the linear assumption for this loadcase is still

acceptable for a maximum angle of rotation of 10 degrees. For loadcases with larger angles of rotation the assumption needs to be re-evaluated.

The results for the tip deflection for the "PTS Baseline" and PTS "BIAX_E1_E2_min" loadcases show a relatively small difference between the two analysis types. This is somewhat a surprise as the tip deflection is much larger than the thresholds set by the guidelines. However, the tip deflection for the other loadcase, PTS "UD_E1_min", did change significantly. The difference with the other two cases is that the maximum angle of rotation is three times larger for the PTS "UD_E1_min" loadcase, see Table 5-4. This confirms that the geometric non-linearity is driven by the angle of rotation for the current blade model. Moreover, the results indicate that the threshold for the angle of rotation is around 20 degrees rather than the 10 degrees described by the guidelines.

Another observation is that the tip deflection reduces when including the geometric non-linearity. For a cantilever beam under bending, the applied load can be resolved into a tangential and normal component in the beam. The tangential component is not seen in a linear analysis. The tangential component applies tension in the beam to which the material resists, which in turn restricts the deflection of the beam. This restriction is taken into account in the non-linear analysis resulting in the reduction in tip deflection. This difference between the two analyses makes that the linear analysis provides a worst case scenario.

Given that the linear analysis provides a worst case scenario, the results of the sensitivity study described in the previous sections are still valuable. The goal of the sensitivity study was to evaluate which material properties are critical for the blade design. Changing from a linear to a non-linear analysis will likely only change the absolute value of the percentage change in output, while the trends will remain the same. As the trends are the most valuable output of the sensitivity study the results can still be used for the material selection and redesign process.

Finally, the largest difference were observed in the "UD_E1_min" test case. Since the stiffness of NFRCs is significantly smaller compared to GFRC it is important to include the geometric non-linearity in a blade redesign with NFRCs. This will facilitate a fair comparison between the different materials. Furthermore, the applied loads are derived from the HAWC2 simulations which include geometric non-linearity as well. So including the geometric non-linearity in the Abaqus model allows for a fair comparison between the tower clearance calculated by both models.

Table 5-5: Percentage difference in sensitivity study output between the linear model and non-linear model of the DTU 12.6 m blade for the selected Torque and PTS loadcases.

	Torque baseline	UD_G12_G13_min	BIAX_G12_min
RM3	-0.94 %	-0.66 %	-0.19 %
	PTS baseline	UD_E1_min	BIAX_E1_E2_min
Tip deflection	-3.1 %	-20.7 %	-3.2 %

5-6 Material selection based on results sensitivity study

With the obtained knowledge the materials for the redesign of the blade can be selected. For the UD material it is important to find a NFRC that has a high longitudinal stiffness, high shear stiffness and high longitudinal and shear strengths. For the BIAx material it is important to find a NFRC that has a high longitudinal stiffness, high shear stiffness, low Poisson's ratio ν_{12} and high longitudinal and shear strengths. Additionally, for both materials, a high strain to failure characteristic may be beneficial as the material can stretch more without failing. This parameter can be used to help choose a material when two NFRCs scores are close together.

It will be difficult to find one material that scores the best on all the identified design driving material properties. Thus, it is important to find a balance. The minima and maxima value per material property were identified with red and green respectively in Table 4-6 and Table 4-10. This information was used to select the UD and BIAx biocomposites. For the significant engineering constants the maximum and minimum value with the corresponding NFRC are summarised in Table 5-6 along with the values of the selected NFRCs. This table will help explain the choice for the selected NFRCs and place their properties in perspective to minima and maxima of the six NFRCs.

Table 5-6: Summary of the minima and maxima values for the design driving engineering constants within the set of NFRCs and their corresponding NFRC, along with values of the selected NFRCs for the redesign in Chapter 6 and Chapter 7.

Eng. Const.	UD Max.	UD Selected	UD Min.	BIAx Max.	BIAx Selected	BIAx Min.
E_1 [GPa]	Flax 24	Flax 24	Sisal 8.2	Ramie 8.9	Ramie 8.9	Flax 6.1
G_{12} [GPa]	Bamboo 3.2	Flax 1.8	Flax 1.8	Flax 6.5	Ramie 5.1	Sisal 2.9
σ_1^t [MPa]	Flax 340	Flax 340	Sisal 149	Flax 72	Ramie 53	Sisal 31
σ_1^c [MPa]	Bamboo 210	Flax 120	Flax 120	Ramie/Bamboo 52	Ramie 52	Flax 26
σ_2^t [MPa]	Hemp 36	Flax 19	Flax 19	Flax 79	Ramie 61	Sisal 42
σ_2^c [MPa]	Hemp 110	Flax 53	Flax 53	Ramie 62	Ramie 62	Flax 42
τ [MPa]	Hemp/Sisal 30	Flax 29	Bamboo 25	Bamboo 38	Ramie 36	Flax 21
ϵ_f [-]	Jute 0.02	Flax 0.014	Hemp 0.01	Flax 0.012	Ramie 0.006	Hemp 0.004

The NFRC that is selected for the UD material in the redesign is the Flax/PLA material. In Table 5-6 it can be seen that the Flax/PLA scores best in terms of the longitudinal bending stiffness and strength. However, the Flax scored lowest in terms of longitudinal

compression strength and shear stiffness for which Bamboo/PLA would be the best option. The reason Bamboo/PLA was not chosen is its significantly smaller longitudinal bending stiffness compared to flax which cannot be accepted due to its significance for the blade design. Compared to the shear stiffness the longitudinal stiffness showed to be of larger significance during the sensitivity study. If the low shear stiffness and strength values of the Flax/PLA turn out to be an issue for the torsional stiffness and bending it can be decided to add UD Ramie/PLA in the blade. Ramie is chosen instead of Bamboo as Ramie scores second best on the longitudinal stiffness and strength values as well while the Bamboo scores even lower. The Ramie composite thus balances out the different desires making it a good runner up. Alternatively, more BIAx material can be added to the design to increase the strength of the blade and its torsional stiffness.

The NFRC that is selected for the BIAx material in the redesign is the Ramie/PLA material. For the bending loadcases the longitudinal bending stiffness and longitudinal strengths are the most important to limit deflection and stress levels. The Ramie composite scores best at the longitudinal bending stiffness and compression strength, and second best for the longitudinal tension strength, see Table 5-6. However, another important function of the BIAx material is to provide torsional stiffness which directly affects the aeroelastic behaviour of the blade. In that regard the Flax/PLA composite scores better. However, it is important for the redesign to select a material that best balances out all desires, which in this case will be the Ramie/PLA which scores either first or second best for all important properties. However, if changing the amount of BIAx and/or thickness of the shearwebs cannot provide sufficient torsional stiffness in the redesign, it can be decided to add/use BIAx Flax/PLA.

The hybridisation of composites are a compelling solution. The interaction of different fibres in such a hybrid composite should be further investigated. The different properties of each material could for example lead to unexpected failure modes. For the sake of the current work, it will be assumed that the hybrid composite will behave the same as a uniform composite.

With the results of the sensitivity analysis and the selected NFRC materials, the structural redesign of the DTU 12.6 m blade can be performed. The next chapter will outline the methodology for the redesign process.

Methodology - Structural Redesign of DTU 12.6 m Blade with NFRCs

With the selected NFRCs of the sensitivity study the structural redesign of the DTU 12.6 m blade can start. This process will aid in answering research sub-questions 2 and 3. Firstly, the model parameters for the redesign process will be outlined where the design loadcases and inputs will be defined. The method of changing the design will be discussed followed by the methodology of the redesign process itself and the redesign evaluation strategy.

6-1 Model parameters

Before diving into the actual redesign process, it is important to establish the model parameters under which the redesign will take place. The blade is designed for wind class IA from IEC 61400-1 which refers to an average wind speed of 10 m/s, a reference wind speed of 50 m/s and a reference wind turbulence intensity of 0.16 [20]. Furthermore, the rated rotor speed is 68 rpm and together with the rotor radius of 13 m this results in a rated wind speed of 9.475 m/s. The minimum rotor speed is set equal to 20 rpm = 2.0933 rad/s and the aerodynamic rated power is 153.06 kW. The tower was modelled as a stiff tower since the aim of the present study is to investigate the wind turbine's blade design. By using a stiff tower its influence on the blade's behaviour is eliminated.

Furthermore, the design loadcases that have been evaluated for the current blade design are DLC1.2 and DLC1.3 from the IEC 61400-1 [20]. DLC1.2 provides the fatigue loads under normal operation using a normal turbulence model. DLC1.3 provides the ultimate loads under normal operation with an extreme turbulence model. The DLC1.3 will be used for the redesign of the blade with bio-based materials. The other design loadcases will not yet be considered. It is first required to establish if a bio-based blade design is feasible for normal operation. If that is not the case, it will not be worth it to look at the other DLC's.

Furthermore, the redesign will be performed using a simulation of a static load test as required for certification. During a static test the blade is manufactured and the true materials are

present. Therefore, no safety factors are applied with regards to the material properties. Since the redesign will simulate such a static test, the material properties in the model will also not include a safety factor. This is deemed acceptable as the current study focusses on the preliminary design only. This might lead to a more positive outcome on the feasibility of bio-based blades. However, the materials used in the redesign are highly estimated and on the conservative side of the spectrum. Once it is established that a bio-based blade design is feasible with these material properties, it will be useful to obtain the true material properties from testing. The design with the true material properties will need to include the material safety factors to meet certification standards.

The static load test is represented as four point loads in the Abaqus model. These loads are calculated from the bending loads, see DLC1.3 in Figure 3-3, by using the distance to each load application point. This means solving the system " $[M] = [A] \cdot F$ " for F , with $[M]$ the matrix with bending loads and $[A]$ the matrix with the moment arms for the forces in F . The resulting forces for each load direction of the DLC1.3 loadcase are summarised in Table 6-1. It is important to note that these values already include the partial safety factor (SF) for loads of $1.1 \cdot 1.35 = 1.485$. The partial safety factor of 1.1 accounts for the scatter of rotor blade characteristic in series production for statics tests, as specified by DNVGL-ST-0376 standard for wind turbine rotor blades [56]. The safety factor of 1.35 is required for DLC1.3 loads as specified by the IEC 61400-1 standard [20].

Table 6-1: Point forces to represent the DLC1.3 loadcase in the Abaqus DTU 12.6 m blade model.

R [m]	PTS [N]	STP [N]	TTL [N]	LTT [N]
2.6	4130	-1690	3030	-2120
5.2	6850	-4430	2430	-1460
7.9	8620	-6210	2270	-2010
10.8	9850	-8610	3250	-2730

Furthermore, as the sensitivity study showed only small differences between the two flapwise and edgewise loadcases, it is decided to only focus on one edgewise and one flapwise loadcase. The most important flapwise loadcase is PTS, as this is critical for the tower clearance. For the edgewise loadcase the TTL load is the most important as it has the largest stress/strains.

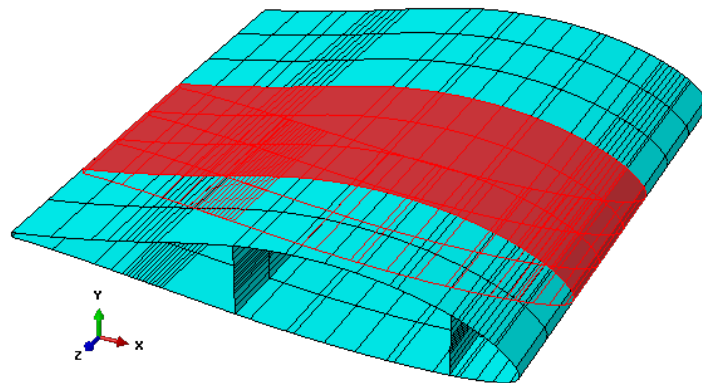


Figure 6-1: Clamped surface of the DTU 12.6 m blade at $r = 10.8$ m for load application.

In the Abaqus model, the loads are applied to the blade through clamps on the blade which distribute the load over the entire blade circumference. The width of the clamps will be simulated as being 10 centimetres, which is 2 to 3 elements wide. The load is applied to a reference point at the elastic centre of the cross-section which is coupled to the clamping surface through a continuum coupling constraint. The clamping surface is visualised in Figure 6-1. The application of the loads is the same as for the sensitivity study and visualized in Figure 4-2 for the PTS, TTL and Torque loadcases.

The blade needs to be designed to resist torsional loads. The torque loadcase will prescribe a rotational displacement to the clamp at the tip, at $r = 10.8$ m. In order to apply this rotation to the clamp, the continuum coupling constraint at $r = 10.8$ m is changed into a kinematic coupling constraint so that the motion of the clamp follows the rigid body motion of the reference node [57]. The prescribed rotation to the reference node will be 10 degrees which converts to 0.175 radians.

To ensure a fair comparison between each design iteration, the reference baseline model will use the calculated UD and BIAX material properties as specified in Section 4-1-4. Table 6-2 provides a summary of all the material properties of the materials used in the redesign process along side those of the GFRCs used in the baseline model.

Table 6-2: Material properties of the NFRCs that will be used during the DTU 12.6 m blade redesign process along side the material properties of the conventional GFRCs [21] used in the baseline design.

Property	UD Flax/PLA	BIAX Ramie/PLA	BIAX Flax/PLA	UD GFRC	BIAX GFRC
E_1 [MPa]	24000	8850	6060	42700	14300
E_2 [MPa]	5500	8850	6060	12600	14300
E_3 [MPa]	5500	8550	6190	12600	13400
G_{12} [MPa]	1830	5080	6530	4610	12500
G_{13} [MPa]	1830	3100	1830	4610	4610
G_{23} [MPa]	1830	3100	1830	4610	4610
ν_{12} [-]	0.38	0.43	0.65	0.26	0.55
ν_{13} [-]	0.38	0.24	0.2	0.26	0.17
ν_{23} [-]	0.49	0.27	0.2	0.36	0.17
ρ [g/cm ³]	1.23	1.25	1.23	1.95	1.95
σ_1^t [MPa]	340	53	72	1000	223
σ_2^t [MPa]	19	61	79	47	223
σ_1^c [MPa]	120	52	26	813	209
σ_2^c [MPa]	53	62	42	147	209
τ_{12} [MPa]	29	36	21	48	155
V_f [-]	0.41	0.4	41	0.534	0.53

The Abaqus model that is used in the redesign is the conventional 2D shell element model as described in Section 3-2-2. The model will include geometric non-linearity as deemed required per Section 5-5. To ensure a fair comparison between the different designs it is chosen to use the same mesh for all designs and only change the used materials and layup definitions. To facilitate this method, Philipp Haselbach generated a specific workflow to

generate the conventional blade model, see Figure 6-2. The workflow starts off with the abaqus model with just the geometry, mesh, materials, constraints, boundary conditions, loads and requested output parameters specified. The structural design is specified in the Blade Modelling Tool by specifying the different layups with their materials for the different sections across the blade. This information is read in by a Matlab script which consequently writes three python scripts. These python scripts can be read in by Abaqus to build up the model. They have to be run in a specific order. Before running these three scripts, another script has to be run by Abaqus to import libraries and expressions needed to run the three python scripts. Consequently the generated python scripts can be run. The first python script generates the section layers. The second script generates the composite layups and the third script creates the section assignments, thereby completing the model.

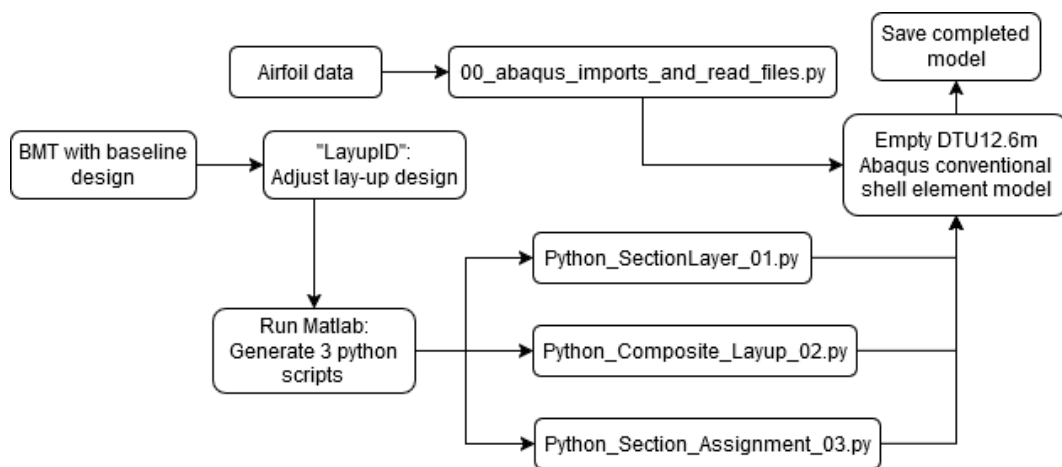


Figure 6-2: Workflow to generate Abaqus conventional shell element model of the DTU 12.6 m blade from the BMT where the lay-up design is specified.

6-2 Redesign evaluation methodology

With all the model parameters established, the redesign process can start. The first step is to establish the methodology to be followed in this redesign process. The current baseline design is deemed feasible, hence, the goal of the redesign is to match the structural behaviour of this baseline design. The idea is that if the structural behaviour of the blade is fairly similar, the aeroservoelastic behaviour of the wind turbine will also be similar. This is important for the wind turbine performance and stability, as well as future design load iterations. The methodology is visualised in Figure 6-3

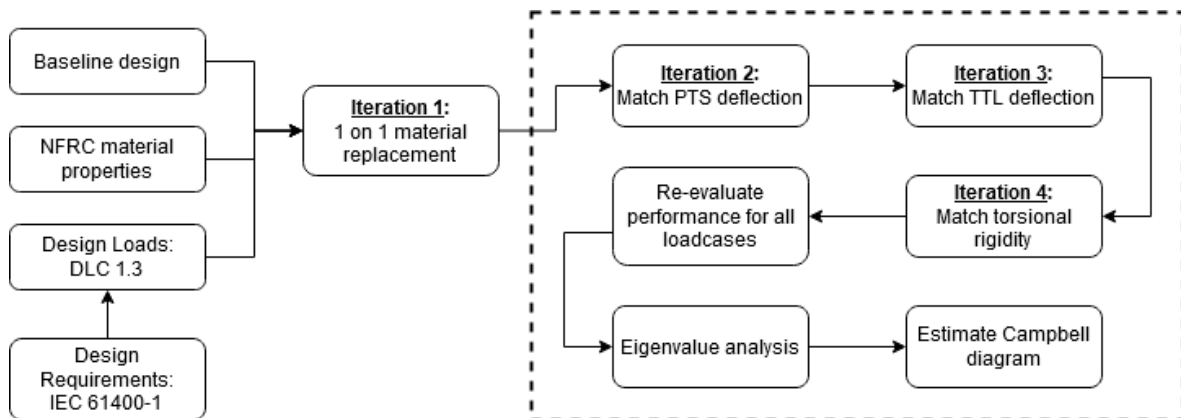


Figure 6-3: Methodology of the redesign process where NFRCs will replace the GFRCs in the DTU 12.6 m research wind turbine blade. The workflow in the dotted lines, using NFRCs, is the scientific contribution of this thesis.

The first design iteration will replace the UD and BIAx materials of the baseline design with the NFRCs selected in Section 5-6. This design will be referred to as "1on1" as the only difference with the baseline is the 1-on-1 material replacement. The results of this design iteration provide information on the structural implications of switching to NFRCs, and will form the starting point for the further redesign.

The second design iteration will focus on matching the deflection in the PTS loadcase which will be driven by the UD material. The redesign methodology will be informed by the sensitivity study. The sensitivity study showed that the PTS loadcase will likely drive the redesign due to the significant impact of the longitudinal stiffness on the deflection, whose design limit is set by the tower clearance. The longitudinal stiffness also has a significant impact on the edgewise loadcase, but this impact is significantly smaller compared to the flapwise loadcase. Hence, the order of first looking at the PTS loadcase followed by looking into the TTL loadcase.

The third iteration will focus on matching the deflection of the TTL loadcase with the baseline design, driven by both the UD and BIAx material. However, the BIAx material also plays a significant role in withstanding the stresses and strains, thereby influencing the failure limit. Hence, the redesign for TTL deflection will focus on the BIAx material design. For the edgewise loadcase the maximum stress and strains are the most critical parameters for the redesign. However, the set goal is to match the structural behaviour of the baseline design. Moreover, the edgewise stiffness will also influence the eigenfrequencies of the blade and thereby influence the aeroelastic stability. This is why the initial focus is to match the deflection curve for the TTL loadcase as well. Afterwards the maximum Tsai-Wu criteria will be investigated to ensure the materials can withstand the load.

The fourth iteration will then focus on the torsional rigidity of the blade as this is critical for the aeroservoelastic behaviour of the wind turbine. The goal is to match the torsional rigidity by analysing the reaction moment to a prescribed rotation as described in Section 4-1-6. The idea is that by matching the torsional rigidity, a stable aeroservoelastic design is achievable just as for the baseline wind turbine. This iteration will focus on the design of the shearwebs as well as the biax material design.

Once the fourth iteration is finished, it is important to check the PTS and TTL loadcases for this new design. The stress and strain levels in all loadcases need to be analysed. If the design fails prematurely it is important to go into a fifth design iteration where more BIAX material is added to reduce the stress levels and delay failure.

Another aspect of the design that will be analysed in all iterations is the mass of the blade. An optimised design can fulfil the structural requirements at the lowest weight possible. The natural fibre reinforced composites are significantly lighter than the glass fibre reinforced composites. It is interesting to see whether the reduced structural properties can be compromised by the low material density. A blade design that is significantly heavier than the current GFRC design will not be considered desirable nor feasible.

Once a design is reached that fulfils the structural requirements of the static load tests, an eigenvalue analysis will be performed. From the resulting eigenvalues an estimate can be made of the Campbell diagram for this new blade design. This will provide insights in the aeroelastic differences between the baseline and redesigned blade.

The next chapter will present the results of the structural redesign process of the DTU 12.6 m research wind turbine blade.

Results & Discussion: Structural Redesign DTU 12.6 m Blade with NFRCs

This chapter will present the results of the redesign process of the structural design of the DTU 12.6 m blade, utilising natural fibre reinforced composites. The order in which the results are presented will follow the methodology described in the previous chapter.

7-1 Design Iteration 1 - 1 on 1 material replacement

The first design iteration replaces the UD and BIAx materials of the baseline design with the NFRCs selected in Section 5-6. This design will be referred to as "1on1". The results of this design iteration provide information on the structural implications of switching to NFRCs, and will form the starting point for the further redesign.

The sensitivity study indicated that the flapwise deflection is mainly dependent on the longitudinal stiffness of the UD material. The difference in longitudinal stiffness of the UD glass composite and UD flax composite is about 44%. From the established relation curve in Figure 5-4 it can be derived that a deflection of about 60% to 70% in tip deflection can be expected when making the switch to the natural fibre reinforced composites, with possible higher numbers as the BIAx material will change simultaneously. The deflection curves for the different designs under PTS loading are presented in Figure 7-1, where "U2" stands for the deflection in the flapwise direction. The results confirm a large increase in deflection when the materials are replaced without changing the design. The tip deflection has increased from about 2.48 m to 3.94 m, an increase of 59%, which is inline with the expectations based on the sensitivity study results.

The sensitivity study indicated that the edgewise deflection is mainly dependent on the longitudinal stiffness of both the UD and BIAx material. The difference in longitudinal stiffness

of the BIAx glass composite and BIAx Ramie composite is about 38%. From the established relation curve in Figure 5-8 it can be derived that an increase in tip deflection of about 25% can be expected when switching to NFRC UD material, and an additional 35% increase from switching to NFRC BIAx material, with possible higher numbers from the combined effect of changing both the UD and BIAx material. The deflection curves for the different designs under TTL loading are presented in Figure 7-3. From the difference in baseline results and the "1 on 1" design result, it can be concluded that the increase in edgewise tip deflection is the combined effect of changing the UD and BIAx material. The tip deflection has increased from 0.231 m to 0.377 m, which is an increase of 64%.

The sensitivity study indicated that the torsional rigidity is mainly dependent on the in-plane shear stiffness of the BIAx and UD material. The difference in shear stiffness of the UD glass composite and UD flax composite is about 60%, and 59% for the BIAx shear stiffness' of glass and ramie. From the established relation curve in Figure 5-1 it can be derived that a decrease in reaction moment at the root of about 16% can be expected when switching to Flax UD material, and an additional 45% increase from switching to Ramie BIAx material. Comparing the baseline with the "1 on 1" design results shows that the reaction moment at the root to the prescribed rotation of 10 degrees has decreased from 4.896e+06 Nmm to 2.057e+06 Nmm. This is a reduction of 58% which indicates the combined effect of changing both UD and BIAx materials.

Furthermore, the mass of the blade was reduced from 404 kg to 273 kg as the density of the NFRCs are significantly lower, a 32% reduction.

7-2 Design Iteration 2 - match tip deflection curve of PTS loadcase

In order to match the deflection curve with the baseline design, the bending stiffness of the blade needs to increase. The bending stiffness is defined by $E \cdot I$, where E is the Young's modulus and I is the area moment of inertia. For a non-uniform cross-section, the different members may have different stiffnesses. The equivalent bending stiffness of the cross-section is then obtained by the summation of those of the different members: $(EI)_{eq} = \sum (EI)_i$ [71]. The spar caps provide the majority of the bending stiffness of a wind turbine blade in the PTS direction. This is due to the large distance of the spar caps to the neutral axis which yields a high moment of inertia. Further increasing the bending stiffness of this region will be the most effective method to increase the equivalent bending stiffness of the blade. This can be done by increasing the amount of UD plies in the spar cap laminates. Increasing the amount of UD plies will both increase the Young's modulus of the laminate and increase the area moment of inertia of the spar caps.

Since the cross-section varies with blade length, so does the bending stiffness. Through Hooke's law it can be established that the larger the experienced load, the higher the stiffness needs to be to limit deflections. Since the bending moments are highest at the blade root, see Figure 3-3, this section needs to pose the highest bending stiffness. This is why the thickness and amount of UD is largest at the root in the baseline design. Identifying the regions with the largest change in deflection in the high load regions will inform where to add more UD material in the spar caps for the redesign. Comparing the deflection curve of the baseline and design iteration 1 in Figure 7-1 indicates that the region between 2 and 8 meters of the blade

length requires additional UD material reinforcement.

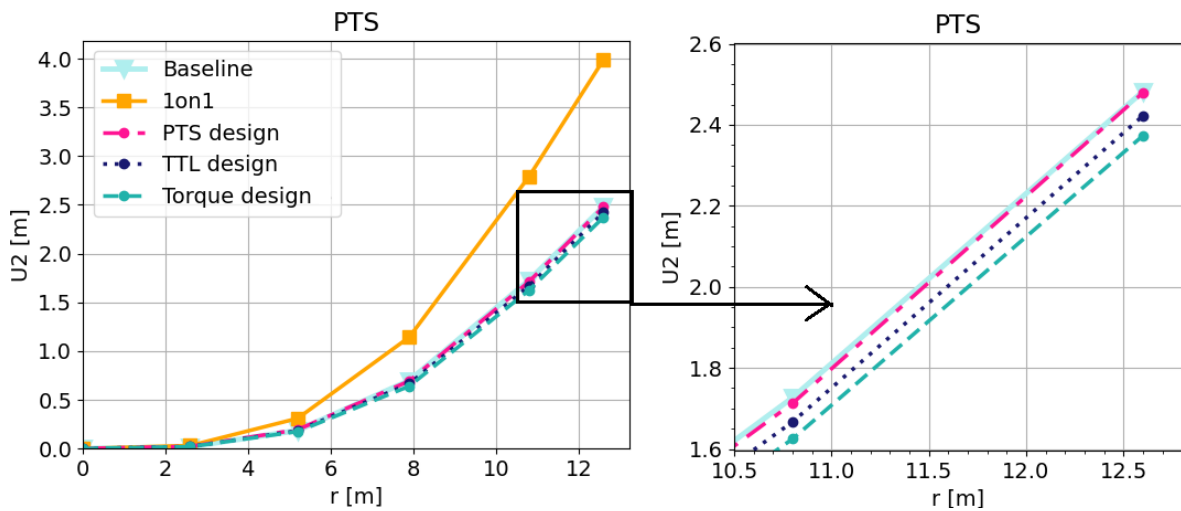


Figure 7-1: DTU 12.6 m blade flapwise deflection under PTS loading for different designs with NFRCS (left) compared to the baseline design with GFRC, with a zoom-in on the blade tip deflection (right).

The design that matches the deflection curve has an increased UD thickness in the root by 5 plies (from 69.3 mm to 73.6 mm), which extends to a blade length of 6.3 meters. From there onwards the thickness is reduced stepwise towards the tip. Figure 7-2 compares the layup design of the spar caps (indicated by the term "flanges" in the BMT) for design iteration 1 ("1 on 1" material replacement) and this PTS redesign iteration. The total mass of the design equals 342 kg, still 14% below the baseline design. The maximum Tsai-Wu value is about 0.9 which means this is still within the failure limit. However, this value must be met with caution due to the high uncertainty in the Poisson's ratio of the materials. The sensitivity study pointed out that changes in the in-plane Poisson's ratio of the BIAX material could lead to a higher maximum Tsai-Wu value. To increase certainty in the structural performance of the blade a lower Tsai-Wu value would be desirable. Before making any changes to the design to accommodate for this uncertainty, the design iterations for the other loadcases will be carried out first.

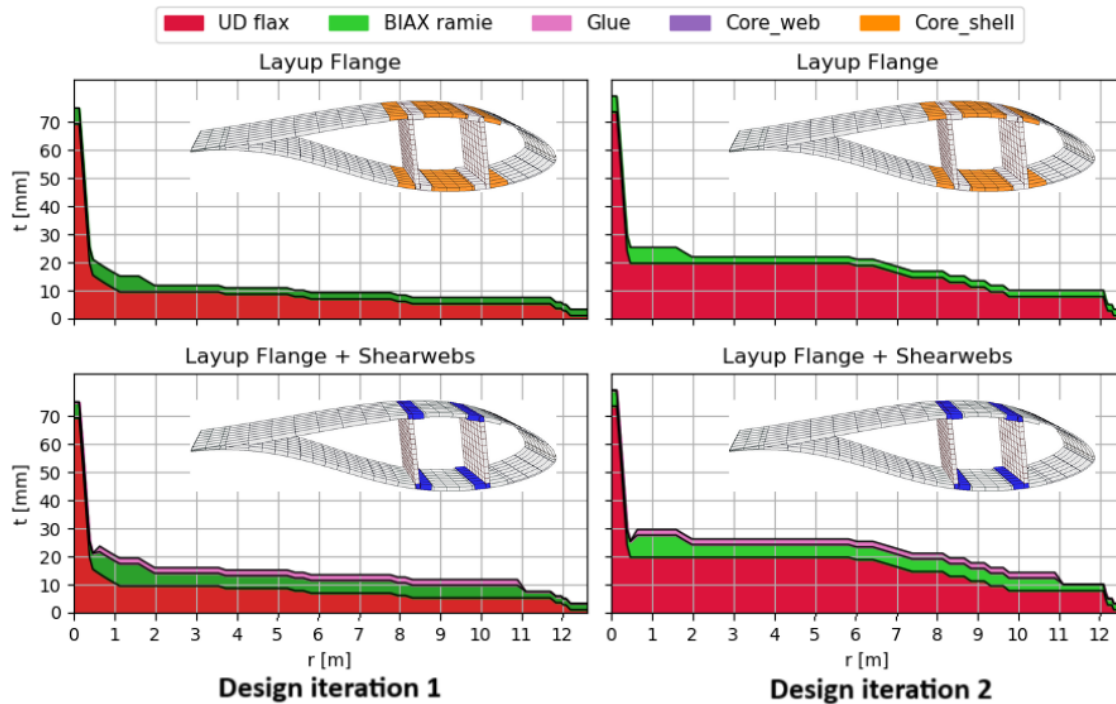


Figure 7-2: Comparison of layup design of the spar caps (indicated by "flanges" in the BMT) for the DTU 12.6 m blade baseline layup of design iteration 1 and the PTS redesign iteration layup with NFRCs.

7-3 Design Iteration 3 - match tip deflection curve of TTL loadcase

As the set goal is to match the structural behaviour of the baseline design, the initial focus is to match the deflection curve for the TTL loadcase as well. Afterwards the maximum Tsai-Wu criteria will be investigated to ensure the materials can withstand the load.

The sensitivity study indicated that the deflection is mainly dependent on the longitudinal stiffness of the UD and BIAx material. The deflection curves for the different designs under TTL loading are presented in Figure 7-3. From the difference in baseline results and the "1 on 1" design result of the first iteration, it can be concluded that the tip deflection has increased from 0.231 m to 0.377 m, which is an increase of 64%. As the tip deflection depends on both the provided longitudinal stiffness of the UD and BIAx material, it is interesting to see the result of the second design iteration where more UD material was added to the blade. Indeed a reduction in tip deflection is seen, to 0.30 m which is about 30% higher than the baseline design. As the BIAx material plays an important role in both the edgewise deflection and stress limits of the blade, the focus of this third iteration is placed on the BIAx material design.

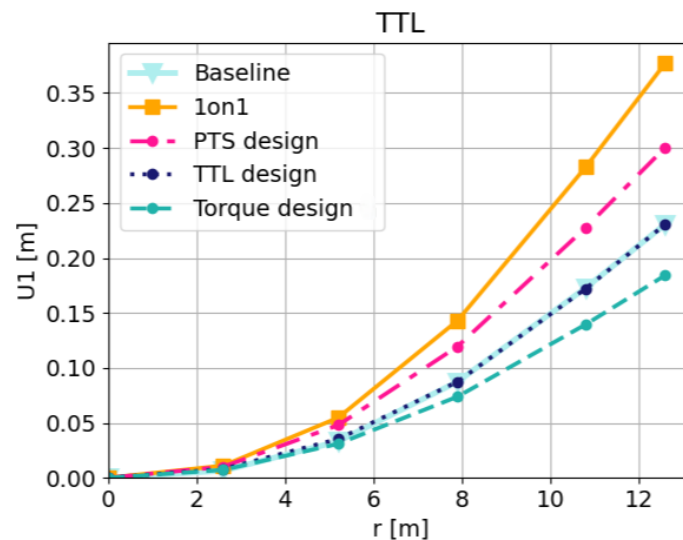


Figure 7-3: DTU 12.6 m blade deflection under TTL loading for different design iterations with NFRCs compared to that of the baseline design with GFRC.

The same theoretical approach as outlined for the second design iteration applies to this third design iteration. However, in the edgewise load direction it is the leading edge and trailing edge that are furthest away from the neutral axis. Reinforcing these areas in the regions with the largest change in deflection in the high load regions was the first step. From the deflection curves it can be identified that the deflection already deviates from the root onwards. Hence, the leading and trailing edges were reinforced with BIAx from the root up to 7.5 meters. Unfortunately this approach was not as effective in changing the deflection of the blade. When the blade is loaded in the TTL direction the trailing edge will experience tension, the leading edge will experience compression, but the upper and lower part of the blade will also experience shearing. Reinforcing these regions will increase the shear stiffness and thereby the overall edgewise bending stiffness of the blade. Hence, in the next attempt the entire circumference is reinforced with BIAx from the root up to 7.5 meters. This change to the design lead to a sufficient reduction in tip deflection. The reinforcement is largest at the root and the plies drop in number at a radial position of 4, 5 and 7.5 meters.

Figure 7-4 shows the design of this iteration and can be compared with the baseline design in Figure 3-11.

The total mass of this new design equals 3834 kg, still 5% below the baseline design. The maximum Tsai-Wu value is about 0.4 which means this is still within the failure limit, despite it having doubled compared to the baseline design.

It is also interesting to see how the design of this iteration performs under the PTS loadcase. The deflection curve for PTS loading is presented in Figure 7-1 as well. It can be seen that the tip deflection has slightly decreased to below baseline levels. This is expected as the added BIAx material increased the overall bending stiffness of the blade. The maximum Tsai-Wu failure has also slightly reduced from 0.91 to 0.89, as the stresses are mainly carried by the BIAx material this is expected. The more BIAx materials the load can distribute itself over, the lower the stress in the individual plies, thereby increasing the distance to the failure limit represented as a lower Tsai-Wu value.

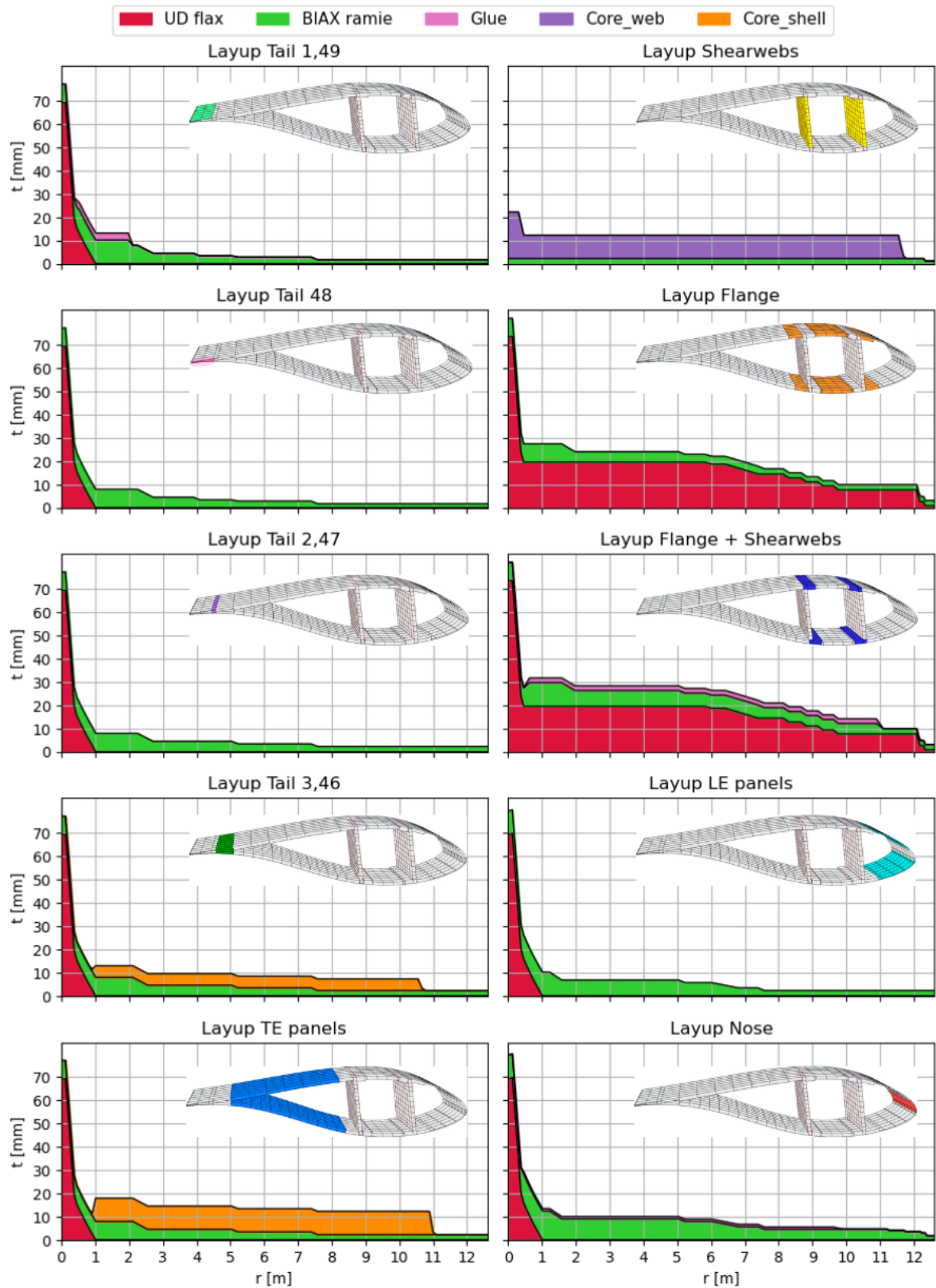


Figure 7-4: Layup design for all sections of the DTU 12.6 m blade in the TTL redesign iteration with NFRCs.

7-4 Design Iteration 4 - match RM3 of Torque loadcase

The fourth iteration's goal is to match the torsional rigidity by analysing the reaction moment to a prescribed rotation as described in Section 4-1-6. The idea is that by matching the torsional rigidity, a stable aeroservoelastic design is achievable just as for the baseline wind turbine design. The to be analysed reaction moment equals the required torsion load to reach a twist of 10° at $r = 10.8$ m. The larger this reaction moment the larger the torsional rigidity of the blade according to the general torsion equation [70].

The torsional rigidity is defined by $G \cdot J$, where G is the shear stiffness and J is the polar moment of inertia. For a non-uniform cross-section, the different members may have different stiffnesses. The equivalent torsional rigidity of the cross-section is then obtained by the summation of those of the different members: $(GJ)_{eq} = \sum(GJ)_i$ [71].

The sparcaps and shearwebs in a wind turbine blade form the load carrying beam. This can be approximated by a box-beam model. For a hollow rectangular cross-section the polar moment of inertia is the summation of its area moments of inertia I_x and I_y . This means that increasing the area moments of inertia will increase the polar moment of inertia, which in turn increases the torsional rigidity. The most weight effective method to increase the polar moment of inertia is to increase the thickness of the shearwebs by increasing the core thickness. Further increasing the shear stiffness of the cross-sectional members can be done by adding more material, specifically BIAx material.

The first redesign iteration where the materials of the baseline design were replaced with the NFRCs resulted in a significant decrease in RM3 of 58%, see Figure 7-5a. A reduction was expected as the shear stiffness of the materials are lower compared to the baseline.

The second redesign iteration in Section 7-2 added a significant amount of UD material to the sparcaps, 19% added volume w.r.t the baseline. This would have increased the thickness of the sparcaps as well as the shear stiffness. This increase resulted in a slight increase in RM3 compared to the first iteration, to minus 55% w.r.t. the baseline design, see Figure 7-5a. This is a relatively small difference, however, the torsional rigidity is more dependent on the BIAx material than the UD material.

The third redesign iteration in Section 7-3 added a significant amount of BIAx material to the second design iteration, 11% added volume w.r.t. the baseline. The resulting torsional rigidity did improve but only slightly, RM3 increased to minus 52% w.r.t the baseline design, see Figure 7-5a. Compared to the seen improvements from the previous iterations, one might have expected a larger improvement. With the rigidity still far from desired levels, these results indicate that the redesign to match the torsional rigidity won't be straightforward.

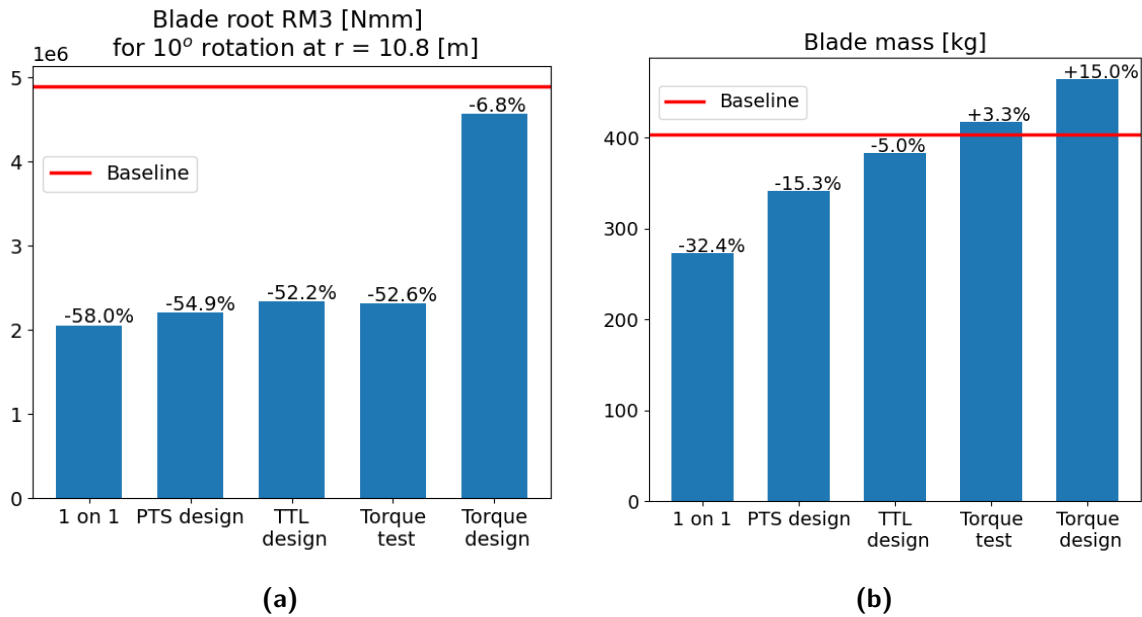


Figure 7-5: Evolution of the required torque RM3 (a) and total blade mass (b) through the different redesign iterations of the DTU 12.6 m blade with NFRCs.

To further increase the torsional rigidity of the blade, the core thickness of the shearwebs were increased significantly. The original thickness was 20 mm in the root and 10 mm throughout the rest of the blade. To test the impact of the shearweb core thickness, the thickness was increased to 40 mm throughout the blade. The change in thickness is visualised in Figure 7-6. Contrary to what is expected, the torsional rigidity was not increased according to the results of the FEA. The reaction moment at the root even showed a very slight decrease from 2340 Nm to 2319 Nm, see "Torque test" in Figure 7-5a. This result might be the consequence of using the 2D shell elements to model the blade. In this model the thickness is not explicitly modelled in the geometry but incorporated in the element definition [57]. Therefore, the effect of thickness on torsional rigidity may not always be fully captured.

The option of using an Abaqus model with 3D continuum shell elements was not available to this project. Therefore, an attempt was made to come up with a design in the 2D shell element model that has the desired torsional rigidity according to its model results.

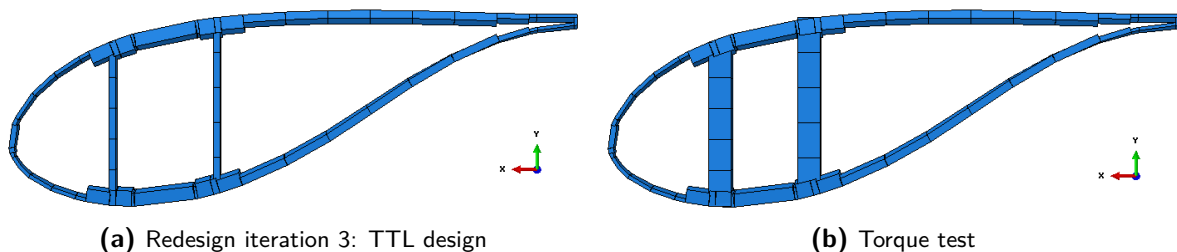


Figure 7-6: Cross-section at r = 2.6 m of DTU 12.6 m redesign iteration 3 and a test design for the Torque redesign iteration where the core thickness of the shearwebs have been increased significantly.

To inform the next steps, the rotational displacement "UR3" along the blade is plotted, see Figure 7-7. The rotation will always be the same at $r = 10.8\text{m}$ as this is the load introduction point using a prescribed rotation. The other points can still provide information on where the blade twists the most. The steeper the curve, the larger the change in angular deformation, indicating a lower torsional rigidity. Analysing this plot for the third design iteration shows that the root of the blade is stiffer compared to the baseline while the tip is significantly weaker. The increased stiffness of the blade at the root can be explained by the added BIAX material to those regions. As the tip twists so easily, the required moment to reach the set rotation is significantly lower. The first steps to improve the torsional rigidity will have to focus on reinforcing the second half of the blade which will be done by adding more BIAX material.

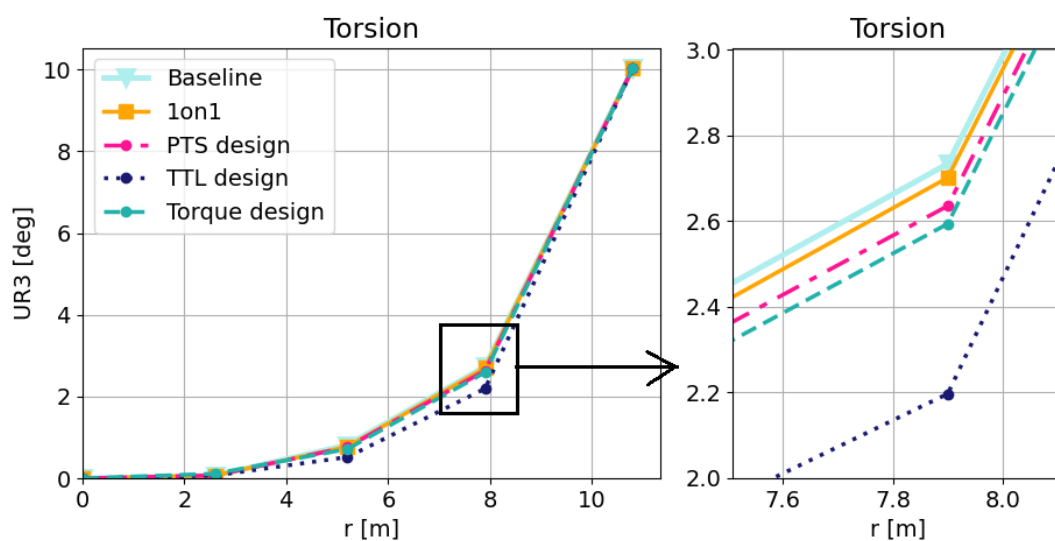


Figure 7-7: Rotational displacement along the DTU 12.6 m blade (left) leading to the applied twist of 10° at $r = 10.8\text{ m}$, with a zoom-in on the twist at $r = 7.9\text{ m}$ (right).

Initial trials focused on added BIAX material to the shearwebs which did improve results but by far not enough to reach the desired rigidity. Additionally, extra BIAX was added towards the tip of the blade in the circumference which improved results further. However, the weight of the blade quickly succeeded that of the baseline design without being close to the desired torsional rigidity. This indicates that it can be more efficient and/or effective to implement other structural changes, besides adding more material to the existing structure. These structural changes can be the addition of a third shearweb, or ribs like in a wingbox structure. Or even diagonal ribs/webs/rods to specifically target the torsional loading. The addition of stiffeners to the inside of the flanges and/or outside of the shearwebs is another option. However, these design methods require significant changes to the geometry of the blade model. This is unfortunately not possible in the current workflow using the Abaqus model and BMT. Trying to implement these changes will not be feasible within the timeframe of this research. Hence, the next step focused on answering the following question: What changes to the layup design of the blade are required given the current geometry and material options to reach the desired torsional rigidity?.

The first step taken was to change the BIAX material from Ramie to Flax as this material has

a higher shear stiffness. Solely changing the material was not sufficient as the shear stiffness of the BIAx Flax material is still significantly lower than the original Glass fibre material. More BIAx material was added along the blade in both the shearwebs and circumference, the latter focusing on reinforcing the second half of the blade, as seen from the UR3-plot in Figure 7-7 as required. This did lead to a design with sufficient torsional rigidity, however, the stress levels exceeded the material limits in both the torsion and PTS loadcases. This is due to the reduced strengths of the Flax material compared to the Ramie material. This means that the replacement of material to increase torsional rigidity cannot be justified.

Taking the established redesign with BIAx Flax material and changing the BIAx back to Ramie did reduce the maximum stress levels to below the material limits. However, the torsional rigidity dropped significantly below the baseline performance due to the reduction in material shear stiffness.

Finally the effect of using a hybrid of both Flax BIAx and Ramie BIAx material was explored. Thereby combining the strength of the Ramie material with the higher shear stiffness of the Flax material. The design from the TTL iteration was taken as the basis onto which Flax BIAx was added. More BIAx material was added along the blade in both the shearwebs and circumference, the latter focusing on reinforcing the second half of the blade. This final design reached a torsional rigidity of minus 6.8% w.r.t. the baseline and a weight of 15% above the baseline design, see Figure 7-5. In absolute numbers this means a required torsion moment of $4.565e+06$ Nmm and a total mass of 465 kg. The maximum Tsai-Wu levels are acceptable across all loadcases. From all the iterations performed, this design matches the structural requirements best.

The evolution of the blade mass through the different iterations is shown in Figure 7-5 alongside the evolution of the RM3 response of the different design iterations. To further optimise the weight, different core materials can be explored with lower densities. However, it is best to first analyse the design with a 3D element model to accurately assess the torsional rigidity of the blade and the impact of the core thickness. Moreover, it must be noted that the maximum Tsai-wu levels, although below 1, are significantly higher than in the baseline model. The other design loadcases described in the IEC 61400-1 [20] will have to be analysed to see if the design is also sufficient under these other load conditions. For this purpose an accurate characterisation of the NFRC properties, especially its strength values, is desirable.

The final layup design is presented in Figure 7-8 which also visualizes the total thickness and can be compared with the baseline design in Figure 3-11. It can be seen that the total added BIAx thickness is constant along the blade, as this provided the best torsional rigidity. However, the BIAx Ramie is only added in the first half of the blade and is equal to the design from the TTL iteration. The remainder BIAx is from Flax and the amount of added Flax increases towards the tip to maintain equal BIAx thickness along the blade, while also reinforcing the weaker part of the blade in torsion. Furthermore, it can be seen that the thickness of the core material in the shearwebs are reduced by 5 mm. This was done to compromise the added weight of the BIAx and deemed possible due to the added thickness of the extra BIAx in the sandwich faces. Regarding the latter, it must be noted that the model did not fully capture the effect of the thickness on the torsional rigidity as was established earlier on. Future research should investigate the torsional rigidity of a NFRC blade with a FEA with 3D elements. This will also allow for the further investigation of sustainable core material options.

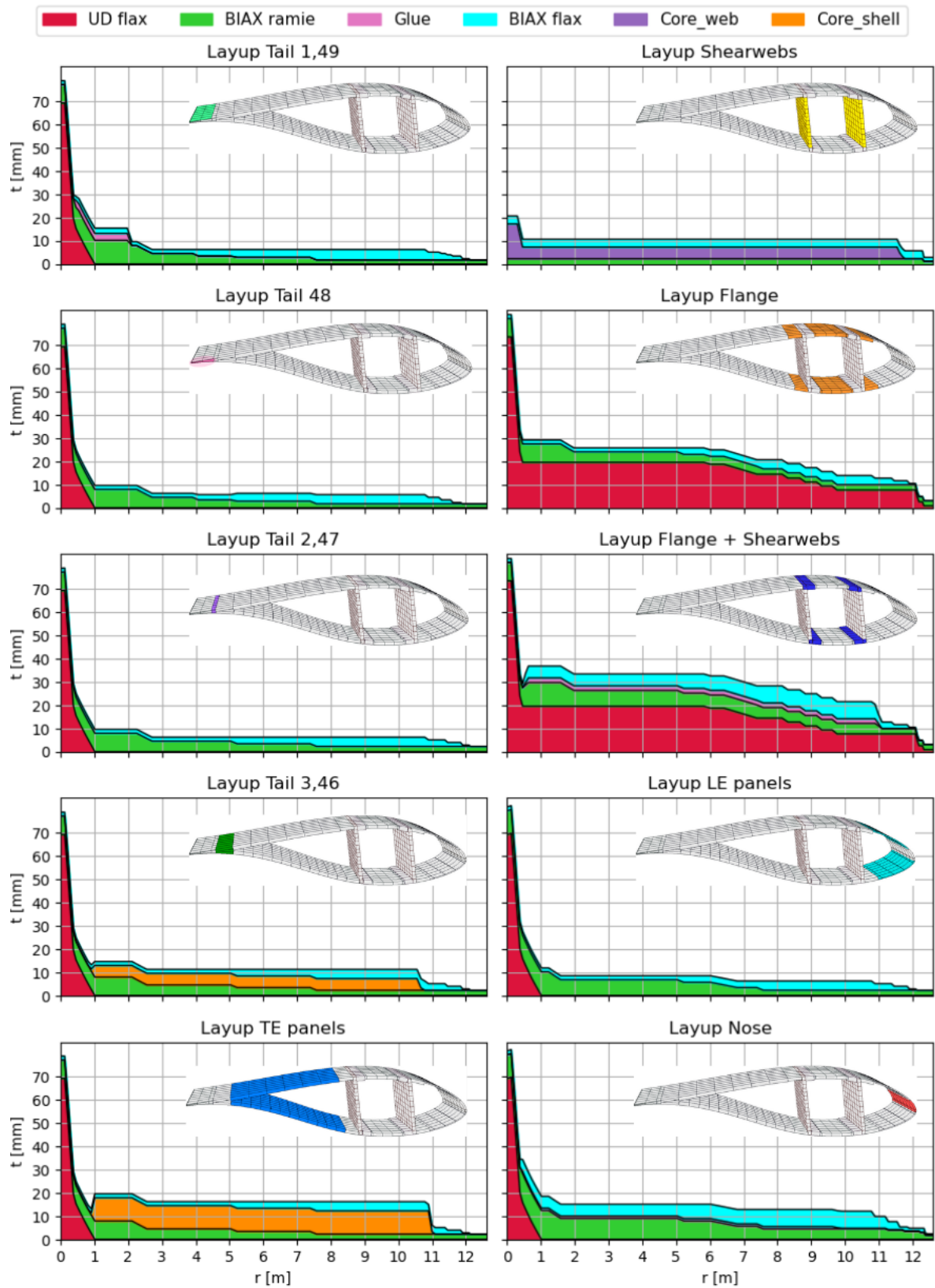


Figure 7-8: Layup design for all sections of the DTU 12.6 m blade in the final (Torque) redesign iteration with NFRCs.

7-5 Final redesign evaluation

A more detailed analysis of the final redesign, established in the fourth design iteration, will be outlined in hereafter.

The final redesign was also analysed under the PTS and TTL loading. The deflection curve of this design under PTS loading is presented in Figure 7-1 as well. It can be seen that the tip deflection has slightly decreased compared to the other iterations and is slightly below baseline levels. This is expected as the added BIAx material increased the overall bending stiffness of the blade. However the change isn't very significant as the flapwise bending stiffness mainly dependent on the UD material design. The maximum Tsai-Wu failure level has also further reduced to a value of 0.718 and is located at the quarter blade length, at the intersection of the TE shearweb and flange, see Figure 7-10 and Figure 7-11. The failure mode is longitudinal compression failure in the inner most BIAx ply, similar to the baseline design. Since the stresses are mainly carried by the BIAx material the reduction in value is expected given the increase in BIAx material. However, the location of the maximum Tsai-Wu value did shift compared to the baseline design. The baseline design has its maximum Tsai-Wu value around the mid-blade point right on the flange where a ply drop in UD material occurs, see Figure 7-9. A possible explanation could be the use of two different BIAx materials in the redesign, and the difference in their layup thickness between the flange and shearweb design. Furthermore, the baseline design was mainly driven by the deflection, whereas the redesign is driven by the torsion and failure criteria. One final observation to point out is that the material failure occurs in the inner most ply. Under PTS loading the largest compression would be expected in the outer ply, furthest away from the neutral axis. The inner most ply refers to the flax BIAx material in the flange of the shear web that is glued to the sparcap. The longitudinal compression strength of the flax material is significantly lower than that of the ramie material which is likely why the first ply failure is expected in the inner most ply rather than the outer most ply.

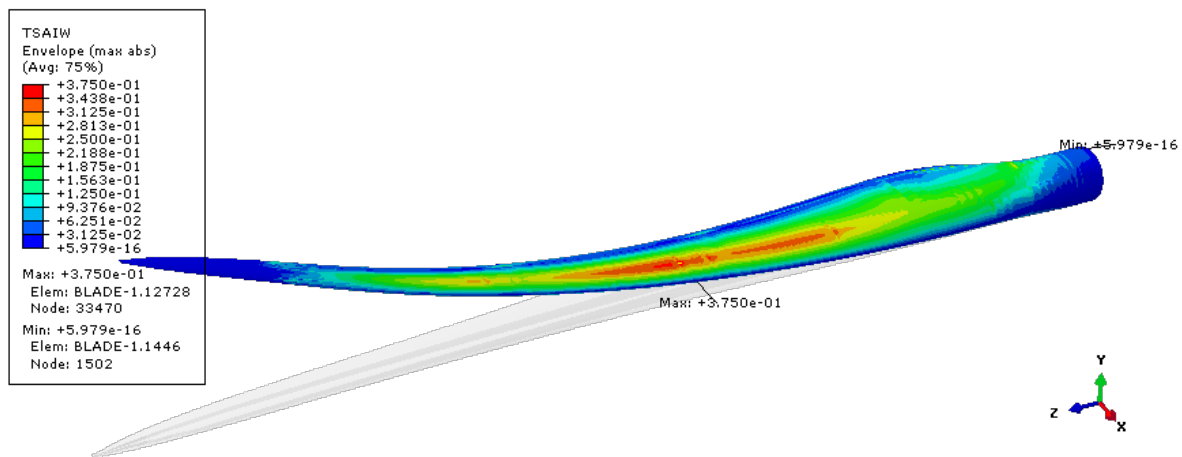


Figure 7-9: Maximum Tsai-Wu value distribution of DTU 12.6 m blade baseline design under PTS loading.

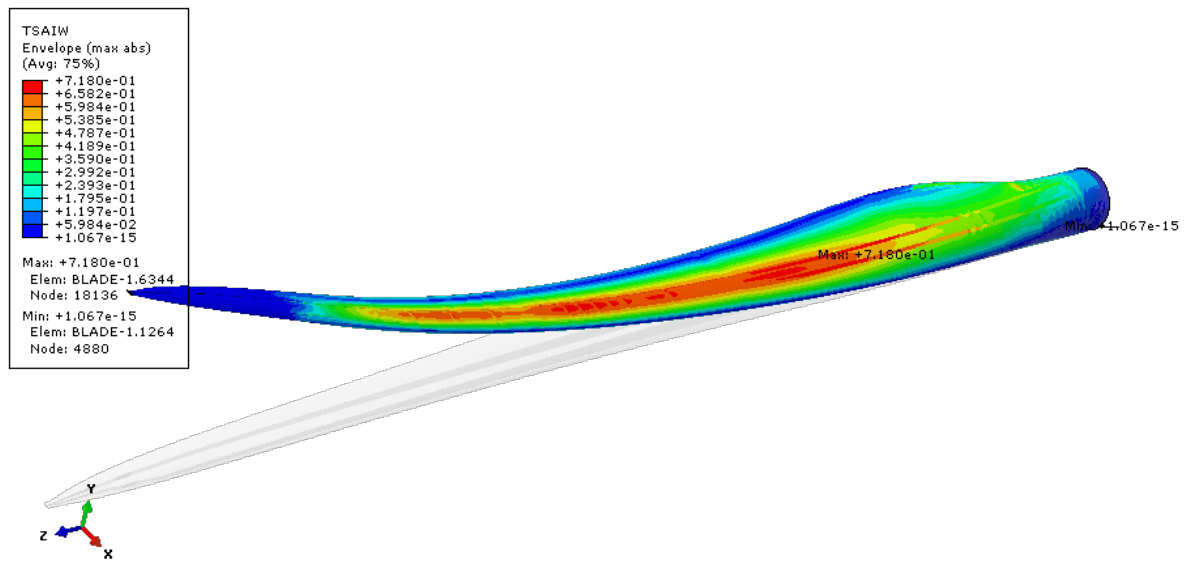


Figure 7-10: Maximum Tsai-Wu value distribution of DTU 12.6 m blade design iteration 4, redesign for Torque with NFRCs, under PTS loading.

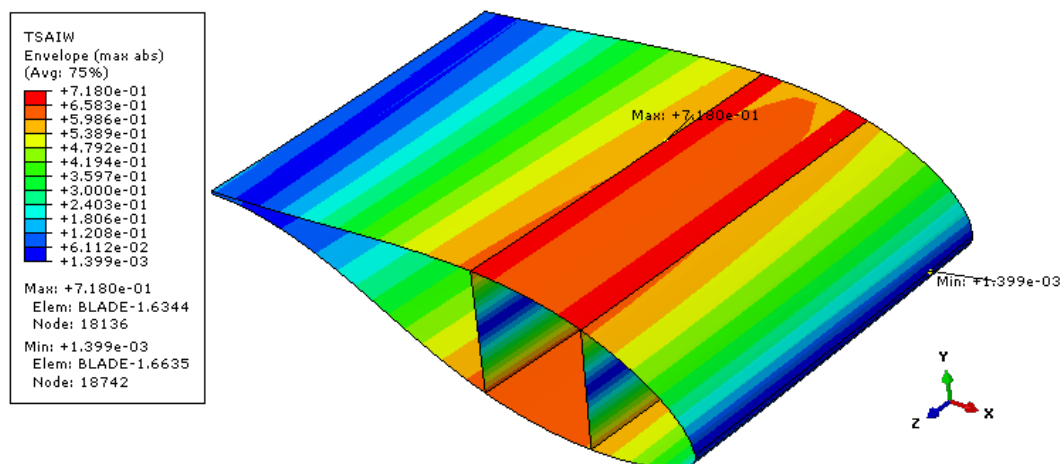


Figure 7-11: Maximum Tsai-Wu value distribution of DTU 12.6 m blade design iteration 4, redesign for Torque with NFRCs, under PTS loading. Zoom-in on location with overall highest Tsai-Wu value at $r = 3.72$ m.

The deflection curve of the final design iteration under TTL loading is presented in Figure 7-3 as well. It can be seen that the tip deflection has decreased significantly to 0.184 m, well below the baseline deflection curve. This can be expected as the Torque iteration required a significant amount of extra BIAx material which plays a large role in the edgewise bending stiffness as well as the torsional rigidity. As expected, the maximum Tsai-Wu failure level has also reduced, to a value of 0.348 and is located on the trailing edge at the root, see Figure 7-13 and Figure 7-14. The failure mode is longitudinal tension failure in the inner most BIAx ply, similar to the baseline design. Since the stresses are mainly carried by the BIAx material the reduction in value is expected given the increase in BIAx material. The location at the root

coincides with the final ply drop to zero in UD material in the trailing edge, which causes a stress concentration as the loads have to redistribute over less material. However, the location on the blade of the maximum Tsai-Wu value did shift compared to the baseline design. The baseline design has its maximum Tsai-Wu value around one third of the blade where a ply drop in BIAx material in the trailing edge occurs, see Figure 7-12. This difference is likely caused by the additional BIAx material along the blade stiffening the blade further towards the tip, thereby moving the location of the maximum Tsai-Wu to another weak point. The weak point now being the transition of the root into the airfoil shape combined with the drop in UD material. One final observation to point out is that again the material failure occurs in the inner most ply. Under TTL loading the largest tension would be expected in the outer ply, furthest away from the neutral axis. A possible explanation can be the level of interaction between the different stress components. The Tsai-Wu criterion accounts for this interaction and may indicate failure even if the individual components are within the failure limit of the material. The inner most ply experiences not only high longitudinal tension stresses, but also high transverse tension and some shear stresses.

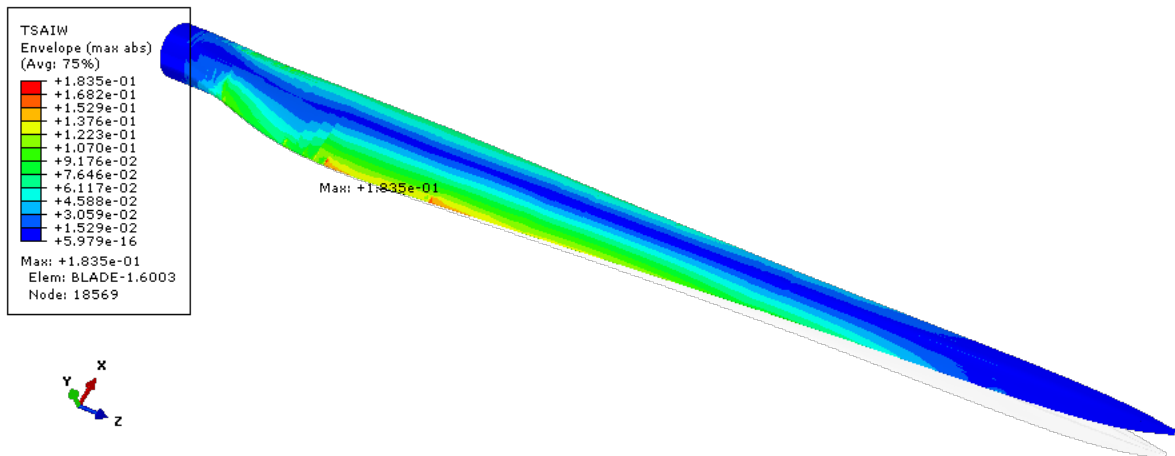


Figure 7-12: Maximum Tsai-Wu value distribution of DTU 12.6 m baseline design under TTL loading.

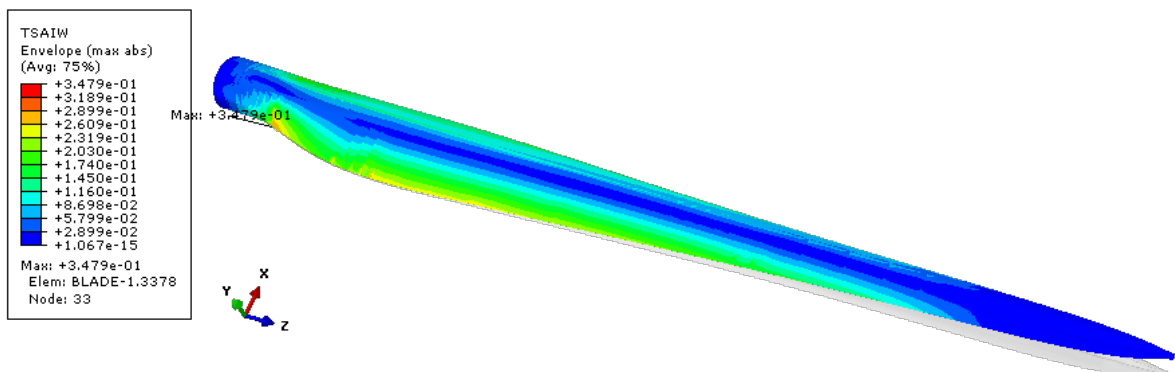


Figure 7-13: Maximum Tsai-Wu value distribution of DTU 12.6 m blade design iteration 4, redesign for Torque with NFRCs, under TTL loading.

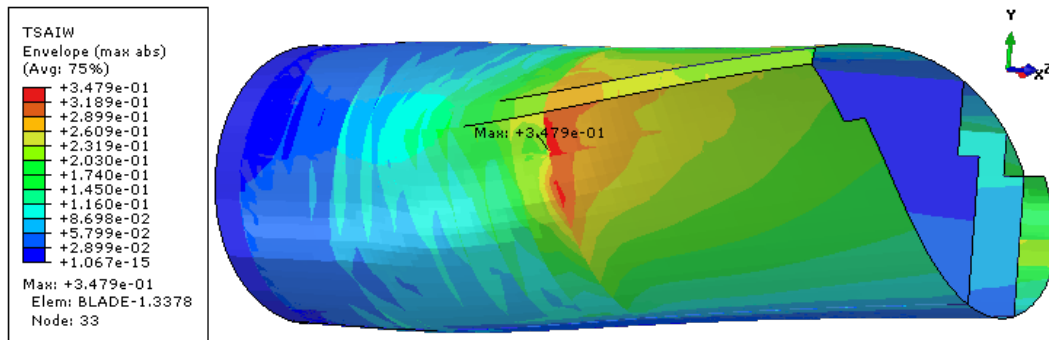


Figure 7-14: Maximum Tsai-Wu value distribution of DTU 12.6 m design iteration 4, redesign for Torque, under TTL loading. Zoom-in on location with overall highest Tsai-Wu value: TE at the root at $r = 1$ m.

Finally, the maximum Tsai-Wu value in the Torque loadcase equals 0.81 for the final design iteration. It must be noted that there is a location with a Tsai-Wu value of 1.08, which would indicate failure. However, this value occurs at the load introduction point and is highly localised. This indicates that this value is a numerical error and not what can be expected in reality. Moreover, the failure type at this location shows longitudinal compression failure of the inner most BIAx ply, which is not expected in this loadcase. Hence, the highest Tsai-Wu value outside this point that is deemed a realistic result is the value of 0.81, see Figure 7-15. The failure type in this region shows shear failure of the outer BIAx ply. This is a logical result given that torsion loads mainly introduce shear stresses and deformations.

The maximum Tsai-Wu value plot of the baseline design did not indicate numerical issues and shows the highest Tsai-Wu value at the leading edge transition into the nose region, see Figure 7-16. The failure type is shear failure in the inner BIAx ply. The failure likely occurs at the inner ply due to stresses introduced by the lap joint of the upper and lower half of the LE panels in the nose region. In the transition from the nose to the LE panel the stresses have to redistribute itself. The plies drop at the inside of the blade, likely causing the stress concentration to be the highest at the inner BIAx ply.

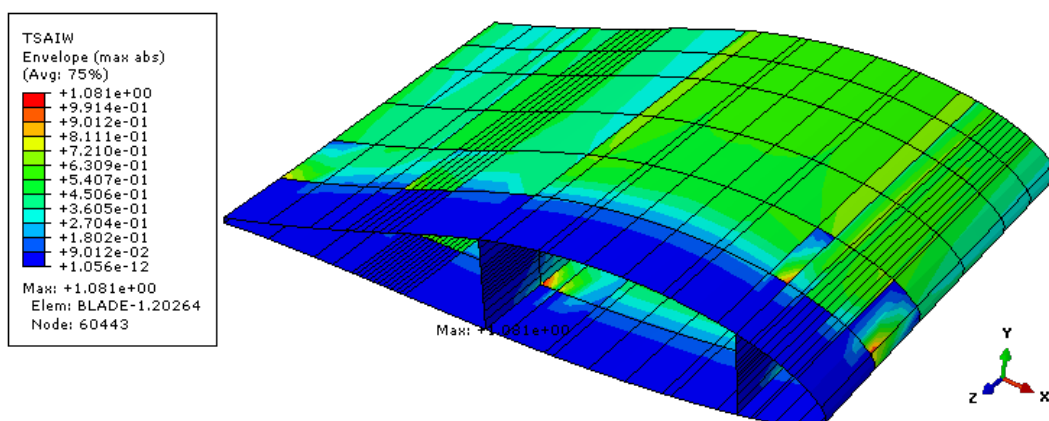


Figure 7-15: Maximum Tsai-Wu value distribution DTU 12.6 m blade design iteration 4, redesign for Torque with NFRCS, under Torsion load. Zoom-in on blade tip at with load introduction at $r = 10.8$ m.

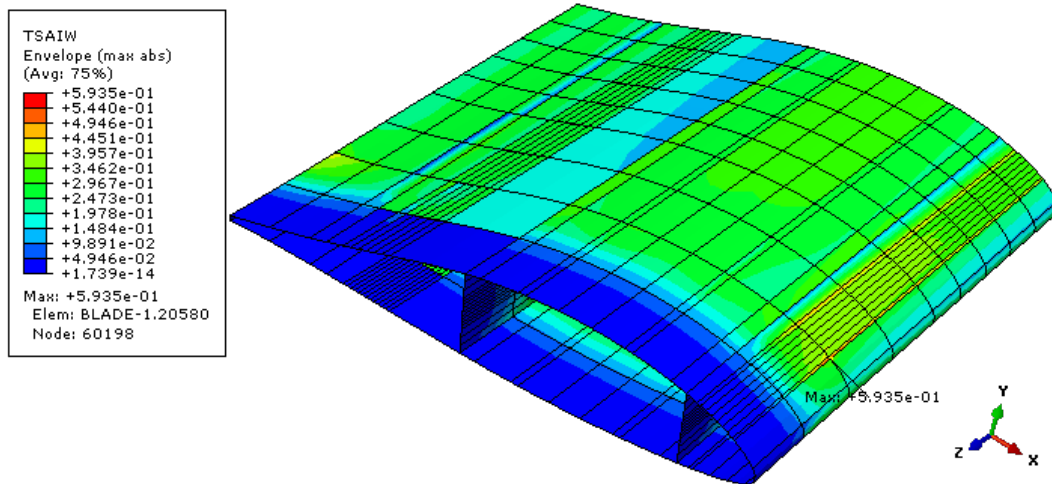


Figure 7-16: Maximum Tsai-Wu value distribution of the DTU 12.6 m baseline design under Torsion load. Zoom-in on blade tip at with load introduction at $r = 10.8$ m.

A non-linear buckling analysis as well as the analysis of creep deformations need to be performed to further evaluate the design and inform additional design iterations. However, given the limitations in the design of the current work along with the time constraints of the project, it was decided that these analyses will not be performed for the current body of work. These steps will have to be part of future research.

7-5-1 Estimated Structural Campbell Diagram and Aeroelasticity Predictions

Finally, the new blade design will have to be tested in an aeroservoelastic simulation, like HAWC2, to establish its performance in an operating wind turbine. This is especially critical given the slightly lower torsional rigidity and increased edgewise rigidity of the blade as well as the significant weight increase. This analysis will also lead to an iteration of the design loads which should then be checked with Abaqus again to see if the design withstands these updated loads. However, the process of obtaining the structural input file for the HAWC2 analysis is labour intensive and required additional software. Given the limited time frame of this research, these steps have to be handed to future research.

Using the eigenvalue analysis in Abaqus, an estimate can be made of the Campbell diagram of the new blade design. Although the structural Campbell diagram neglects the aerodynamic forces, it is still a useful tool to check for possible resonance issues. The estimation of the structural Campbell diagram [75] is based on the assumption that the mode shapes are dominated by blade motion for the standstill rotor modes. The symmetric blade modes are typically invariant with the windspeed. The forward whirling modes increase linearly with windspeed, and the backward whirling modes decrease linearly with windspeed. Starting from the natural frequencies at zero wind speed, the lines can be drawn for each mode. The forcing frequencies are multiples of the rotor speed indicated by 1P, 3P and 6P. Any overlaps between the P-harmonics and lightly damped modes indicate the potential of resonance. Table 7-1 summarises the natural frequencies obtained from the eigenvalue analysis performed in Abaqus. Figure 7-17 presents the estimated structural campbell diagram along with the

P-harmonics.

Table 7-1: Natural frequencies as calculated by Abaqus for the conventional shell element model of the DTU 12.6 m baseline (GFRC) and redesigned (NFRCs) blade.

	Baseline [Hz]	Redesign [Hz]
1st Flap	2.28	2.09
1st Edge	4.23	4.06
2nd Flap	7.78	6.58
2nd Edge	15.2	13.6

In reality the motion of the tower also impacts the rotor mode shapes and will cause small deviations between theory and reality, especially for the flapwise modes. Furthermore, the edgewise collective mode is difficult to predict due to the free boundary condition on the shaft that changes the cantilevered mode shape into a free-free mode shape [75]. Therefore, the edgewise collective modes for operating turbines will generally be significantly higher than the whirling modes, contrary to the prediction in Figure 7-17. The other modes will generally match well with the theoretical modes [75].

In Figure 7-17 it can be seen that the forward whirling edgewise mode shape overlaps with the 6P-harmonic. Since this mode is lightly damped, resonance can be an issue. A full aeroelastic Campbell diagram needs to be analysed to confirm if resonance will be an issue. The same holds for the backward whirling edgewise mode shape that crosses with the 3P-harmonic.

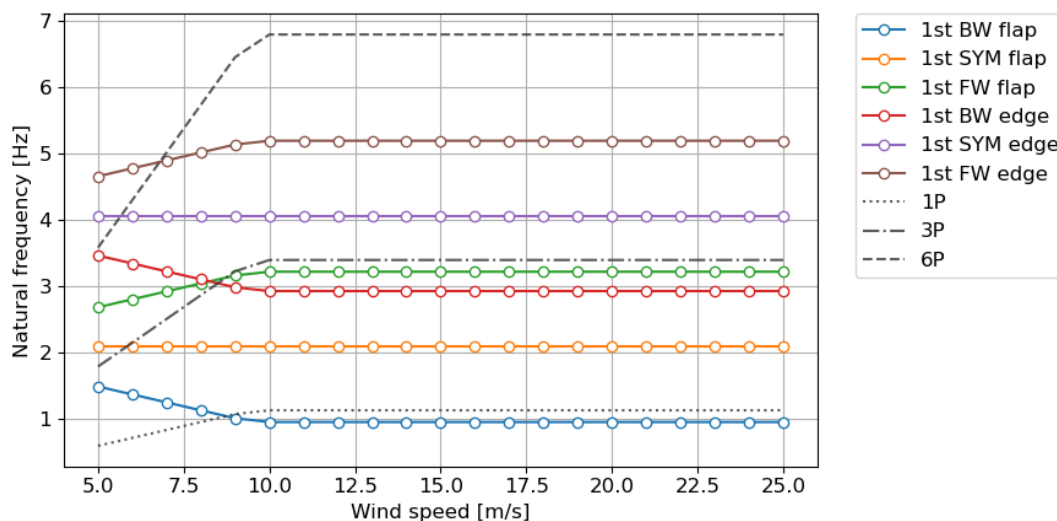


Figure 7-17: The estimated structural Campbell diagram for the first order blade modes of the DTU 12.6 m redesigned blade with NFRCs.

The expectation is that the aeroelastic behaviour as a whole changes, making it complicated to make predictions without actually performing the analysis. What can be noted, is that generally speaking, small blades are very stiff when comparing their deflection to the blade length. The more flexible a blade is, the larger the impact of the blade design on the aeroelastic behaviour. Changing the blade design for this small blade would likely not lead to significant changes in the aerodynamic forces. When assuming unchanged aerodynamic forces, one can

look into the inertia loads expectations.

The significant increase in blade mass will effect four load channels. The yaw bearing pitch, in-plane BRM and tower base moments.

In terms of yaw bearing pitch, the added weight will counteract part of the thrust, thereby reducing the extreme loads driven by thrust. The yaw bearing pitch fatigue loads will likely be unchanged as the gravity loads do not play a big role in fatigue for this load channel.

The in-plane blade root moment will experience higher fatigue loads. Moreover, it might be required to reinforce the blade root to support the added weight.

The tower base side-side and fore-aft moments will likely increase in terms of both extreme and fatigue loads. Additionally, the added blade mass will reduce the natural frequency of the tower. This leads to possible resonance occurring at a lower rpm. This would be beneficial as it allows the minimum rotor speed to be reduced, thereby producing energy at a larger range of wind speeds.

Furthermore, it must be noted that design for fatigue was outside the scope of this research and will have to be investigated in future works.

In conclusion, the aeroelastic simulation, currently beyond the scope of this research, is essential to evaluate the impact of the NFRC blade design on the overall turbine behaviour. The estimated structural Campbell diagram highlights potential resonance issues, particularly with the lightly damped edgewise blade modes which overlap with the 3P- and 6P-harmonic forcing frequencies. Future research must address these areas, including fatigue design and comprehensive aeroelastic behaviour analysis, to ensure the blade's reliability and performance in practical applications.

Chapter 8

Conclusions

This thesis investigated the structural implications of using bio-based materials, specifically natural fibre-reinforced polymer composites (NFRCs), in wind turbine blade design. The primary focus was on redesigning the DTU 12.6 m research wind turbine blade to enhance environmental sustainability while maintaining structural integrity.

8-1 Conclusions

The findings from the literature study indicate that while NFRCs can significantly reduce the environmental footprint of wind turbine blades, their lower mechanical properties - such as bending and shear stiffness and strength - limit their direct replacement of traditional glass fibre composites. The higher porosity levels, lower fibre volume content, and interface challenges of NFRCs contribute to these performance limitations. Furthermore, the literature study identified that bio-based composite systems with fibres like flax, ramie, hemp and bamboo, combined with a bio-based matrix like PLA, show potential for application in wind turbine blades.

A sensitivity study was performed to investigate the influence of utilising NFRC materials on blade performance. This sensitivity study on the implications of the different material engineering constants identified the longitudinal and shear stiffnesses and strengths of the UD and BIAX materials as the critical design parameters when switching to NFRCs. The UD longitudinal stiffness drives both the deflections and consequently the failure limits defined by the Tsai-Wu criterion. The BIAX longitudinal stiffness also impacts the edgewise deflections and resulting failure limits. The shear stiffness and strength of the BIAX material mainly dominates the torsional rigidity and failure limit. The impact of the thickness of the shearweb core thickness also needs to be considered for the torsional rigidity. Furthermore, it can be derived that the Pressure Towards Suction side deflection will likely drive the design process, as is typical for wind turbine blades. This led to the material selection of UD Flax/PLA and BIAX Ramie/PLA for the redesign of the DTU 12.6 m blade.

The redesign process revealed that torsional rigidity and material strengths are the primary

drivers for bio-based blade design. This differs from the conventional blade design where the tip deflection and therefore specific stiffnesses are the main drivers. To address the reduced torsional rigidity, the core thickness of the shear webs was significantly increased. However, contrary to expectations, this adjustment did not improve torsional rigidity in the model results. This discrepancy may stem from limitations in the 2D shell element model used, where thickness is not explicitly modelled in the geometry but is instead incorporated into the element definition [57]. As a result, the influence of increased core thickness on torsional rigidity may not have been fully captured. The use of 3D continuum shell elements in future studies is required to provide an accurate torsional analysis and full design validation.

Using the 2D shell model, the structural redesign of the DTU 12.6 m blade focussing on the UD and BIAx layup design showed that the hybridization of NFRCs is a promising strategy to address the material weaknesses. However, meeting structural requirements required significant increases in material use, leading to a blade mass over 15% higher than the original GFRC design despite the lower density of NFRCs. In order to meet the design requirements the structural blade design will need to be rethought, for example by incorporating other structural elements like stiffeners and ribs.

The estimated structural Campbell diagram of the established redesign indicates possible resonance issues for the edgewise forward and backward whirling mode shapes. Full aeroelastic analyses should confirm whether resonance becomes an issue on an operating turbine.

The findings highlight the need for further refinement of both the material properties and the modelling techniques to fully assess and realize the potential of bio-based materials in wind turbine blade applications. Enhancing NFRC mechanical properties, validating advanced material models, and addressing the limitations of current design approaches will be essential to overcome the technical barriers to using NFRCs in wind turbine blades effectively.

8-2 Recommendations

To advance the development and application of bio-based wind turbine blades, the following recommendations are proposed based on the conducted research:

- Conduct experimental validation of the mechanical properties of natural fibres, bio-based matrix properties, and their resulting composite properties.
- Conduct extensive model validation and refinement of the micro-mechanical model for NFRCs.
- Enhance the mechanical performance of NFRCs, particularly stiffness, strength, and shear stiffness. For example through material refinement, focusing on reducing porosity and improving fibre-matrix compatibility.
- Investigate possible challenges that may result from the use of different natural fibres in a hybrid composite.
- Investigate the torsional rigidity of NFRCs blades using advanced 3D continuum shell element models.

-
- Investigate the integration of stiffeners, ribs, and additional shear webs to improve rigidity and strength while minimizing weight increases.
 - Explore alternative NFRC materials, such as bamboo strips, for improved sustainability and performance.
 - Conduct aeroservoelastic studies to assess the dynamic behaviour of bio-based blades in operational conditions, ensuring their robustness and stability.
 - Investigate the lifespan expectancy for NFRC blades, accounting for issues like moisture resistance and creep among others.
 - Conduct a Life Cycle Assessment (LCA) to evaluate the environmental impact of utilising natural fibre reinforced composites in wind turbine blades.

HAWC2 controller re-tuning process

Section 3-1 describes the aeroservoelastic HAWC2 model that is used to obtain the design loads for the blade design. An existing model was received that needed to be verified. In theory the static loads assumed in the received Abaqus model of the blade, see Section 3-2, should originate from the DLC1.3 simulation of the blade with HAWC2. The analysis showed a clear discrepancy, see Figure A-1. Therefore, the HAWC2 model needs to be analysed and verified in more detail.

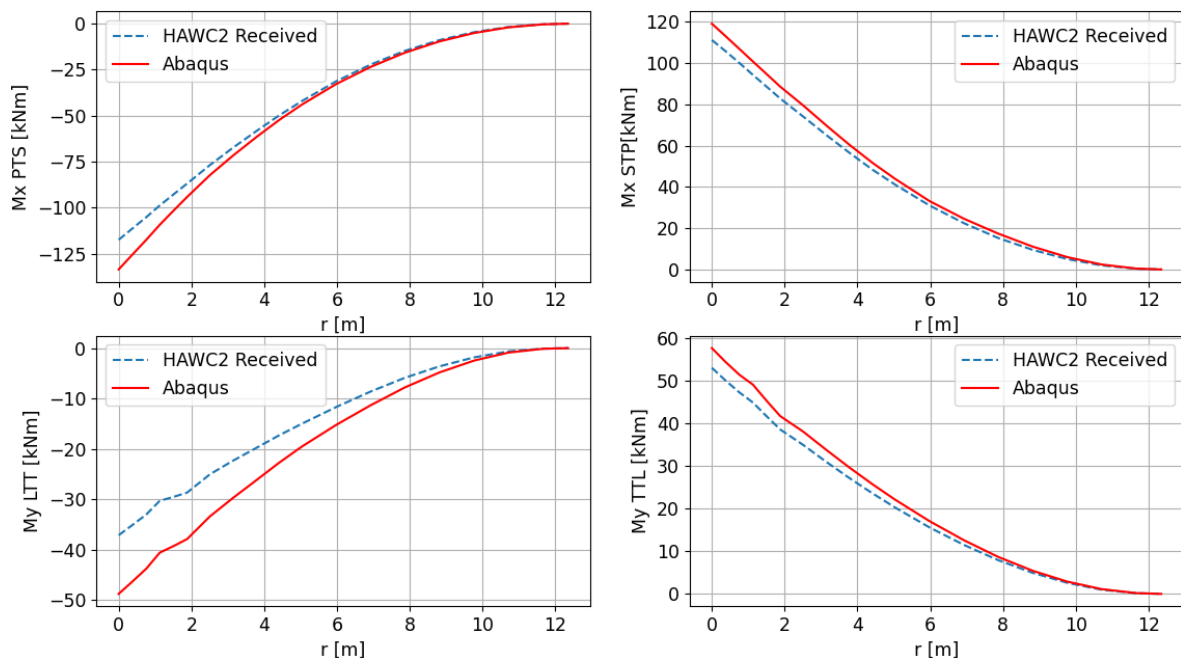


Figure A-1: Extreme design loads from DLC1.3 calculated from received HAWC2 model and provided to the Abaqus model of the DTU 12.6 m blade. Upper left subplot: flapwise bending moment towards tower, upper right subplot: flapwise bending moment away from tower, lower left subplot: edgewise bending moment towards trailing edge, lower right subplot: edgewise bending moment towards leading edge.

To verify that the HAWC2 model runs correctly, the first test is running a stepwind simulation. Such a simulation shows a turbine's behaviour at different steady windspeeds. Furthermore, it shows how quickly the turbine responds to a change in windspeed by finding its new equilibrium state. The latter information can give an indication of how well the controller works. The stepwind results for the received HAWC2 model are presented in Figure A-2. The simulation starts at the cut-in wind speed of 4 m/s and ends at the cut-out wind speed of 25 m/s where each step has a duration of 40 seconds. The first 100 seconds are disregarded to eliminate transient influences from starting up the simulation.

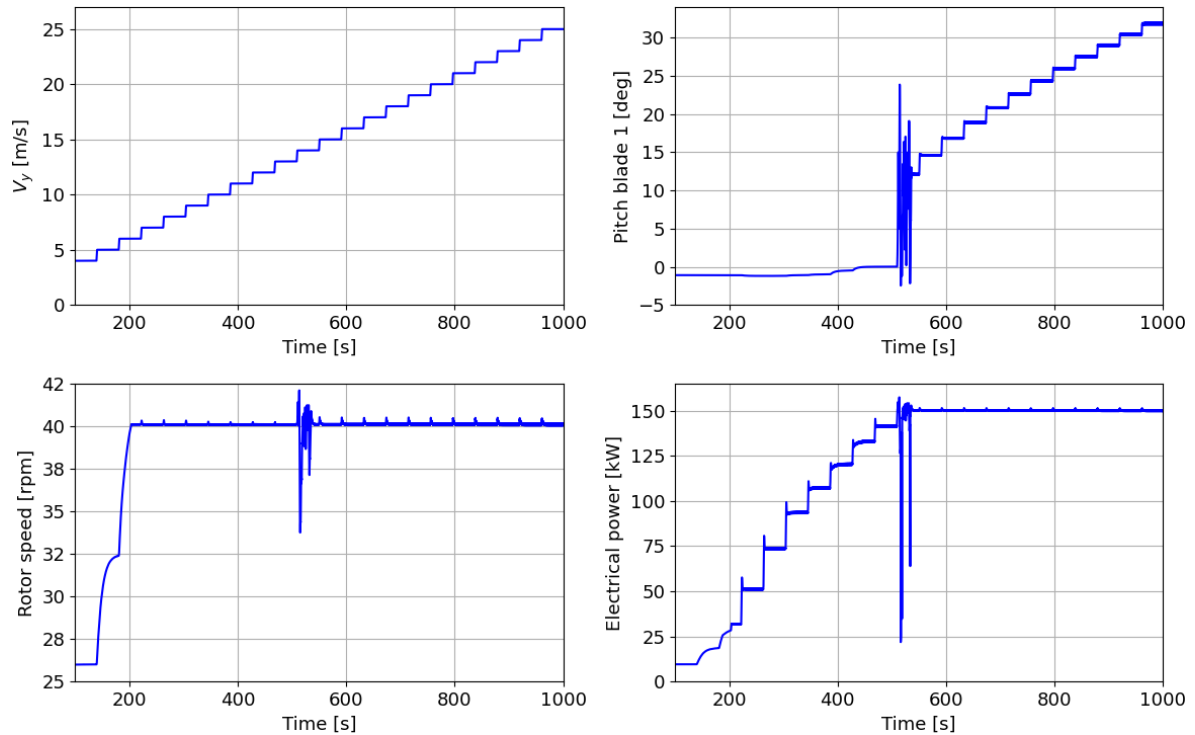


Figure A-2: Stepwind results of original HAWC2 model of the DTU 12.6 m blade as received.

Analysing the results, it is immediately clear that there is a huge instability present around the rated wind speed of 14 m/s where the power reaches rated power of 150 kW. The pitch, rotor speed and power overshoot dramatically upon this steps in wind speed and cannot reach a state of equilibrium within the 40 seconds of this step duration. This is likely an instability caused by the controller which fails to regulate the turbine's behaviour at these wind speeds. It is likely that the extreme loads previously calculated originate from this unstable region, thereby making the calculated extreme loads unreliable and thus unsuitable as design loads for the wind turbine blade. It is therefore required to re-tune the controller of the HAWC2 model with the original 12.6 m blade to generate a stable model that produces realistic and reliable design loads for the redesign. The models of the DTU 12.6 m research wind turbine blade are unfortunately poorly documented at the moment of writing. Therefore, an article on a 100 kW wind turbine with an 11 m wind turbine blade by Gözcü et al. [76] was used as reference to guide the controller re-tuning process.

To calculate the controller tuning parameters the HAWC2S software is used. This software

requires some operational settings as well as the frequencies and damping ratios (called poles) for which the controller shall be tuned. The first parameter is the optimal tip speed ratio which is set to 9.77 in accordance with the reference article [76]. Furthermore, the rated rotor speed will be based on the maximum tip speed of 95 m/s yielding a maximum allowable rotor speed of:

$$\Omega_{max\ allowed} = \frac{V_{max\ tip\ speed}}{R} = \frac{95}{13} = 7.308\ rad/s = 1.163\ Hz = 69.78\ rpm \quad (A-1)$$

To built in a small margin it is chosen to use a rated rotor speed of 68 rpm. Together with the rotor radius of 13 m this results in a rated wind speed of 9.475 m/s. The minimum rotor speed is set equal to 20 rpm = 2.0933 rad/s as noted in the comments in the original model file. The aerodynamic rated power is assumed equal to the electrical rated power divided by the generator efficiency. The latter is 98% as specified in the original model leading to an aerodynamic rated power of $\frac{150}{0.98} = 153.06$ kW. The minimum pitch is set to -1.1 degrees, a value found in a different HAWC2S model file for the DTU 12.6 m wind turbine on the cluster.

Finally, the controller tuning inputs were set for quadratic gain scheduling and constant power. The PI controllers are tuned for a specific frequency and damping ratio, called the poles of the controller. So the goal of the initial re-tuning process of the controller is to find a set of poles that generate stable turbine behaviour. For the initial re-tuning attempt, the tuning frequency and damping ratio were set to 0.1 Hz and 70% for both the torque controller in the partial load region and the pitch controller in the full load region, equal to the poles used in the reference article. The goal was to find the poles that result in controller parameters, proportional and integral gains of the PI controller, in the same order of magnitude as for the HAWC2 model of blade-1 in the reference article [76]. It is chosen to find results more similar to this model as the model in the article produced stable results whereas the original DTU 12.6 m model is unstable. Furthermore, it must be noted that the damping ratio of 70% is very typical for a wind turbine and is thus kept equal throughout the re-tuning process. It controls the amount of overshoot in the output signal as a response to a change in input signal. A larger damping ratio means less overshoot. The tuning frequency determines how quickly the output signal can respond to a change in input signal. A higher frequency thus means a faster response.

The different poles that have been tested are listed in Table A-1. Attempt 1 has the poles as aforementioned. Attempt 2 and attempt 3 half and double the frequencies of attempt 1 to see how the controller tuning parameters change with an increase and decrease in tuning frequency. The results are presented in Table A-2 alongside the tuning parameters of the original model and the model of blade-1 in the reference article. It must be noted that the optimal C_p tracking factor K is constant with changing tuning poles. It depends on the maximum C_p , optimal tip speed ratio, rotor radius and generator efficiency. Additionally, the full load parameters K_1 and K_2 are determined by fitting a curve to the derivative of aerodynamic torque w.r.t. the collective pitch angle, based on the assumptions of quasi-steady aerodynamics and constant induced velocities [54]. These parameters are inherently tied to the aerodynamic design and operational characteristics of the wind turbine blade, therefore remaining constant with changing tuning poles.

Table A-1: Poles for the controller re-tuning of the DTU 12.6 m HAWC2 model.

Attempt #	Partial load		Full load	
	f_n [Hz]	ζ [-]	f_n [Hz]	ζ [-]
1	0.1	0.7	0.1	0.7
2	0.05	0.7	0.05	0.7
3	0.2	0.7	0.2	0.7
4	0.3	0.7	0.3	0.7
5	0.1	0.7	0.2	0.7
6	0.3	0.7	0.2	0.7

Comparing the results it can be stated that the attempt 1 results show relatively similar results to the blade-1 in the reference article for the partial load region, the full load region differs more. Furthermore, the proportional gains indeed vary proportionally with the tuning frequency when comparing attempt 1 with attempt 2 and 3. The integral gains vary quadratically with the tuning frequency. As the gains of these first three attempts still differ from the gains in the article, other controller poles were explored.

On the DTU cluster a tuning file for the DTU 12.6 m blade was found with the tuning frequencies both equal to 0.3 Hz and damping ratios to 70%. The controller tuning parameters for the partial load of that tuning model matched the parameters in the original HAWC2 model received. Therefore, these poles were tested as well for the newly set up tuning file, named attempt 4. Indeed the partial load gains were similar to the original HAWC2 model, however, the full load gains differed significantly from both the original HAWC2 model and the article.

The next attempt (attempt 5) was selected to match the controller tuning parameters of the reference article blade-1 as closely as possible. This meant selecting the tuning frequency of 0.1 Hz for the partial load region and 0.2 Hz for the full load region. It must be noted that the focus was on matching the proportional gains as they are more straight forward to adjust the tuning frequencies to. Additionally, another attempt (attempt 6) was performed choosing the tuning frequency of 0.3 Hz in the partial load region to match with the original HAWC2 model while keeping the full load tuning frequency at 0.2 Hz to match the stable model from the reference article. The resulting sets of controller tuning parameters for these two attempts were tested by running a stepwind simulation. This was done to identify whether these parameters result in a stable model as well as to compare the two options to choose the better performing one. The stepwind time series results are shown in Figure A-3. The stepwind results are only presented for attempts 5 and 6 as their set of gains are of the order of magnitudes that are expected to produce stable results.

Table A-2: Controller tuning parameters for the DTU 12.6 m blade for the various controller poles in Table A-1, alongside those of the model in the reference article by Gözcü et al. [76].

	Original model	Article model	attempt 1	attempt 2	attempt 3	attempt 4	attempt 5	attempt 6
K	$\frac{\text{Nm}}{(\text{rad/s})^2}$ 474.384	195.747	360	360	360	360	360	360
K_{Pg}	$\frac{\text{Nm}}{(\text{rad/s})}$ 132889	28479.5	44281.9	22141	88563.8	132846	44281.9	132846
K_{Ig}	$\frac{\text{Nm}}{\text{rad}}$ 178921	12781.6	19873.7	4968.42	79494.7	178863	19873.7	178863
K_P	$\frac{\text{rad}}{(\text{rad/s})}$ 1.1	0.420796	0.212748	0.112803	0.412636	0.612525	0.412636	0.412636
K_I	$\frac{\text{rad}}{\text{rad}}/\text{rad}$ 0.6	0.176573	0.0897098	0.0224274	0.358839	0.807388	0.358839	0.358839
K_1	deg 20	8.87476	10.8443	10.8443	10.8443	10.8443	10.8443	10.8443
K_2	deg ² 0	1388.00172	368.01584	368.01584	368.01584	368.01584	368.01584	368.01584

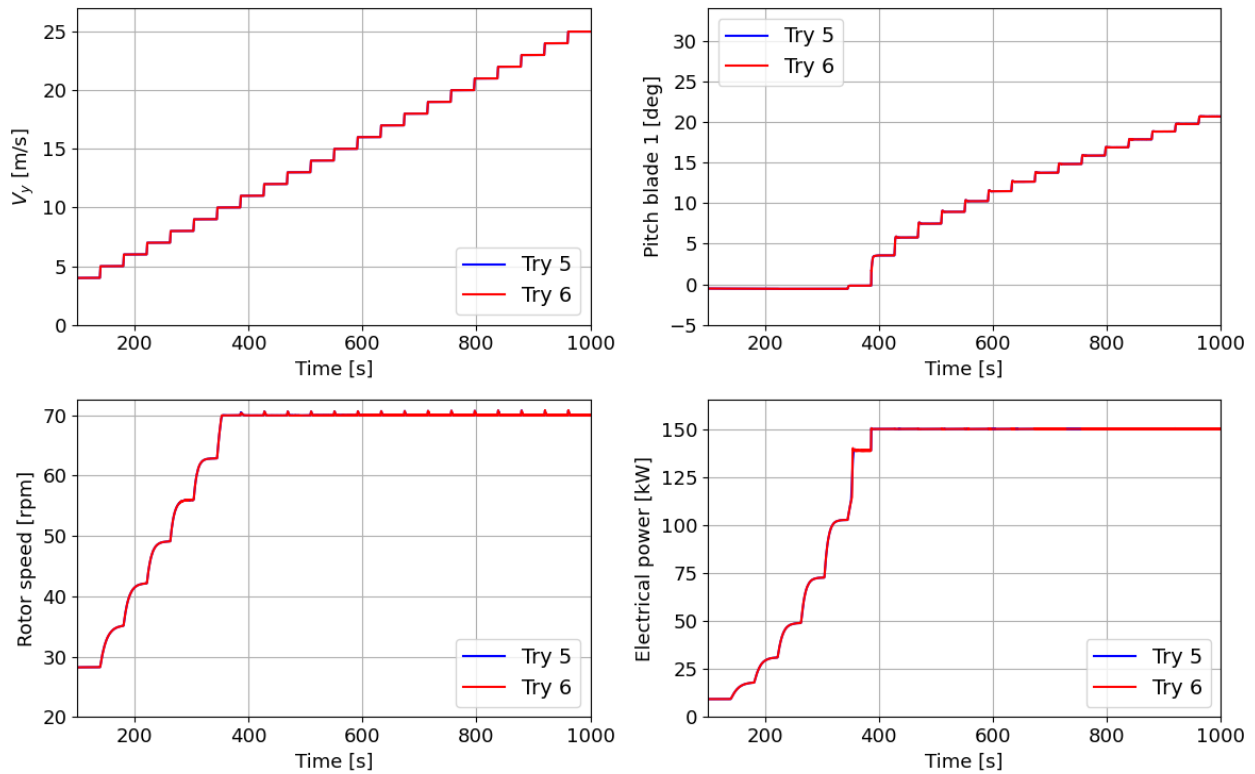


Figure A-3: Stepwind results of new HAWC2 model of the DTU 12.6 m blade with the controller tuning parameters from attempt 5 and attempt 6.

It can be seen that the results of both sets of tuning parameters are very similar. Moreover, there are no apparent instabilities in the response of the output parameters. The output signals show small overshoot and especially from around rated windspeed the new set-point is reached quickly. The set-point is not reached within the set 40 seconds per wind step for the lower windspeeds. This has to do with the K factor for optimal C_p tracking as that value sets the set-point. This can only be changed by changing for example the tip speed ratio and aerodynamic design of the blade, however, the aerodynamic design is outside the scope of the current research. The goal for the current work is to obtain a stable model to establish realistic design loads for the structural redesign, which is achieved.

To be able to distinguish between the results of the two datasets of controller tuning parameters, the pitch and electrical power curves were zoomed in on, see Figure A-4. The step zoomed in on in the pitch curve is the one from a windspeed of 10 m/s to 11 m/s. There is a small irregularity visible in the pitch curve of which the attempt 5 curve is more smooth. Whether this poses a real issue will be analysed by testing the model with a turbulent wind simulation. Furthermore, the overshoot in electrical power when stepping up from 10 m/s to 11 m/s is smaller for the attempt 5 curve while its response is a bit slower than the attempt 6 curve. However, the variation once the set-point is reached, after 364 s, is larger for the attempt 6 curve.

From the discussed small differences between the two datasets it is chosen to go with the controller tuning parameters of attempt 5 as the pitch curve is slightly smoother, the overshoot in electrical power slightly lower as well as the steady state variation in the latter.

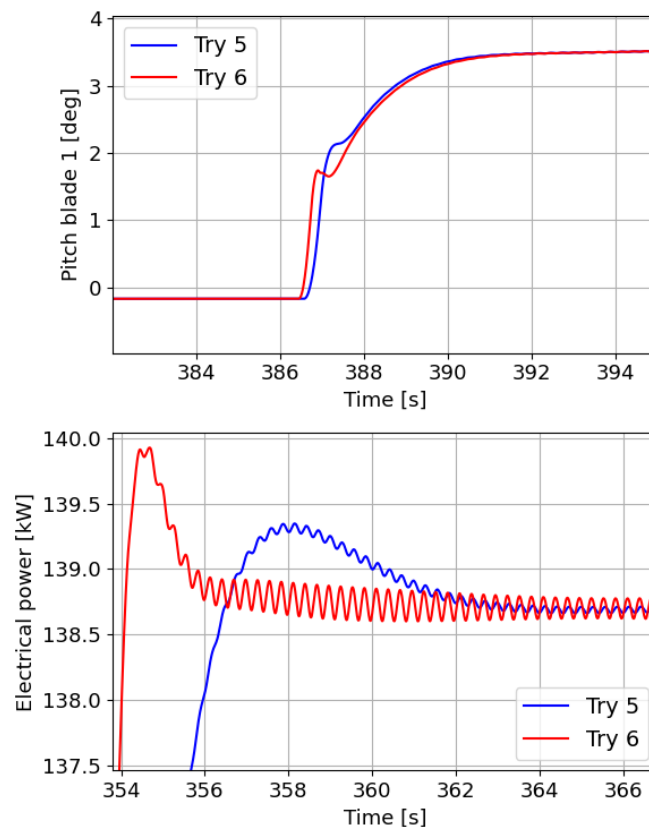


Figure A-4: Zoom in on stepwind pitch and electrical power results of new HAWC2 model of the DTU 12.6 m blade with the controller tuning parameters from attempt 5 and attempt 6.

Besides the controller parameters obtained with HAWC2S there are a few other parameters of the controller that need to be adjusted. The HAWC2S software also calculated the optimal pitch angle for each wind speed to obtain maximum power output. These pitch angles will be used as minimum pitch angle for the wind speeds below rated power and are specified in a file named "wpdata.100". The content of this file is presented in Table A-3. The minimum pitch angle at a wind speed of 50 m/s is set equal to that of the last wind speed before rated power. This means that for any wind speed of 9 m/s or higher the minimum pitch angle is equal to that specified value.

Another parameter is the generator control switch which is set to 0.95, where 0 means constant torque and 1 means constant power, set equal to the model in the reference article [76]. Furthermore, the time constant of 1st order filter on wind speed used for minimum pitch as well as the time constant of 1st order filter on pitch angle used for gain scheduling shall be equal to $[1/1P]$ which is 0.88235 given the new rated rotor speed of 68 rpm.

Table A-3: Content "wpdata.100" file specifying the minimum pitch angle for HAWC2.

V	θ
m/s	degrees
0	-0.520993
4	-0.520993
5	-0.536761
6	-0.548933
7	-0.558490
8	-0.567163
9	-0.572136
50	-0.572136

To ensure that there are no resonance issues with the new rotor speed, a modal analysis was performed. The aeroelastic Campbell diagram is shown in Figure A-5 and the corresponding aeroelastic damping diagram is presented in Figure A-6. Eigenmodes with damping percentages higher than 10% are typically considered highly damped. Around 10% is medium damping and below 5% is considered low damping. Furthermore, it must be noted that there are no tower modes present in the diagrams. This is due to the use of a stiff tower resulting in a very high resonance frequency for the tower modes making them irrelevant. The eigenmodes that are likely to cause resonance issues are those that are poorly damped and cross with a low multiple of the rotor speed, i.e. 1P, 3P and 6P. The higher the multiple of the rotor speed, the less likely it is to generate resonance issues. The one mode that forms a real threat is the first backwards whirling edgewise blade mode which crosses the 3P line at approximately 8.7 m/s, see Figure A-5, and has low damping, see Figure A-6. The only method to avoid this crossing is by increasing the edgewise stiffness of the blade by adjusting the design of the blade. This is only truly necessary when the simulations in turbulent wind indicate the presence of resonance, indicated by the presence of an outlier in the edgewise blade loads around a wind speed of 8.7 m/s. As the current blade design has already been manufactured and tested it is likely that there were no occurrences of resonance. To verify this the new HAWC2 model was analysed with turbulent wind simulations. Alternatively, if resonance becomes an issue, an alternative method to avoid it is to adjust the controller in such a way that it prevents the turbine from operating at a certain rotor speed at the wind speed that poses the risk of resonance.

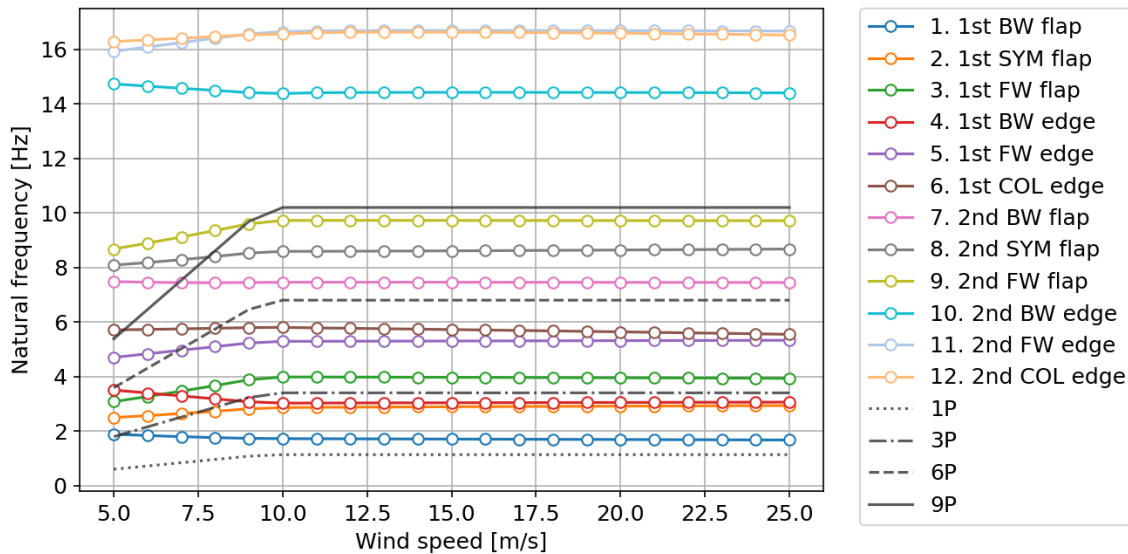


Figure A-5: Aeroelastic campbell diagram of new stable HAWC2 model of the DTU 12.6 m blade.

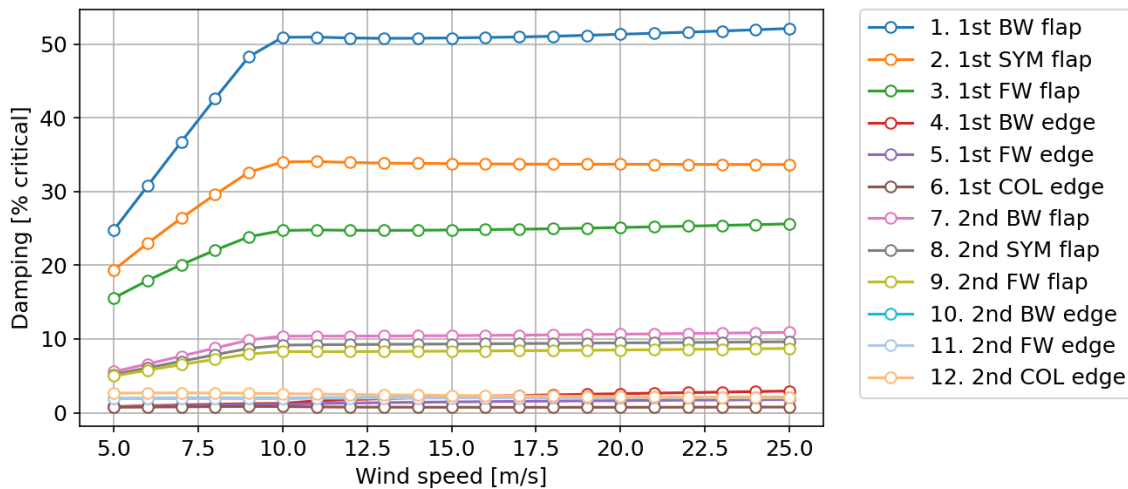


Figure A-6: Aeroelastic damping diagram of new stable HAWC2 model of the DTU 12.6 m blade.

The next phase is to run the new HAWC2 model with a turbulent wind to verify the turbine's behaviour. This is done by running the DLC1.1 simulations which are then processed to obtain statistical data, visualised in Figure A-7 to Figure A-9.

For the turbulent wind simulation it must be noted that the original resolution of the turbulence box was $8192 \times 32 \times 32$ points (longitudinal, lateral and vertical, respectively). For the final model the turbulence resolution in the longitudinal direction was reduced to 1024 to speed up the simulations. An article by Jamie Liew et al. [77] investigated the required turbulence resolution for convergence in a 10 minute simulation on one turbine for the DTU 10MW reference turbine. Analysing the results in the article it was concluded that the reduced turbulence box can still provide sufficiently accurate results while increasing simulation efficiency. It must be noted that this turbulence box is not the best option for high accuracy results. However, the goal in this project is to perform a relative comparison between two designs. Therefore, the chosen turbulence box is sufficient as long as the same settings are used for both design evaluations.

The resulting statistical data for DLC1.1 immediately showed a clear outlier in the data at a wind speed of 16 m/s which is unexpected. This was especially clear in the tower clearance in Figure A-7 as well as the thrust in Figure A-8. The effect of the outlier is also visible in the absolute maximum out-of-plane blade root moment, see Figure A-9, which corresponds to the simulation that produces the outlier in the tower clearance. This simulation is the one with a wind speed of 16 m/s at a yaw angle of 10 degrees and seed number 1605.

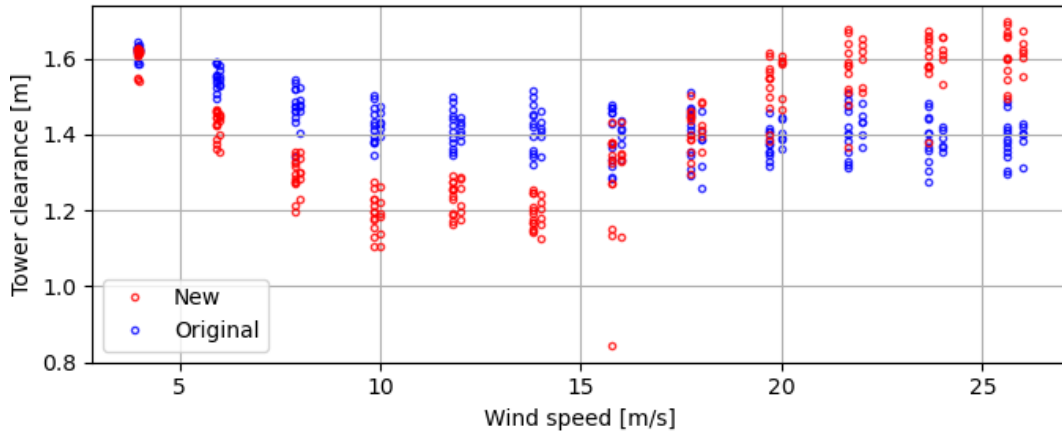


Figure A-7: Minimum tower clearance comparison between new and original HAWC2 model for the DTU 12.6 m blade in DLC1.1.

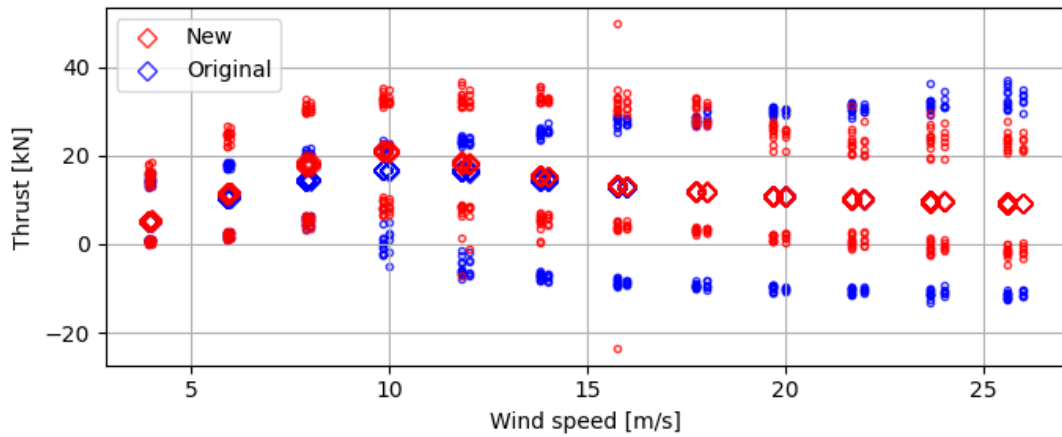


Figure A-8: Aerodynamic thrust maxima, minima and mean comparison between new and original HAWC2 model for the DTU 12.6 m blade in DLC 1.1

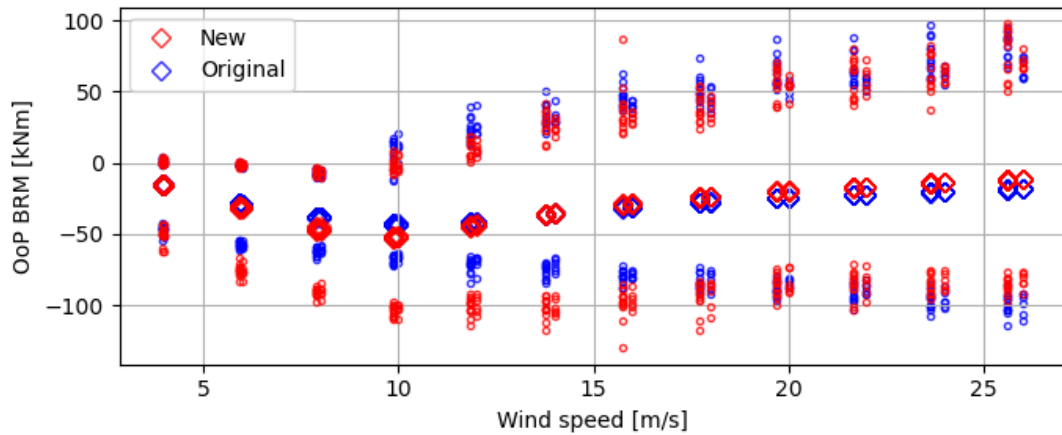


Figure A-9: Out of plane blade root moment maxima, minima and mean comparison between new and original HAWC2 model for the DTU 12.6 m blade in DLC 1.1

The time series result corresponding to the simulation that produces the outlier in the tower clearance is analysed in detail to evaluate the origin of this unexpected behaviour. The time series outputs of the wind speed, pitch angle, rotor speed, electrical power and generator torque are presented in Figure A-10. The results show clear unstable behaviour around 400 seconds. This region of the time series is zoomed in on and presented in Figure A-11. The instability starts after 390 seconds and corresponds with the wind speed increasing from below to above the rated wind speed of 9.475 m/s. This indicates that there is likely something going wrong in the controller when it needs to switch from torque control (below rated) to pitch control (above rated). Alternatively, the unstable behaviour can be a numerical issue. The analysed turbine is a relatively small system that comes with higher frequencies. It can be that the time step of 0.005 s is too large to capture all turbine behaviour. The simulation was rerun using a time step of 0.0005 s, however, the unstable behaviour was still present. Hence, the issue is likely with the controller and needs further investigation.

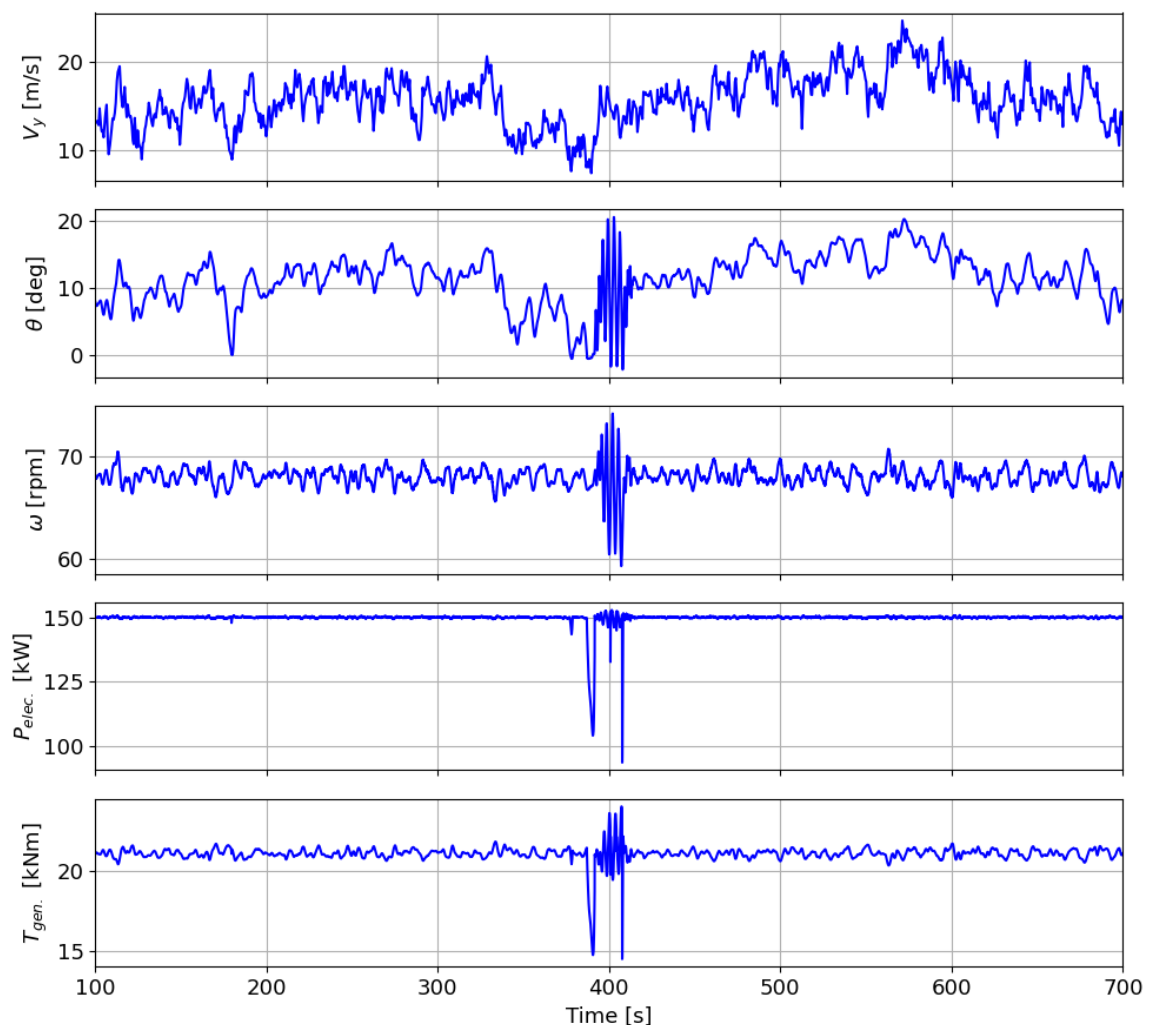


Figure A-10: Time series outputs for original simulation dlc12_wsp16_wdir010_s16005.htc for the DTU 12.6 m blade. Showing from top to bottom the wind speed, pitch angle, rotor speed, electrical power and generator torque.

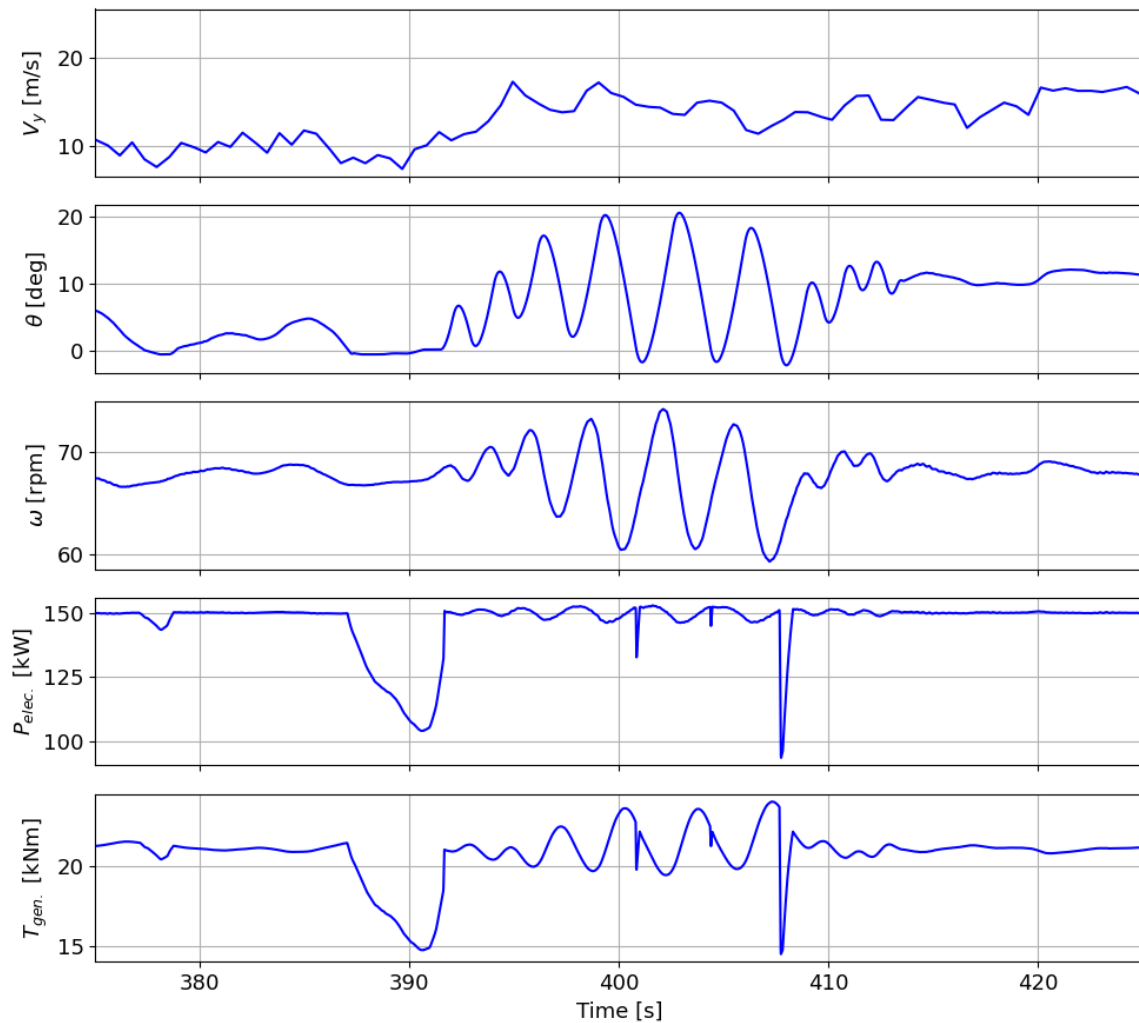


Figure A-11: Close-up of time series outputs for original simulation dlc12_wsp16_wdir010_s16005.htc for the DTU 12.6 m blade. Showing from top to bottom the wind speed, pitch angle, rotor speed, electrical power and generator torque.

Besides the controller tuning parameters in Table A-2 there are many other parameters that make up the design of the turbine controller. So far, these have been kept equal to the values in the original received model. These will now be looked into to identify possible solutions for the unstable behaviour. There are two sets of constants that have an impact on the behaviour of the controller when a switch between control regions is required. These are the proportional and integral power error gains (constants 19 and 20), the time for the maximum torque rate (constant 33) and the upper angle above the lowest minimum pitch angle for switching (constant 34). When constant 34 is equal to the minimum pitch angle specified by constant 5, it means there is a hard switch between the partial and full load region. As the issue seems to be with the switching of regions the first attempts were put into trying different combinations for parameter 34. The original model has parameter 34 equal to 0.5 The parameter 34 was set to 1.5 in the reference article as well as in the PR0011 model found on the cluster, a softer switch. This setting was tested first and did show an

improvement in the response but still not stable, see Figure A-12. Next, it was tested if a slower torque rate could further improve the results. Hence the following test set parameters 33 and 34 both equal to 1.5. Figure A-12 shows that the response is better than the original response but worse than the previous attempt. This means that a slower torque rate did not improve the results of the previous attempt. Hereafter, a different set of parameters was chosen to create an even softer switch with a more shallow slope by increasing parameter 34 to 3.0. Additionally the maximum torque rate is increased slightly by setting parameter 33 equal to 1.0. This combination of parameters resulted in an almost fully stable output, see Figure A-12. Only a small irregularity remains in the pitch angle between 390 and 395 seconds.

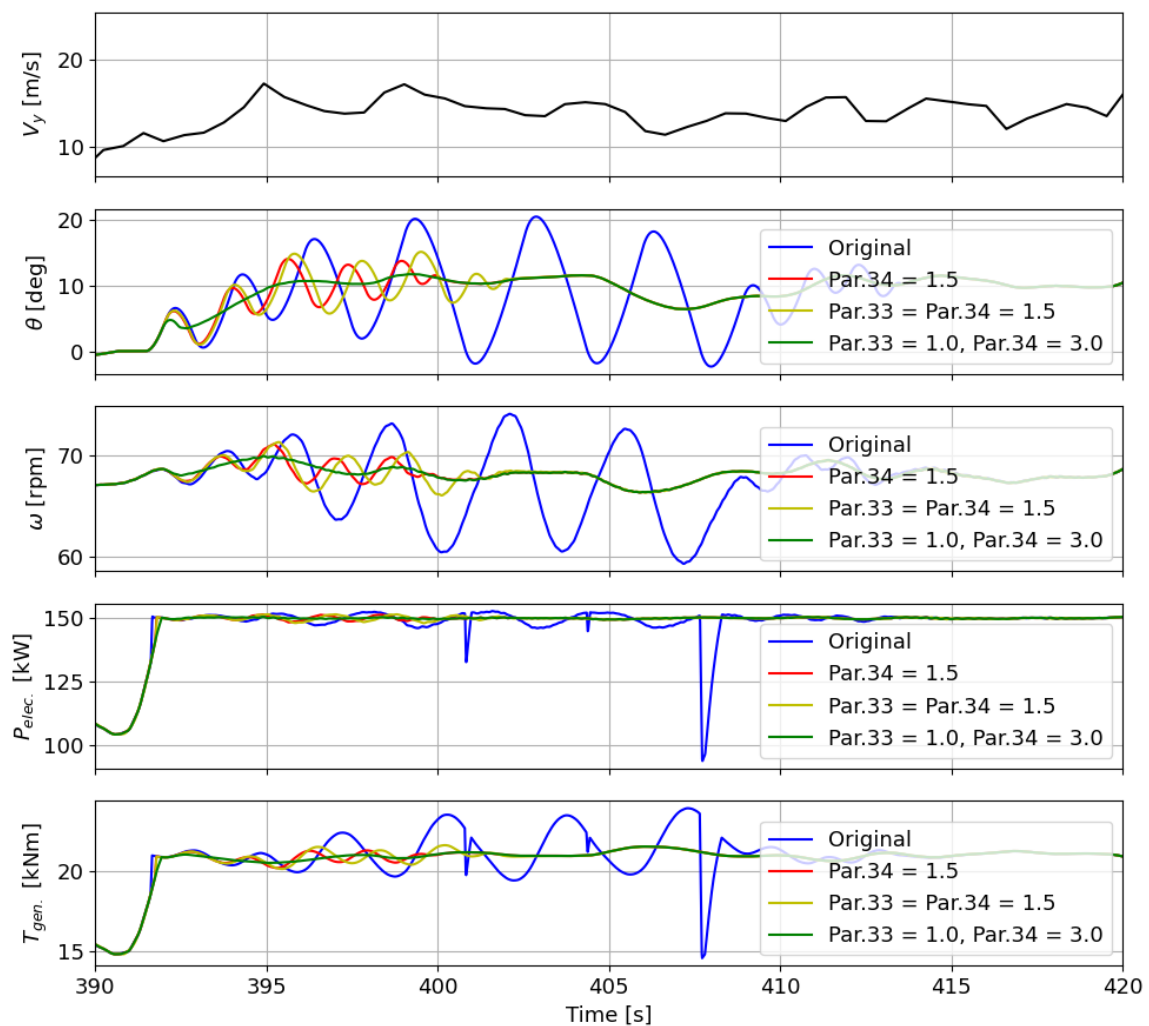


Figure A-12: Close-up of time series outputs for dlc12_wsp16_wdir010_s16005.htc for the DTU 12.6m blade with variations in controller parameters 33 and 34. Showing from top to bottom the wind speed, pitch angle, rotor speed, electrical power and generator torque.

The effect of parameters 19 and 20 is difficult to predict and was thus also analysed to see if changing these parameters could further improve the results. For these tests the parameters

33 and 34 were kept equal to the original values of 0.5. In the model file of the original model there were a few different sets suggested in the comments for parameters 19 and 20. These were all tested to see if one of these would result in a stable model, see Figure A-13. The original combination set parameter 19 equal to $3e-6$ and parameter 20 equal to $6e-6$. The first new combination of setting both parameters equal to $4e-6$ (based on the PR0011 model) resulted in an even more unstable output from 390 seconds and on-wards, the outputs do not stabilise at all. The combination of parameter 19 equal to $6e-6$ and parameter 20 equal to $8e-4$ (no origin mentioned) showed even worse results with instabilities throughout the full duration of the simulation. However, the combination of parameter 19 equal to $2e-6$ and parameter 20 equal to $4e-6$ did show an improvement compared to the original model. This combination originated from the model used in the Blatigue project from DTU. However, there is still some oscillation present in the region between 390 and 400 seconds.

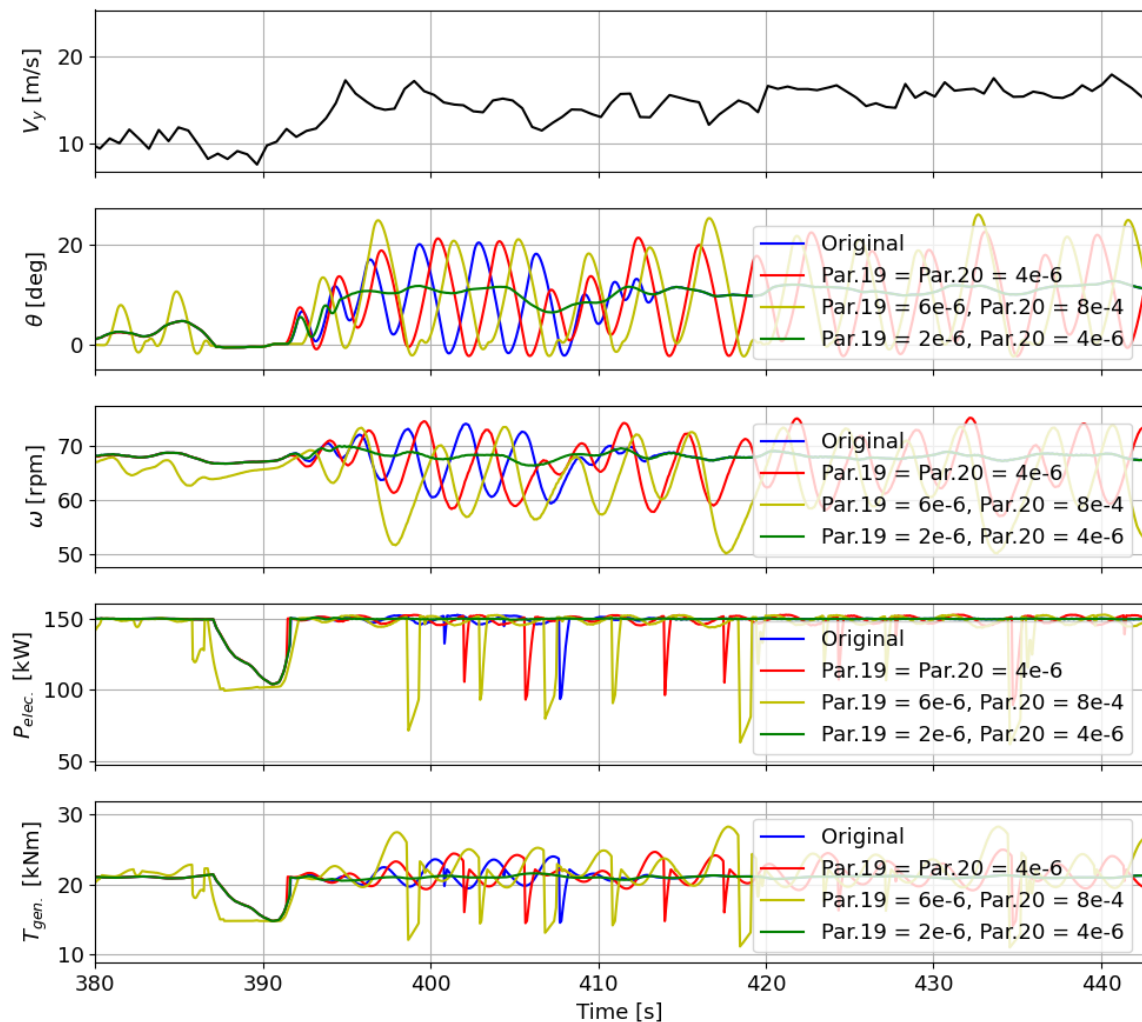


Figure A-13: Close-up of time series outputs for dlc12_wsp16_wdir010_s16005.htc for the DTU 12.6 m blade with variations in controller parameters 19 and 20. Showing from top to bottom the wind speed, pitch angle, rotor speed, electrical power and generator torque.

As the test with different combinations of parameters 19 and 20 all used different values for both parameters compared to the original model it is difficult to isolate the effect of each individual parameter. It was thus decided to test the individual parameters as the previous test did show that these two parameters significantly impact the controller behaviour in the region of interest. The original value of parameter 19 was set equal to $3e-6$. The parameter was reduced to $2e-6$ as well as increased to $4e-6$ to see the effect of increasing/decreasing this parameter. The results in Figure A-14 show that decreasing the value improved the results significantly while increasing the value worsened the results. The initial value of parameter 20 was set to $6e-6$ and is now tested for a lower value of $4e-6$ as well as a higher value of $8e-6$ to see the effect on increasing/decreasing this parameter. The results in Figure A-15 show that increasing the value improved the results while decreasing the value significantly worsened the results, which is opposite of what was seen for parameter 19.

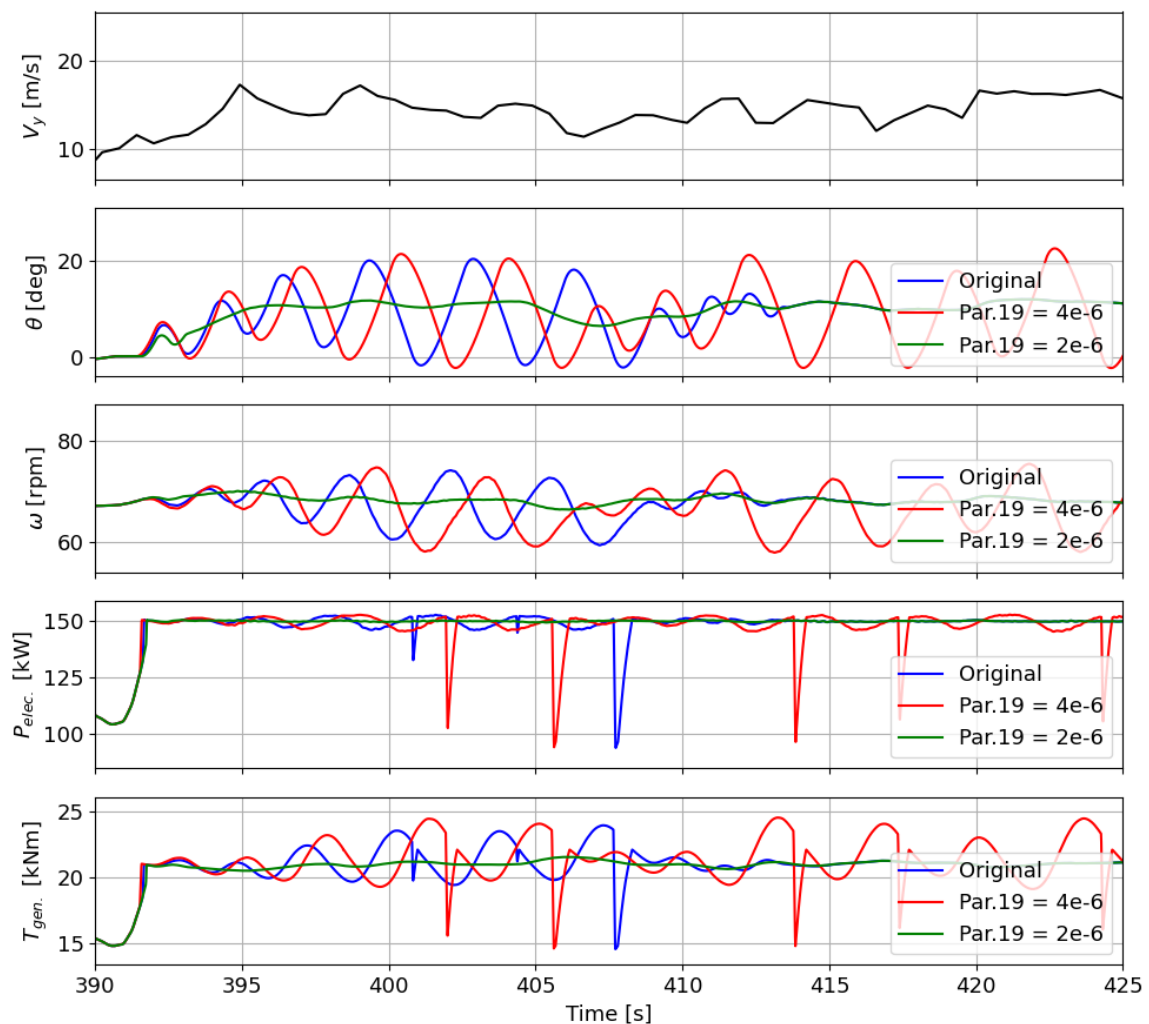


Figure A-14: Close-up of time series outputs for dlc12_wsp16_wdir010_s16005.htc for the DTU 12.6 m blade with variations in controller parameter 19. Showing from top to bottom the wind speed, pitch angle, rotor speed, electrical power and generator torque.

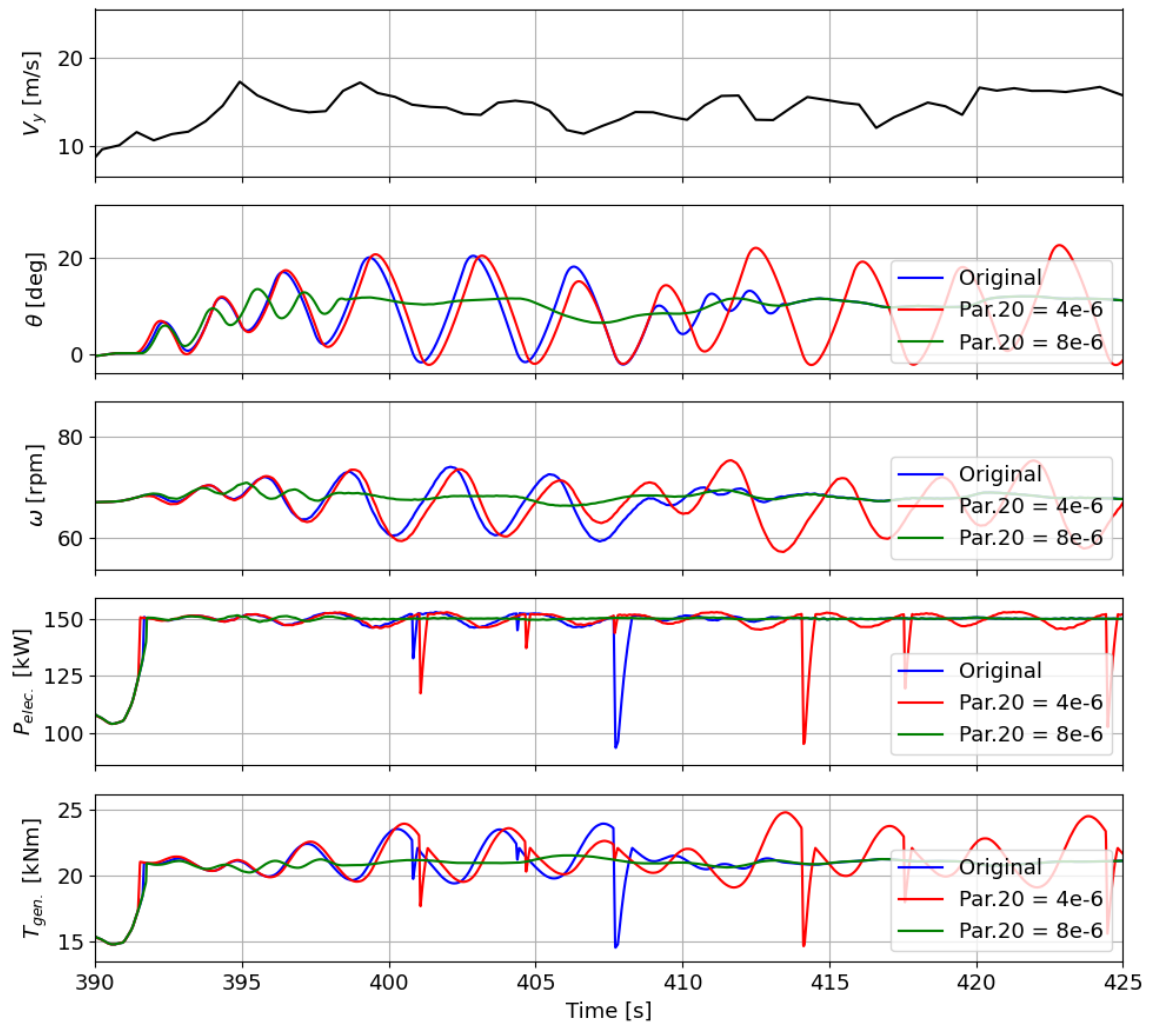


Figure A-15: Close-up of time series outputs for dlc12_wsp16_wdir010_s16005.htc for the DTU 12.6 m blade with variations in controller parameter 20. Showing from top to bottom the wind speed, pitch angle, rotor speed, electrical power and generator torque.

The information from the tests of the individual parameters 19 and 20 were combined into a new set of parameters. Parameter 19 was decreased to $1e-6$ and parameter 20 was increased to $9e-6$, the extremes while keeping the same order of magnitude. These results are showcased in Figure A-16 alongside the results from the best combination of parameters 33+34. The new combination of parameters 19 and 20 show very stable results, there is only a small irregularity in generator torque and electrical power between 380 and 385 seconds. Furthermore, the new combination of parameters 19 and 20 only is slightly better than the new combination of parameters 33 and 34 only, see behaviour between 390 and 395 seconds. To see if the results can be further improved, the best combination of parameters 19 and 20 were combined with that of parameters 33 and 34. This means that parameters 19 and 20 were set to $1e-6$ and $9e-6$ respectively, while parameters 33 and 34 are set to 1.0 and 3.0 respectively. The results in Figure A-16 show that the irregularity between 380 and 385 seconds is now also removed and the final resulting model is fully stable. However, this small irregularity in the other two

model versions is actually the controller responding more accurately to the dip in wind speed. It is therefore decided that the final model will be the model where only parameters 19 and 20 are adapted (to 1.0×10^{-6} and 9.0×10^{-6} respectively) and parameters 33 and 34 kept equal to the original model values of 0.5 (changes as little as possible to the original model).

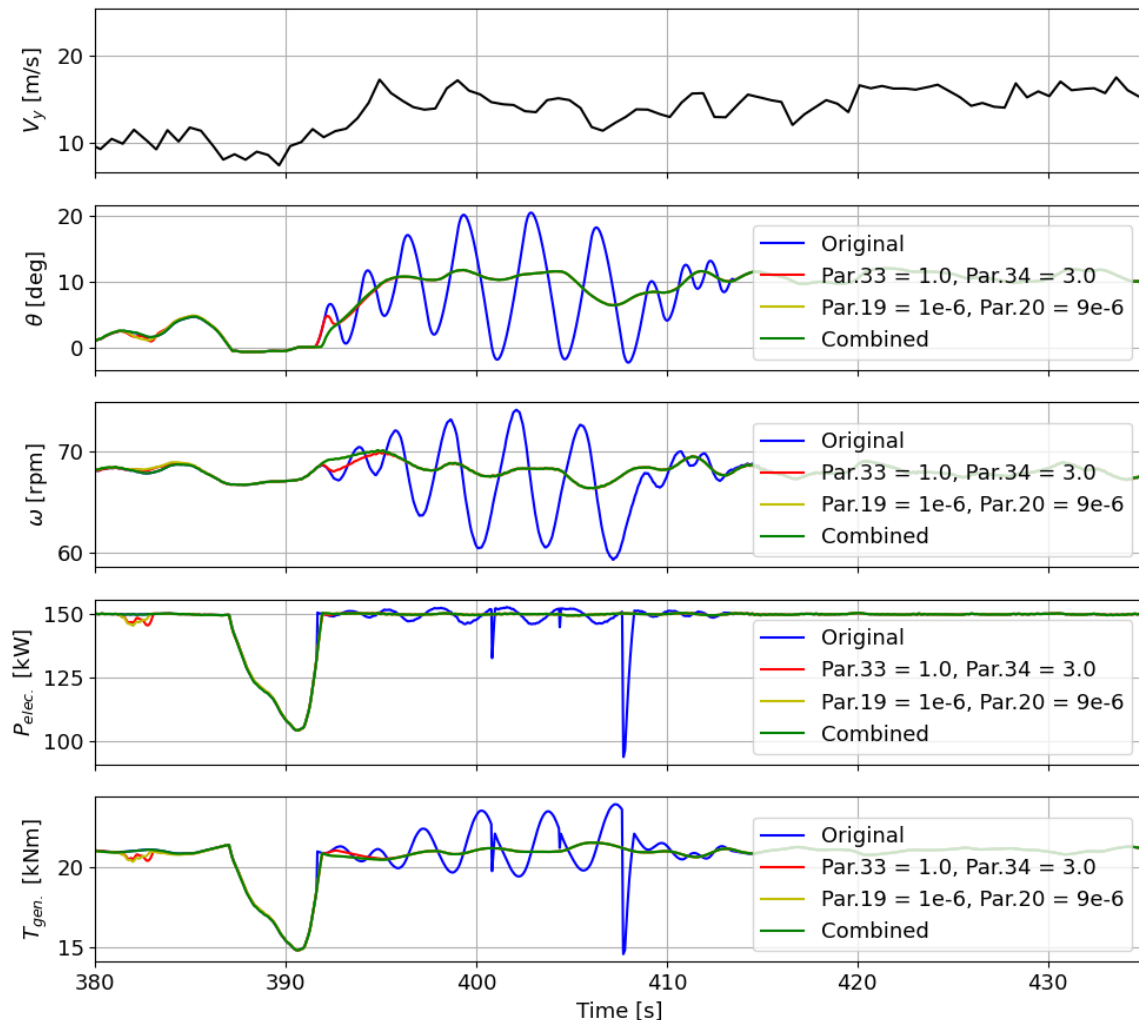


Figure A-16: Close-up of time series outputs for dlc12_wsp16_wdir010_s16005.htc for the DTU 12.6 m blade with variations in controller parameters 19, 20, 33 and 34. Showing from top to bottom the wind speed, pitch angle, rotor speed, electrical power and generator torque.

To verify that the new model is indeed fully stable the DLC1.1 was run again. The results were checked for outliers which were now not present. To further confirm that the model functions properly the time series of three simulations of the DLC1.1 were checked; for a low wind speed below rated, for a wind speed around rated and for a wind speed close to the cut-out wind speed. All showed stable results and the new HAWC2 model is finalised. The DLC1.1 results are shown and discussed in the following section. The obtained new design loads from DLC1.3 are presented in Section 6-1.

A-1 Final HAWC2 model results - DLC1.1 statistical data

The operational data results for DLC1.1 for the original and new model are presented in Figure A-17 to Figure A-21 to analyse the turbines behaviour. The small dots represent the minima and maxima and the diamonds represent the mean values. Each graph will be discussed whereby the behaviour is compared to what is typically expected from a wind turbine.

The mean pitch values in Figure A-17 should in theory match the pitch curve from the step wind simulation in Figure A-1. This holds for both models. However, the extremes are significantly larger for the original model which even reach an unrealistic value of 50 degrees. This is caused by the controller instabilities identified earlier causing extreme pitch variations. The extreme pitch values for the new model are still within an acceptable range.

The rated rotor speed for the new model is higher than for the original model which is confirmed in Figure A-18. In the above rated region the extremes in the original model are significantly larger than for the new model. This can be related to the extremes in pitch angles. The relation between power and torque is given through the rotor speed with the equation $P = \omega T$. Above rated the power is kept constant. If the pitch then increases drastically the blades will experience stall which reduces the torque which then needs to be compensated by a higher rotor speed. Smaller variations in pitch will thus also require less variation in the rotor speed to maintain constant power which is the case for the new model.

The electrical power should increase up to rated power and then stay constant. For the original model the controller was designed for constant torque which introduces some variation in the electrical power. The new model was designed for constant power and this is indeed visible in Figure A-19 confirming that the controller works properly. Running the turbine for constant power also means that the maxima for the power above rated will coincide with the mean values which is indeed observed for the new turbine. The maxima for the original model will deviate from the mean values as the turbine runs for constant torque. However, the extremes deviate significantly from the mean, especially the minimum values. This is undesirable as it means that less power is generated making the turbine less profitable.

As the original model runs for constant torque one should see the extremes coincide with the mean values in Figure A-20. However, this is not the case, especially for the minima which are extremely low. This is another indication that the controller of the original model does not function properly. The new design runs for constant power and some variation are expected in the above rated region which is indeed observed. The variation is relatively small which is in line with the variation present in the rotor speed that relates the generator torque to the constant power. It is important to keep in mind what the generator torque curve looks like as the turbine loads in the direction perpendicular to the wind generally follow the same shape.

Finally, the thrust curves are presented in Figure A-21. The thrust should increase with increasing wind speed up to rated velocity after which it should reduce again to maintain rated power. This trend is indeed visible for the new design, however the maxima for the original design does not follow this trend which is another indication that the original model does not function as it should. Furthermore, the maximum thrust reached around rated wind speed is higher for the new model due to the higher rated rotor speed. It is important to keep in mind what the thrust curve looks like as the turbine loads in the direction of the wind

relate to the thrust.

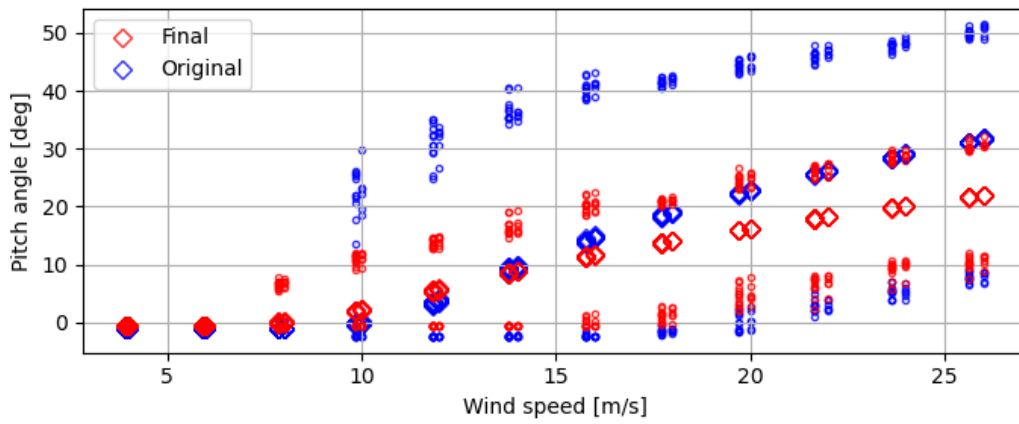


Figure A-17: Pitch angle maxima, minima and mean comparison between final and original HAWC2 model of the DTU 12.6 m blade in DLC1.1.

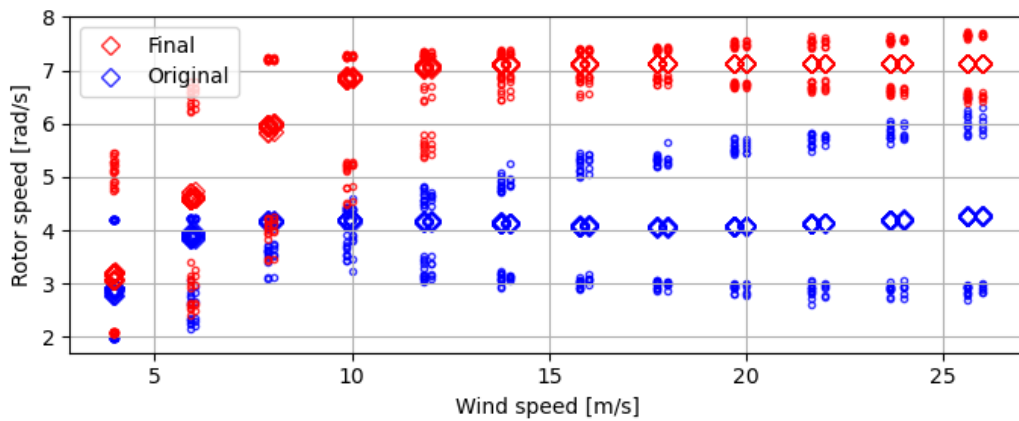


Figure A-18: Rotor speed maxima, minima and mean comparison between final and original HAWC2 model of the DTU 12.6 m blade in DLC1.1.

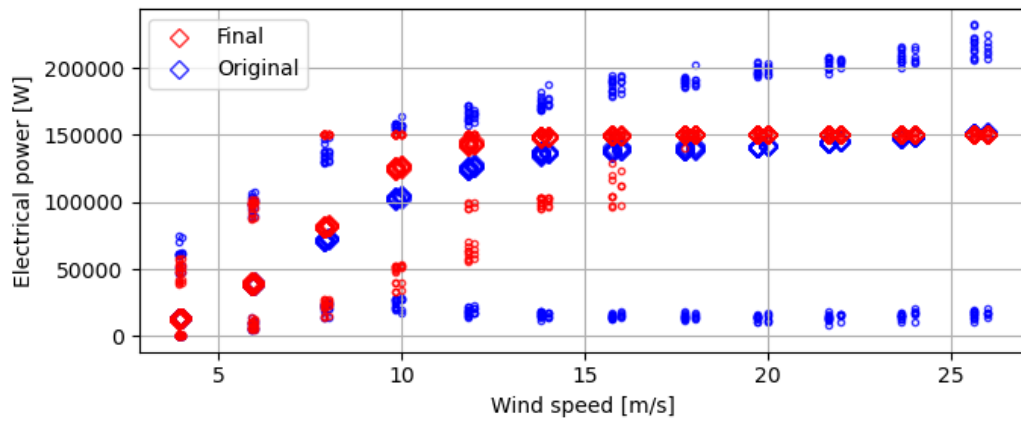


Figure A-19: Electrical power maxima, minima and mean comparison between final and original HAWC2 model of the DTU 12.6 m blade in DLC1.1.

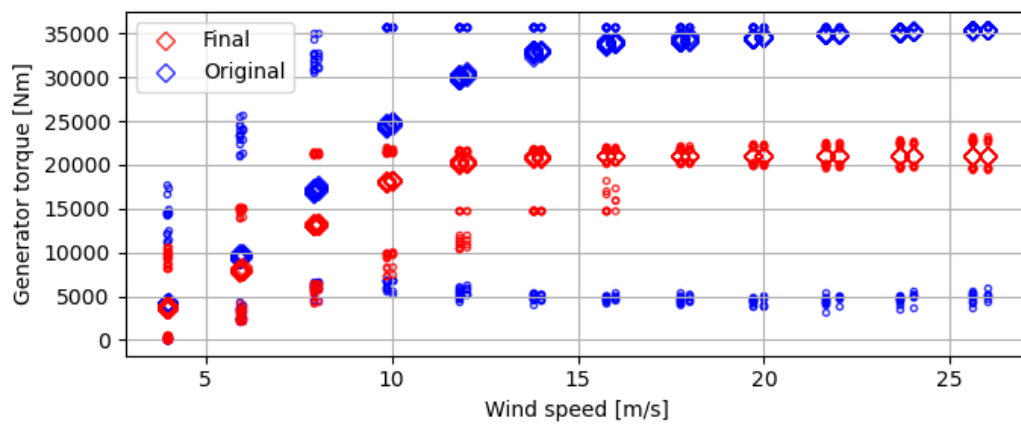


Figure A-20: Generator torque maxima, minima and mean comparison between final and original HAWC2 model of the DTU 12.6 m blade in DLC1.1.

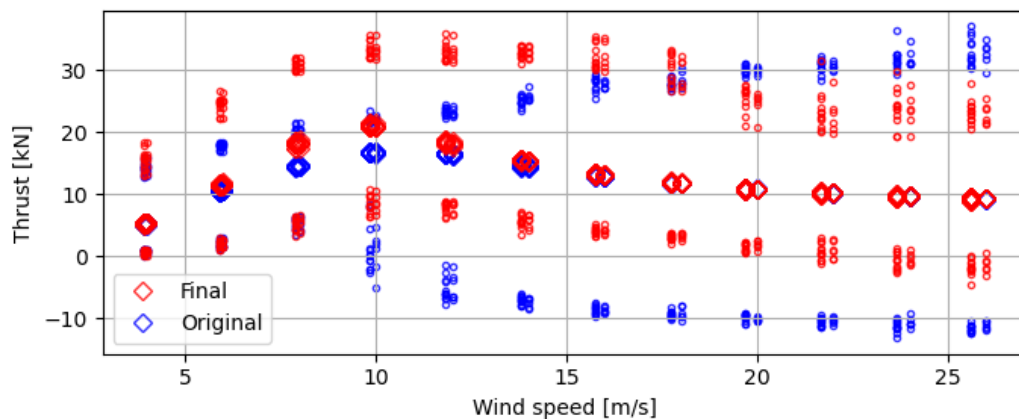


Figure A-21: Aerodynamic thrust maxima, minima and mean comparison between final and original HAWC2 model of the DTU 12.6 m blade in DLC1.1.

The different extreme turbine load results for DLC1.1 for the original and new model are presented in Figure A-22 to Figure A-29 where the small dots represent the minima and maxima and the diamonds represent the mean values. Each graph will be discussed whereby the behaviour is compared to what is typically expected from a wind turbine.

The tower-base Fore-Aft (FA) moment follows the thrust curve which is indeed observed for the new model in Figure A-22. The mean values of the original model follow the thrust as well, however, the maximum values keep increasing above rated opposite of what is expected. In fact, the tower base FA moment does follow the thrust but the maxima in the thrust curve of the original model also continue increasing above rated. Furthermore, the difference between the minima and maxima is smaller for the new model compared to the original which is beneficial for the fatigue loads in the tower.

The tower-base Side-Side (SS) moment is induced by wind shear and asymmetric loading. This means that for increasing turbulence levels, which increase with increasing wind speed, the tower-base SS moments increase as well. The results in Figure A-23 are in line with this expectation for both models where the difference between the minima and maxima keeps increasing for increasing wind speeds.

The yaw-bearing pitch moment follows the thrust curve in principle which is indeed seen in the mean value trends in Figure A-24. However, the loads seem to increase again once the wind speed reaches above 15 m/s. Moreover, the difference between the maxima and minima grows with increasing wind speed. This is due to the influence of wind shear on this loading which depends on the turbulence levels. The turbulence levels increase for increasing wind speeds causing the trends observed.

The yaw-bearing roll moment should follow the shape of the torque curve which is indeed observed in Figure A-25. The loads are significantly lower for the new model compared to the original. This is due to the higher rated rotor speed. An increase in rotor speed means that the mass of the blades spends less time in the "heavy" position which reduces the load that is built up in that position. Furthermore, the extreme minima of the original model are undesirable and a result of the poor controller design.

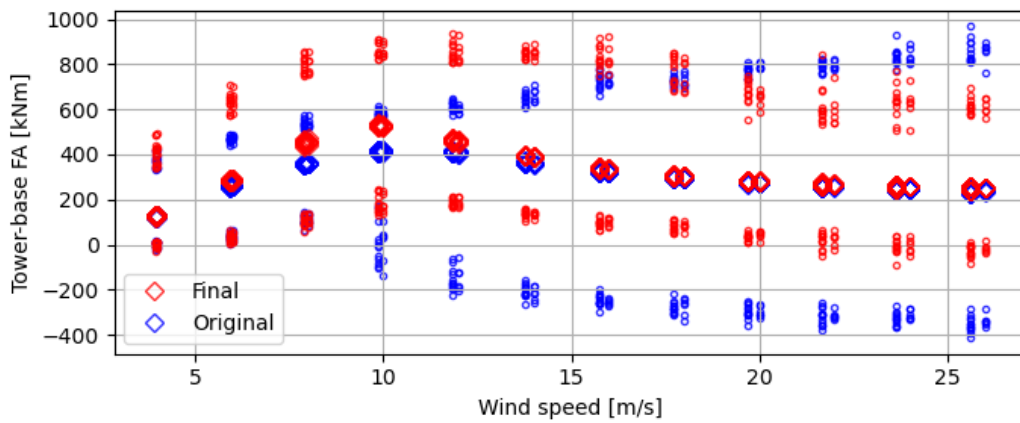


Figure A-22: Tower base Fore-Aft moment maxima, minima and mean comparison between final and original HAWC2 model of the DTU 12.6 m blade in DLC1.1.

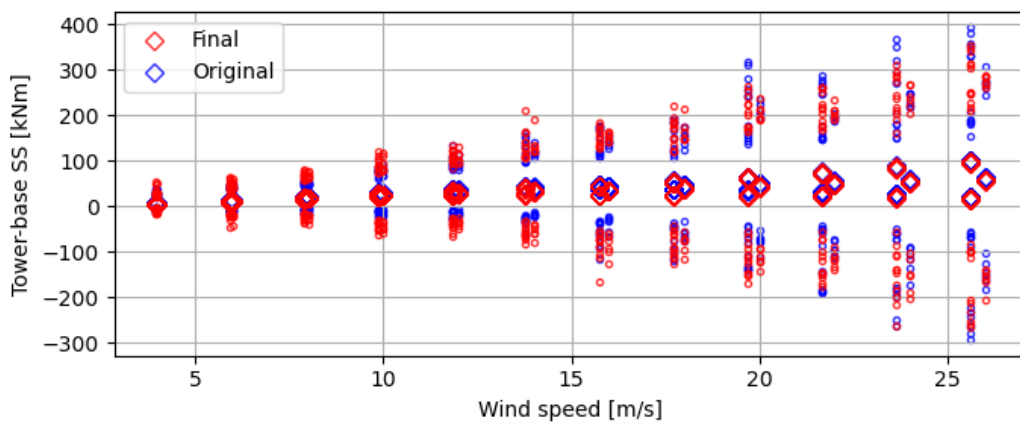


Figure A-23: Tower base Side-Side moment maxima, minima and mean comparison between final and original HAWC2 model of the DTU 12.6 m blade in DLC1.1.

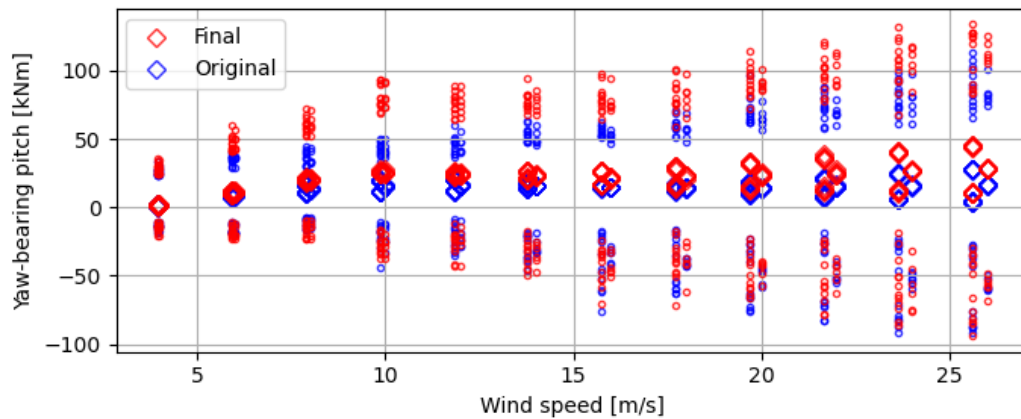


Figure A-24: Yaw bearing pitch moment maxima, minima and mean comparison between final and original HAWC2 model of the DTU 12.6 m blade in DLC1.1.

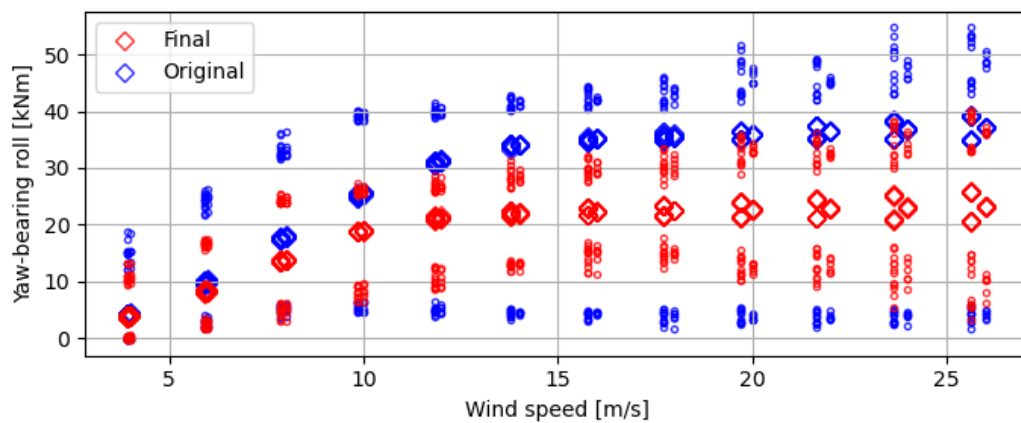


Figure A-25: Yaw bearing roll moment maxima, minima and mean comparison between final and original HAWC2 model of the DTU 12.6 m blade in DLC1.1.

The shaft torsion moment is caused by the aerodynamic moment generated by the wind over the blades and by the generator torque controller. The curve should thus follow the shape of the torque curve which is indeed observed in Figure A-26 but flipped up side down due to the sign convention. Furthermore, the rated rotor speed influences the height of this load as well through $P = \omega T$. As the new model has a higher rotor speed the shaft torsion is reduced which is indeed observed. The increasing difference between the minima and maxima of the original model are caused by the extreme pitch extrusions which influence the aerodynamic moment. These large fluctuations are undesirable for fatigue life.

The Out-of-Plane Blade Root Moment (OoP BRM) should follow the thrust curve which is indeed observed in Figure A-27 where the flapwise BRM is plotted for both models. It is important to note that the flapwise BRM is measured in the coordinate system of the blade that pitches when the blade pitches, while the OoP BRM is measured in the coordinate system of the hub and does not rotate when the blade pitches. The most negative flapwise BRM for

the new model is higher than for the original model as the maximum thrust is higher with the higher rotor speed. Besides the thrust force, the wind shear also influences the flapwise BRM which explains the increasing difference between the minima and maxima for increasing wind speeds, which have increasing turbulence levels.

The In-Plan Blade Root Moment (IP BRM) is also influenced by the aerodynamic moment as that moment makes the blades turn which then generates the in-plane loads. This is why the IP BRM mean curves are more similar to the shape of the torque curve. However, the edgewise BRM is measured, see Figure A-28, where the torque does not always act on the same direction due to the pitching of the blade. This is why the edgewise BRM starts decreasing slightly above the rated wind speed. Furthermore, variations in the edgewise load are present due to varying gravity loads and the operation of the torque controller. The edgewise BRM of the new model are slightly lower than that of the original model which can be explained by the higher rotor speed that reduces the torque. A higher rotor speed also means the blades spend less time in the "heavy" position preventing a high build up of in-plane gravitational loads.

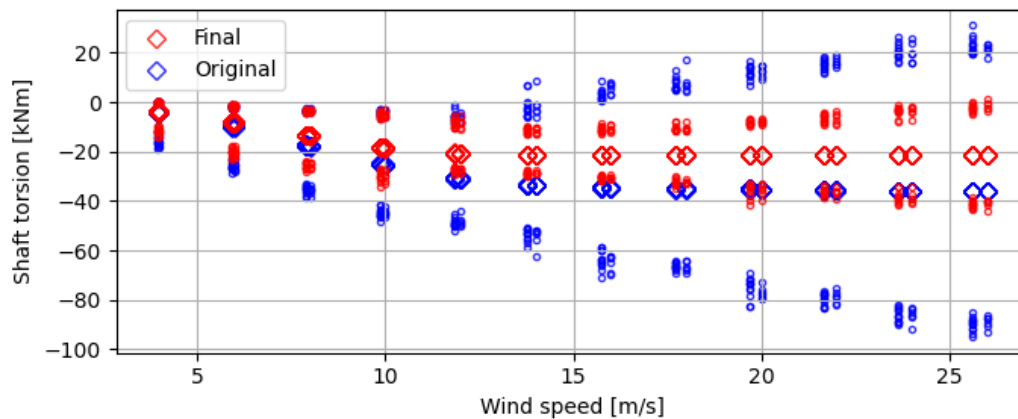


Figure A-26: Shaft torsion moment maxima, minima and mean comparison between final and original HAWC2 model of the DTU 12.6 m blade in DLC1.1.

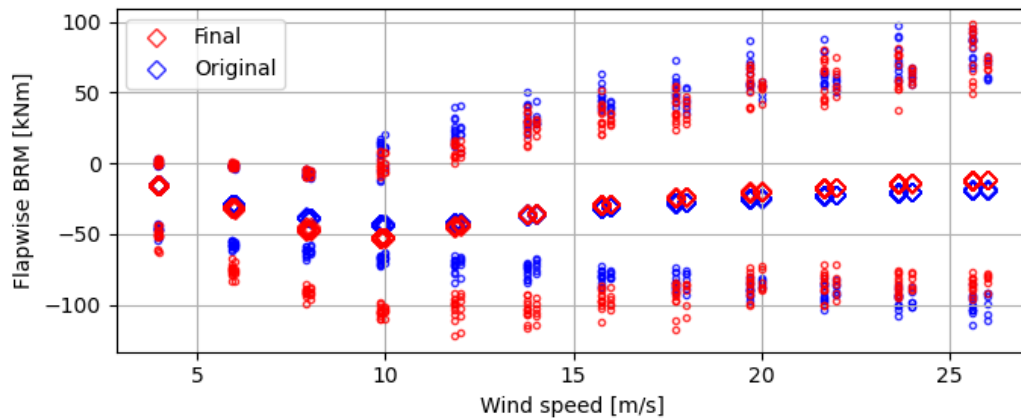


Figure A-27: Flapwise blade root moment maxima, minima and mean comparison between final and original HAWC2 model of the DTU 12.6 m blade in DLC1.1.

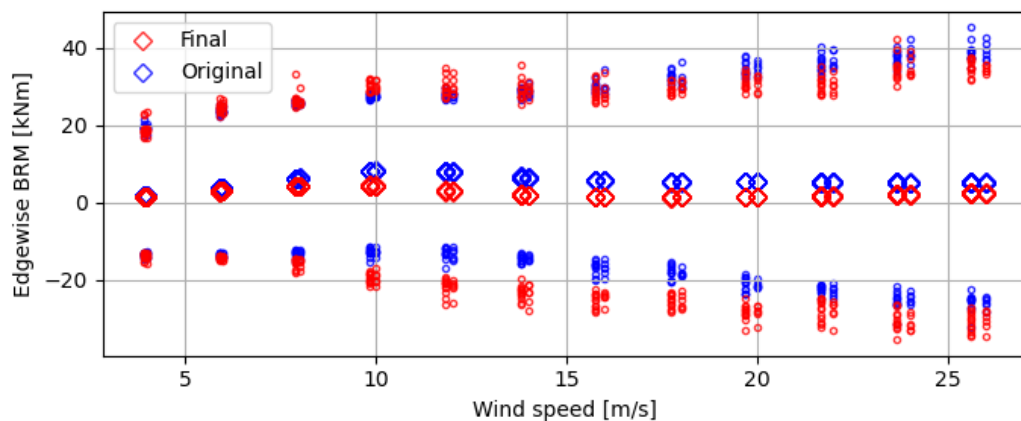


Figure A-28: Edgewise blade root moment maxima, minima and mean comparison between final and original HAWC2 model of the DTU 12.6 m blade in DLC1.1.

Finally, the minimum tower clearance is presented in Figure A-29. The tower clearance relates to the flap-wise deflection of the blades which is driven by the OoP BRM. The curve should thus follow the inverse of the thrust curve which is indeed observed for the new model. However, the original model maintains a small tower clearance for higher wind speeds which is in line with the minima trend of the OoP BRM which follows the maxima trend of the thrust curve which indeed kept increasing for the original model. Furthermore, the minimum tower clearance for the new model is significantly smaller compared to the original model due to the higher thrust force at rated wind speed due to the higher rotor speed. Fortunately, the tower clearance is still larger than the minimum tower clearance required by DNV GL [56]. They require a minimum tower clearance of 30% of the unloaded tower clearance. The unloaded tower clearance of the current model is 2.26 m of which 30% equals 0.68 m which is still significantly lower than the observed minimum tower clearance in Figure A-29.

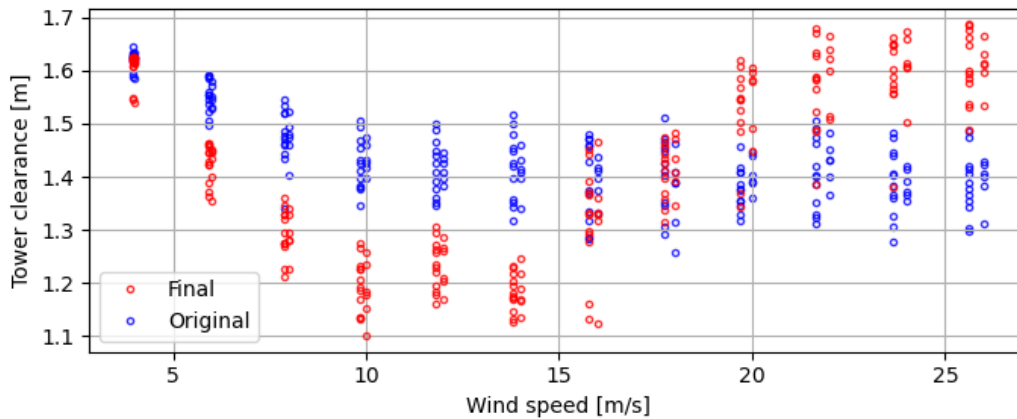


Figure A-29: Minimum tower clearance comparison between final and original HAWC2 model of the DTU 12.6 m blade in DLC1.1.

From the DLC1.3 load simulations the new maximum blade loads can be extracted and they are compared with the original model loads as well as the loads in the received Abaqus, see Figure 3-3. It can be observed that the edgewise loads are lower for the new model compared to the loads in Abaqus. Furthermore, the flap-wise loading away from the tower (STP) is very similar to the current load in Abaqus. However, the flap-wise loading towards the tower is approximately 15% higher than the load in Abaqus which could pose a challenge for the redesign. This load is related to the higher thrust forces in the new HAWC2 model. This could be reduced through peak shaving but that turned out to be insufficient. The alternative is to reduce the rated rotor speed to reduce the maximum thrust. An attempt was made to reduce the rotor speed to 55 rpm, midway between the original and new HAWC2 model. However, new instabilities arose and it turned out too complicated to resolve these instabilities through adapting the controller.

A-1-1 AEP comparison

Now that the full turbine behaviour of the new HAWC2 model has been analysed and determined to be realistic, the next step is to compare the Annual Energy Production (AEP) of the two different models. It was already observed that the electrical power was more often at rated for the new model compared to the original model. This suggests that the AEP for the new model will be higher as well which indeed is the case. The AEP has increased from 738.4 kWh to 822.1 kWh which is an added bonus.

Micro-Mechanical Model for Fibre Reinforced Composite Lamina

To predict the mechanical properties of a composite from the properties of its constituents, a micro-mechanical model can be used. The micro-mechanical model and its equations used in the current research are elaborated upon in this section.

The micro-mechanical model needs the volumetric composition as input. The volumetric composition is the volume fraction of fibres, matrix and porosity. Generally, the fibre volume fraction is a given input. If the fibre volume fraction V_f is given the porosity volume fraction can be found with the following equation [43]:

$$V_p = \frac{\alpha_{pf(1)} + \alpha_{pf(2)} + \alpha_{pf(3)} - \alpha_{pm(1)}}{1 + \alpha_{pm(1)}} V_f + \frac{\alpha_{pm(1)}}{1 + \alpha_{pm(1)}} \quad (\text{B-1})$$

Where $\alpha_{pm(1)}$ is the matrix porosity constant related to voids in pure matrix regions. The α_{pf} values are the fibre porosity constants where the first relates to voids inside the fibres (fibre porosity), the second relates to voids at the interface between a fibre and the matrix (interface porosity), and the third relates to voids due to poor impregnation of the fibre bundles with the matrix (impregnation porosity). The different porosity types are illustrated in Figure B-1. The given equation is only valid when the fibre volume fraction is lower than the maximum fibre volume fraction, meaning no structural porosity (dry spots).

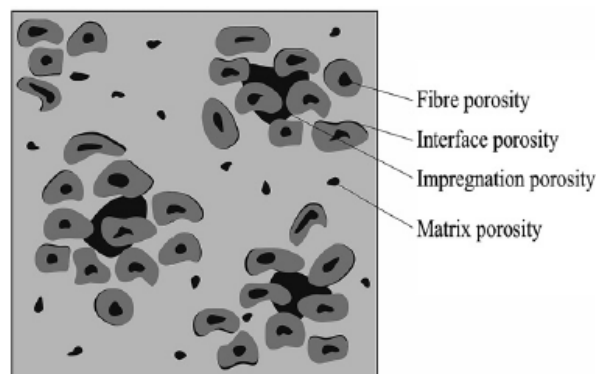


Figure B-1: Schematic illustration of the four different porosity sub-components that have been identified from composite cross-sections [43].

Once the fibre and porosity volume fractions are known the matrix volume fraction can be found with $V_m = 1 - V_f - V_p$. If instead of the fibre volume fraction the fibre weight fraction is provided, the fibre volume fraction can be calculated with [43]:

$$V_f = \frac{W_f \rho_m}{W_f \rho_m (1 + \alpha_{pf}) + (1 - W_f) \rho_f (1 + \alpha_{pm})} \quad (\text{B-2})$$

Where α_{pf} is the fibre porosity constant which is a summation of three sub-components related to the fibre porosity, interface porosity and impregnation porosity. The α_{pm} is the matrix porosity related to voids in regions of pure matrix. Similarly to the fibre volume fraction the porosity volume fraction can also be calculated from the fibre weight fraction through [43]:

$$V_p = \frac{W_f \rho_m \alpha_{pf} + (1 - W_f) \rho_f \alpha_{pm}}{W_f \rho_m (1 + \alpha_{pf}) + (1 - W_f) \rho_f (1 + \alpha_{pm})} \quad (\text{B-3})$$

With the volumetric composition known, the composite density can be calculated with [78]:

$$\rho_c = V_f \rho_f + V_m \rho_m \quad (\text{B-4})$$

Where ρ_f and ρ_m are the densities of the fibres and matrix materials.

The composite Young's modulus $E_{c,1}$ can be calculated using the combined rule of mixture for longitudinal composite stiffness [78]:

$$E_{c,1} = (\eta_o \eta_l V_f E_f + V_m E_m) (1 - V_p)^n \quad (\text{B-5})$$

Where E_f and E_m are the fibre and matrix longitudinal stiffness' respectively. Furthermore, n is the porosity efficiency exponent which is typically equal to 2 for plant fibres. It quantifies the effect of porosity giving stress concentrations in the composite. The η_o is the fibre orientation efficiency factor which equals 1 for unidirectional composites with the fibres in the loading direction. And the η_l is the fibre length efficiency factor which equals 1 for long fibres.

To calculate the transverse composite stiffness, the regular inverse rule of mixture is used [78]:

$$\frac{1}{E_{c,2}} = \frac{1}{E_{c,3}} = V_f \frac{1}{E_{f,2}} + V_m \frac{1}{E_m} \quad (\text{B-6})$$

Where $E_{f,2}$ is the transverse stiffness of the fibres. The porosity is in this case only taken into account through the slight reduction in fibre and matrix volume fractions. Furthermore, it is assumed that $E_{c,2} = E_{c,3}$.

The composite shear stiffness is calculated with the following formula found in the Blade Modelling Tool excel sheet provided by DTU. This formula was used to calculate the composite shear stiffness for the GFRC of the DTU blade:

$$G_{12} = G_{13} = G_{23} = \frac{G_m}{1 - \sqrt{V_f} \left(1 - \frac{G_m}{G_f}\right)} \quad (\text{B-7})$$

Where G_f and G_m are the shear stiffness of the fibre and matrix respectively. It is assumed that the shear stiffness is the same in all three directions.

The in-plane poisson's ratio of the composite is also given by the rule of mixture [78]:

$$\nu_{12} = \nu_{13} = V_f \nu_{12,f} + V_m \nu_{12,m} \quad (\text{B-8})$$

Where $\nu_{12,f}$ and $\nu_{12,m} = \nu_m$ (isotropic) are the poisson's ratios of the fibres and matrix. The out-of-plane poisson's ratio of the composite is calculated with the following equation which is the rewritten equation for shear stiffness of a transversely isotropic material:

$$\nu_{23} = \frac{E_{c,2}}{2G_{23,c}} - 1 \quad (\text{B-9})$$

To calculate the longitudinal tensile strength of the composite the simple strength models will be used. This model assumes no fibre strength variation, equal strain until failure, and the Hooke's law to calculate the failure strains of the matrix, $\epsilon_{mu} = \frac{\sigma_{mu}}{E_m}$, and the fibres $\epsilon_{fu} = \frac{\sigma_{fu}}{E_f}$. Where σ_{mu} and σ_{fu} are the tensile failure strengths of the matrix and the fibre materials respectively. There are multiple tensile failure types for a composite. Either the matrix is brittle and fails before the fibres do, $\epsilon_{mu} < \epsilon_{fu}$, or the fibres are brittle and fail before the matrix does, $\epsilon_{mu} > \epsilon_{fu}$. In case the matrix fails before the fibres do, the failure type can either be a single matrix crack if the fibres cannot carry the entire load alone, or multiple matrix cracking if the fibres can carry the entire load alone. In the former case the failure strain of the composite is equal to that of the matrix and the composite strength is given by [65]:

$$\sigma_{cu}^L = (1 - V_f)\sigma_{mu} + V_f \sigma'_f \quad (\text{B-10})$$

Where,

$$\sigma'_f = E_f \frac{\sigma_{mu}}{E_m} \quad (\text{B-11})$$

σ'_f is the stress carried by the fibres when the matrix fails. In the case of multiple matrix cracking the failure strain of the composite equals that of the fibres, and the strength of the composite is given by [65]:

$$\sigma_{cu}^L = V_f \sigma_{fu} \quad (\text{B-12})$$

The criterion on the fibre volume fraction for multiple matrix cracking to occur is [65]:

$$V_f > \frac{1}{\frac{\sigma_{fu}}{\sigma_{mu}} - \frac{E_f}{E_m} + 1} = V_{fc,m} \quad (\text{B-13})$$

In case the fibres are brittle and fail before the matrix does, two different failure types are possible. Again a single fracture can occur when the matrix cannot carry the load alone and

the composite failure strain will equal that of the fibres. In that case the composite strength is given by [65]:

$$\sigma_{cu}^L = (1 - V_f)\sigma'_m + V_f\sigma_{fu} \quad (\text{B-14})$$

Where,

$$\sigma'_m = E_m \frac{\sigma_{fu}}{E_f} \quad (\text{B-15})$$

σ'_m is the stress carried by the matrix when the fibres fail. Alternatively, the fibres can also fail through multiple cracking if the matrix can carry the full load alone. In that case the failure strain of the composite equals that of the matrix, and the composite strength is given by [65]:

$$\sigma_{cu}^L = (1 - V_f)\sigma_{mu} \quad (\text{B-16})$$

The criterion on the fibre volume fraction for multiple fibre cracking to occur is [65]:

$$V_f < \frac{\sigma_{mu} - \sigma'_m}{\sigma_{mu} - \sigma'_m + \sigma_{fu}} = V_{fc,f} \quad (\text{B-17})$$

The transverse tensile strength of the composite, including effect of porosity, can be calculated with the empirical equation developed by Ever J. Barbero [79]:

$$\sigma_{cu}^T = \sigma_{mu} C_v (1 - V_f^{\frac{1}{3}}) \frac{E_{c,2}}{E_m} \quad (\text{B-18})$$

Where,

$$C_v = 1 - \sqrt{\frac{4V_v}{\pi(1 - V_f)}} \quad (\text{B-19})$$

Where V_v is the void volume fraction which is assumed to equal V_p . The same strength equation can be used to calculate the transverse compression strength of the composite by replacing the tensile failure strength of the matrix by the compression failure strength σ_{mu}^c .

The composite shear strength can also be calculated using the C_v factor with the following equation [79]:

$$\tau_{cu} = \tau_{mu} C_v [1 + (V_f - \sqrt{V_f})(1 - \frac{G_m}{G_f})] \quad (\text{B-20})$$

Finally, the longitudinal compression strength of the composite can be calculate with the following equation [79]:

$$\sigma_{cu}^L = \frac{kG_m}{1 - V_f} \approx kG_{12,c} \quad (\text{B-21})$$

Where k is an empirical correction factor determined from an experimental test. The equation also ignores fibre misalignment and assumes a linear shear stress vs strain relation.

Appendix C

Classical Laminate Theory

The classical laminate theory facilitates the calculation of the global properties of a laminate composing of several lamina, with varying orientations.

The laminate theory to calculate laminate properties from ply properties starts with the compliance matrix which relates the stresses with the strains. In general, the compliance matrix of a laminate looks as follows [80]:

$$\begin{Bmatrix} \varepsilon_x \\ \varepsilon_y \\ \varepsilon_z \\ \gamma_{yz} \\ \gamma_{xz} \\ \gamma_{xy} \end{Bmatrix} = \begin{bmatrix} S_{11} & S_{12} & S_{13} & 0 & 0 & S_{16} \\ S_{12} & S_{22} & S_{23} & 0 & 0 & S_{26} \\ S_{13} & S_{23} & S_{33} & 0 & 0 & S_{36} \\ 0 & 0 & 0 & S_{44} & S_{45} & 0 \\ 0 & 0 & 0 & S_{45} & S_{55} & 0 \\ S_{16} & S_{26} & S_{36} & 0 & 0 & S_{66} \end{bmatrix} \begin{Bmatrix} \sigma_x \\ \sigma_y \\ \sigma_z \\ \tau_{yz} \\ \tau_{xz} \\ \tau_{xy} \end{Bmatrix} \quad (\text{C-1})$$

The terms that make up the compliance matrix can be calculated for each individual ply k which has an orientation angle θ by transforming the ply properties, to the laminate coordinate system. This is done with the following equations [80] where $s = \sin\theta$ and $c = \cos\theta$:

$$S_{11}^k = \frac{c^4}{E_{11}} + \left(\frac{1}{G_{12}} - \frac{2\nu_{12}}{E_{11}} \right) s^2 c^2 + \frac{s^4}{E_{22}} \quad (\text{C-2})$$

$$S_{12}^k = \left(\frac{1}{E_{11}} + \frac{1}{E_{22}} - \frac{1}{G_{12}} \right) s^2 c^2 - \frac{\nu_{12}}{E_{11}} (s^4 + c^4) \quad (\text{C-3})$$

$$S_{13}^k = -\frac{\nu_{13}}{E_{11}} c^2 - \frac{\nu_{23}}{E_{22}} s^2 \quad (\text{C-4})$$

$$S_{16}^k = \frac{2}{E_{11}} c^3 s - \frac{2}{E_{22}} c s^3 + \left(\frac{1}{G_{12}} - \frac{2\nu_{12}}{E_{11}} \right) (c s^3 - c^3 s) \quad (\text{C-5})$$

$$S_{26}^k = \frac{2}{E_{11}} c s^3 - \frac{2}{E_{22}} c^3 s + \left(\frac{1}{G_{12}} - \frac{2\nu_{12}}{E_{11}} \right) (c^3 s - c s^3) \quad (\text{C-6})$$

$$S_{36}^k = 2 \left(\frac{v_{23}}{E_{22}} - \frac{v_{13}}{E_{11}} \right) cs \quad (C-7) \quad S_{44}^k = \frac{1}{G_{13}} s^2 + \frac{1}{G_{23}} c^2 \quad (C-8)$$

$$S_{45}^k = \left(\frac{1}{G_{13}} - \frac{1}{G_{23}} \right) sc \quad (C-9) \quad S_{55}^k = \frac{1}{G_{13}} c^2 + \frac{1}{G_{23}} s^2 \quad (C-10)$$

$$S_{66}^k = 4 \left(\frac{1}{E_{11}} + \frac{1}{E_{22}} + \frac{2v_{12}}{E_{11}} \right) s^2 c^2 + \frac{1}{G_{12}} (s^4 + c^4 - 2s^2 c^2) \quad (C-11)$$

From the compliance matrix of a single ply the stiffness matrix of that single ply can be obtained by taking the inverse of the compliance matrix: $\mathbf{C} = \mathbf{S}^{-1}$. Then the laminate stiffness matrix can be constructed from the equal strain assumption [80]:

$$C_{ij} = \frac{1}{h} \sum_{k=1}^n C_{ij}^k t_k \quad (C-12)$$

Where h is the total thickness of the laminate and t_k is the ply thickness. The resulting matrix equation is:

$$\begin{pmatrix} \sigma_x \\ \sigma_y \\ \sigma_z \\ \tau_{yz} \\ \tau_{xz} \\ \tau_{xy} \end{pmatrix} = \begin{bmatrix} C_{11} & C_{12} & C_{13} & 0 & 0 & C_{16} \\ C_{12} & C_{22} & C_{23} & 0 & 0 & C_{26} \\ C_{13} & C_{23} & C_{33} & 0 & 0 & C_{36} \\ 0 & 0 & 0 & C_{44} & C_{45} & 0 \\ 0 & 0 & 0 & C_{45} & C_{55} & 0 \\ C_{16} & C_{26} & C_{36} & 0 & 0 & C_{66} \end{bmatrix} \begin{pmatrix} \varepsilon_x \\ \varepsilon_y \\ \varepsilon_z \\ \gamma_{yz} \\ \gamma_{xz} \\ \gamma_{xy} \end{pmatrix} \quad (C-13)$$

From the global stiffness matrix the global laminate properties can be determined. This can be done by setting the stress tensor to zero except for one entry. The resulting system of equations can be solved to find expressions for the different laminate properties. For example, to derive the axial stiffness E_x and corresponding poisson's ratios v_{xy} and v_{xz} , all stresses will be set to zero except for σ_x , from which an expression for E_x , v_{xy} and v_{xz} can be derived as function of the stiffness matrix entries. Solving this system of equations provides the expression for E_x . The final results for all laminate properties will be shown below [80]:

$$E_x = C_{11} - v_{xy} \left(C_{12} - \frac{C_{16}C_{26}}{C_{66}} \right) - v_{xz} \left(C_{13} - \frac{C_{16}C_{36}}{C_{66}} \right) - \frac{C_{16}^2}{C_{66}} \quad (C-14)$$

$$E_y = C_{22} - v_{yx} \left(C_{12} - \frac{C_{16}C_{26}}{C_{66}} \right) - v_{yz} \left(C_{23} - \frac{C_{26}C_{36}}{C_{66}} \right) - \frac{C_{26}^2}{C_{66}} \quad (C-15)$$

$$E_z = C_{33} - v_{zx} \left(C_{13} - \frac{C_{16}C_{36}}{C_{66}} \right) - v_{zy} \left(C_{23} - \frac{C_{26}C_{36}}{C_{66}} \right) - \frac{C_{36}^2}{C_{66}} \quad (C-16)$$

Where,

$$v_{xy} = \frac{C_{12}C_{36}^2 - C_{13}C_{26}C_{36} - C_{16}C_{23}C_{36} + C_{16}C_{26}C_{33} + C_{13}C_{23}C_{66} - C_{12}C_{33}C_{66}}{C_{66}C_{23}^2 - 2C_{23}C_{26}C_{36} + C_{33}C_{26}^2 + C_{22}C_{36}^2 - C_{22}C_{33}C_{66}} \quad (C-17)$$

$$v_{yx} = \frac{C_{12}C_{36}^2 - C_{13}C_{26}C_{36} - C_{16}C_{23}C_{36} + C_{16}C_{26}C_{33} + C_{13}C_{23}C_{66} - C_{12}C_{33}C_{66}}{C_{66}C_{13}^2 - 2C_{13}C_{16}C_{36} + C_{33}C_{16}^2 + C_{11}C_{36}^2 - C_{11}C_{33}C_{66}} \quad (\text{C-18})$$

$$v_{xz} = \frac{C_{13}C_{26}^2 - C_{16}C_{23}C_{26} - C_{12}C_{26}C_{36} + C_{16}C_{22}C_{36} + C_{12}C_{23}C_{66} - C_{13}C_{22}C_{66}}{C_{66}C_{23}^2 - 2C_{23}C_{26}C_{36} + C_{33}C_{26}^2 + C_{22}C_{36}^2 - C_{22}C_{33}C_{66}} \quad (\text{C-19})$$

$$v_{yz} = \frac{C_{16}^2C_{23} - C_{13}C_{16}C_{26} - C_{12}C_{16}C_{36} + C_{11}C_{26}C_{36} + C_{12}C_{13}C_{66} - C_{11}C_{23}C_{66}}{C_{66}C_{13}^2 - 2C_{13}C_{16}C_{36} + C_{33}C_{16}^2 + C_{11}C_{36}^2 - C_{11}C_{33}C_{66}} \quad (\text{C-20})$$

$$v_{zx} = \frac{C_{13}C_{26}^2 - C_{16}C_{23}C_{26} - C_{12}C_{26}C_{36} + C_{16}C_{22}C_{36} + C_{12}C_{23}C_{66} - C_{13}C_{22}C_{66}}{C_{66}C_{12}^2 - 2C_{12}C_{16}C_{26} + C_{22}C_{16}^2 + C_{11}C_{26}^2 - C_{11}C_{22}C_{66}} \quad (\text{C-21})$$

$$v_{zy} = \frac{C_{16}^2C_{23} - C_{13}C_{16}C_{26} - C_{12}C_{16}C_{36} + C_{11}C_{26}C_{36} + C_{12}C_{13}C_{66} - C_{11}C_{23}C_{66}}{C_{66}C_{12}^2 - 2C_{12}C_{16}C_{26} + C_{22}C_{16}^2 + C_{11}C_{26}^2 - C_{11}C_{22}C_{66}} \quad (\text{C-22})$$

And,

$$G_{xy} = C_{66} - v_{xyy} \left(C_{26} - \frac{C_{12}C_{16}}{C_{11}} \right) - v_{xyz} \left(C_{36} - \frac{C_{13}C_{16}}{C_{11}} \right) - \frac{C_{16}^2}{C_{11}} \quad (\text{C-23})$$

Where,

$$v_{xyz} = \frac{C_{12}^2C_{36} - C_{12}C_{13}C_{26} - C_{12}C_{16}C_{23} + C_{13}C_{16}C_{22} + C_{11}C_{23}C_{26} - C_{11}C_{22}C_{36}}{C_{33}C_{12}^2 - 2C_{12}C_{13}C_{23} + C_{22}C_{13}^2 + C_{11}C_{23}^2 - C_{11}C_{22}C_{33}} \quad (\text{C-24})$$

$$v_{xyy} = \frac{C_{13}^2C_{26} - C_{13}C_{16}C_{23} - C_{12}C_{13}C_{36} + C_{12}C_{16}C_{33} + C_{11}C_{23}C_{36} - C_{11}C_{26}C_{33}}{C_{33}C_{12}^2 - 2C_{12}C_{13}C_{23} + C_{22}C_{13}^2 + C_{11}C_{23}^2 - C_{11}C_{22}C_{33}} \quad (\text{C-25})$$

And finally,

$$G_{yz} = C_{44} - \frac{C_{45}^2}{C_{55}} \quad (\text{C-26})$$

$$G_{xz} = C_{55} - \frac{C_{45}^2}{C_{44}} \quad (\text{C-27})$$

Appendix D

Natural Fibre Material Properties from Literature

Table D-1: Bamboo dry fibre properties obtained from literature.

Source	ρ [g/cm ³]	E_1 [MPa]	E_2 [MPa]	σ_1^t [MPa]	G_{12} [MPa]	ν_{12} [-]
[49]	1.18	32000	-	800	-	-
[34]	0.85	21500	-	470	-	-
Fibre bundle [81]	0.8	35900	-	441	-	-
[82]	0.802	-	-	200.5	-	-
[83]	-	26000	-	323	-	-
Single fibre [66]	-	34620	-	930	-	-
Vascular bundle [66]	0.86	28590	-	470.87	-	-
Bundle fibre [66]	-	16500	-	290	-	-
Fibre bundle [84]	0.68	12020	-	179.23	-	-
Average	0.86	25890	-	456	-	-

Table D-2: Hemp dry fibre properties obtained from literature.

Source	ρ [g/cm ³]	E_1 [MPa]	E_2 [MPa]	σ_1^t [MPa]	G_{12} [MPa]	ν_{12} [-]
Fibre bundle, no heat treatment [85]	-	-	-	702	-	-
Table 2 [67]	1.15	45000	-	690	-	-
Table 1 [49]	1.48	70000	-	900	-	-
[34]	1.45	56750	-	585	-	-
[33]	-	70000	-	-	-	-
[35]	1.35	45000	-	820	-	-
Average	1.36	57350	-	740	-	-

Table D-3: Flax dry fibre properties obtained from literature.

Source	ρ [g/cm ³]	E_1 [MPa]	E_2 [MPa]	σ_1^t [MPa]	G_{12} [MPa]	ν_{12} [-]
[86]	-	52500	8000	-	2410	0.498
[87]	1.5	56000	-	-	-	-
[88]	1.47	62000	-	-	-	-
[89]	1.4	-	-	-	-	-
[49]	1.5	80000	-	1500	-	-
[90]	1.55	60000	-	700	-	-
[41]	1.46	70000	-	700	-	-
[33]	1.4	70000	-	-	-	-
[35]	1.38	65000	-	850	-	-
[34]	1.45	65300	-	1171.5	-	-
[44]	-	67600	-	883	-	-
[91]	1.44	84000	-	921.5	-	-
Average	1.455	66582	8000	960	2410	0.498

Table D-4: Sisal dry fibre properties obtained from literature.

Source	ρ [g/cm ³]	E_1 [MPa]	E_2 [MPa]	σ_1^t [MPa]	G_{12} [MPa]	ν_{12} [-]
[92]	-	39500	-	690	-	-
Table 2 [67]	1.295	19500	-	580	-	-
Table 1 [49]	1.45	38000	-	700	-	-
[34]	1.415	23500	-	531.5	-	-
[33]	1.33	38000	-	-	-	-
Average	1.37	31700	-	625	-	-

Table D-5: Ramie dry fibre properties obtained from literature.

Source	ρ [g/cm ³]	E_1 [MPa]	E_2 [MPa]	σ_1^t [MPa]	G_{12} [MPa]	ν_{12} [-]
Table 3 [93]	-	15500	-	525.9	-	-
Table 2 [67]	1.5	44000	-	685	-	-
[34]	1.275	76250	-	700	-	-
[35]	1.44	23000	-	915	-	-
Average	1.41	40000	-	706	-	-

Table D-6: Jute dry fibre properties obtained from literature.

Source	ρ [g/cm ³]	E_1 [MPa]	E_2 [MPa]	σ_1^t [MPa]	G_{12} [MPa]	ν_{12} [-]
Table 2 [94]	1.46	20000	-	600	-	-
Table 2 [67]	1.45	20000	-	600	-	-
Table 1 [49]	1.46	30000	-	800	-	-
[34]	1.395	43000	-	560	-	-
[33]	1.46	20000	-	-	-	-
[35]	1.23	46250	-	547.5	-	-
Average	1.41	37000	-	706	-	-

Sensitivity Study Details

E-1 Calculation volume percentage UD/BIAX material

The relative amount of UD and BIAX material in the blade is calculated as volume percentage to help interpret the results of the performed sensitivity study. The Blade Modelling Tool (BMT) divides the cross-section into 19 sections plus the two shear webs for all 98 radial positions from root to tip. For each radial position the arc-length of each section is given as well as the material layup. As the airfoil is split in sections the curvature per section is small and it will be assumed that the cross-sectional area can be calculated as the arc-length times the thickness. Furthermore, the lay-up is specified through alternating UD and BIAX plies by specifying the thickness of the consecutive UD or BIAX plies. Thus, the cross-sectional area consisting of UD or BIAX material for each radial position can be calculated as follows:

$$A_m = \sum_{n=1}^{21} t_n \cdot s_n \quad (\text{E-1})$$

Where t_n is the sum of the thickness of either the UD or BIAX plies in section n and s_n is the arc-length of section n . To calculate the volume, the cross-sectional area needs to be multiplied by a radial section length. As the cross-sectional area of a wind turbine blade varies along the blade it is decided to use an averaging method to determine the volume for each radial section. For each radial section half the radial section length will be multiplied by the cross-sectional area of the first radial position and half the radial length will be multiplied by the cross-sectional area at the next radial position. The total volume is then calculated using the following formula:

$$V = \sum_{m=1}^{97} \frac{r_{m+1} - r_m}{2} (A_m + A_{m+1}) \quad (\text{E-2})$$

Where, r is the radial position and A the cross-sectional area taken up by the material of interest. As the BMT tool splits the blade in many sections it is possible to distinguish the amount of UD/BIAX material in the whole blade, the load carrying beam and the spar caps only. The percentage of UD and BIAX material in the blade is presented in Table E-1 where 100% is the summation of the two materials.

Table E-1: Volume percentage UD and BIAx material for different blade components of the DTU 12.6 m blade.

	Entire blade	Load carrying beam only	Spar caps only
UD	56.6	61.1	72.7
BIAx	43.5	39.0	27.3

The results are in line with typical wind turbine designs where the distribution UD/BIAx is 60/40%. What is also visible is that the relative amount of UD material in the spar caps is significantly higher compared to the rest of the blade. This is logical as the spar caps provide the longitudinal bending stiffness which in turn is provided through many layers of the UD material. This also means that the UD engineering constants likely have a larger impact on the outputs compared to the BIAx engineering constants when analysing the flapwise loads in the sensitivity study.

E-2 Torque full results

The results for all sensitivity tests for the UD and BIAx material for the torsional load is presented in Figure E-1 and Figure E-2.

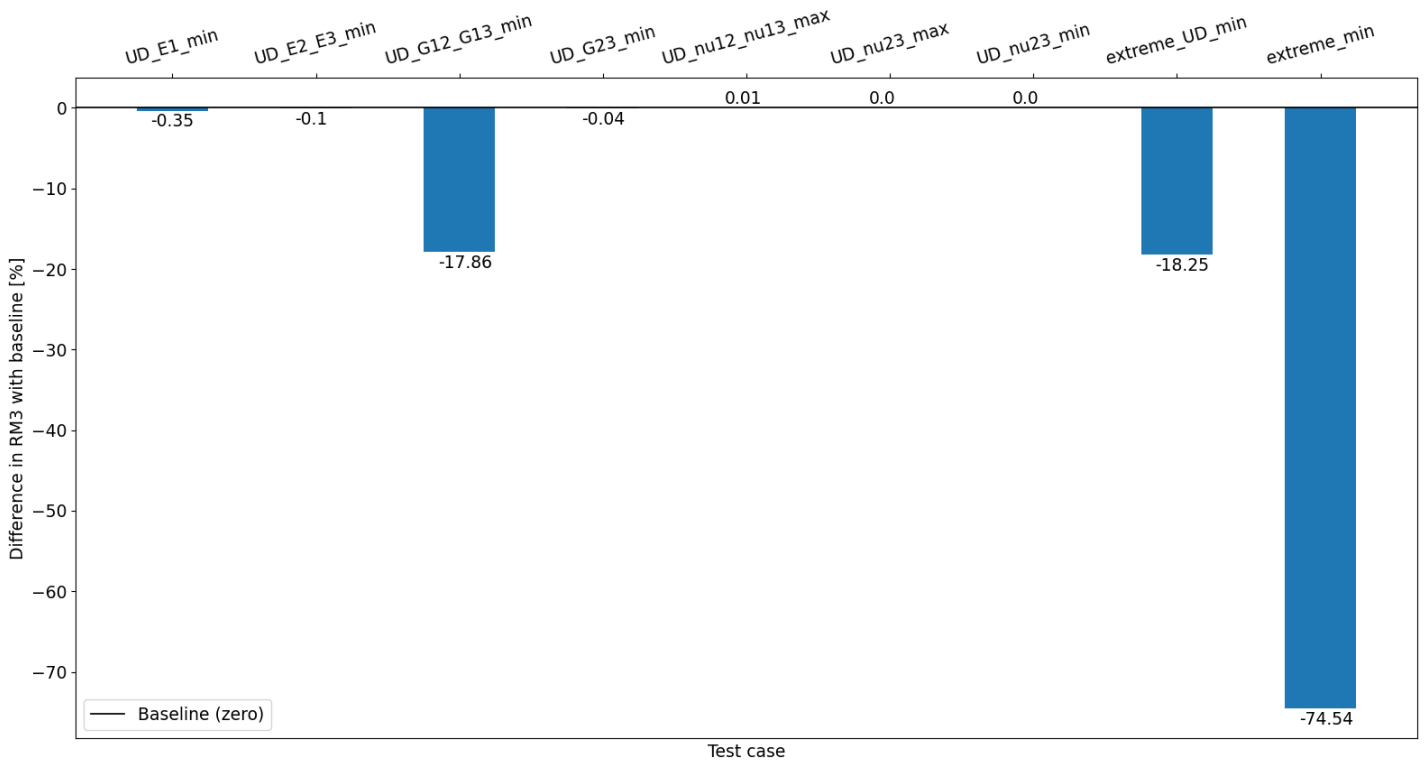


Figure E-1: Percentage difference in RM3 as a result of a 10° twist at $r = 10.8$ m of the DTU 12.6 m blade: UD sensitivity results.

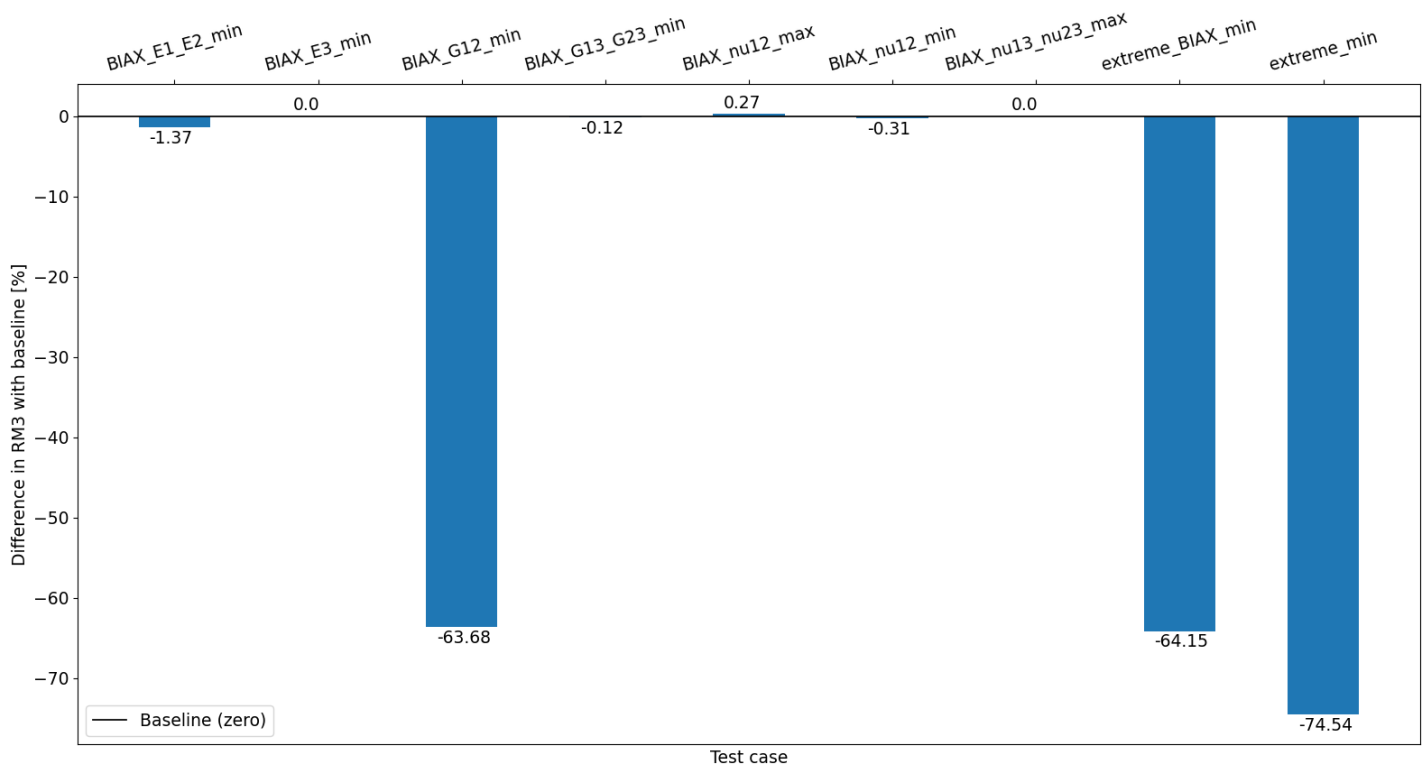


Figure E-2: Percentage difference in RM3 as a result of a 10° twist at $r = 10.8$ m of the DTU 12.6 m blade: BIAE sensitivity results.

E-3 PTS full results

The results for all sensitivity tests for the UD and BIAE material for the tip deflection under the PTS loading is presented in Figure E-3 and Figure E-4. The "extreme_min" result is not presented in the BIAE plot as it is significantly larger than the values in the BIAE plot and would reduce the visibility of the other results.

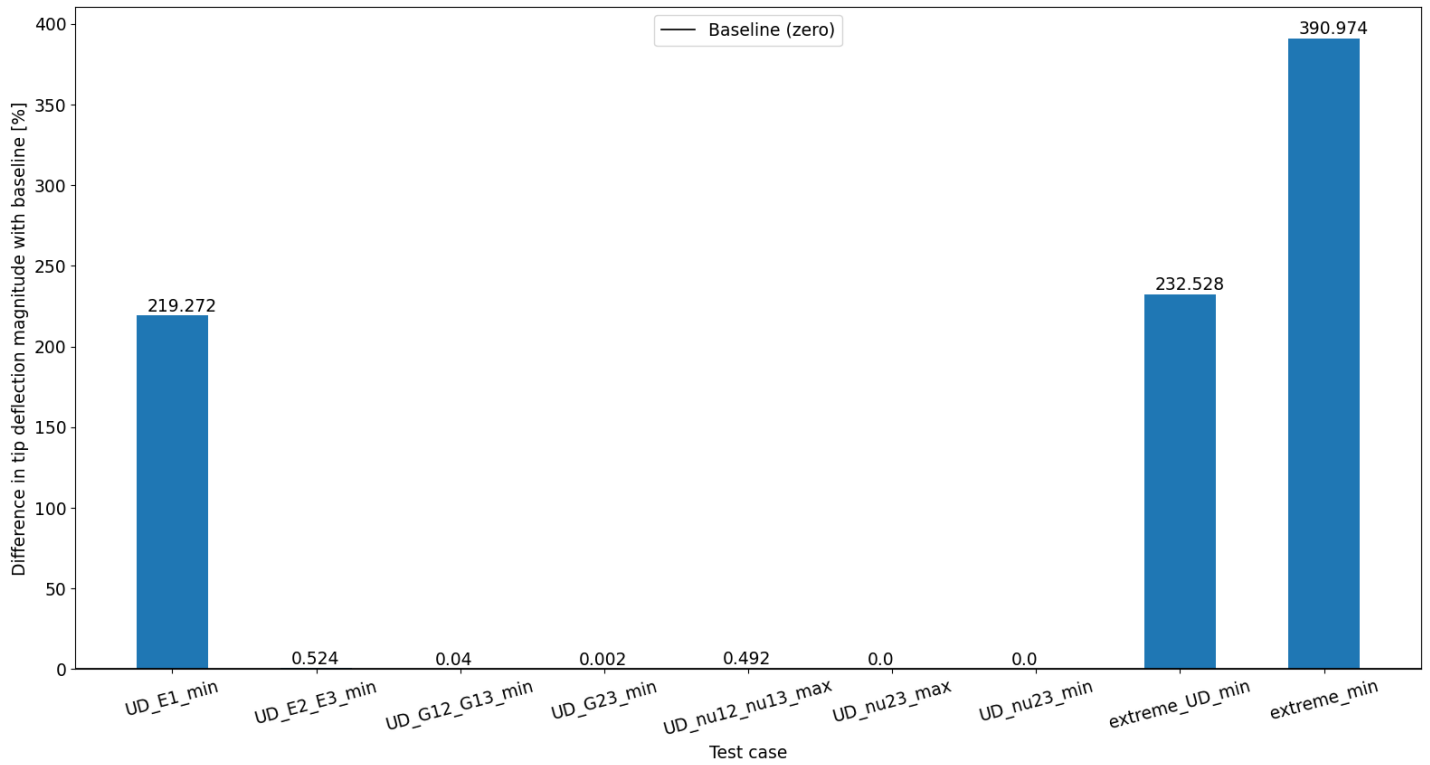


Figure E-3: Percentage difference in tip deflection magnitude of the DTU 12.6 m blade: UD sensitivity results in PTS loading

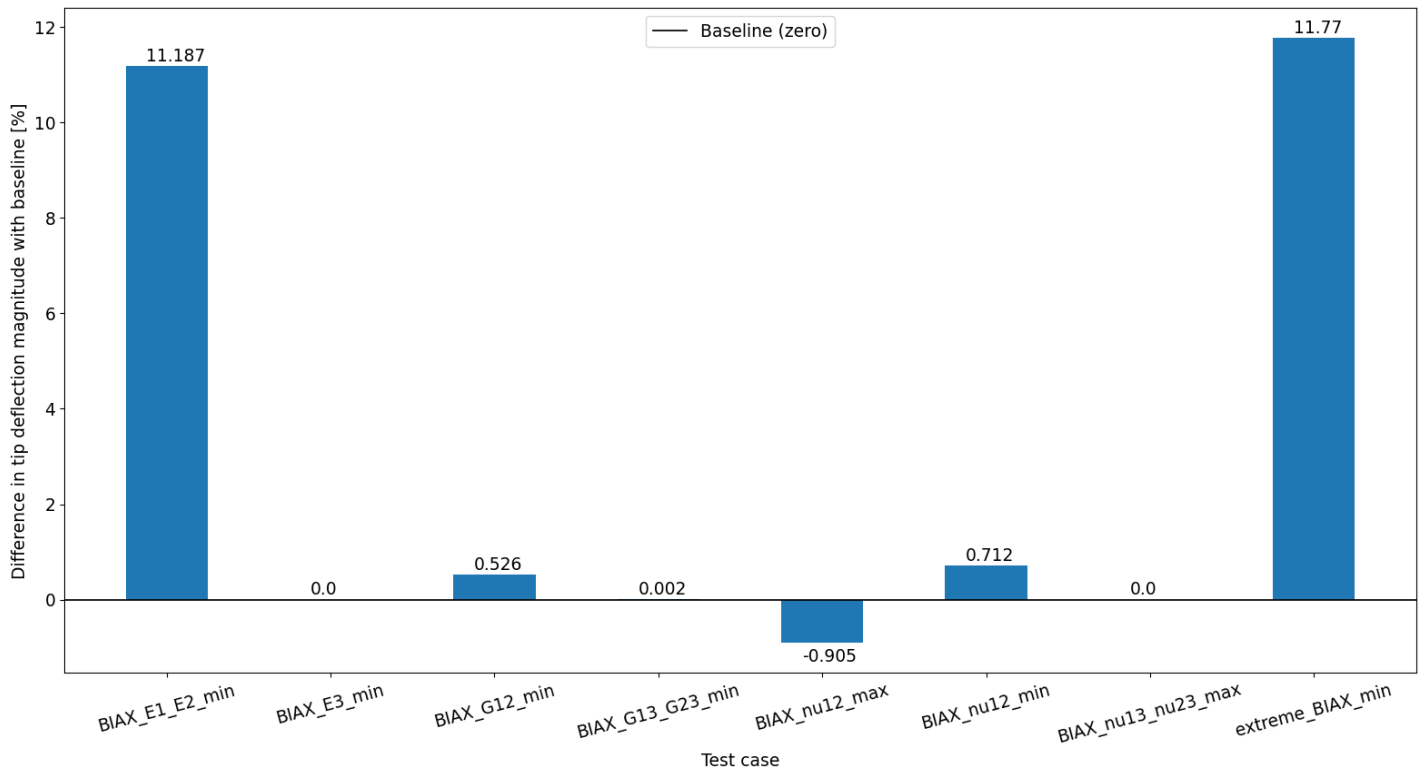


Figure E-4: Percentage difference in tip deflection magnitude of the DTU 12.6 m blade: BIAx sensitivity results in PTS loading

The results for all sensitivity tests for the UD and BIAx material for the maximum Tsai-Wu value under the PTS loading is presented in Figure E-5 and Figure E-6. The "extreme_min" result is not presented in the BIAx plot as it is significantly larger than the values in the BIAx plot and would reduce the visibility of the other results.

Analysing the results it can be stated that the maximum Tsai-Wu value is significantly impacted by the longitudinal bending stiffness E1 of the UD material. The comparison with the baseline is valid as the maximum Tsai-Wu value is not artificial and originates from the same ply and approximately the same location as the baseline results.

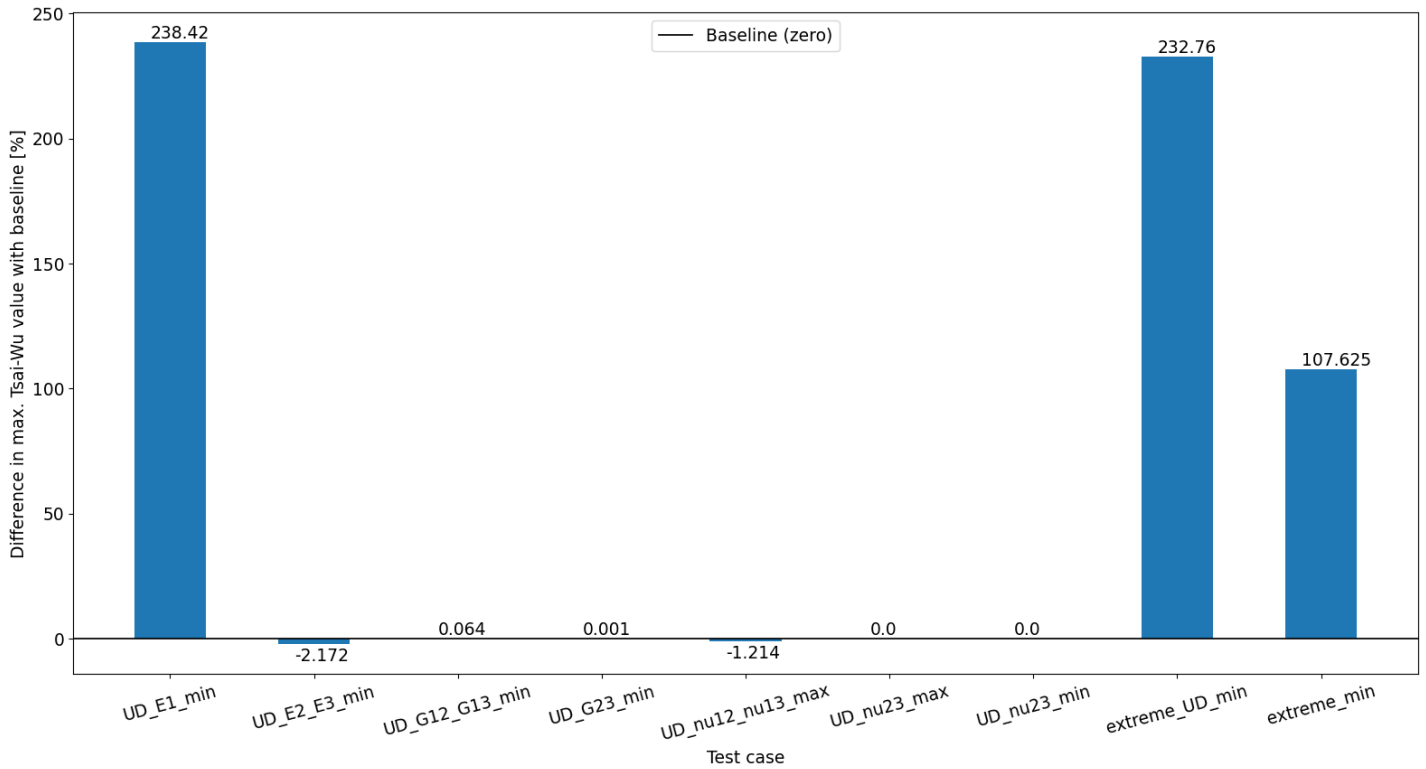


Figure E-5: Percentage difference in maximum Tsai-Wu value of the DTU 12.6 m blade: UD sensitivity results under PTS loading.

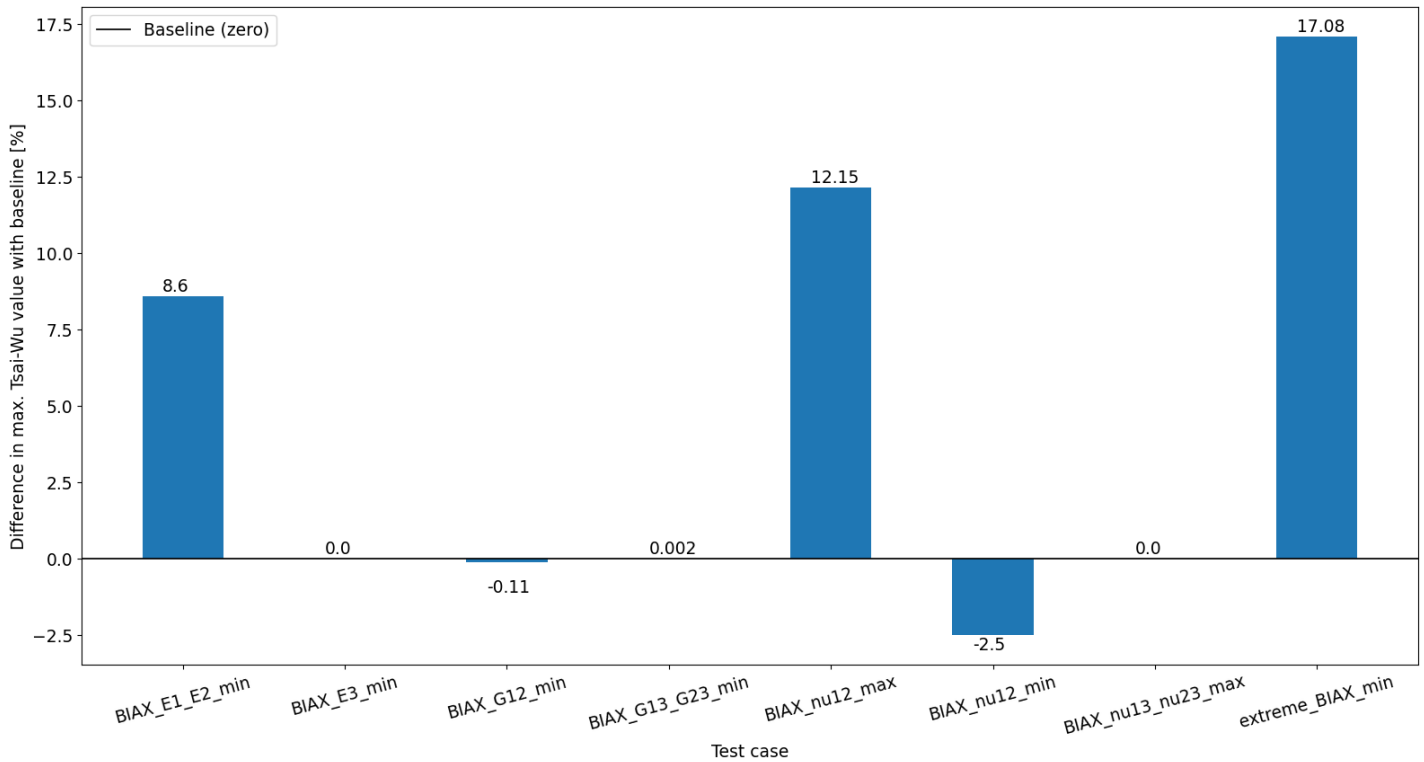


Figure E-6: Percentage difference in maximum Tsai-Wu value of the DTU 12.6 m blade: BIAx sensitivity results under PTS loading.

E-4 STP full results

The results for all sensitivity tests for the UD and BIAx material for the tip deflection under the STP loading is presented in Figure E-7 and Figure E-8. The "extreme_min" result is not presented in the BIAx plot as it is significantly larger than the values in the BIAx plot and would reduce the visibility of the other results. The comparison of the significant parameters is presented in Figure E-9. The relationship between the longitudinal stiffness inputs and the tip deflection output for the STP loadcase is presented in Figure E-10.

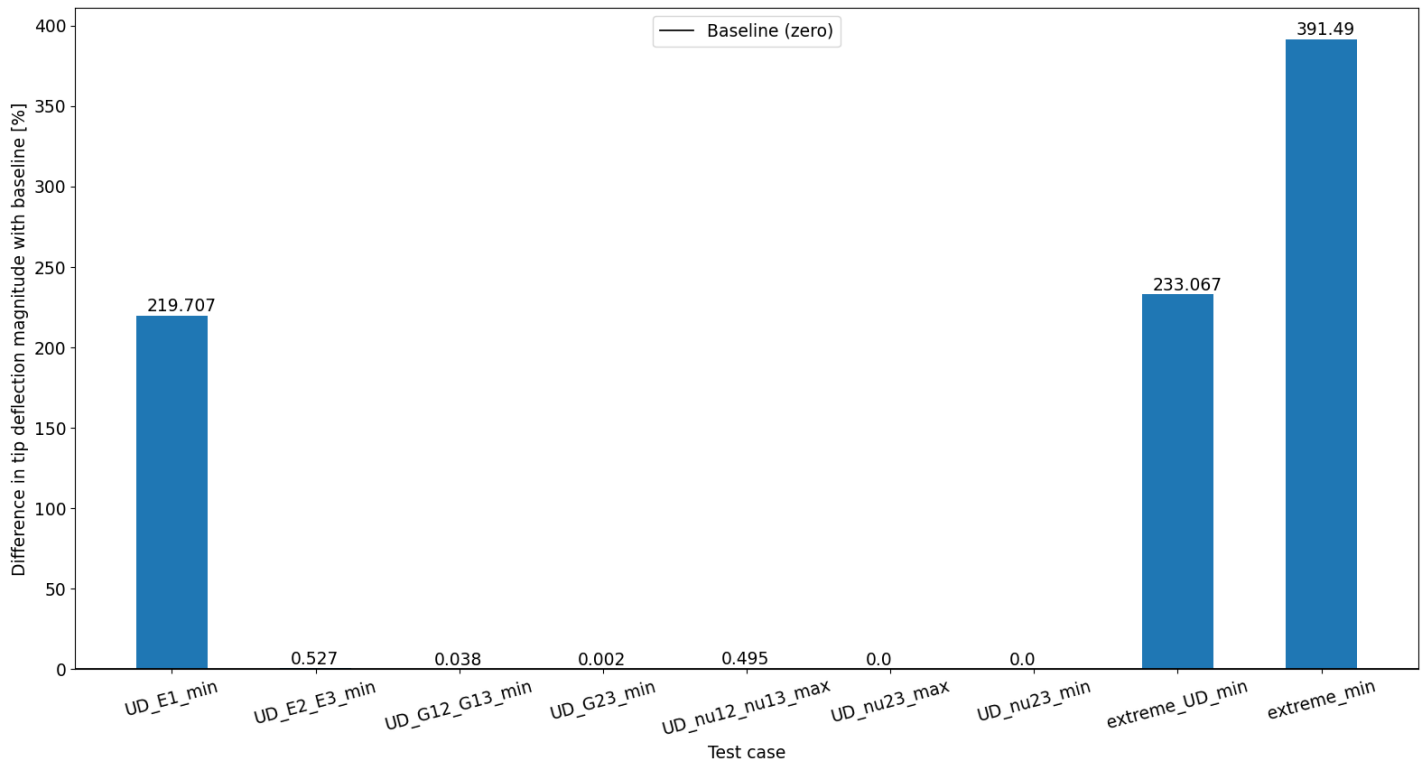


Figure E-7: Percentage difference in tip deflection magnitude of the DTU 12.6 m blade: UD sensitivity results under STP loading.

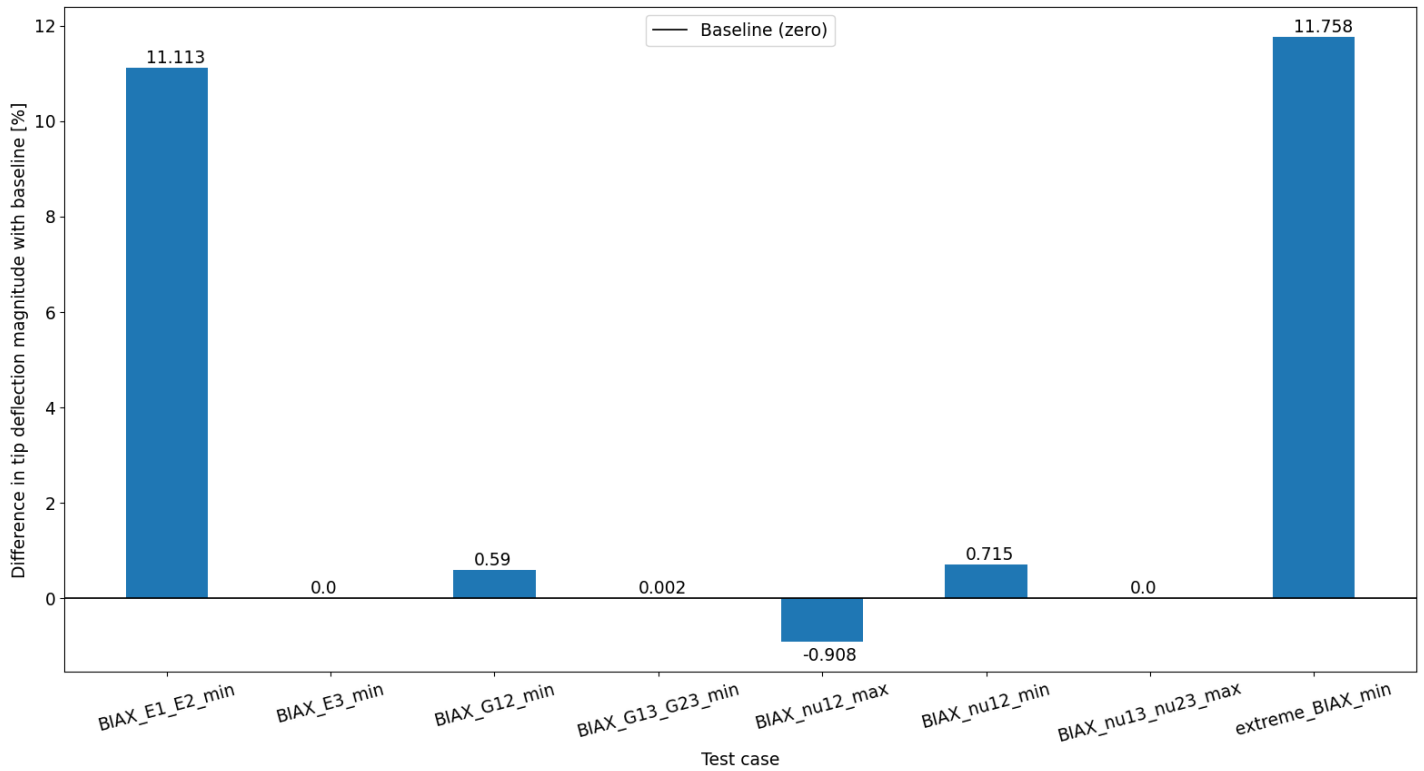


Figure E-8: Percentage difference in tip deflection magnitude of the DTU 12.6 m blade: BIAx sensitivity results under STP loading.

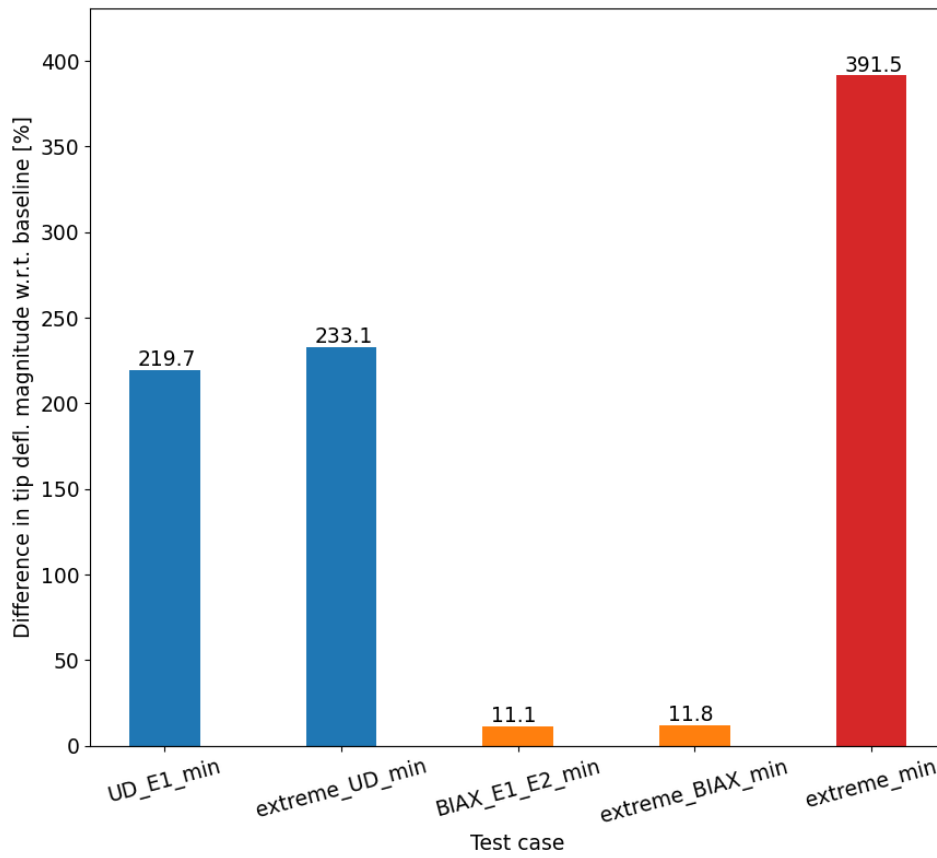


Figure E-9: Percentage difference in tip deflection magnitude of the DTU 12.6 m blade under STP loading: significant parameters from sensitivity study.

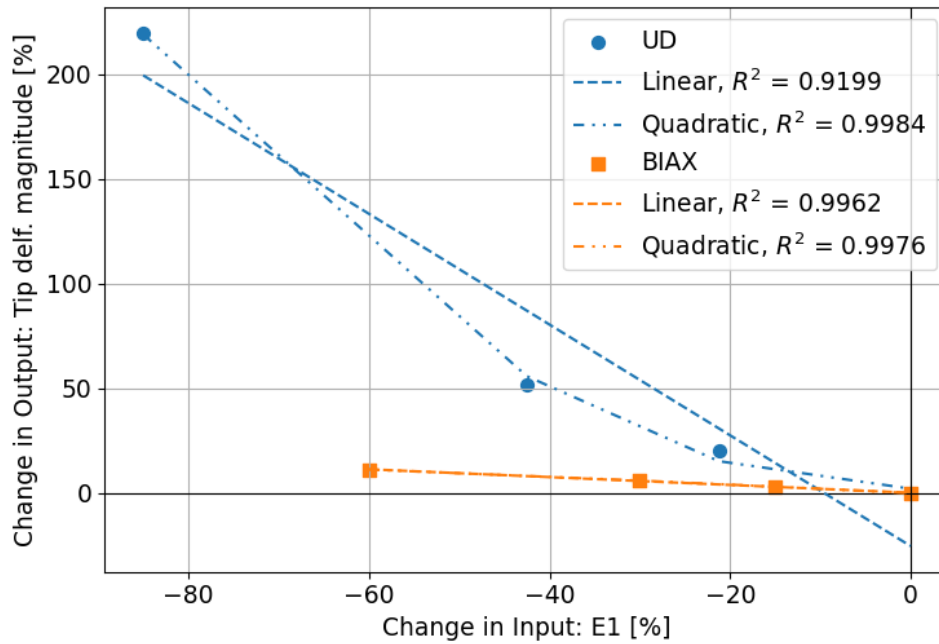


Figure E-10: Percentage difference in tip deflection magnitude vs percentage change in E_1 input for the DTU 12.6 m blade under STP loading.

The results for all sensitivity tests for the UD and BIAx material for the maximum Tsao-Wu value under the STP loading is presented in Figure E-11 and Figure E-12. The "extreme_min" result is not presented in the BIAx plot as it is significantly larger than the values in the BIAx plot and would reduce the visibility of the other results. The comparison of the significant parameters is presented in Figure E-13. The relationship between the longitudinal stiffness inputs and the maximum Tsai-Wu value output for the STP loadcase is presented in Figure E-14. The relationship between the BIAx in-plane poisson's ratio input and the maximum Tsai-Wu value output for the STP loadcase is presented in Figure E-15.

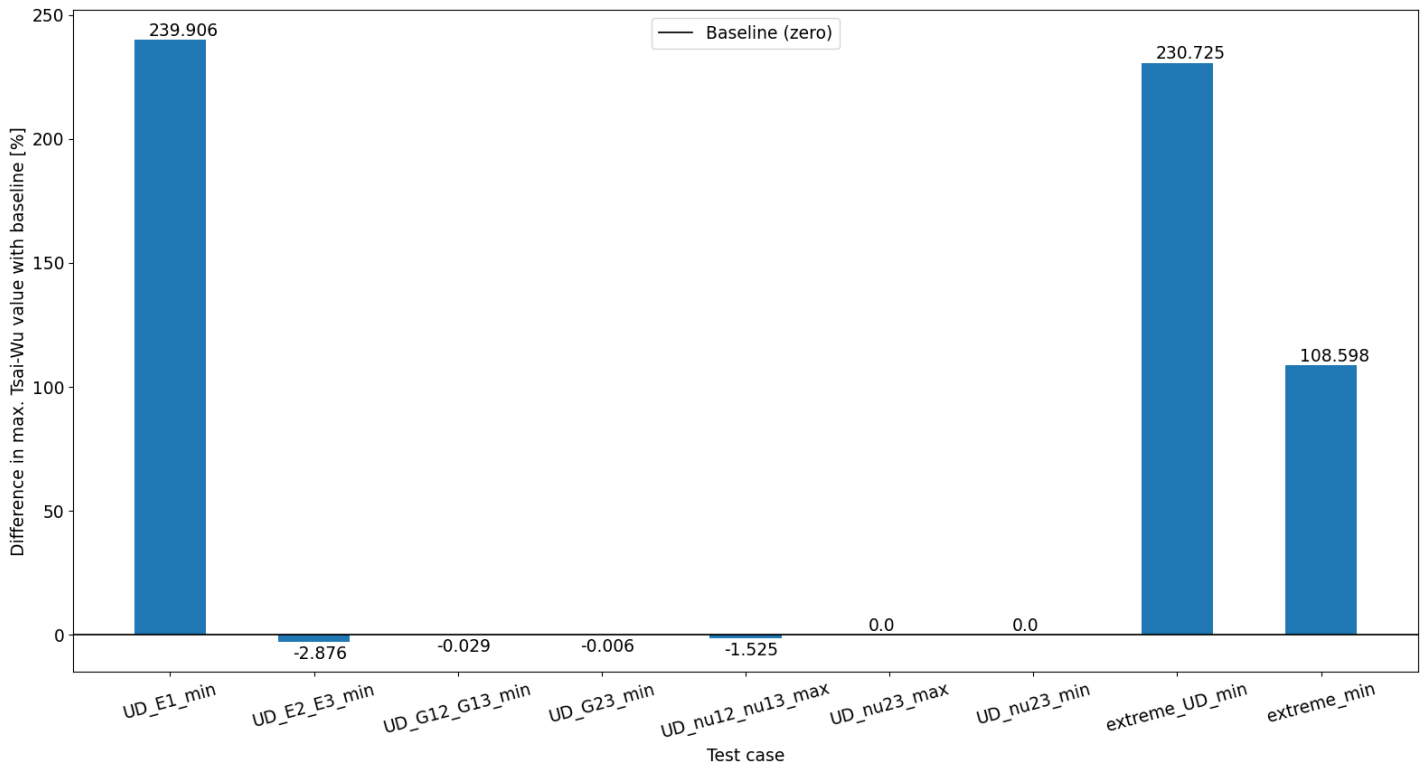


Figure E-11: Percentage difference in maximum Tsai-Wu value of the DTU 12.6 m blade: UD sensitivity results under STP loading.

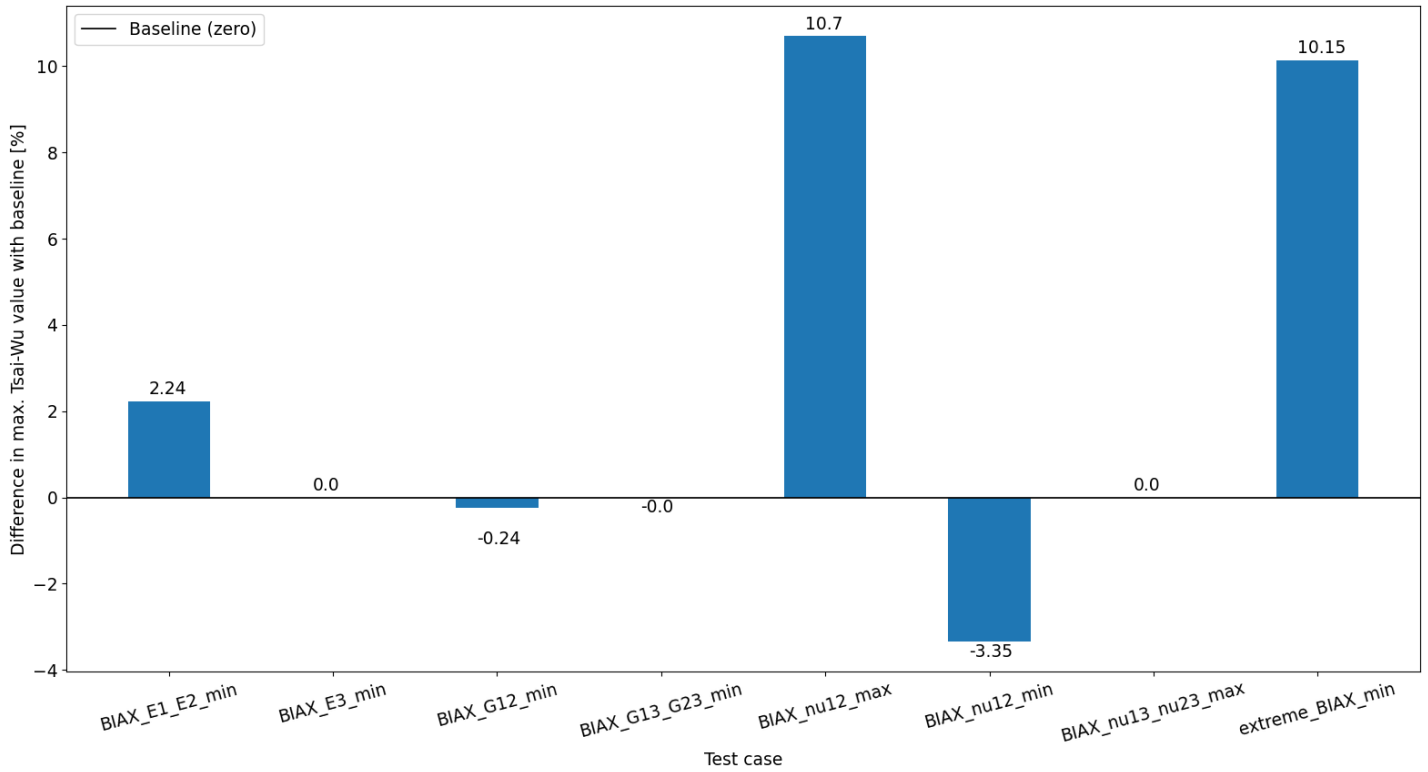


Figure E-12: Percentage difference in maximum Tsai-Wu value of the DTU 12.6 m blade: BIAx sensitivity results under STP loading.

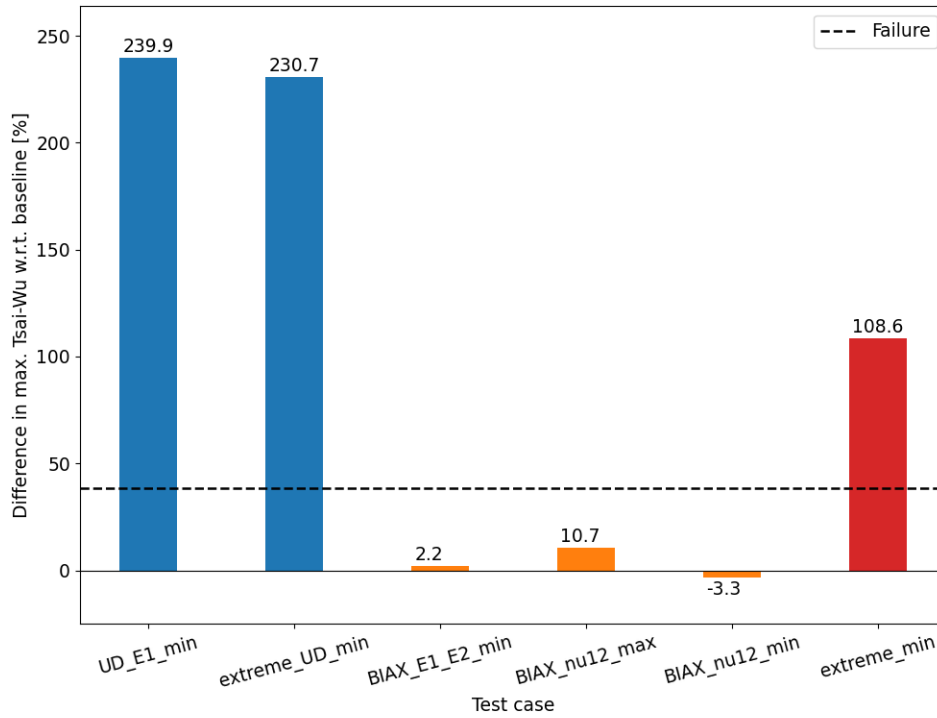


Figure E-13: Percentage difference in maximum Tsai-Wu value for the DTU 12.6 m blade under STP loading: significant parameters from sensitivity study.

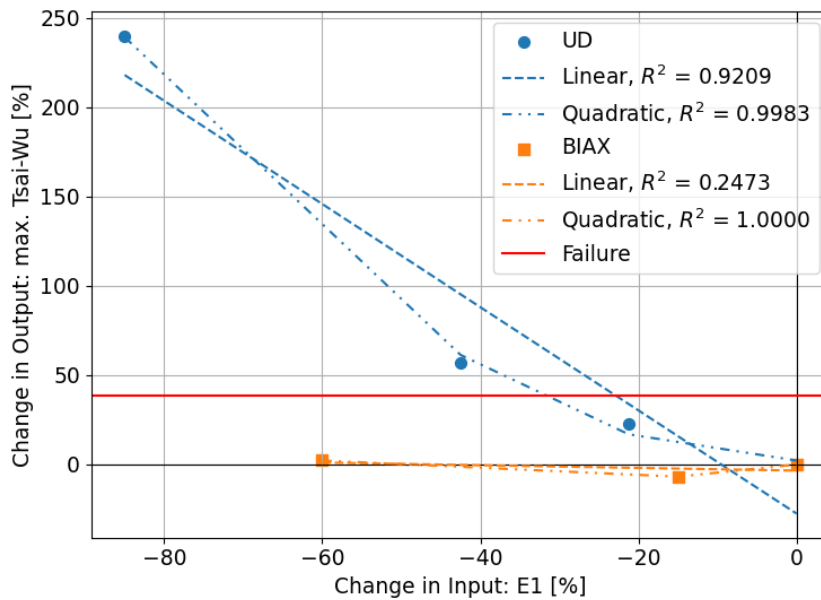


Figure E-14: Percentage difference in max. Tsai-Wu value vs percentage change in E_1 input for the DTU 12.6 m blade under STP loading.

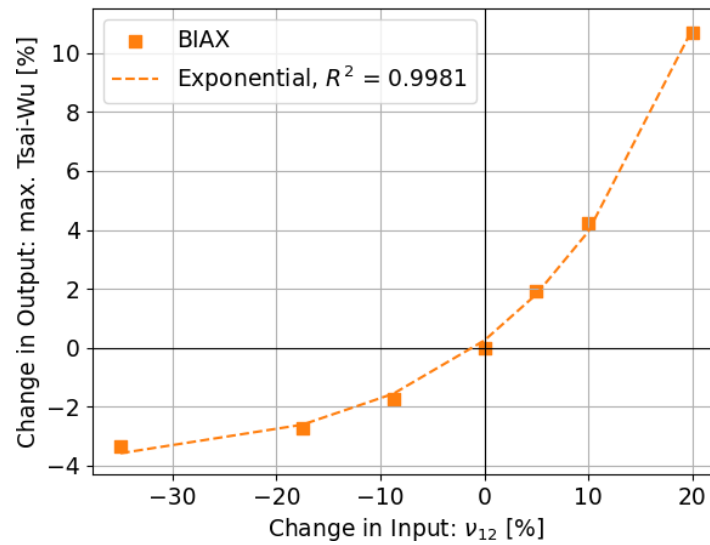


Figure E-15: Percentage difference in max. Tsai-Wu value vs percentage change in ν_{12} input for the DTU 12.6 m blade under STP loading.

E-5 TTL full results

The results for all sensitivity tests for the UD and BIAX material for the maximum tip deflection under the TTL loading is presented in Figure E-16 and Figure E-17. The "extreme_min" result is not presented in the BIAX plot as it is significantly larger than the values in the BIAX plot and would reduce the visibility of the other results.

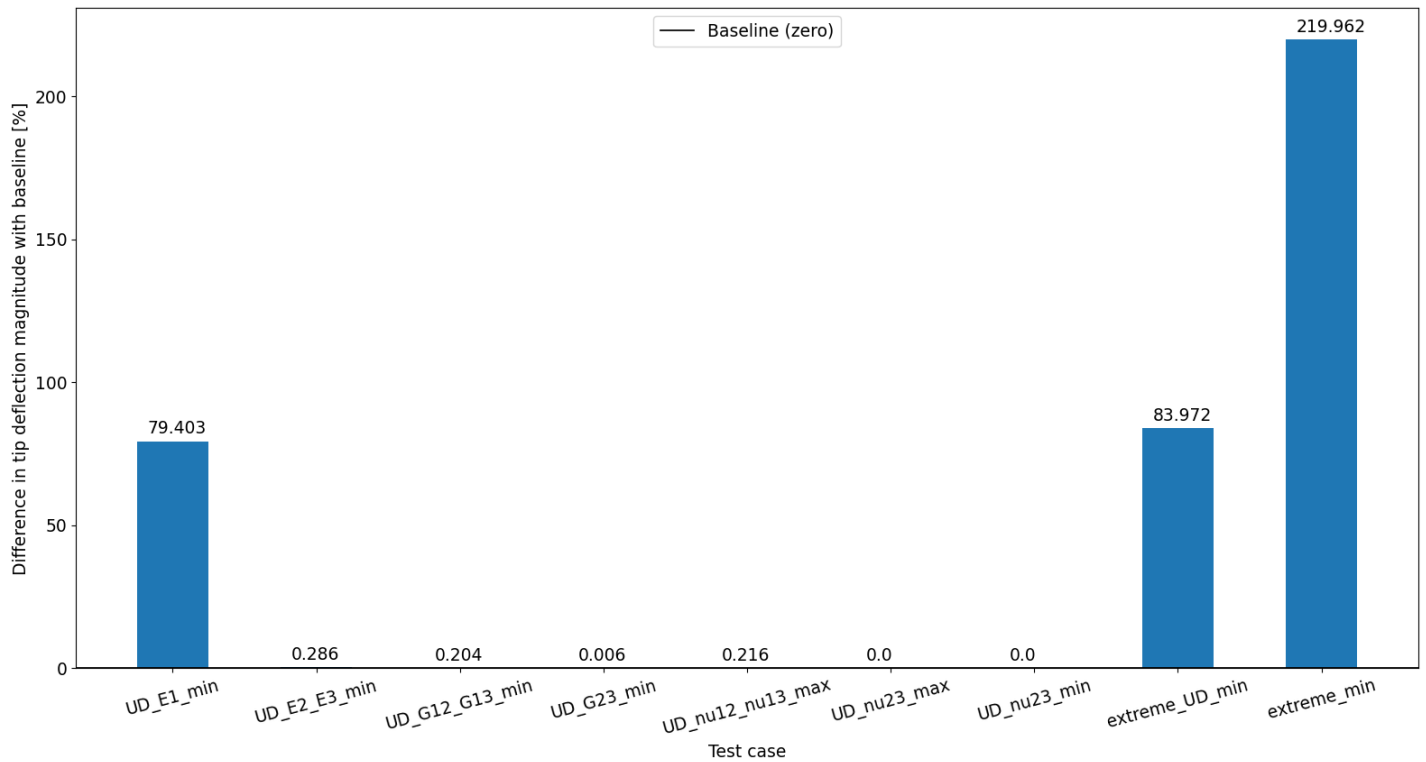


Figure E-16: Percentage difference in tip deflection magnitude of the DTU 12.6 m blade: UD sensitivity results under TTL loading.

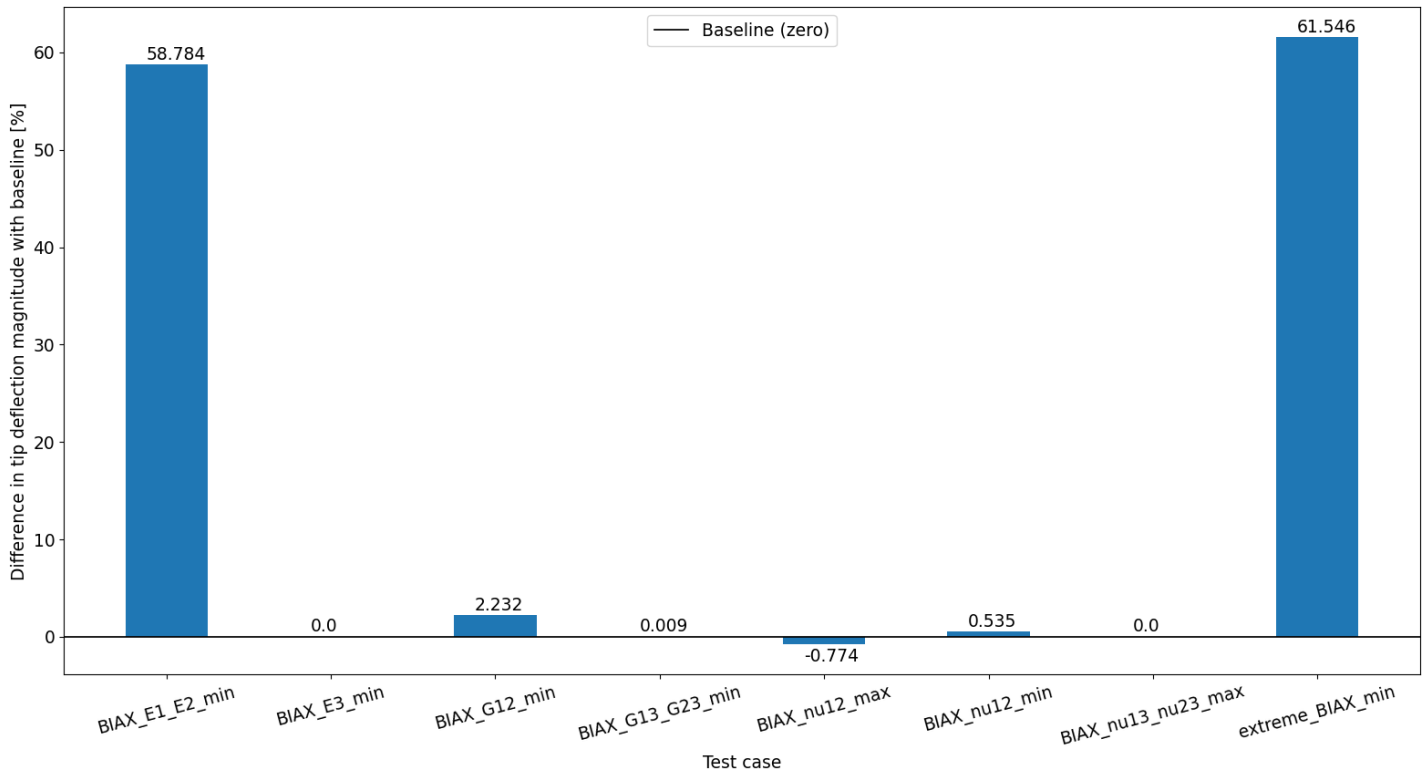


Figure E-17: Percentage difference in tip deflection magnitude of the DTU 12.6 m blade: BIAX sensitivity results under TTL loading.

The results for all sensitivity tests for the UD and BIAX material for the maximum Tsai-Wu value under the TTL loading is presented in Figure E-18 and Figure E-19. It must be noted that the analysis of the results lead to the conclusion that some values were artificial as a result of numerical issues. These results include the "BIAX_E1_E2_min", "BIAX_G12_min", "BIAX_nu12_max" and "extreme_BIAX_min" test cases. This complicates the analysis of the influence of the different engineering properties on the stress levels and failure limits.

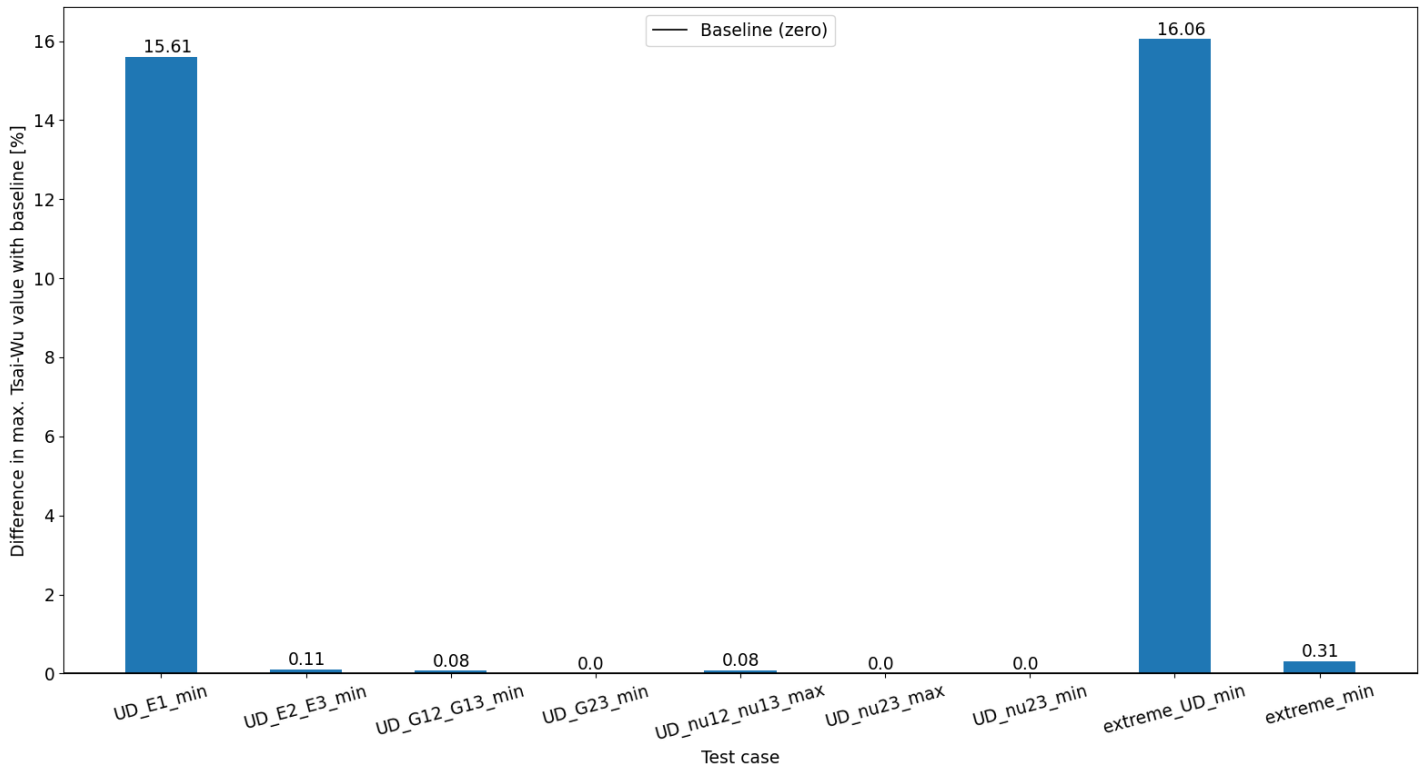


Figure E-18: Percentage difference in maximum Tsai-Wu value for the DTU 12.6 m blade: UD sensitivity results under TTL loading.

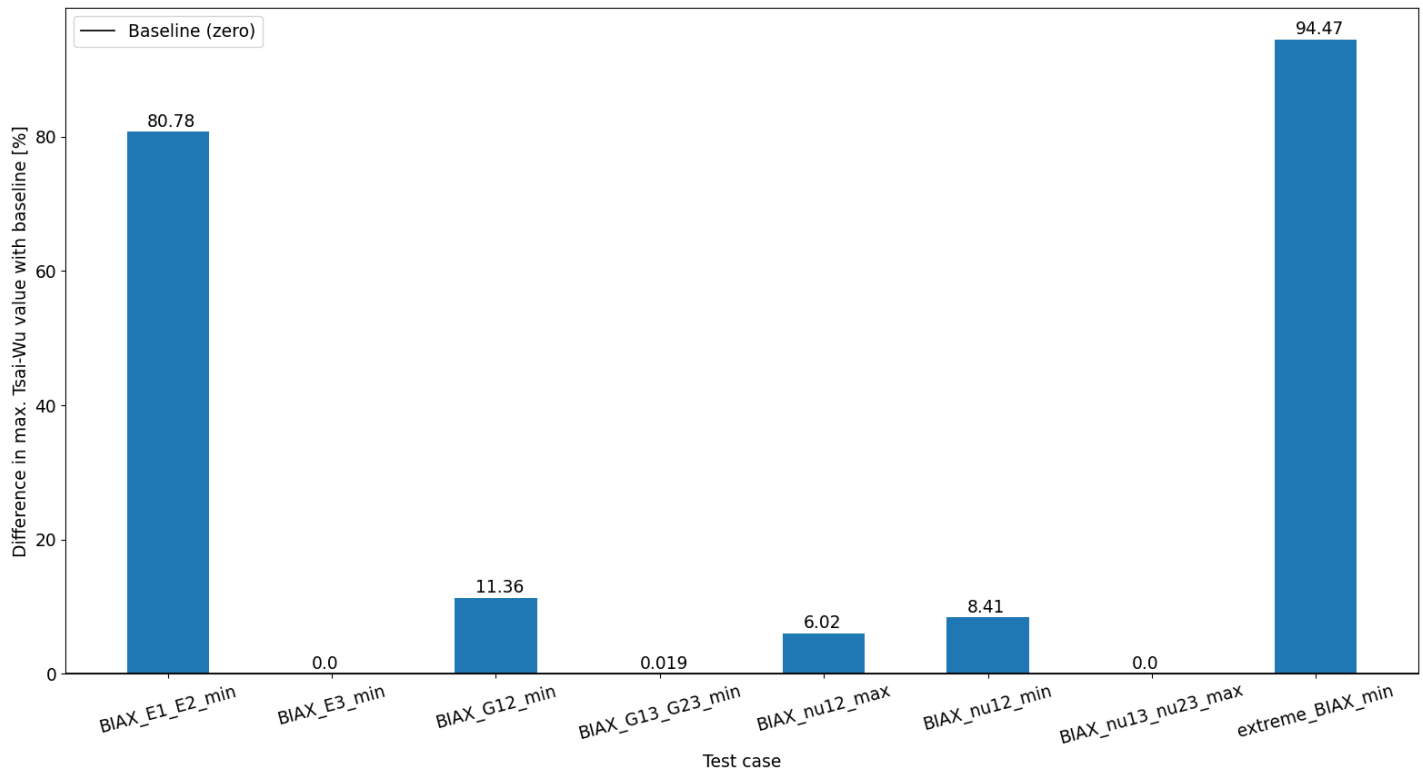


Figure E-19: Percentage difference in maximum Tsai-Wu value for the DTU 12.6 m blade: BIAx sensitivity results under TTL loading.

The full results of the sensitivity study of the tip deflection for the TTL loadcase are presented in Appendix E, the significant results are presented in Figure E-20. It can be observed that the tip deflection in the edgewise direction mainly depends on the UD longitudinal stiffness and BIAx longitudinal stiffness. The influence of the UD and BIAx stiffness is much more similar in this loadcase compared to the flapwise loadcases. This is because the bending stiffness in the edgewise load direction mainly comes from the material along the trailing and leading edge which consist for the majority of BIAx material, thus explaining the larger influence of the BIAx longitudinal stiffness compared to the flapwise loadcases. However, as the longitudinal stiffness of the UD material of 42.7 GPa is significantly larger than that of the BIAx material with 14.3 GPa, means that the UD material also provides a significant amount of the blade's bending stiffness in the edgewise direction. This explains why the UD longitudinal stiffness also has a significant impact on the tip deflection in this loadcase.

Another interesting observation is that the transverse bending stiffness of the UD material does not play a significant role in the edgewise bending stiffness of the blade. This is likely caused by the fact that the longitudinal stiffness of 42.7 GPa is significantly larger than the transverse stiffness of 12.6 GPa causing its influence to overpower that of the transverse stiffness.

Furthermore, despite the stiffness of the UD and BIAx material contributing approximately equally to the tip deflection, it must be noted that the tip deflection when changing both materials is significantly larger compared to their individual results. This can be explained similarly as for the flapwise loading. The reduction in stiffness of one material is no longer

compensated by the higher baseline stiffness of the other material causing the significant increase in deflection.

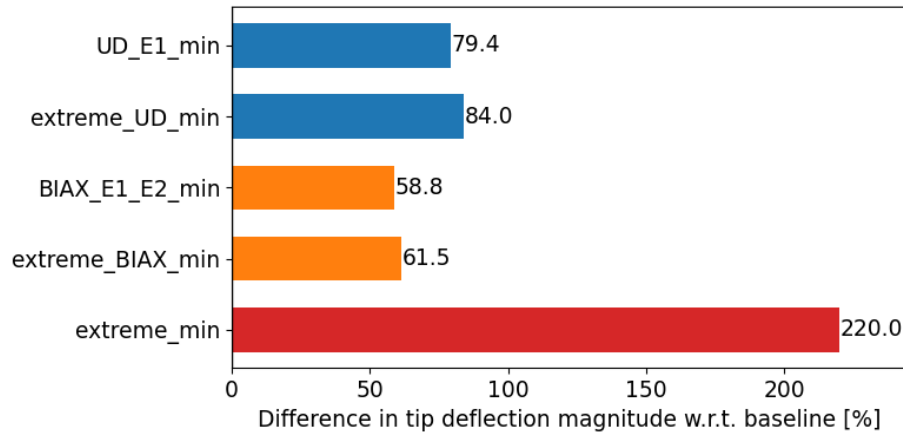


Figure E-20: Significant results of sensitivity study on TTL loadcase for the DTU 12.6 m blade: percentage difference in tip deflection magnitude.

As the impact of the UD and BIAX longitudinal stiffness is more similar in this loadcase it is important to plot the percentage input versus percentage output to create a fair comparison. The same additional data points are evaluated as for the PTS loadcase, see Table 4-11 and Table 4-12. The results presented as percentage change in E1 versus tip deflection output are shown in Figure E-21. Both a linear and quadratic curve-fitting is presented to evaluate which type of relation better fits the data. For the BIAX material the linear and quadratic curve are close together so one could conclude that the relation is practically linear. For the UD material the quadratic curve fits the data better. Comparing the curves of the UD and BIAX material show that the BIAX material has a larger impact than the UD material as the BIAX curve lies above the UD curve. However, the difference in impact is significantly smaller than for the flapwise loadcases as the two curves lie relatively close together.

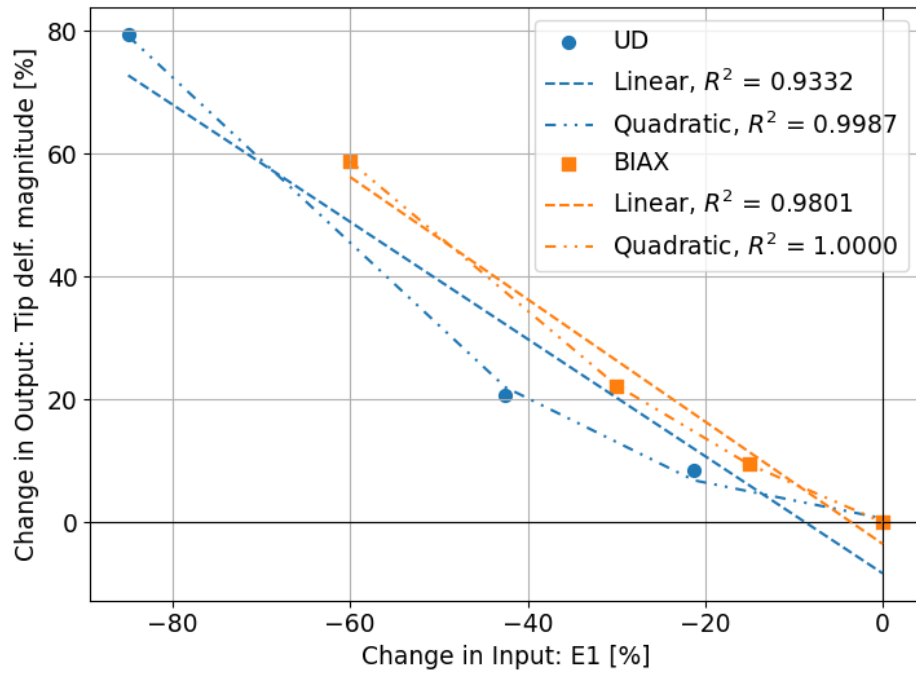


Figure E-21: Percentage difference in tip deflection magnitude vs percentage change in E_1 input for the TTL loadcase of the sensitivity study on the DTU 12.6 m blade.

Bibliography

- [1] IPCC, “Summary for policymakers,” *Climate Change 2021: The Physical Science Basis. Contribution of Working Group I to the Sixth Assessment Report of the Intergovernmental Panel on Climate Change*, V. Masson-Delmotte, P. Zhai, A. Pirani, *et al.*, Eds., 2021.
- [2] United Nations Environmental Program (UNEP), “Emissions gap report 2021: The heat is on – a world of climate promises not yet delivered,” Nairobi, Kenya, 2021, ISBN: 978-92-807-3890-2. [Online]. Available: <https://www.unep.org/emissions-gap-report-2021>.
- [3] International Energy Agency (IEA), “World energy outlook 2021,” International Energy Agency, Paris, France, Oct. 13, 2021. [Online]. Available: <https://www.iea.org/reports/world-energy-outlook-2021>.
- [4] B. H. Jørgensen, P. Madsen, G. Giebel, I. Martí, and K. Thomsen, “Introduction, trends and key messages,” in *DTU International Energy Report 2021 – Perspectives on Wind Energy*, Danmarks Tekniske Universitet, Institut for Vindenergi, Risø Campus, 4000, Roskilde, Denmark, 2021. DOI: [10.11581/DTU.00000201](https://doi.org/10.11581/DTU.00000201).
- [5] J. Lee and F. Zhao, “GWEC global wind report 2021,” Global Wind Energy Council, Brussels, Belgium, 2021.
- [6] D. J. Hall. “Cleaning up the steel industry: Reducing CO2 emissions with CCUS.” (Jan. 2021), [Online]. Available: <https://www.carbonclean.com/blog/steel-co2-emissions>.
- [7] M. Carus and L. Dammer, “The circular bioeconomy—concepts, opportunities, and limitations,” *Industrial Biotechnology*, vol. 14, no. 2, pp. 83–91, Apr. 2018. DOI: [10.1089/ind.2018.29121.mca](https://doi.org/10.1089/ind.2018.29121.mca).
- [8] ETIPWind Executive Committee, “How wind is going circular - blade recycling,” European Technology & Innovation Platform on Wind energy, Sep. 2019. [Online]. Available: <https://etipwind.eu/files/reports/ETIPWind-How-wind-is-going-circular-blade-recycling.pdf>.

- [9] Reliablade Consortium. “ReliaBlade,” ReliaBlade. (2021), [Online]. Available: <https://www.reliablade.com/>.
- [10] J. Beauson and P. Brøndsted, “Wind turbine blades: An end of life perspective,” in *MARE-WINT: New Materials and Reliability in Offshore Wind Turbine Technology*, W. Ostachowicz, M. McGugan, J.-U. Schröder-Hinrichs, and M. Luczak, Eds., Cham: Springer International Publishing, 2016, pp. 421–432. DOI: [10.1007/978-3-319-39095-6_23](https://doi.org/10.1007/978-3-319-39095-6_23).
- [11] J. Chen, J. Wang, and A. Ni, “Recycling and reuse of composite materials for wind turbine blades: An overview,” *Journal of Reinforced Plastics and Composites*, vol. 38, no. 12, pp. 567–577, Jun. 2019. DOI: [10.1177/0731684419833470](https://doi.org/10.1177/0731684419833470).
- [12] Decomblades Consortium. “Recycling technologies,” Decomblades. (2021), [Online]. Available: <https://decomblades.dk/>.
- [13] Siemens Gamesa Renewable Energy. “RecyclableBlade - pioneering technology.” (Oct. 2022), [Online]. Available: <https://www.siemensgamesa.com/global/en/home/explore/journal/recyclable-blade.html>.
- [14] M. Menéndez, “Siemens gamesa pioneers wind circularity: Launch of world’s first recyclable wind turbine blade for commercial use offshore,” Siemens Gamesa Renewable Energy, Zamudio, Biscay, Spain, Press release, Sep. 2021. [Online]. Available: <https://www.siemensgamesa.com/newsroom/2021/09/launch-world-first-recyclable-wind-turbine-blade>.
- [15] WindEurope. “Wind energy and the environment.” (2024), [Online]. Available: <https://windeurope.org/about-wind/wind-energy-and-the-environment/>.
- [16] H. Vella, “An industry in the making: Diverting wind turbine blades from landfill,” *E+T Engineering and Technology*, Oct. 2022. [Online]. Available: <https://eandt.theiet.org/content/articles/2022/10/an-industry-in-the-making-diverting-wind-turbine-blades-from-landfill/>.
- [17] “Diversion of waste from landfill in europe,” European Environment Agency. (Dec. 17, 2024), [Online]. Available: <https://www.eea.europa.eu/en/analysis/indicators/diversion-of-waste-from-landfill?activeAccordion=>.
- [18] Leonidas Milios, *Municipal waste management in the netherlands*, 2013.
- [19] E. Martínez, F. Sanz, S. Pellegrini, E. Jiménez, and J. Blanco, “Life cycle assessment of a multi-megawatt wind turbine,” *Renewable Energy*, vol. 34, no. 3, pp. 667–673, Mar. 2009. DOI: [10.1016/j.renene.2008.05.020](https://doi.org/10.1016/j.renene.2008.05.020).
- [20] International Electrotechnical Commission (IEC), “Wind energy generation systems - part 1: Design requirements,” International Standard IEC 61400-1:2019, Feb. 8, 2019.
- [21] P. U. Haselbach, F. Zahle, P. Berring, S. Semenov, L. Voltá I Roqueta, and D. R. Verelst, “Blade research and demonstration platform,” vol. 1618, no. 5, p. 052073, 2020. DOI: [10.1088/1742-6596/1618/5/052073](https://doi.org/10.1088/1742-6596/1618/5/052073).
- [22] I. E. Commission, “Wind energy generation systems - part5: Wind turbine blades,” International Standard IEC 61400-5:2020, Jun. 2020.
- [23] I. E. Commission, “Wind turbines- part 23: Full-scale structural testing of rotor blades,” International Standard IEC 61400-23, Apr. 2014.

- [24] T. J. Larsen and A. M. Hansen, “How 2 HAWC2, the user’s manual,” DTU Wind Energy, Roskilde, Denmark, Technical Report Risø-R-1597(ver. 12.9)(EN), Oct. 2021.
- [25] A. Bunsell and J. Renard, *Fundamentals of Fibre Reinforced Composite Materials*, 1st ed. CRC Press, Jun. 15, 2005. DOI: [10.1201/9781420056969](https://doi.org/10.1201/9781420056969).
- [26] P. Brøndsted, H. Lilholt, and A. Lystrup, “COMPOSITE MATERIALS FOR WIND POWER TURBINE BLADES,” *Annual Review of Materials Research*, vol. 35, no. 1, pp. 505–538, Aug. 4, 2005. DOI: [10.1146/annurev.matsci.35.100303.110641](https://doi.org/10.1146/annurev.matsci.35.100303.110641).
- [27] G. Marsh, “Could thermoplastics be the answer for utility-scale wind turbine blades,” *reinforcedplastics*, Feb. 8, 2010. [Online]. Available: <https://www.reinforcedplastics.com/content/features/could-thermoplastics-be-the-answer-for-utility-scale-wind-turbine-blades>.
- [28] “THERMO-BLADE-SPINE: Development of efficient, high-rate, thermoplastic composite production methods as technology building blocks for the sustainable production of wind turbines,” Fraunhofer. (), [Online]. Available: <https://www.iwes.fraunhofer.de/en/research-projects/current-projects/thermo-blade-spine.html>.
- [29] Nantes. “ZEBRA project revolutionizes wind turbine blade recycling with arkema’s innovative closed-loop system,” EuropaWire. (Oct. 3, 2024), [Online]. Available: <https://news.europawire.eu/zebra-project-revolutionizes-wind-turbine-blade-recycling-with-arkemas-innovative-closed-loop-system/eu-press-release/2024/10/03/16/11/38/141570/>.
- [30] L. Mishnaevsky, “Sustainable end-of-life management of wind turbine blades: Overview of current and coming solutions,” *Materials*, vol. 14, no. 5, p. 1124, Feb. 27, 2021. DOI: [10.3390/ma14051124](https://doi.org/10.3390/ma14051124).
- [31] UNFCCC, “The paris agreement,” in *Paris Climate Change Conference*, Paris, France, 2015. [Online]. Available: <https://www.un.org/en/climatechange/paris-agreement>.
- [32] 3B fibreglass, *Datasheet: SE 2020 - direct roving for epoxy resins*.
- [33] A. K. Mohanty, M. Misra, and L. T. Drzal, “Sustainable bio-composites from renewable resources: Opportunities and challenges in the green materials world,” *Journal of Polymers and the Environment*, vol. 10, no. 1, pp. 19–26, Apr. 1, 2002. DOI: [10.1023/A:1021013921916](https://doi.org/10.1023/A:1021013921916).
- [34] A. La Rosa and G. Cicala, “LCA of fibre-reinforced composites,” in *Handbook of Life Cycle Assessment (LCA) of Textiles and Clothing*, Elsevier, 2015, pp. 301–323. DOI: [10.1016/B978-0-08-100169-1.00014-9](https://doi.org/10.1016/B978-0-08-100169-1.00014-9).
- [35] Y. G. Thyavihalli Girijappa, S. Mavinkere Rangappa, J. Parameswaranpillai, and S. Siengchin, “Natural fibers as sustainable and renewable resource for development of eco-friendly composites: A comprehensive review,” *Frontiers in Materials*, vol. 6, p. 226, Sep. 27, 2019. DOI: [10.3389/fmats.2019.00226](https://doi.org/10.3389/fmats.2019.00226).
- [36] A. La Rosa, G. Recca, J. Summerscales, A. Latteri, G. Cozzo, and G. Cicala, “Bio-based versus traditional polymer composites. a life cycle assessment perspective,” *Journal of Cleaner Production*, vol. 74, pp. 135–144, Jul. 2014. DOI: [10.1016/j.jclepro.2014.03.017](https://doi.org/10.1016/j.jclepro.2014.03.017).

- [37] B. Madsen and T. L. Anderson, "Volumetric composition: Fibre content and porosity," in *Green Materials; processing technologies, properties and applications*, vol. 5, World Scientific Publishers, 2013.
- [38] S. Farah, D. G. Anderson, and R. Langer, "Physical and mechanical properties of PLA, and their functions in widespread applications — a comprehensive review," *Advanced Drug Delivery Reviews*, vol. 107, pp. 367–392, Dec. 2016. DOI: [10.1016/j.addr.2016.06.012](https://doi.org/10.1016/j.addr.2016.06.012).
- [39] MatWeb LLC. "MatWeb material property data." (), [Online]. Available: <https://matweb.com/index.aspx>.
- [40] S. Joshi, L. Drzal, A. Mohanty, and S. Arora, "Are natural fiber composites environmentally superior to glass fiber reinforced composites?" *Composites Part A: Applied Science and Manufacturing*, vol. 35, no. 3, pp. 371–376, Mar. 2004. DOI: [10.1016/j.compositesa.2003.09.016](https://doi.org/10.1016/j.compositesa.2003.09.016).
- [41] J. Müssig and M. Hughes, "Reinforcements: Fibres," in *Flax and Hemp Fibres: A Natural Solution for the Composite Industry*. JEC Composites, 2012, pp. 39–60.
- [42] B. Madsen and H. Lilholt, "Guidelines for mechanical design with biocomposites - properties, weight and costs," *JEC Composites Magazine*, no. 37, Dec. 2007.
- [43] B. Madsen, A. Thygesen, and H. Lilholt, "Plant fibre composites – porosity and volumetric interaction," *Composites Science and Technology*, vol. 67, no. 7, pp. 1584–1600, Jun. 2007. DOI: [10.1016/j.compscitech.2006.07.009](https://doi.org/10.1016/j.compscitech.2006.07.009).
- [44] D. U. Shah, P. J. Schubel, and M. J. Clifford, "Can flax replace e-glass in structural composites? a small wind turbine blade case study," *Composites Part B: Engineering*, vol. 52, pp. 172–181, Sep. 2013. DOI: [10.1016/j.compositesb.2013.04.027](https://doi.org/10.1016/j.compositesb.2013.04.027).
- [45] F. Bottoli and L. Pignatti, "Design and processing of structural components in biocomposite materials – rotor blade for wind turbine cars," Risø DTU, Aug. 2011.
- [46] A. La Rosa, G. Cozzo, A. Latteri, *et al.*, "Life cycle assessment of a novel hybrid glass-hemp/thermoset composite," *Journal of Cleaner Production*, vol. 44, pp. 69–76, Apr. 2013. DOI: [10.1016/j.jclepro.2012.11.038](https://doi.org/10.1016/j.jclepro.2012.11.038).
- [47] N. Gkoloni and V. Kostopoulos, "Life cycle assessment of bio-composite laminates. a comparative study," *IOP Conference Series: Earth and Environmental Science*, vol. 899, no. 1, p. 012041, Nov. 1, 2021. DOI: [10.1088/1755-1315/899/1/012041](https://doi.org/10.1088/1755-1315/899/1/012041).
- [48] C. Markussen, F. Bottoli, L. Pignatti, *et al.*, "Applying the MECO principle to assess the environmental impact of conventional and bio-based composite materials in a case study of a small-scale wind turbine blade," 2011.
- [49] T. Batu, H. Lemu, and B. Sirhabizuh, "Study of the performance of natural fiber reinforced composites for wind turbine blade applications," *Advances in Science and Technology Research Journal*, vol. 14, no. 2, pp. 67–75, Jun. 1, 2020. DOI: [10.12913/22998624/118201](https://doi.org/10.12913/22998624/118201).
- [50] S. Boria, C. Santulli, E. Raponi, F. Sarasini, and J. Tirillò, "Evaluation of a new green composite solution for wind turbine blades," *Multiscale and Multidisciplinary Modeling, Experiments and Design*, vol. 2, no. 2, pp. 141–150, Jun. 2019. DOI: [10.1007/s41939-019-00043-4](https://doi.org/10.1007/s41939-019-00043-4).

- [51] B. Y. Mekonnen and Y. J. Mamo, “Tensile and flexural analysis of a hybrid bamboo/jute fiber-reinforced composite with polyester matrix as a sustainable green material for wind turbine blades,” *International Journal of Engineering, Transactions B: Applications*, vol. 33, no. 2, pp. 314–319, Feb. 2020, Publisher: Materials and Energy Research Center. DOI: [10.5829/IJE.2020.33.02B.16](https://doi.org/10.5829/IJE.2020.33.02B.16).
- [52] A. Gherissi, F. Alahmari, M. Fadhl, *et al.*, “Wind turbine blades structure based on palm cellulose fibers composite material,” *Epitoanyag - Journal of Silicate Based and Composite Materials*, vol. 73, no. 3, pp. 109–114, 2021. DOI: [10.14382/epitoanyag-jsbcm.2021.16](https://doi.org/10.14382/epitoanyag-jsbcm.2021.16).
- [53] G. R. Kalagi, R. Patil, and N. Nayak, “Experimental study on mechanical properties of natural fiber reinforced polymer composite materials for wind turbine blades,” *Materials Today: Proceedings*, vol. 5, no. 1, pp. 2588–2596, 2018. DOI: [10.1016/j.matpr.2017.11.043](https://doi.org/10.1016/j.matpr.2017.11.043).
- [54] M. H. Hansen and L. C. Henriksen, “Basic DTU wind energy controller,” DTU Wind Energy, Roskilde, Denmark, Technical Report E-0018, 2013.
- [55] J. Rinker, *How wind turbines are modelled in HAWC input files*, LAC course 46320.
- [56] DNVGL, “Rotor blades for wind turbines,” International Standard DNVGL-ST-0376, Dec. 2015.
- [57] *Abaqus 6.6 user manual*. [Online]. Available: <https://classes.engineering.wustl.edu/2009/spring/mase5513/abaqus/docs/v6.6/>.
- [58] P. U. Haselbach, *Workflow from blade modelling tool to abaqus model with conventional shell elements*. 2022.
- [59] P. U. Haselbach and P. Berring, “Spar cap/shear web debonding under fatigue loading studied on the DTU 12.6m wind turbine blade,” *Procedia Structural Integrity*, vol. 57, pp. 169–178, 2024. DOI: [10.1016/j.prostr.2024.03.020](https://doi.org/10.1016/j.prostr.2024.03.020).
- [60] Dassault Systèmes, *SIMULIA user assistance*, 2022.
- [61] P. Ulrich Haselbach, X. Chen, and P. Berring, “Place smart, load hard - structural reinforcement of the trailing edge regions of a wind turbine blade strengthening the buckling resistance,” *Composite Structures*, no. 300, Aug. 2022. DOI: <https://doi.org/10.1016/j.compstruct.2022.116068>.
- [62] R. D. Bitsche, “Modelling of wind turbine blades with abaqus,” DTU Risø campus, Roskilde, Denmark, Presentation at the Composites Seminar, Mar. 2015. [Online]. Available: http://orbit.dtu.dk/files/106681216/Modelling_WTB_ABAQUS_Bitsche.pdf.
- [63] P. U. Haselbach, “An advanced structural trailing edge modelling method for wind turbine blades,” *Composite Structures*, vol. 180, pp. 521–530, Nov. 2017. DOI: [10.1016/j.compstruct.2017.08.029](https://doi.org/10.1016/j.compstruct.2017.08.029).
- [64] Y. Saadati, G. Lebrun, J.-F. Chatelain, and Y. Beauchamp, “Experimental investigation of failure mechanisms and evaluation of physical/mechanical properties of unidirectional flax–epoxy composites,” *Journal of Composite Materials*, vol. 54, no. 20, pp. 2781–2801, Aug. 2020. DOI: [10.1177/0021998320902243](https://doi.org/10.1177/0021998320902243).

- [65] B. Madsen, B. F. Sørensen, and H. Lilholt, “Topic 6: Stiffness of composites,” DTU Wind Energy, Roskilde, Denmark, Lecture Slides Course 46420 - Composite Materials and Fibres, 2020.
- [66] G. Wang and F. Chen, “Development of bamboo fiber-based composites,” in *Advanced High Strength Natural Fibre Composites in Construction*, Elsevier, 2017, pp. 235–255. DOI: [10.1016/B978-0-08-100411-1.00010-8](https://doi.org/10.1016/B978-0-08-100411-1.00010-8).
- [67] P. Madhu, M. R. Sanjay, P. Sentharamaikannan, S. Pradeep, S. S. Saravanakumar, and B. Yogesha, “A review on synthesis and characterization of commercially available natural fibers: Part-i,” *Journal of Natural Fibers*, vol. 16, no. 8, pp. 1132–1144, Nov. 17, 2019. DOI: [10.1080/15440478.2018.1453433](https://doi.org/10.1080/15440478.2018.1453433).
- [68] M. Heidari-Rarani, K. Bashandeh-Khodaie-Naeini, and S. M. Mirkhalaf, “Micromechanical modeling of the mechanical behavior of unidirectional composites – a comparative study,” *Journal of Reinforced Plastics and Composites*, vol. 37, no. 16, pp. 1051–1071, 2018.
- [69] Z.-M. Huang and C.-C. Zhang, “A critical assessment on the predictability of 12 micromechanics models for stiffness and strength of UD composites,” presented at the 21st International Conference on Composite Materials, Aug. 2017.
- [70] R. C. Hibbeler, *Mechanics of Materials*, 9th ed. Pearson, 2013.
- [71] C. Kassapoglou, *Design and Analysis of Composite Structures - With Applications to Aerospace Structures*, 2nd ed. Delft University of Technology, The Netherlands: John Wiley & Sons Ltd, 2013.
- [72] R. caendkoelsch. “Geometric nonlinearity – what does it mean? examples and applications,” A blog for FEM enthusiasts. (Mar. 14, 2019), [Online]. Available: https://caendkoelsch.wordpress.com/2019/03/14/geometric-nonlinearity-what-does-it-mean-post-1-2/?utm_source=chatgpt.com.
- [73] M. Peksen, “Multiphysics modelling of structural components and materials,” in *Multiphysics Modelling*, vol. 4, Elsevier, 2018, pp. 105–138. [Online]. Available: <https://doi.org/10.1016/B978-0-12-811824-5.00004-3>.
- [74] S. Corp., *Understanding nonlinear analysis*. [Online]. Available: https://www.solidworks.com/sw/docs/Nonlinear_Analysis_2010_ENG_FINAL.pdf.
- [75] J. Rinker, *Estimating a structural campbell diagram*, 2024.
- [76] O. Gözcü, T. Kim, D. R. Verelst, and M. K. McWilliam, “Swept blade dynamic investigations for a 100 kW small wind turbine,” *Energies*, vol. 15, no. 9, p. 3005, Apr. 20, 2022. DOI: [10.3390/en15093005](https://doi.org/10.3390/en15093005).
- [77] J. Liew and G. C. Larsen, “How does the quantity, resolution, and scaling of turbulence boxes affect aeroelastic simulation convergence?” *Journal of Physics: Conference Series*, vol. 2265, no. 3, p. 032049, May 1, 2022. DOI: [10.1088/1742-6596/2265/3/032049](https://doi.org/10.1088/1742-6596/2265/3/032049).
- [78] B. Madsen, B. F. Sørensen, and H. Lilholt, “Topic 7: Composite micromechanics: Strength,” DTU Wind Energy, Roskilde, Denmark, Lecture Slides Course 46420 - Composite Materials and Fibres, 2020.
- [79] E. J. Barbero, “Micromechanics,” in *Introduction to composite materials design*, ser. Composite materials analysis and design, Third edition, Boca Raton London New York: CRC Press, Taylor & Francis Group, 2017.

- [80] N. van Hoorn, C. Kassapoglou, and W. van den Brink, “Impact response of thick composite structures,” Nederlands Lucht- en Ruimtevaartcentrum (NLR), Netherlands, Technical Report NLR-TP-2017-460, Dec. 2017.
- [81] K. Okubo, T. Fujii, and Y. Yamamoto, “Development of bamboo-based polymer composites and their mechanical properties,” *Composites Part A: Applied Science and Manufacturing*, vol. 35, no. 3, pp. 377–383, Mar. 2004. DOI: [10.1016/j.compositesa.2003.09.017](https://doi.org/10.1016/j.compositesa.2003.09.017).
- [82] S. Jain, R. Kumar, and U. C. Jindal, “Mechanical behaviour of bamboo and bamboo composite,” *Journal of Materials Science*, vol. 27, no. 17, pp. 4598–4604, Sep. 1, 1992. DOI: [10.1007/BF01165993](https://doi.org/10.1007/BF01165993).
- [83] T. Richmond, L. Lods, J. Dandurand, *et al.*, “Physical and dynamic mechanical properties of continuous bamboo reinforcement/bio-based epoxy composites,” *Materials Research Express*, vol. 9, no. 1, p. 015 505, Jan. 1, 2022. DOI: [10.1088/2053-1591/ac4c1a](https://doi.org/10.1088/2053-1591/ac4c1a).
- [84] Y. Yu, X. Huang, and W. Yu, “A novel process to improve yield and mechanical performance of bamboo fiber reinforced composite via mechanical treatments,” *Composites Part B: Engineering*, vol. 56, pp. 48–53, Jan. 2014. DOI: [10.1016/j.compositesb.2013.08.007](https://doi.org/10.1016/j.compositesb.2013.08.007).
- [85] S. Ochi, “Development of high strength biodegradable composites using manila hemp fiber and starch-based biodegradable resin,” *Composites Part A: Applied Science and Manufacturing*, vol. 37, no. 11, pp. 1879–1883, Nov. 2006. DOI: [10.1016/j.compositesa.2005.12.019](https://doi.org/10.1016/j.compositesa.2005.12.019).
- [86] D. Scida, A. Bourmaud, and C. Baley, “Influence of the scattering of flax fibres properties on flax/epoxy woven ply stiffness,” *Materials & Design*, vol. 122, pp. 136–145, May 2017. DOI: [10.1016/j.matdes.2017.02.094](https://doi.org/10.1016/j.matdes.2017.02.094).
- [87] Bcomp, *Product datasheet: ampliTex 5057*, 2021. [Online]. Available: <https://www.bcomp.ch/products/amplitex/>.
- [88] Bcomp, *Product datasheet: ampliTex 5025*, 2021. [Online]. Available: <https://www.bcomp.ch/products/amplitex/>.
- [89] Eco-Technilin SAS, *Technical data sheet: FLAXDRY*, 2019. [Online]. Available: <https://eco-technilin.com/img/cms/2019%20-%20TDS%20FlaxDry.pdf>.
- [90] H. Lilholt and B. Madsen, “Properties of flax and hemp composites,” in *Flax and Hemp Fibres: A Natural Solution for the Composite Industry*. Paris, France: JEC Composites, 2012, pp. 119–140.
- [91] A. Pozo Morales, A. Güemes, A. Fernandez-Lopez, V. Carcelen Valero, and S. De La Rosa Llano, “Bamboo–polylactic acid (PLA) composite material for structural applications,” *Materials*, vol. 10, no. 11, p. 1286, Nov. 9, 2017. DOI: [10.3390/ma10111286](https://doi.org/10.3390/ma10111286).
- [92] B. Zuccarello, G. Marannano, and A. Mancino, “Optimal manufacturing and mechanical characterization of high performance biocomposites reinforced by sisal fibers,” *Composite Structures*, vol. 194, pp. 575–583, Jun. 2018. DOI: [10.1016/j.compstruct.2018.04.007](https://doi.org/10.1016/j.compstruct.2018.04.007).

-
- [93] P. Lodha and A. N. Netravali, “Characterization of stearic acid modified soy protein isolate resin and ramie fiber reinforced ‘green’ composites,” *Composites Science and Technology*, vol. 65, no. 7, pp. 1211–1225, Jun. 2005. DOI: [10.1016/j.compscitech.2004.12.036](https://doi.org/10.1016/j.compscitech.2004.12.036).
- [94] A. Bledzki and A. Jaszkiwicz, “Mechanical performance of biocomposites based on PLA and PHBV reinforced with natural fibres – a comparative study to PP,” *Composites Science and Technology*, vol. 70, no. 12, pp. 1687–1696, Oct. 2010. DOI: [10.1016/j.compscitech.2010.06.005](https://doi.org/10.1016/j.compscitech.2010.06.005).

Glossary

List of Abbreviations

Abbreviation	Property
2D	2-Dimensional
3D	3-Dimensional
abs.	absolute value
AEP	Annual Energy Production
APS	Announced Pledges Scenario
BECAS	BEam Cross-sectional Analysis Software
BIAX	Bi-axial, fibres aligned in two directions
BMT	Blade Modelling Tool
BW	Backward Whirling mode
CFD	Computational Fluid Dynamics
CO ₂	Carbon dioxide
COI	Collective edgewise mode
COP26	Climate Change Conference 26
COVID-19	Coronavirus Disease 2019
Diff.	Difference
DLC	Design Load Case
DNV GL	company: Det Norske Veritas and Germanischer Lloyd
DOF	Degrees of Freedom
DTU	Technical University of Denmark
E-glass	glass characterised by its suitability for electrical insulation
EGR	Emissions Gap Report
Eng. const.	Engineering constant
EoL	End of Life
EU	European Union
FE	Finite Element
FEA	Finite Element Analysis
FEM	Finite Element Method
FW	Forward Whirling mode
GFRC	Glass Fibre Reinforced Composite
GHG	Green House Gases
HAWC2	Horizontal Axis Wind Turbine Code second generation
HAWC2S	frequency based aeroservoelastic code for steady states computation and stability analysis of horizontal axis wind turbines
IEA	International Energy Agency
IEC 61400-1	International Electrotechnical Commission report 61400-1
IP BRM	In-Plane Blade Root Moment

Abbreviation	Property
IPCC AR6 WGI	Intergovernmental Panel on Climate Change Sixth Assessment Report Working Group I
LCA	Life Cycle Analysis
LTT	Leading edge To Trailing edge
max	maximum
min	minimum
MPC	Multiple Point Constraint
n.a.	not available
NDC	Nationally Determined Contributions
NFRC	Natural Fibre Reinforced Composite
NZE	Net Zero Emissions
OoP BRM	Out-of-Plane Blade Root Moment
Par.	Parameter
PGA	Polyglycolide or poly(glycolic acid)
PHB	Polyhydroxybutyrate
PI	Proportional Integral
PLA	Poly(lactic Acid)
PLLA	Ply-l-Lactic Acid
PTS	Pressure To Suction
S8R	8-node conventional double curved thick Shell element with Reduced integration
SC8R	8-node Continuum Shell element with Reduced integration
SCF	Stress Concentration Factor
STP	Suction To Pressure
SYM	Symmetric flapwise mode
TBD	To Be Determined
Triaxial	fibres aligned in three directions
TRL	Technology Readiness Level
TRL	Technology Readiness Level
TTL	Trailing edge To Leading edge
TU	Technical University
TU	Technical University
UD	Unidirectional, fibres aligned in one direction
UD90	Unidirectional with the fibres aligned in the direction of 90 degrees
UN	United Nations
UNEP	United Nations Environmental Program
wrt	with respect to

List of Symbols

Symbol	Unit	Property
$\alpha_{pf(1)}$	[-]	Fibre porosity constant related to fibre porosity
$\alpha_{pf(2)}$	[-]	Interface porosity constant
$\alpha_{pf(3)}$	[-]	Impregnation porosity constant
α_{pf}	[-]	Fibre porosity constant
$\alpha_{pm(1)}$	[-]	Matrix porosity constant
α_{pm}	[-]	Matrix porosity constant
δ	[mm]	Elongation
ϵ	[mm]	Material strain
ϵ_{fu}	[-]	Fibre failure strain
ϵ_{mu}	[-]	Matrix failure strain
ϵ_f	[-]	Failure strain
ϵ_i	[mm]	Material strain in the i -direction

Symbol	Unit	Property
η_{tot}	[-]	Total Efficiency
η_l	[-]	Fibre length efficiency factor
η_o	[-]	Fibre orientation efficiency factor
γ	[<i>mm</i>]	Material shear strain
γ_{ij}	[<i>mm</i>]	Material shear strain in the <i>ij</i> -plane
ν	[-]	Poisson ratio
ν_{ij}	[-]	Poisson ratio in the <i>ij</i> -plane
$\nu_{12,f}$	[-]	Fibre Poisson ratio in the 12 plane
$\nu_{12,m}$	[-]	Matrix Poisson ratio in the 12 plane
ω	[<i>rad/s</i>]	Rotational speed
$\Omega_{max \text{ allowed}}$	[<i>rad/s</i>]	Maximum allowable rotor speed
ρ	[<i>g/cm</i> ³]	Density
ρ_c	[<i>g/cm</i> ³]	Composite density
ρ_f	[<i>g/cm</i> ³]	Fibre density
ρ_m	[<i>g/cm</i> ³]	Matrix density
σ	[<i>MPa</i>]	Stress
σ	[<i>MPa</i>]	Material stress
Σ	[-]	Summation
σ_{cu}^L	[<i>MPa</i>]	Longitudinal composite strength
σ_{cu}^T	[<i>MPa</i>]	Transverse composite strength
σ'_f	[<i>MPa</i>]	Stress carried by the fibres upon matrix failure
σ_{fu}	[<i>MPa</i>]	Tensile failure strength of the fibres
σ'_m	[<i>MPa</i>]	Stress carried by the matrix upon fibre failure
σ_{mu}	[<i>MPa</i>]	Tensile failure strength of the matrix
σ_1^c	[<i>MPa</i>]	Longitudinal compression strength
σ_1^t	[<i>MPa</i>]	Longitudinal tensile strength
σ_2^c	[<i>MPa</i>]	Transverse compression strength
σ_2^t	[<i>MPa</i>]	Transverse tensile strength
σ_i	[<i>MPa</i>]	Material stress in the <i>i</i> -direction
τ	[<i>MPa</i>]	Shear strength
τ_{cu}	[<i>MPa</i>]	Composite shear strength
τ_{ij}	[<i>MPa</i>]	Shear strength in the <i>ij</i> -plane
τ_{mu}	[<i>MPa</i>]	Matrix shear strength
θ	[<i>deg</i>]	Orientation angle
θ	[<i>deg</i>]	Pitch angle
A'	[<i>m</i> ²]	Area
A	[<i>m</i> ²]	Cross-section
A_m	[<i>mm</i> ²]	Cross-sectional area of cross-section <i>m</i>
c	[-]	Parameter equal to cosine of θ
C	[-]	Laminate stiffness matrix
C_{ij}	[-]	Laminate stiffness matrix entries
C_p	[-]	Power coefficient
C_v	[-]	Void coefficient
E	[<i>MPa</i>]	Young's Modulus
$E_{c,1}$	[<i>MPa</i>]	Composite longitudinal stiffness
$E_{c,2}$	[<i>MPa</i>]	Composite transverse stiffness
$E_{c,3}$	[<i>MPa</i>]	Composite out-of-plane stiffness
$E_{f,2}$	[<i>MPa</i>]	Fibre transverse stiffness
E_i	[<i>MPa</i>]	Young's Modulus in the <i>i</i> -direction
E_{ij}	[<i>MPa</i>]	Young's Modulus in the <i>ij</i> -plane
E11	[-]	Strain in the direction of coordinate axis 1 (longitudinal)
E12	[-]	Strain in the coordinate axis 12 plane (shear)
E22	[-]	Strain in the direction of coordinate axis 2
E_f	[<i>MPa</i>]	Fibre (longitudinal) stiffness
E_m	[<i>MPa</i>]	Matrix (longitudinal) stiffness
$E_{m,2}$	[<i>MPa</i>]	Matrix transverse stiffness

Symbol	Unit	Property
F	[N]	Force
F_i	[-]	Coefficients of the Tsai-Wu failure criterion
G	[MPa]	Shear Modulus
$G_{12,c}$	[MPa]	Composite shear stiffness in the 12 plane
$G_{23,c}$	[MPa]	Composite shear stiffness in the 23 plane
G_i	[MPa]	Shear Modulus in the i -direction
G_{ij}	[MPa]	Shear Modulus in the ij -plane
G_f	[MPa]	Fibre shear stiffness
G_m	[MPa]	Matrix shear stiffness
h	[mm]	laminate thickness
i	[-]	Indexing number
j	[-]	Indexing number
K	[Nm/(rad/s) ²]	Optimal C_p tracking K factor
k	[-]	Emperical correction factor
K_{Iq}	[Nm/(rad/s)]	Integral gain of torque controller
K_{Pg}	[Nm/(rad/s)]	Proportional gain of torque controller
K_1	[deg]	Coefficient of linear term in aerodynamic gain scheduling
K_2	[deg ²]	Coefficient of quadratic term in aerodynamic gain scheduling
K_i	[Nm/rad]	Integral gain of torque controller
K_i	[rad/rad]	Proportional gain of pitch controller
K_p	[Nm/(rad/s)]	Proportional gain of torque controller
K_p	[rad/(rad/s)]	Proportional gain of pitch controller
L	[m]	Length
m	[kg]	Mass
M	[Nm]	Moment
m	[-]	Indexing number
N	[-]	Amount
n	[-]	Indexing number
n	[-]	Porosity efficiency exponent
P	[W]	Power
P_{elec}	[W]	Electrical power
R	[m]	Radius
r_m	[mm]	Radial position of cross-section m
R	[-]	Correlation coefficient
RM3	[N/mm]	Reaction moment around coordinate axis 3
s	[-]	Parameter equal to sine of θ
S	[-]	Laminate compliance matrix
S11	[MPa]	Stress in the direction of coordinate axis 1 (longitudinal)
S12	[MPa]	Stress in the coordinate axis 12 plane (shear)
S22	[MPa]	Stress in the direction of coordinate axis 2
S^L	[MPa]	Transverse shear strength
S^T	[MPa]	Longitudinal shear strength
S_{ij}	[-]	Laminate compliance matrix entries
s_n	[mm]	Curve length of region n
T	[N]	Thrust
T	[Nm]	Torque
t	[mm]	Thickness
t	[mm]	laminate ply thickness
t	[s]	Time
t_n	[mm]	Thickness of laminate region n
U	[mm]	Deflection
U1	[mm]	Deflection along coordinate axis 1
U2	[mm]	Deflection along coordinate axis 2
U3	[mm]	Deflection along coordinate axis 3
UR	[°]	Rotational deflection
v	[m/s]	Velocity
v	[mm]	Deflection

Symbol	Unit	Property
V	$[m/s]$	Wind speed
V	$[mm^3]$	Volume
$V_{fc,f}$	$[-]$	Fibre volume fraction criterion for multiple fibre cracking failure mode
$V_{fc,m}$	$[-]$	Fibre volume fraction criterion for multiple matrix cracking failure mode
$V_{rated\ tip\ speed}$	$[m/s]$	Rated wind speed
V_f	$[-]$	Fibre volume fraction
V_m	$[-]$	Matrix volume fraction
V_p	$[-]$	Porosity volume fraction
V_v	$[-]$	Void volume fraction
V_y	$[m/s]$	Wind speed in the direction of the y-coordinate
W_f	$[-]$	Fibre weight fraction
X^C	$[MPa]$	Longitudinal compression strength
X^T	$[MPa]$	Longitudinal tensile strength
Y^C	$[MPa]$	Transverse compression strength
Y^T	$[MPa]$	Transverse tensile strength
1P	[Hz]	frequency equal to 1x the rotational speed
3P	[Hz]	frequency equal to 3x the rotational speed
6P	[Hz]	frequency equal to 6x the rotational speed
9P	[Hz]	frequency equal to 9x the rotational speed

